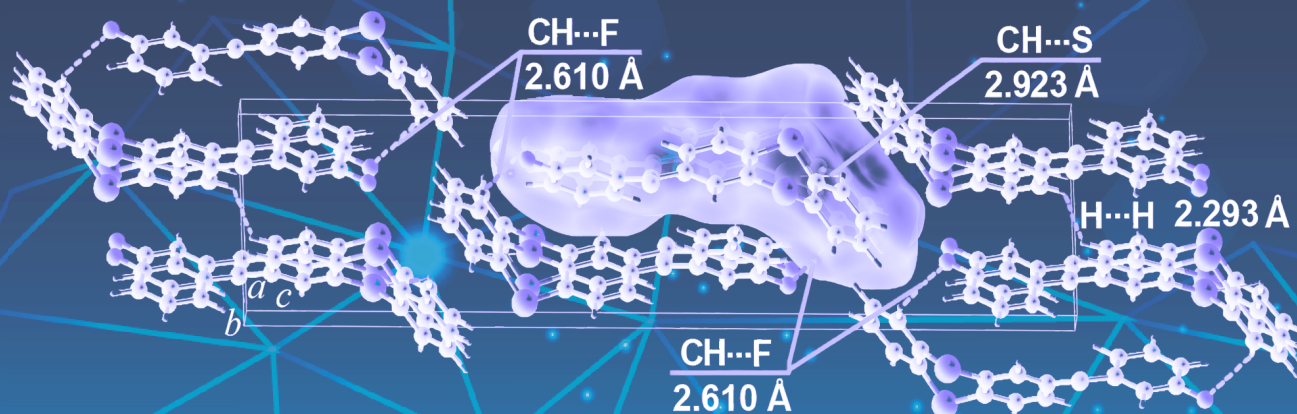# EURASIAN JOURNAL OF CHEMISTRY

2023. No. 3(111)

Special Issue

Quantum Chemistry and Quantum Nanotechnologies of Materials

Guest Editors:
Prof. Hans S. Ågren, Prof. Rashid R. Valiev, Prof. Irina S. Irgibaeva

CH···F
2.610 Å

CH···S
2.923 Å

H···H 2.293 Å

CH···F
2.610 Å

EURASIAN JOURNAL OF CHEMISTRY

2023

No. 3(111)

Special Issue

Quantum Chemistry and Quantum Nanotechnologies of Materials

Guest Editors: *Prof. Hans S. Ågren, Prof. Rashid R. Valiev, Prof. Irina S. Irgibaeva*

July–August–September

September 30th, 2022

Founded in 1996

Published 4 times a year

Karaganda, 2023

CONTENTS

PREFACE

MEMORABLE DATES

QUANTUM CHEMISTRY AND QUANTUM NANOTECHNOLOGIES OF MATERIALS

PREFACE

Hans S. Ågren[1] , Rashid R. Valiev[2, 3] , Irina S. Irgibaeva[4]

[1]Uppsala University, Sweden;
[2]University of Helsinki, Finland;
[3]National Research Tomsk State University, Russia;
[4]L.N. Gumilyov Eurasian National University, Astana, Kazakhstan

Special Issue Foreword from Guest Editors

The editors, guest editors and advisory board members of «*Eurasian Journal of Chemistry»* decided to dedicate this Special Issue entitled «***Quantum Chemistry and Quantum Nanotechnologies of Materials»*** to the anniversaries of our colleagues working in this field:

- 90th anniversary of Professor **Muldakhmetov Zainulla Muldakhmetovich** (Academician of the National Academy of Sciences of the Republic of Kazakhstan, Doctor of Chemical Sciences, Professor, Institute of Organic Synthesis and Coal Chemistry of the Republic of Kazakhstan, Karaganda, Kazakhstan);
- 80th anniversary of Professor **Minaev Boris Filippovich** (Doctor of Chemistry, Professor, Bohdan Khmelnytsky National University of Cherkasy, Cherkasy, Ukraine; Uppsala University, Uppsala, Sweden);
- 70th anniversary of Professor **Beznosyuk Sergey Alexandrovich** (Doctor of Physics and Mathematics, Professor, Altai State University, Barnaul, Russia).

In the frame of this Special Issue colleagues from Sweden, Finland, Ukraine, Kazakhstan, Russia, USA, Latvia and Nigeria share their research with readers of the «*Eurasian Journal of Chemistry»*.

The contribution of Professor **Zainulla Muldakhmetovich Muldakhmetov** to the first appearance and development of quantum chemical research in Kazakhstan is outlined in the essay by Prof. **Gazaliyev Arstan M.** and **Ivanova Nina M.** (*Institute of Organic Synthesis and Coal Chemistry of the Republic of Kazakhstan*). The essay briefly describes the creation of a scientific school of quantum chemistry in Kazakhstan with the direct participation of Professor Z.M. Muldakhmetov.

An essay dedicated to the 80th anniversary and 55 years of scientific activity of Professor Boris Filippovich Minaev is presented by Prof. **Irgibaeva Irina S.** (*L.N. Gumilyov Eurasian National University, Astana, Kazakhstan)* and **Minaeva Valentina A.** (*Bohdan Khmelnytsky National University, Cherkasy, Ukraine)*. The paper reflects Minaev's great contribution to scientific research and informs about his achievements in physical organic chemistry and molecular electronics.

Professor **Sergey Alexandrovich Beznosyuk** as the founder and leader of a new direction of quantum field chemistry in subatomic quantum nanotechnologies of materials is presented in the essay by Assoc. Prof. **Zhukovsky Mark S.** (*Altai State Technical University of the name of I.I. Polzunov, Barnaul, Russia*) and **Maslova Olga A.** (*Altai State University, Barnaul, Russia*). The contribution of Professor S.A. Beznosyuk to the establishment and development of two scientific schools, namely quantum field chemistry of the condensed state at the Buketov Karaganda University and subatomic quantum nanotechnology of materials at Altai State University is shown.

An article by Prof. **Minaev Boris F.** from *Uppsala University (Sweden)* dedicates to the 90th anniversary of Zainulla M. Muldakhmetov and considers chemistry as a science about spin and electric charge of

microparticles which provide driving forces of atomic interactions and molecular structure transformations. The tria(trichlorophenyl)methyl-carbazole (TTM-Cz) radical covalently coupled with anthracene were studied in this paper in order to explain how the doublet excitation delocalized to the linked anthracene during a picosecond lifetime can be evolved into the high-multiplicity (quartet) spin state of the mixed radical-triplet type at low excitation energy in the visible region.

A review by Prof. **Beznosyuk Sergey A.** *(Altai State University, Barnaul, Russia)* analyzes the future development of quantum nanotechnology based on attosecond physics of the subatomic level of the condensed. Author considered in the paper the ways of realizing the main achievements of the second quantum revolution in subatomic nanotechnologies of materials, namely quantum entanglement, quantum contextuality and quantum dissipativity.

A review by Prof. **Kucherenko Michael G.** and Prof. **Chmereva Tatiana M**. (*Orenburg State University, Russia*) is focused on the quantum theory of electronic energy transfer in a layered nanostructure with molecular J-aggregates of polymethine dyes. The authors briefly analyze a series of works that laid the foundation for a general quantum description of the features of the exciton-plasmon and exciton-exciton interactions in hybrid organometallic nanosystems, as well as the kinetics of phototransformations of quasiparticles, taking into account the mesoscopic specifics inherent in such nanosystems.

Prof. *Valiev Rashid R.* and coauthors (*National Research Tomsk State University, Russia)* studied relationship between the electric polarizability and aromaticity of metallocene-containing macrocycles. Magnetically induced ring currents, polarizability and second hyperpolarizability for metallocene-containing macrocyclic molecules were evaluated by means of density functional theory (B3LYP/def2-TZVP) calculations. It was shown that the aromatic character and the number of conjugated electrons in the structure are the key factors leading to an increase in the polarizability of the studied molecules.

Prof. **Ibrayev Niyazbek Kh.** and Dr. **Seliverstova Evgeniya V.** from *Karaganda University of the name of academician E.A. Buketov, Kazakhstan* synthesized S,N-doped carbon quantum dots (CQD) based on citric acid and L-cysteine. The properties of the long-lived luminescence of CQDs solutions were studied. It was shown that the synthesized CQDs species are the singlet oxygen sensitizers, as evidenced by the observed luminescence of molecular oxygen upon excitation of solutions in the CQDs absorption band.

The article by Prof. **Semire Banjo** (*Ladoke Akintola University of Technology, Ogbomoso, Nigeria*) and coauthors is focused on the TD-DFT and DFT investigation of electron transporting efficiency of 2-cyano-2-pyran-4-ylidene-acetic acid and 2-cyanoprop-2-enoic acid as acceptors for thiophene-based π-linkers dye-sensitized solar cells. B3LYP/6-31G** level of theory was used by authors to study the molecular architecture of the donor-π-acceptor (D-π-A) type of dyes. The molecular and electronic properties, light harvesting efficiency, open circuit voltage (V_{OC}), injection force (ΔG^{inject}), regeneration force (ΔG^{regen}) and excitation state lifetime (τ_{esl}) were calculated.

Researchers from *National Research Tomsk State University, Russia* (Prof. **Cherepanov Victor N.** and **Sunchugashev Dmitry A.**) studied vibronic emission spectra of dithiophene and terthiophene molecules and their complexes with hydrogen sulfide and its dimmer at the TD-DFT / CAM-B3LYP / 6-31G(d) theory level. Clear vibronic structure was shown for the emission spectra of bithiophene and terthiophene molecules. As a result of calculations, it was found that the positions of peaks in the vibronic emission spectra of these compounds agreed well with the experimental data.

Prof. **Minaev Boris F.** (*Bohdan Khmelnytsky National University, Cherkasy, Ukraine*) and coauthors highlight IR absorption spectra of the recently synthesized series of benzoyl-containing thianthrene derivatives in the context of their structural identification. A good agreement between experimental data and DFT calculated by the author's IR spectra provides additional structural support to results of the X-ray diffraction analysis of all synthesized compounds. The paper also presents the Hirshfeld surfaces analysis of the 3-fluorobenzoylthianthrene (**T3F**), which was carried out to study intermolecular interactions in the T3F crystal.

Mechanisms of docking of superoxide ions in the catalytic cycle of manganese and iron superoxide dismutases was studied by Prof. **Beznosyuk Sergey A.** *(Altai State University, Barnaul, Russia)* and coauthors. At the level of a pure quantum-chemical calculation using an ORCA 5.0.3 program, a PBE functional and a def2-SVP and def2-TZVP basis sets, the possible mechanisms of superoxide ions binding to the active sites of enzymes, the electron transfer distances and their characteristics were established.

Prof. **Irgibaeva Irina S.** (*L.N. Gumilyov Eurasian National University, Astana, Kazakhstan*) and coauthors presented quantum-chemical study of 5-(4'-dimethylaminobenzylidene)barbituric acid aggregation. The

unusual spectral behavior of 5-(4'-dimethylaminobenzylidene)barbituric acid was shown theoretically by DFT and TD DFT methods using the Gaussian 98 program. Zindo and *ab initio* calculations confirmed the appearance of a new band during aggregation and its shift to the red region with an increase in the number of molecules.

Quantum-chemical calculations of the magnetic properties (magnetically induced ring-current strength, magnetizability) of even- and odd-number cyclo[n]carbons (n = 10–34) is reported by Prof. **Valiev Rashid R.** and coauthors (*National Research Tomsk State University, Russia*). The total energy of the studied molecules as a function of the external magnetic field was found for the first time. The obtained dependences predict correctly the magnetic nature of cyclo[*n*]carbons.

Dr. *Aldongarov Anuar A.* and coauthors (*L.N. Gumilyov Eurasian National University, Astana, Kazakhstan*) presented theoretical study of charge mobility properties of complexes $Si(DPP)(CH_3)_2$ and $Si(bzimpy)(CH_3)_2$. Data on the calculation of reorganization energies, intermolecular transfer integrals, transfer rates and charge mobility for the optimized structures of pentacoordinated silicon complexes $Si(DPP)(CH_3)_2$ and $Si(bzimpy)(CH_3)_2$ were obtained using the B3LYP hybrid functional and the 6-31G* basis set with the help of Gaussian09 program.

Theoretical approach was used by Prof. **Abulyaissova Lyazzat K.** and coauthors (*Karaganda University of the name of academician E.A. Buketov, Kazakhstan*) to study the intramolecular interactions of two aminoglycoside antibiotics. Quantum chemical modeling and full geometry optimization of sisomicin and gentamicin were carried out by the authors using Gaussian16 program and DFT-based B3LYP method with a split-valence 6-311G(d) and Dunning's correlation consistent cc-pVDZ basis sets. Based on the obtained data, classical electrostatic nature of the weak H-bonds and conjugation effects stabilizing the molecules were suggested.

The team of authors led by Prof. **Nikolskiy Sergey N.** (*Karaganda University of the name of academician E.A. Buketov, Kazakhstan*)) reported the theoretical study of proton transfer dynamics in complexes of some substituted benzoic acids with 3,6-di-tert-butyl-2-hydroxyphenoxyl radical. The calculations were performed by the DFT method at the UB3LYP/6-31G+(d,p) level of theory in vacuum and toluene medium using Gaussian16 program. Geometric and kinetic parameters of complexes with o-, p-, and m-isomers of nitrobenzoic and chlorobenzoic acids were calculated.

In this Special Issue you will find authors from 8 countries, with 12 of the 17 papers involving researchers from outside the Kazakhstan. The Guest Editors of this Special Issue are really pleased with the result and hope what the compiled articles will provide a lot of new knowledge and a positive reader experience!

Information about Guest Editors*

Ågren, Hans S. — Doctor of Physical Sciences, Professor, Ångstrom Laboratory, Department of Physics and Astronomy, Uppsala University, P.O. Box 256, SE-752 37, Uppsala, Sweden; e-mail: hans.agren@physics.uu.se, hagren@kth.se; https://orcid.org/0000-0002-1763-9383

Valiev, Rashid Rinatovich — Doctor of Chemical Sciences, Senior Researcher, University of Helsinki, P.O. Box 4 (Yliopistonkatu 3), 00014, Helsinki, Finland; Assistant Professor, National Research Tomsk State University, 36 Lenin Avenue, 634050, Tomsk, Russia; e-mail: valievrashid@mail.ru; http://orcid.org/0000-0002-2088-2608

Irgibaeva, Irina Smailovna — Doctor of Chemical Sciences, Professor of Chemistry Department, L.N. Gumilyov Eurasian National University, Satpayev street, 2, 010000, Astana, Kazakhstan; e-mail: irgsm@mail.ru; https://orcid.org/0000-0003-2408-8935

_____
*The editor's name is presented in the order: *Last Name, First and Middle Names*

MEMORABLE DATES

Arstan M. Gazaliyev [ID], Nina M. Ivanova* [ID]

LLP "Institute of Organic Synthesis and Coal Chemistry of the Republic of Kazakhstan", Karaganda, Kazakhstan
(*Corresponding author's e-mail: nmiva@mail.ru)

Z.M. Muldakhmetov — a Creator of the Scientific School of Quantum Chemistry in Kazakhstan

This year, the famous scientist and organizer of science and education in Kazakhstan, Academician of the National Academy of Sciences of the Republic of Kazakhstan Z.M. Muldakhmetov turns 90 years old. His scientific activity is closely connected with such branches of the theory of the structure of matter as molecular spectroscopy and quantum chemistry. His path in science reflects the history of the development of these scientific disciplines. The article gives a brief description of the creation of a scientific school of quantum chemistry in Kazakhstan with the direct participation of Z.M. Muldakhmetov.

One of the significant merits of Zainulla Muldakhmetovich Muldakhmetov is the introduction and development of quantum-chemical research in Kazakhstan. The rapid development of the ideas of quantum mechanics and quantum chemistry during the formative years of Z.M. Muldakhmetov as a scientist and understanding of their role in creating the foundations of the theory of the structure of matter led him to the desire to continue his spectroscopic research using the methods of quantum chemistry.

Zainulla Muldakhmetovich was born on August 3, 1933 in the village of Oktyabr, Presnovsky district, North Kazakhstan region. In 1952, he finished Chistov secondary school and entered the Faculty of Physics and Mathematics of the Alma-Ata Pedagogical Institute named after Abay. After graduation from the Institute Z.M. Muldakhmetov worked as a physics teacher in a rural school for three years. In 1959, he entered the graduate school of the Moscow Institute of Fine Chemical Technology named after M.V. Lomonosov.

In graduate school under the guidance of Professor M.M. Sushchinsky, the young scientist studied second-order lines in the vibrational spectra of molecules [1–3]. A comprehensive study of the second-order lines in the Raman spectra (RS) and infrared (IR) absorption spectra of a number of polyatomic molecules was conducted: benzene, hexadeuterobenzene, chloroform, deuterochloroform, deuterocyclohexane, etc. The spectra of the last two deuteroderivatives were studied for the first time. For these compounds, quantitative data were obtained on frequencies, intensities, and the degree of depolarization of the observed lines, and the vibration anharmonicity coefficients were calculated. Based on the studies of second-order lines and comparison of the obtained results with the literature data, some fundamental frequencies were refined. In 1963 Z.M. Muldakhmetov successfully defended his dissertation for a candidate degree in physical and mathematical sciences.

Spectroscopic studies of polyatomic molecules Z.M. Muldakhmetov could continue in 1965 after a short teaching career at the Kazakh State University named after S.M. Kirov and work as Vice-Rector of the

Tselinograd Pedagogical Institute. He was appointed head of the Laboratory of spectroscopy of the Chemical and Metallurgical Institute of the Academy of Sciences of the Kazakh SSR and worked in this position for almost ten years. It was when Z.M. Muldakhmetov and his collaborators began research on the study of the structure of organic molecules using quantum chemistry methods. During these years, the laboratory was equipped with modern equipment necessary for research: two German IR spectrophotometers, UV, NMR and Raman spectrometers. An important acquisition at that time was the electronic computer "Minsk-22" (Photo 1). The research objects of the laboratory were numerous new compounds synthesized in other laboratories of the Institute, but the main attention was paid to ethylene oxide and a number of its derivatives, including epichlorohydrin, divinyl oxide, styrene oxide, esters of glycidic acids, acetylenic and nitrile derivatives, etc. The influence of substituents, temperature, the reaction medium for their preparation on vibrational spectra, conjugation of chemical bonds, and the appearance of rotational isomers of various α-oxide compounds were studied [4–6]. The studies were carried out both by the methods of IR, Raman, NMR spectroscopy, and by semi-empirical methods of quantum chemistry (EHM (Extended Hückel method), then CNDO/2, INDO). The calculations were carried out on the Minsk-22 computer, as well as BECM-3M (Big electronic calculating machine-3M). According to the results of these studies, Z.M. Muldakhmetov and co-workers wrote the fundamental monograph "The Structure of Ethylene Oxide Derivatives" [7], which became the basis of the Z.M. Muldakhmetov's doctoral thesis "Study of structural features of α-oxide compounds molecules", which was defended in 1972.

Photo 1. Employees of the Laboratory of spectroscopy at work on the computer "Minsk-22":
S.Kh. Fazylov, I.S. Irgibaeva, N.S. Kupriyanov, and K.A. Akhmetkarimov

From 1974 to 1980, toward the Ministry of Higher and Specialized Secondary Education of the Kazakh SSR, Z.M. Muldakhmetov first worked as a Vice-Rector for scientific work at Karaganda State University (KarSU), then as a Rector of the Kazakh Chemical Technology Institute (KazChTI) in Chimkent. He paid great attention to the training of highly qualified young specialists, improving the quality of the teaching staff, construction of new educational buildings and re-equipping laboratories with the newest facilities. Zainulla Muldakhmetovich oversaw scientific research in several areas, but the main one was study of the electronic structure of molecules, intermolecular interactions and reaction mechanisms by spectroscopic and quantum chemical methods. In co-authorship with his colleagues in ongoing research, a number of articles have been published [8-11].

In the same period, a meeting occurred between Z.M. Muldakhmetov with future well-known scientists in the field of quantum chemistry — candidates of physical and mathematical sciences Boris Filippovich Minaev and Sergey Aleksandrovich Beznosyuk, who are graduates of different years of Tomsk State University. Deeply understanding the spectroscopic subtleties of the structure of molecules, Zainulla Muldakhmetovich immediately recognized in them high-level specialists and huge scientific potential in this field, and for many years provided them with comprehensive support. B.F. Minaev in 1974 was hired at

KarSU, first at the Faculty of Physics, and then he headed the Chair of Physical Chemistry at the Chemical Faculty. S.A. Beznosyuk, having arrived in 1979 on vacation from Tomsk to Chimkent, looked, in his words "from the street", to the Rector of KazChTI to know what they were doing in this Institute. Here is how he recalled this meeting: "The Rector showed great interest in my scientific direction — the quantum theory of the structure of matter. He was especially interested in a new theoretical approach at that time — the density functional method. Without hesitation Zainulla Muldakhmetovich suggested me to move to Chimkent and join his scientific team dealing with the problems of quantum chemistry. So, our long-term cooperation in the field of theoretical chemistry began" [12].

In 1980, in order to better know the scientists of Kazakhstan new achievements in the field of quantum chemistry, as well as to present Kazakhstan theoretical developments, Z.M. Muldakhmetov organized the All-Union School of Quantum Chemistry based on KazChTI. The leading scientists of quantum chemistry N.D. Sokolov, I.G. Kaplan, and many others took part in it. The classes were held in the most beautiful place — the Mashat gorge near Chimkent, and in general, according to the opinions of the school participants, it was organized very excellent.

In 1980, Z.M. Muldakhmetov was appointed Rector of the KarSU and remained in this post until 1988. During the work as a rector of this University Z.M. Muldakhmetov proved to be an experienced and skillful leader, administrator, scientist and teacher. During this period, educational buildings of the biological and physical faculties, student dormitories, a sanatorium and other facilities of the University were built. There was a computer center in which regular visitors were employees of the Chair of Physical Chemistry, who carried our quantum chemical calculations on the ES-2030 computer machine.

With his great employment, Zainulla Muldakhmetovich continued to pay much attention to the development of quantum chemical research and molecular spectroscopy at KarSU. In 1982, he organized the All-Union Conference on Theoretical Chemistry, which was also held for a week in one of the most beautiful places in Kazakhstan — Karkaralinsk. With great gratitude, Professor A.S. Masalimov, who was directly involved in this conference and who was also invited by Z.M. Muldakhmetov in 1980 still a young Candidate of sciences to work at KarSU as a specialist in the field of EPR spectroscopy, spoke in detail about this event [12]. The forum turned out to be grandiose. Well-known soviet scientists not only in the field of chemistry, but also physics, mathematics and metallurgy delivered lectures, whole discussions flared up on the fundamental problems of physical chemistry. Z.M. Muldakhmetov's followers-colleagues also made presentations: B.F. Minaev, G.A. Ketsle, S.A. Beznosyuk, I.S. Irgibaeva, V.V. Bryukhanov — the future doctors of sciences and professors. The holding of such scientific forums, when well-known scientists from all over the Soviet Union came, gave impetus to the implementation of the own research, and also contributed to the creation of friendly relations with the leading scientific centers of the country.

Z.M. Muldakhmetov with great desire attended scientific seminars of the Chair of Physical Chemistry, headed by B.F. Minaev, participated in discussions on the problems of the influence of spin-orbit interaction (SOI) on the spectral characteristics of molecules and the mechanisms of chemical reactions. We (including the author of this article, N.M. Ivanova) carried out quantum-chemical calculations mainly using the MINDO/3 method, taking into account the configurational interaction and SOI. At the same time, the members of the Chair and with the participation of the physicist-programmer I.M. Danilovich created the software package MINDO/3 + CI-2, which makes it possible to carry out calculations of molecular systems, taking into account singly and doubly excited configurations. Based on the results of calculations, several articles were published on the manifestations of SOI in molecules and its role in chemical reactions, among which are articles [13–15], as well as the fundamental monograph "Optical and magnetic properties of the triplet state" [16]. In this monograph the methods for research of triplet state of molecules are described, the calculations of the electronic structure and spectra of a number of molecules are given, the mechanisms of the occurrence of SOI in oxygen molecule and its effect on singlet-triplet transitions in organic molecules are explained, etc.

In 1984, another important event initiated by Z.M. Muldakhmetov took place for the KarSU: the second Chair of Quantum Chemistry after the Leningrad State University in the USSR was opened, which until 1989 was headed by Doctor of chemical sciences B.F. Minaev. It was the recognition of the results of research in the field of quantum chemistry, conducted by a group of scientists headed by Z.M. Muldakhmetov. In 1985, Candidate of Chemical Sciences S.A. Beznosyuk and his wife were invited to work at the Chair, A.E. Buketova and G.I. Kobzev also were hired. Photo 2 shows the members of the Chair of Quantum Chemistry. The teachers of Physics Faculty of the KarSU Yu.A. Serebrennikov, R. Mukhin and others, closely interacted with the staff of Quantum Chemistry chair. It was a very fruitful period for all members of

the Chair of Quantum Chemistry headed by Z.M. Muldakhmetov. In 1984, the Republican scientific-theoretical conference on photochemistry and photophysics of singlet oxygen was held based on KarSU. The monograph "Quantum Electrochemistry of Alkaloids" (1986) [17] was published as a result of quantum chemistry and electrochemistry chair's staff collaboration using the example of alkaloids. On the development of new approaches to the density functional theory, the theory of quantum density topology, the republican publishing house also released a monograph "Electronic theory of the structure of molecules. New Aspects" (1988) [18].

Photo 2. Employees of the Department of Quantum Chemistry: in the first row — N.M. Ivanova, I.S. Irgibaeva, E.P. Sim, in the second row — Yu.A. Kazantsev, S.A. Beznosyuk, B.F. Minaev, G.D. Rempel

In 1988 Z.M. Muldakhmetov was elected as Academician-secretary of the Central Kazakhstan Branch of the Academy of Sciences of the KazSSR and came to grips with coordinating the activities of all academic institutions in this region. In 1989 Z.M. Muldakhmetov was elected an Academician of the Academy of Sciences of the KazSSR in physical chemistry.

In the same year, the Chair of Quantum Chemistry at KarSU was headed by Dr. Chem. Sc. S.A. Beznosyuk after leaving of Professor B.F. Minaev for Ukraine to continue his research in the field of quantum chemistry at the Cherkasy State Technological University, then at the Bohdan Khmelnytsky National University of Cherkasy, where he still works, having trained a whole pleiad of students. Boris Filippovich repeatedly came to Kazakhstan, to Karaganda, lectured University students, participated in conferences and met with Z.M. Muldakhmetov. After one of these visits, Boris Filippovich sent a letter of thanks to Zainulla Muldakhmetovich, in which he wrote: "Time flies, but the warmth of human friendship remains between us. Your friendship and the years that we worked together at KarSU are especially dear to me. I have always appreciated it, you were that person who gave me the impetus not to stop, helped me to overcome difficult phases in life, and taught me to fight for my goals."

From 1991 to the present, Z.M. Muldakhmetov is the Director of the Institute of Organic Synthesis and Coal Chemistry of the National Academy of Sciences of the Republic of Kazakhstan (today LLP "IOSCCh RK"). After his arrival at the Institute Zainulla Muldahmetovich again took up the creation of the Laboratory of spectroscopy and the organization of quantum chemical studies of the structure of organic molecules and the mechanisms of their reactions. At IOSCCh at that time, the methods of quantum chemistry were already being used in the Laboratory of catalytic synthesis and, in particular, by L.K. Abulyaissova, whose scientific and pedagogical activity is still connected with quantum chemistry at the Chair of Physical and Analytical Chemistry in the E.A. Buketov Karaganda University. At the beginning of the 90s, honored chemists worked at IOSCCh, including Doctors of Chemical Sciences I.V. Kirilyus, K.A. Ayapbergenov, A.M. Gazaliev, S.M. Adekenov, Professor A.V. Shchelkunov, and young scientists were also taken on the Chair: Candidates of Physical and Mathematical Sciences K.M. Turdybekov and M.E. Agelmenev, Candidates of Chemical Sciences A.T. Edrisov, G.D. Rempel and N.M. Ivanova , united by a common direction of research into the

structure of matter under the guidance of Z.M. Muldakhmetov, but developing their own narrow research topics [19–23]. Despite the difficult financial situation in science, and throughout sovereign Kazakhstan in the 90s, personal computers began to be purchased at IOSCCh, which together with the ready-made software packages for semi-empirical calculation methods (MOPAC, AMPAC), then non-empirical methods (GAMESS, GAUSSIAN, QChem and others) contributed to the incredibly rapid spread and development of quantum chemical research in chemistry and physics.

In 1993 Z.M. Muldakhmetov was awarded the Honorary title "Honored Science Worker of the Republic of Kazakhstan".

In 1998, on the initiative of Academician Z.M. Muldakhmetov, the Russian-Kazakhstan Modern Humanitarian University was opened, later renamed the Kazakh-Russian University, with branches in many cities of Kazakhstan, which implemented an innovative opportunity to receive education remotely.

In September 2004, based on LLP "IOSCCh RK", an International scientific and theoretical conference "Molecular spectroscopy and quantum chemistry of organic compounds" was organized. Z.M. Muldakhmetov presented a review report "Quantum Chemistry and Molecular Spectroscopy in Kazakhstan" [24]. Active participation in the conference was also taken by former colleagues and students of Z.M. Muldakhmetov — B.F. Minaev, V.V. Bryukhanov, A.S. Masalimov, I.S. Irgibaeva, N.A. Mazhenov and others.

Z.M. Muldakhmetov received many awards both during the existence of the Soviet Union and in 30 years of independent Kazakhstan for his great contribution to the development of science and high technology education. And he can be proud of the achievements of his followers in scientific research, confirming the D.I. Mendeleev's well-known expression: "**All the pride of the teacher is in the students, in the growth of the seeds sown by him**." Z.M. Muldakhmetov was the supervisor and scientific consultant of dissertations at 9 Doctors of Sciences and 25 Candidates of Sciences. His followers and collaborators share their knowledge with students and young scientists not only in Kazakhstan, but also in Russia, Ukraine, and Germany.

The IOSCCh RK collective cordially congratulates You on Your magnificent 90th anniversary and wishes You further creative success, good health for many years, the joy of communicating with grandchildren and great-grandchildren, warmth and home comfort!

References

1 Muldakhmetov, Z.M. & Sushchinsky, M.M. (1963). Ob angarmonichnosti nekotorykh kharakteristicheskikh kolebanii [On the anharmonicity of certain characteristic vibrations]. *Optika i Spektroskopiia — Optics and spectroscopy*, *14*, 819–821 [in Russian].

2 Muldakhmetov, Z.M. & Sushchinsky, M.M. (1964). Issledovanie linii vtorogo poriadka v kolebatelnykh spektrakh benzola i geksadeiterobenzola [Investigation of the second-order lines in the vibrational spectra of benzene and hexadeuterobenzene]. *Optika i Spektroskopiia — Optics and spectroscopy*, *16*(2), 234–239 [in Russian].

3 Muldakhmetov, Z.M. & Sushchinsky, M.M. (1964). Linii vtorogo poriadka i angarmonichnost kolebanii molekul khlorophorma i deiterokhlorophorma [Second-order lines and anharmonicity of vibrations of chloroform and deuterochloroform molecules]. *Optika i Spektroskopiia — Optics and spectroscopy*, *17*, 45–50 [in Russian].

4 Mai, I.I., Muldakhmetov, Z.M., Ayapbergenov, K.A. & Kupriyanov, N.S. (1971). Behavior of molecules of nitriles of glycidic acids in the liquid state according to IR spectra. *Journal of Applied Chemistry, 14*, 201–204. https://doi.org/10.1007/BF00613173

5 Shokanov, A.K. & Muldakhmetov, Z.M. (1970). Issledovanie sopriazheniia khimicheskikh sviazei etilovykh efirov glitsidnykh kislot metodom kombinatsionnogo rasseianiia sveta [Investigation of the conjugation of chemical bonds of ethyl esters of glycidic acids by the method of Raman scattering of light]. Kyiv: Naukova Dumka [in Russian].

6 Muldakhmetov, Z.M., Shchelkunov, A.V., Ayapbergenov, K.A. & Mai, I.I. (1971). Electronic distribution and reactivity in certain α-epoxides. *Teor. Exp. Chem. 7*(3). 324–327. https://doi.org/10.1007/BF00525538

7 Muldakhmetov, Z.M., Ayapbergenov, K.A., Mai, I.I. & Fazylov, S.Kh. (1973). Structura proizvodnykh okisi etilena [Structure of ethylene oxide derivatives]. Alma-Ata: Nauka [in Russian].

8 Muldakhmetov, Z.M., Krichevsky, L.A. & Byistro, V.K. (1976). Okisi tretichnykh fosfinov, soderzhashchie α-epoksitsikl [Oxides of tertiary phosphines containing α-epoxycycle]. *Zhurnal obshchei khimii — Journal of General Chemistry, 46*, 4, 783–785 [in Russian].

9 Minaev, B.F., Tlebergenov, T.O. & Muldakhmetov, Z.M. (1978). Interpretatsiia fosforestsentno-mikrovolnovogo dvoinogo rezonansa v molekule SO$_2$ [Interpretation of the phosphorescent-microwave double resonance in the SO$_2$ molecule]. *Optika i spektroskopiia — Optics and Spectroscopy, 45*, 4, 679–683 [in Russian].

10 Minaev, B.F., Irgibaeva, I.S., Gabdrakipov, V.Z. & Muldakhmetov, Z.M. (1978). Study of the mechanism of the photo-decomposition of aldehydes of "type II" according to Norrish, by the CNDO/3 method. *J. Struct. Chem., 19*, 209–213. https://doi.org/10.1007/BF00746955

11 Bobrov, A.V. & Muldakhmetov, Z.M. (1981). Spectroskopiia kombinatsionnogo rasseianiia sveta [Spectroscopy of Raman scattering of light]. Alma-Ata: Nauka [in Russian].

12 Uchonyi, pedagog, nastavnik: 80-letiiu akademika Z. Moldakhmetұly posviashchaetsia [Scientist, Teacher, Tutor: Dedicated to the 80th anniversary of Academician Z. Moldakhmetuly]. (2013). Karaganda: Izdatelstvo Karagandinskogo Gosudarstvennogo Tekhnicheskogo Universiteta [in Russian and in Kazakh].

13 Minaev, B.F., Muldakhmetov, Z.M., Irgibaeva, I.S., Tlepbergenov, T.O. & Kyzhner, D.M. (1982). Quantum chemical calculation of phosphorescence microwave double resonance spectra. *Int. J. Quantum Chem., 22*, 5, 863–869. https://doi.org/10.1002/qua.560220502

14 Minaev, B.F. & Muldakhmetov, Z.M. (1984). Vliianie spin-orbitalnogo vzaimodeistviia na intensivnost opticheskikh dublet-dubletnykh i triplet-tripletnykh perekhodov v molekulakh [Influence of spin-orbit interaction on the intensity of optical doublet-doublet and triplet-triplet transitions in molecules]. *Optika i spektroskopiia — Optics and Spectroscopy*, 56, 1, 48–52 [in Russian].

15 Minaev, B.F. & Muldakhmetov, Z.M. (1985). Rol spin-orbitalnogo vzaimodeistviia v khimicheskikh reaktsiiakh [The role of spin-orbit interaction in chemical reactions]. *Doklady AN KazSSR — Reports of the Academy of Sciences of the KazSSR, 3,* 48–53 [in Russian].

16 Muldakhmetov, Z.M., Minaev, B.F. & Ketsle, G.A. (1983). Opticheskie i magnitnye svoistva tripletnogo sostoianiia [Optical and magnetic properties of the triplet state]. Alma-Ata: Nauka [in Russian].

17 Muldakhmetov, Z.M., Zhurinov, M.Zh. & Minaev, B.F. (1986). Kvantovaia elektrokhimiia alkaloidov [Quantum electrochemistry of alkaloids]. Alma-Ata: Nauka [in Russian].

18 Muldakhmetov, Z.M., Minaev, B.F. & Beznosyuk, S.A. (1988). Teoriia electronnogo stroeniia molekul (novye aspekty) [Theory of the electronic structure of molecules (new aspects)]. Alma-Ata: Nauka [in Russian].

19 Turdybekov, K.M., Adekenov, S.M., Raldugin, V.A., Muldakhmetov, Z.M. & Struchkov, Yu.T. (1995). Conformations of the α-methylene-γ-lactone ring and violation of Geissman's rule in sesquiterpene lactones. *Mendeleev Comm., 1*, 42–44. https://doi.org/10.1070/MC1995v005n02ABEH000449

20 Khatipov, S.A., Edrisov, A.T. & Milinchuk, V.K. (1995). Charge transfer during low-temperature radiolysis of styrene-butadiene block copolymers. *High Energy Chemistry, 29*, 3, 169–173.

21 Muldakhmetov, Z.M., Agelmenev, M.E. & Sovetov, E.S. (1999). Effect of substituents on the mesomorphism of acetylene compounds. *Russian J. Phys. Chem A., 73*(11), 1881–1882.

22 Rempel, G.D., Shchelkunov, A.V. & Muldakhmetov, Z.M. (1993). Quantum-chemical evaluation of the role of intermediates in the processes of synthesis-decay of acetylenylcarbinols. *J. Org. Chem., 29*, 5, 951–956 [in Russian].

23 Ivanova, N.M., Muldakhmetov, Z.M. & Shchelkunov, S.A. (1995). Quantum-chemical study of the reasons for the lability of acetylenyl-containing tosylates. *J. Org. Chem., 31*, 7, 1014–1017 [in Russian].

24 Muldakhmetov, Z.M. (2004). Kvantovaia khimiia i molekuliarnaia spektroskopiia v Kazakhstane [Quantum chemistry and molecular spectroscopy in Kazakhstan]. *In Proceedings of the International scientific-theoretical conference "Molecular spectroscopy and quantum chemistry of organic compounds".* Karaganda: Izdatelstvo Kostanaiskogo Regionalnogo Universiteta [in Russian].

Information about addressee and authors*

Muldakhmetov, Zainulla Muldakhmetovich — Doctor of Chemical Sciences, Academician of the National Academy of Sciences, Director of LLP "Institute of Organic Synthesis and Coal Chemistry of the Republic of Kazakhstan", Alikhanov Street, 1, Karaganda, 100000, Kazakhstan, e-mail: zmm_ioscc@mail.ru; https://orcid.org/0000-0001-9497-2545

Gazaliyev, Arstan Maulenovich — Doctor of Chemical Sciences, Academician of the National Academy of Sciences, Deputy Director of LLP "Institute of Organic Synthesis and Coal Chemistry of the Republic of Kazakhstan", Alikhanov Street, 1, Karaganda, 100000, Kazakhstan, e-mail: gazaliyev51@mail.ru; https://orcid.org/0000-0003-2161-0329

Ivanova, Nina Mikhailovna — Full Professor, Doctor of Chemical Sciences, Head of the Laboratory of Electrocatalysis and Quantum-chemical Research, LLP "Institute of Organic Synthesis and Coal Chemistry of the Republic of Kazakhstan", Alikhanov Street, 1, Karaganda, 100000, Kazakhstan; e-mail: nmiva@mail.ru; https://orcid.org/0000-0001-8564-8006

_____

*The author's name is presented in the order: *Last Name, First and Middle Names*

Irina S. Irgibaeva[1]* , Valentina A. Minaeva[2]

[1]L.N. Gumilyov Eurasian National University, Astana, Kazakhstan;
[2]Department of Chemistry and Nanomaterials Science, Bohdan Khmelnytsky National University, Cherkasy, Ukraine
(*Corresponding author`s e-mail: irgsm@mail.ru)

Professor Boris Filippovich Minaev: More than Half a Century of Scientific Activity and the 80th Anniversary of His Birth

The article highlights the main periods of life, scientific and pedagogical activity of Boris Filippovich Minaev: Doctor of Chemical Sciences, Professor, Academician of the Academy of Sciences of the Higher School of Ukraine, Honored Worker of Science and Technology of Ukraine. The article reflects Minaev's great contribution to scientific research and informs about his achievements in the field of physical organic chemistry and molecular electronics. At the end of this article an overview of his most important scientific papers is presented.

The former Head of the Department of Chemistry and Nanomaterials Science at the Bohdan Khmelnytsky National University, Professor Boris Minaev celebrates the 80th anniversary in this year. At the same time, we mark another remarkable date — 55 years of his scientific activity.

B.F. Minaev was born on September 21, 1943 in Sverdlovsk (now Yekaterinburg) in a family of employees. After the war, his father, Filip Prokopovich, supervised the Novgorod and Semipalatinsk Regional Executive Committee, the Ministry of Building Materials Industry in Kazakhstan Republic, therefore the family often moved from one end of the Soviet Union to another. In 1962, B. Minaev graduated from secondary school No. 3 in Karaganda and entered the Faculty of Physics of the Tomsk State University named after V. V. Kuibyshev (TSU). His first scientific research was devoted to the calculations of nitro compounds by the Hückel method. He began this study in his third year at the University. In 1967, Boris Minaev graduated from the University and entered the post-graduate school at the Optics and Spectroscopy Department of TSU. Even then, the young PhD student was fascinated by the quantum chemistry methods, which he used to calculate the electronic and spectral properties of molecules [1]. At the beginning of 1973 he defended his PhD thesis for the degree of Candidate of Physical and Mathematical Sciences on the topic: "Spin-Orbital Coupling Effects in the Optical and EPR Spectra of Molecules and Radicals".

From 1974 to 1988, Boris Minaev worked first as a docent of the Theoretical Physics Department and then as a head of the Physical Chemistry Department at the Karaganda State University. At that time, Minaev developed his famous theory of the singlet-triplet transitions intensity in the visible and near-IR specrtal regions of molecular oxygen [2–9]. In the upper atmosphere, these weak transitions have a purely magnetic nature and occur due to a very specific Spin-Orbit Coupling (SOC) in the O_2 molecule. In 1978, Minaev showed that the well-known red Fraunhofer line of the sunlight absorbed by the atmosphere actually borrows its intensity from the EPR magnetic transition between spin sublevels of the ground triplet state in the O_2 molecule. This unusual nature of optical absorption was for first-time discovered in molecular spectroscopy [2]. Two years later, following the same principles, Minaev explained the specific luminescence enhancement of the singlet ($a^1\Delta_g$) oxygen in solutions.

In 1984, B. Minaev defended his doctoral thesis in the specialty 02.00.04–Physical Chemistry. Subject of doctoral dissertation: "Theoretical Analysis and Prognostication of Spin-Orbit Coupling Effects in Molecular Spectroscopy and Chemical Kinetics". In a letter to the rector of Karaganda State University professor Z.M. Muldakhmetov, signed by the head of the Expert Council of the Suprim Appraisal Commission of the USSR Academician V.A. Legasov, B. Minaev was allowed to apply for the degree of Doctor of Chemical Sciences on the basis of defending an abstract without writing an entire dissertation on the totality of scien-

13

tific articles. The defense took place in the *N.N. Semenov Institute of Chemical Physics* of the USSR Academy of Sciences in Moscow and aroused a great interest in the scientific community. The Dissertation Council of the Institute had a group of leading scientists from the USSR Academy of Sciences (among them two Nobel laureates).

In the same year, Boris Minaev headed a newly created Quantum Chemistry Department at the Karaganda State University (Photo 1) which was the second one in the former Soviet Union. During that time he educated six PhD candidates, five of them later became professors and defended doctoral dissertations (Photo 2).

Photo 1. B.F. Minaev in the Quantum Chemistry Laboratory (Karaganda, 1985)

Photo 2. Boris Minaev with colleagues and PhD students
of the Quantum Chemistry Department (Karaganda, 1980)

That time Minaev and Muldakhmetov's scientific school took a strong position in the quantum chemistry of the former USSR and gained wide popularity abroad. Working at the Karaganda State University, Prof. Minaev developed an actual at that time the Optical Detection of Magnetic Resonance (ODMR) theory in the low-temperature phosphorescence spectra of molecular crystals and the emission intensity of singlet oxygen in the gas phase and solutions [2–5]. This theory was first reported by B. Minaev in 1982 at the All-Union School of Quantum Chemistry (Karkaralinsk, near Karaganda), but the theory was widely recognized only after 1997, when German physicists performed its direct verification based on the impulse experiments.

Growing chaos as a result of perestroika and the collapse of the USSR forced B. Minaev to leave Kazakhstan. He was invited to the post of the head of the department of chemistry at the branch of the Kyiv

Polytechnic Institute in Cherkassy (Ukraine). Since February 1988, he worked in this branch, which was later transformed into the Cherkasy State Technological University (ChSTU). During his work in ChSTU, B. Minaev prepared four candidates of chemical sciences, one of them subsequently defended his doctoral dissertation in chemistry.

At the same time, Professor Minaev gave lectures on quantum chemistry at the National University named after Bohdan Khmelnytsky in Cherkasy (ChNU). In 2007, he was appointed the head of the Department of Organic Chemistry of ChNU, and then (2016) — the head of the Department of Chemistry and Nanomaterials Science of ChNU.

Thus, for the 35-year period of intense work on the electronic structure, spectra, and chemical reactivity of molecules with the account of spin-orbit coupling initiated by Professor B. Minaev, the Cherkasy School of theoretical chemistry and weak magnetic perturbations became the world-known one. In addition to the traditional approach in magnetochemistry, when magnetic perturbations are taken into account for the calculation of the hyperfine structure in EPR spectra of radicals or in a Nuclear Magnetic Resonance (NMR) of diamagnetic molecules [6–25], Minaev focuses on the role of triplet states in chemistry, catalysis, molecular electronics, and biochemistry based on calculations of SOC, spin-spin coupling, g-factor anisotropy and other internal magnetic interactions. B. Minaev with colleagues carried out numerous calculations of the electronic mechanisms for the photochemical and biochemical reactions taking into account SOC, in particular, for the T-S transitions rate in intermediate biradicals and radical pairs [26–39].

Together with colleagues from the Stockholm University, B.F. Minaev carried out quantum chemical calculations of the electronic structure for a number of flavoprotein enzymes and copper containing aminoxidases. In reaction with oxygen these enzymes formed superoxide ion O_2^- by electron transfer; the same happend upon spontaneous oxidation of hemoglobin, ferredoxin and adrenaline [29–32]. Minaev was the first who paid attention to a specific electronic open shell of the superoxide ion, its great SOC effect and explained how the magnetic torque in O_2^- induces the T-S spin inversion in radical pairs of enzyme active centers in oxidases [29, 30], mono- and di-oxygenases [31] including cofactor-free enzymes [32].

B. Minaev pays much attention to the problems of ecology [20–26, 29–35]. It is well known that the singlet $^1\Delta_g$ oxygen participates in the smog formation over smoky cities. In the upper atmosphere there is a permanent O_2 photodissociation into atoms and their reverse recombination with formation of the oxygen metastable forms, including the quintet $O_2(^5\Pi_g)$ state [35]

Recently, Minaev's group carried out quantum chemical calculations to determine intensity of the new oxygen and nitrogen singlet-triplet bands [20–25]. The absorption spectra of the singlet oxygen $b^1\Sigma_g^+ \rightarrow B^3\Sigma_u^-$ were calculated for the first time. It was found that the $a^1\Delta_g \rightarrow c^1\Sigma_u^-$ transition is comparatively intense. This fact was confirmed by the researchers from NASA (USA) [35]. B.F. Minaev has also predicted the spin-orbit effects in photo-decay of the chloric HClO and bromic HBrO acids [34], which play an important role in the photochemical cycle of ozone decay. The study of the spin-selectivity of the photolysis processes for these acids and ozone itself allows conclusion about the possible effect of external magnetic fields on the ozone layer.

In recent years B.F. Minaev pays much attention to the application of quantum chemistry in nanotechnology [36-47]. Currently, nanoclusters can be assembled "manually", which allows them to be embedded in semiconductor structures, used as memory elements, molecular conductors, etc. The unique properties of fullerenes, metal-organic frameworks, and nanotubes allow them to be used in electronics, quantum computers, DNA testing, genetic engineering and medicine [47]. This is a new branch of nanomaterial science — spintronics. These studies are closely related to the problem of spin catalysis, which B. Minaev has been studying for many years [7, 26, 29–40].

In 1993, at a seminar of the Department of Molecular Electronics in Linköping (Sweden), B. Minaev focused attention for the first time on the important spin-orbit coupling effects in Organic Light-Emitting Diodes (OLEDs) because the singlet-triplet transitions increased three-fold efficiency of recombination of electrons and holed during electroluminescence. In 1999, in the United States, this idea was implemented in the use of heavy ion complexes of Iridium. That time B. Minaev was the first who applied the DFT theory for calculation of the spin-orbit coupling in the Ir(III) complex with phenylpyridyllium ligands to explain the work of phosphorescent OLEDs [16]. In the future, the papers devoted to the study of Ir(III) complexes for OLED applications laid the foundation for new directions in the development of molecular electronics, being fixed in cooperation with the Electronics Department, Lviv Polytechnic National University [38, 39]. These OLED studies are summarized in the reviews [21, 38] which were cited 855 times according to Scopus.

An important direction in the development of the ChNU chemistry department was founded in 2011 [40] and was associated with research of circulenes, a new class of organic molecules. These materials have attracted the attention of Boris Minaev due to their high symmetry and their use as promising materials for OLED applications [36–47]. A lot of DFT calculations of the electronic structure, IR and UV-Vis spectra of tetraoxa[8]circulenes, their magnetic and aromatic properties were performed at the Department of Chemistry and Nanomaterials Science of the ChNU. This served as an impetus to strengthening solid-state DFT calculations of two-dimensional nanopolymers based on [8]circulenes, as well as modeling of novel nitrogen-containing high-energy materials. Novel graphene allotropes were proposed [41]. This paper was published in the "Chemical Physics Letters" journal (Elsevier) and was placed on the cover of this journal for the editor's choice as the most significant article in this issue [41] (Photo 3). Quite recently this and other ChNU predicted two-dimensional nano-polymers [47] were synthesized; thus, the "Cherkasit" material becomes reality.

Photo 3. Cover of the "Chemical Physics Letters" journal (Elsevier)
with novel graphene allotropes proposed in Ref. [41]

B. Minaev pays a great attention to work with young students. His lectures on biochemistry, ecology and quantum chemistry do not leave the youth indifferent. They combine high professionalism, scientific depth and emotional tension. The information about atoms and quanta is always reported interestingly, with additions from personal research experience and with humor. Working with graduate students B. Minaev is very demanding and at the same time very generous; he permanently shares his findings, gives ideas and helps a lot in this hard work on the calculation of the electronic structure of molecules. Under the supervision of Prof. Minaev 17 theses for the PhD degree in chemistry were defended.

Scientific Achievements of B. Minaev

B.F. Minaev's scientific potential has more than 600 papers in the high-ranking international journals in the field of quantum chemistry and six monographs. Three of them were published in the USSR "Science" publishing house: "The Theory of Electronic Structure of Molecules" (1988), "Quantum Electrochemistry of Alkaloids" (1986), "Optical and Magnetic Properties of the Triplet State" (1983). The textbook "Organic Electronics" (2014) was published at the Lviv Polytechnic National University, and the monograph "Electronic Structure and Spectral Properties of Heterocirculenes" (2017) was published by the ChNU publishing house. Two great sections were published in the monographs "Organic Light Emitting Diode — Material, Process and Devices" (2011) [36] and "Handbook of Computational Chemistry" (2017). The Linköping University published a voluminous book "Spin Catalysis" for five years of B. Minaev's work in Sweden. The lecture courses "Quantum Chemistry", "Spectral Research Methods", "Physics and Chemistry of Nanomaterials", "Theoretical Foundations of Organic Chemistry", "Fundamentals of Photochemistry", etc. were also developed.

B.F. Minaev was a coordinator of NATO project in terms of the REHE program (Relativistic Effects in Heavy Elements) 1998–1999 together with Prof. Pekka Pyyko, and headed the Organizing Committee of the International Conference "Relativistic Effects in Chemical Reactions" in Torun (Poland) in January 1999. He

is constantly invited for oral presentations and gives talks at the International Conferences (Sweden, Japan, Finland, USA, Spain, China, Poland, Norway, France, etc.) (Photo 4).

Photo 4. B.F. Minaev (in the center) at the Quantum Chemistry Conference in Shimkent (Kazakhstan).
On the left — Professor N.D. Sokolov (ICP, Moscow),
right — Rector of KazHTI Academic Z.M. Muldakhmetov, 1976

Minaev headed a number of scientific grants: the INTAS (1993–1996) project "Spin Catalysis"; together with Professor Tom Slanger the Joint Ukrainian-American grant CRDF (UKC1-2819-CK-06) "Spin-Forbidden Transitions of Molecular Oxygen and New Emission Bands from the Upper Atmosphere" (2006–2007); the Joint Ukrainian-Romanian grant "Design of Novel Sensitizing Dyes for Nanocrystalline TiO_2 Solar Cells on the Basis of Their Electronic Structure Calculations" (with Professor Mihai Girtu, Ovidius University in Konstanca) (2008–2009); headed together with Professor Hans Agren (KTH) Swedish-Ukrainian grant Visby "Organic Light Emitting Diodes Theory" (2008–2011); a number of projects (five) in organic synthesis and electronic structure calculations for development of OLED technology (2008–2022) governed by the Ministry of Education and Science in Ukraine. The late one is: "Interface Architecture and Electronic Mechanisms of Excitons and Excimers Formation in the Multilayer Organic Light-Emitting Diodes and Transistors".

He received the title of "Soros Professor" (1997), and a personal grant from the Chinese Academy of Sciences (CAS) in the framework of the international initiative of the President of CAS of the People's Republic of China for invited scientists (Institute of Chemistry of the Chinese Academy of Sciences, Beijing, 2015). B. Minaev is the winner of the World Prize "World Lifetime Achievement Award ABI-USA-1999", awarded with a medal "25 years for the Central-Kazakhstan Branch of the National Academy of Sciences of the Republic of Kazakhstan" for the merits in development of chemical science in the Republic of Kazakhstan (2010), and honorary title "Honoured Worker of Science and Technology of Ukraine" (2011). Recently he received the prestigious "Scopus Award Ukraine" (2016), medal of the Ukrainian Cabinet of Ministers (2017), Order of the Government of Ukraine: "Za zaslugi" 3rd class (2021).

The scientific works of Professor B.F. Minaev are well known in the world; they are published in the leading international journals and are widely cited in the scientific literature. According to Scopus agency the Hirsch Index of B.F. Minaev is equal IH = 46 (Google Scholar IH =55), and Professor B.F. Minaev ranks among the best chemists in Ukrainian universities.

A prominent scientist in the field of quantum chemistry, Doctor of Chemical Sciences, Professor, Academician of the Academy of Sciences of the Higher School of Ukraine, Honored Worker of Science and Technology of Ukraine, Professor Boris Minaev has devoted more than 55 years of his life to science and education. The personal and leadership qualities of Professor Minaev are unambiguous. On behalf of numerous colleagues, scientific followers, grateful students, we sincerely congratulate Profes-

sor B.F. Minaev on his 80th anniversary and wish great energy, health, new achievements in the scientific field and all the best!

References

1 Minaev, B.F. & Terpugova, A.F. (1969). Spin-orbit interaction in charge-transfer complexes. *Soviet Physics Journal, 12*, 1260–1263.

2 Muldahmetov, Z.M., Minaev, B.F. & Ketsle, G.A. (1983). Optical and magnetic properties of the triplet state. Nauka, Alma-Ata.

3 Minaev, B.F. (1984). Quantum-chemical investigation of the mechanism of chain-reaction initiations during hydrogen combustion. *Khimicheskaia Fizika, 3*(7), 983–987.

4 Minaev, B.F. (1985). Quantum-chemical investigation of the mechanisms of the photosensitization, luminescence, and quenching of singlet $^1\Delta_g$ oxygen in solutions. *Journal of Applied Spectroscopy, 42*(5), 518–523.

5 Irgibaeva, I.S., Minaev, B.F. & Muldakhmetov, Z.M. (1987). Study of the mechanism of the $O+ NO \rightarrow NO_2 + hv$ reaction by the MINDO/2 method taking into account a configuration-interaction. *Himicheskaia Fizika, 6*(2), 170–175.

6 Minaev, B.F., Vaara, J., Ruud, K., Vahtras, O. & Ågren, H. (1998). Internuclear distance dependence of the spin–orbit coupling contributions to proton NMR chemical shifts. *Chemical Physics Letters, 295*(5-6), 455-461.

7 Minaev, B.F. Spin effects in activation of hydrocarbons. (2001). The role of triplet states in catalysis. *Journal of Molecular Catalysis A, 171*(1–2), 53–72. https://doi.org/10.1016/S1381-1169(01)00103-0

8 Minaev, B.F. & Lunell, S. (1993). Classification of spin-orbit coupling effects in organic chemical reactions. *Zeitschrift für Physikalische Chemie, 182*, 263–284. https://doi.org/10.1524/zpch.1993.182.Part_1_2.263

9 Minaev, B.F., Lunell, L. & Kobzev, G.I. (1994). Collision-Induced intensity of the $b^1\Sigma_g^+ - a^1\Delta_g$ transition in molecular oxygen: Model calculations for the collision complex $O_2 + H_2$. *International Journal of Quantum Chemistry, 50*(4), 279–292. https://doi.org/10.1002/qua.560500405

10 Minaev, B.F., Knuts, S., Ågren, H. & Vahtras, O. (1993). The vibronically induced phosphorescence in benzene. *Chemical Physics, 175*(2–3), 245–254. https://doi.org/10.1016/0301-0104(93)85153-Y

11 Minaev, B.F., Shafranyosh, M.I., Svida, Y, Y., Sukhoviya, M.I., Shafranyosh, I.I., Baryshnikov, G.V. & Minaeva, V.A. (2014). Fragmentation of the adenine and guanine molecules induced by electron collisions. *The Journal of Chemical Physics, 140*(17), 05B601_1. https://doi.org/10.1063/1.4871881

12 Minaev, B.F., Kukueva, V.V. & Ågren, H. (1994). Configuration interaction study of the O_2–C_2H_4 exciplex: collision-induced probabilities of spin-forbidden radiative and non-radiative transitions. *Journal of the Chemical Society, Faraday Transactions, 90*(11), 1479–1486. https://doi.org/10.1039/FT9949001479

13 Sen, P., Hirel, C., Andraud, C., Aronica, C., Bretonniere, Y., Mohammed, A., Agren, H., Minaev, B, Minaeva, V. & Lindgren, M. (2010). Fluorescence and FTIR spectra analysis of trans-A_2B_2-substituted di- and tetra-phenyl porphyrins. *Materials, 3*(8), 4446–4475. DOI: 10.3390/ma308444.

14 Lindgren, M., Minaev, B., Glimsdal, E., Vestberg, R., Westlund, R. & Malmstrom, E. (2007). Electronic states and phosphorescence of dendron functionalized platinum(II) acetylides. *Journal of Luminescence, 124*(2), 302–310. https://doi.org/10.1016/j.jlumin.2006.03.019

15 Minaeva, V., Karaush-Karmazin, N., Panchenko, O., Minaev, B.F. & Ågren H. (2023). Hirshfeld and AIM Analysis of the Methylone Hydrochloride Crystal Structure and Its Impact on the IR Spectrum Combined with DFT Study. *Crystals, 13*(3), 383. https://doi.org/10.3390/cryst13030383

16 Minaev, B., Jansson, E., Agren, H. & Schrader, S. (2006). Theoretical study of phosphorescence in dye doped light emitting diodes. *Journal of Chemical Physics, 125*(23), 234704. https://doi.org/10.1063/1.2388263

17 Wu, H., Gu, L., Baryshnikov, G.V., Wang, H., Minaev, B.F., Agren, H. & Zhao, Y. (2020). Molecular Phosphorescence in Polymer Matrix with Reversible Sensitivity. *ACS Applied Materials and Interfaces, 12*(18), 20765–20774. https://doi.org/10.1021/acsami.0c04859

18 Minaev, B. (2004). Theoretical study of the external heavy atom effect on phosphorescence of free-base porphin molecule. *Spectrochimica Acta — Part A: Molecular and Biomolecular Spectroscopy, 60*(13), 3213–3224. https://doi.org/10.1016/j.saa.2004.03.005

19 Liu, Y., Xiao, Z., Liu, Y., Minaev, B., Panchenko, O. & Yan, B. (2023). Spectroscopic constants and transition properties of the SnH^+ ion excited states including spin-orbit coupling. *Journal of Quantitative Spectroscopy and Radiative Transfer, 296*, 108461. https://doi.org/10.1016/j.jqsrt.2022.108461

20 Minaev, B.F., Panchenko, O.O., Minaeva, V.A. & Ågren, H. (2022). Triplet state harvesting and search for forbidden transition intensity in the nitrogen molecule. *Frontiers in Chemistry, 10*, 1005684. https://doi.org/10.3389/fchem.2022.1005684

21 Baryshnikov, G., Minaev, B. & Ågren, H. (2017). Theory and calculation of the phosphorescence phenomenon. *Chemical Reviews, 117*(9), 6500–6537. https://doi.org/10.1021/acs.chemrev.7b00060

22 Minaev, B., Knuts, S. & Ågren, H. (1994). On the interpretation of the external heavy-atom effect on singlet-triplet transitions. *Chemical Physics, 181*(1–2), 15–28. https://doi.org/10.1016/0301-0104(94)85010-0

23 Minaev, B.F., da Silva, R.S., Panchenko, O. & Ågren, H. (2023). Prediction of new spin-forbidden transitions in the N_2 molecule-the electric dipole A′ $^5\Sigma_g^+\rightarrow$ A$^3\Sigma_u^+$ and magnetic dipole a′ $^1\Sigma_u^-\leftarrow$ A$^3\Sigma_u^-$ transitions. *The Journal of Chemical Physics*, *158*(8), 084304. https://doi.org/10.1063/5.0136465

24 Xiao, L., Yan, B. & Minaev, B.F. (2023). Near-Infrared Transitions from the Singlet Excited States to the Ground Triplet State of the S_2 Molecule. *Physchem*, *3*(1), 110–124. https://doi.org/10.3390/physchem3010009

25 Baryshnikov, G.V., Minaev, B.F. & Minaeva, V.A. (2011). Quantum-Chemical Study of Effect of Conjugation on Structure and Spectral Properties of C105 Sensitizing Dye. *Optics and Spectroscopy, 110*(3), 393–400. https://doi.org/10.1134/S0030400X10061025.

26 Minaev, B.F. & Ågren, H. (1996). Spin-catalysis phenomena. *Int. J. Quantum Chemistry, 57*(3), 519–525. https://doi.org/10.1002/(SICI)1097-461X(1996)57:3<519::AID-QUA25>3.0.CO;2-X

27 Loboda, O., Minaev, B., Vahtras, O., Schimmelpfennig, B., Agren, H., Ruud, K. & Jonsson, D. (2003). Ab initio calculations of zero-field splitting parameters in linear polyacenes. *Chemical Physics, 286*(1), 127–137. https://doi.org/10.1016/S0301-0104(02)00914-X

28 Minaev, B.F. (2004). Ab initio study of the ground state properties of molecular oxygen. *Spectrochimica Acta — Part A: Molecular and Biomolecular Spectroscopy, 60*(5), 1027–1041. https://doi.org/10.1016/S1386-1425(03)00334-2

29 Minaev, B.F. (2002). Spin effects in reductive activation of O_2 by oxydase enzymes. RIKEN Review, 44, 147–149.

30 Prabhakar, R., Siegbahn, P.E.M. & Minaev, B.F. (2003). A theoretical study of the dioxygen activation by glucose oxidase and copper amine oxidase. *Biochimica et Biophysica Acta — Proteins and Proteomics*, *1647*(1–2), 173–178. https://doi.org/10.1016/S1570-9639(03)00090-6

31 Minaev, B. (2021). Magnetic torque in superoxide ion is the main driving force of dioxygen activation in aerobic life. *Biomedical Journal of Scientific and Tech. Researches, 38*, 30462–30472. https://doi.org/10.26717/BJSTR.2021.38.006171

32 Minaev, B. (2019). How cofactor-free oxygenases can overcome spin prohibition in substrates oxygenation by dioxygen. *Chemical Physics, 521*, 61–68. https://doi.org/10.1016/j.chemphys.2019.01.021

33 Loboda, O., Tunell, I., Minaev, B. & Ågren, H. (2005). Theoretical study of triplet state properties of free-base porphin. *Chemical Physics, 312*(1–3), 299–309. https://doi.org/10.1016/j.chemphys.2004.11.041

34 Minaev, B.F. (1999). The singlet-triplet absorption and photodissociation of the HOCl, HOBr and HOI molecules calculated by MCSCF quadratic response method. *The Journal of Physical Chemistry A, 103*(36), 7294–7309. https://doi.org/10.1021/jp990203d

35 Minaev, B.F. & Panchenko, A.A. (2020). New Aspects of the Airglow Problem and Reactivity of the Dioxygen Quintet $O_2(^5\Pi_g)$ State in the MLT Region as Predicted by DFT Calculations. *The Journal of Physical Chemistry A, 124*(46), 9638–9655. https://doi.org/10.1021/acs.jpca.0c07310

36 Minaev, B., Li, X., Ning, Z., Tian, H. & Ågren, H. (2012). Organometallic materials for electroluminescent and photovoltaic devices. *In.: Organic light emitting diode — material, process and devices: Published by InTech, Croatia,* 61–100. https://doi.org/10.5772/21145

37 Baryshnikov, G.V., Valiev, R.R., Karaush, N.N., Minaeva, V.A., Sinelnikov, A.N., Pedersen, S.K., Pittelkow, M., Minaev, B.F. & Agren, H. (2016). Benzoannelated aza-, oxa-and azaoxa [8] circulenes as promising blue organic emitters. *Physical Chemistry Chemical Physics*, *18*(40), 28040–28051. https://doi.org/10.1039/c6cp03060b

38 Minaev, B., Baryshnikov, G. & Agren, H. (2014). Principles of phosphorescent organic light emitting devices. *Physical Chemistry Chemical Physics*, *16*(5), 1719–1758. https://doi.org/10.1039/C3CP53806K

39 Ivaniuk, K., Cherpak, V., Stakhira, P., Hotra, Z., Minaev, B., Baryshnikov, G., Stromylo, E., Volyniuk, D. & Grazulievicus, J., (2016). Highly luminous sky-blue organic light-emitting diodes based on the bis[(1,2)(5,6)]indoloanthracene emissive layer. *Journal of Physical Chemistry C*, *120*(11), 6206–6217. https://doi.org/10.1021/acs.jpcc.6b00696

40 Minaev, B.F., Baryshnikov, G.V. & Minaeva, V.A. (2011). Density functional theory study of electronic structure and spectra of tetraoxa[8]circulenes. *Computational and Theoretical Chemistry*, *972*(1–3), 68–74. https://doi.org/10.1016/j.comptc.2011.06.020

41 Karaush, N.N., Baryshnikov, G.V. & Minaev, B.F. (2014). DFT characterization of a new possible graphene allotrope. *Chemical Physics Letters*, *612*, 229–233. https://doi.org/10.1016/j.cplett.2014.08.025

42 Minaeva, V.A., Minaev, B.F., Baryshnikov, G.V., Ågren, H. & Pittelkow, M. (2012). Experimental and theoretical study of IR and Raman spectra of tetraoxa[8]circulenes. *Vibrational Spectroscopy*, *61*, 156–166. https://doi.org/10.1016/j.vibspec.2012.02.005

43 Baryshnikov, G.V., Minaev, B.F. & Minaeva, V.A. (2015). Electronic structure, aromaticity and spectra of hetero[8]circulenes. *Russian Chemical Reviews*, *84*(5), 455–484. https://doi.org/10.1070/RCR4445

44 Xiong, X., Deng, C.L., Minaev, B.F., Baryshnikov, G.V., Peng, X.S. & Wong, H.N.C. (2015). Tetrathio and tetraseleno[8]circulenes: synthesis, structures, and properties. *Chemistry — An Asian Journal, 10*(4), 969–975. https://doi.org/10.1002/asia.201403028

45 Baryshnikov, G.V., Minaev, B.F., Karaush, N.N. & Minaeva, V.A. (2014). Design of nanoscaled materials based on tetraoxa[8]circulene. *Physical Chemistry Chemical Physics, 16*(14), 6555–6559. https://doi.org/10.1039/C3CP55154G

46 Baryshnikov, G.V., Minaev, B.F., Karaush, N.N. & Minaeva, V.A. (2014). The art of the possible: Computational design of the 1D and 2D materials based on the tetraoxa[8]circulene monomer. *RSC Advances*, *4*(49), 25843–25851. https://doi.org/10.1039/C4RA02693D

47 Karaush-Karmazin, N., Baryshnikov, G., Minaeva, V., Panchenko, O. & Minaev, B. (2022). IR, UV-visible, NMR spectra and aromaticity of the covalent organic tetraoxa circulene frameworks. *Computational and Theoretical Chemistry, 1217*, 113900. https://doi.org/10.1016/j.comptc.2022.113900

Information about addressee and authors*

Minaev, Boris Filippovich — Doctor of Chemical Sciences, Professor, Department of Chemistry and Nanomaterials Science, Bohdan Khmelnytsky National University, Shevchenko Boulevard, 81, 18031, Cherkasy, Ukraine; Senior Researcher, Department of Physics and Astronomy, Uppsala University, SE-752 37, Uppsala, Sweden; e-mail: bfmin43@ukr.net; https://orcid.org/0000-0002-9165-9649

Minaeva, Valentina Alexandrovna — Senior Researcher, Assistant Professor, Department of Chemistry and Nanomaterials Science, Bohdan Khmelnytsky National University, Shevchenko Boulevard, 81, 18031, Cherkasy, Ukraine; e-mail: minaeva@cdu.edu.ua; https://orcid.org/0000-0001-9318-1661

Irgibaeva, Irina Smailovna (*corresponding author*) — Doctor of Chemical Sciences, Professor of Chemistry Department, L.N. Gumilyov Eurasian National University, Satpayev street, 2, 010000, Astana, Kazakhstan: irgsm@mail.ru; https://orcid.org/0000-0003-2408-8935

_____

*The author's name is presented in the order: *Last Name, First and Middle Names*

Essay

UDC 538.9+539.2+544.18

Mark S. Zhukovsky[1] (iD), Olga A. Maslova[2]* (iD)

[1]Altai State Technical University of the name of I.I. Polzunov, Barnaul, Russia;
[2]Altai State University, Barnaul, Russia
(*Corresponding author's e-mail: maslova_o.a@mail.ru)

S.A. Beznosyuk as the Founder and Leader of a New Direction of Quantum Field Chemistry in Subatomic Quantum Nanotechnologies of Materials

The article highlights the creative path of S.A. Beznosyuk, an outstanding physico-chemist, who celebrates his 70th anniversary in 2023. The main stages of his career and significant events of his scientific creativity are presented here. The contribution of Professor S.A. Beznosyuk to the establishment and development of two scientific schools, namely quantum field chemistry of the condensed state at the Karaganda Buketov University and subatomic quantum nanotechnology of materials at Altai State University is shown.

The scientist's anniversary is a good occasion to summarize what he has done, to see the significance of his works in the research area. Sergey Aleksandrovich Beznosyuk, Doctor of Physical and Mathematical Sciences, Professor, the founder and leader of a new direction in quantum chemistry and quantum nanotechnologies of materials, is a scientist whose works are widely known in the scientific circles of Russia, Kazakhstan and other countries. His name is associated with the development of a number of modern theoretical models of quantum chemistry and quantum subatomic nanotechnologies of materials.

Sergey Aleksandrovich Beznosyuk was born in the city of Shymkent, South Kazakhstan region, KazSSR, on January 5, 1953. After school, he entered Tomsk State University in the city of Tomsk, which he successfully graduated from in 1974.

After graduation from the university in 1974–1977 S.A. Beznosyuk continued his postgraduate studies at TSU and in January 1978 defended his candidate dissertation entitled "The method of spin-charge density functionals and the ground state of alkali and 3d-transition metals" in the specialty 01.04.07 — Solid State Physics. These were his most significant achievements of that period [1–4]. After graduation from graduate school in 1977, he was competitively elected to the position of a teacher at the Faculty of Physics of TSU.

In 1979, S.A. Beznosyuk received an invitation and was elected to the position of a senior researcher at the Kazakh Institute of Chemical Technology in the city of Shymkent. Here he was engaged in quantum calculations of catalysts until 1984 in a special laboratory of the Institute of Organic Catalysis and Electrochemistry of the Kazakh Academy of Sciences (Almaty). In 1984, he was awarded the academic title of Senior Researcher of the Higher Attestation Commission of the USSR in the specialty "Chemical technology and catalysis". His main works of this period are [5, 6].

In 1985, Sergey Aleksandrovich Beznosyuk was invited to the position of Associate Professor of the Quantum Chemistry Department of Karaganda State University. In the final period (1989–1994) of his fruitful scientific activity in the field of quantum field chemistry of the condensed state, he held the position of the Head of the Department of Quantum Chemistry of Karaganda State University. The main results of this period were published in [7–9].

In 1993, S.A. Beznosyuk successfully defended his doctoral thesis: "Electronic theory of active centers of microstructural transformations of materials" in the specialty 01.04.07 — Condensed Matter Physics at the Institute of Strength Physics and Materials Science (ISPMS) SB RAS (Tomsk). In 1994, he accepted an invitation to become a professor at Altai State University in Barnaul (Russia). Two years later, in 1997, he was awarded the title of Professor by the Higher Attestation Commission of the Russian Federation.

From 1994 to the present time he has been working at Altai State University. For almost 30 years of work at ASU, his track record includes the following list of achievements: Professor of the Faculty of Physics (1994–1996), the main publications of this period are [10, 11]; the Head of the Physical & Colloidal Chemistry Department (1996–2015), the main achievements of this period are published in [12–27]; the Head of the Physical & Inorganic Chemistry Department (2015 – up to the present time), the last period of research is presented in [28–37].

The scientist's authority in the research community can also be confirmed by his membership in dissertation councils. For many years, Sergey Aleksandrovich Beznosyuk was a member of doctoral dissertation councils on physics and mathematics specialties at Altai State University and Altai State Technical University of the name of I.I. Polzunov, Barnaul, Russia. Currently, S.A. Beznosyuk is a member of the Doctoral Dissertation Council in the specialty Condensed Matter Physics in ASU (Barnaul, Russia).

Since 1996 S.A. Beznosyuk has led a number of projects of Russia in the field of critical technology "Computer modeling of nanomaterials, nanodevices and nanotechnologies" on the priority direction of the development of science, technology and engineering in "Industry of nanosystems". Under his leadership, 8 fundamental studies were carried out under the programs of the Ministry of Education and Science of the Russian Federation, as well as under Russian and International grants from the Russian Foundation for Basic Research. Since 2009 Professor S.A. Beznosyuk, heading a number of significant scientific researches, has formed a powerful scientific school "Fundamentals of nanosciences and breakthrough nanotechnologies of the condensed state" at Altai State University. As part of his unique scientific school, he created scientific, methodological and educational units, namely Internet site https://comp-nano.firebaseapp.com (2011), the educational research laboratory "Computer NanoBioDesign" (2014), the network ASU — ISPMS SB RAS research laboratory "Quantum technologies of materials" (2021). The main research areas of Professor S.A. Beznosyuk include the following topics: Quantum chemistry, Physical chemistry, Physicochemistry of the condensed state, Subatomic quantum technologies of materials.

Professor S.A. Beznosyuk devotes much time to training of scientific personnel. Under his supervision 10 candidates of chemical and physical & mathematical sciences defended their theses. In 1997, S.A. Beznosyuk opened in ASU one of the first in Siberia Distance Learning Center and in 2000 created the Scientific and Methodological Institute of Open and Distance Education in ASU, which became a part of the Open University of Siberia. S.A. Beznosyuk for three years (2009–2011) was supervising educational programs for professional retraining of faculty and research staff of universities and scientific institutions of the Russian Federation in the field of nanotechnology within the framework of the unified federal program of the Ministry of Education and Science of the Russian Federation. In 1994, under the guidance of Professor S.A. Beznosyuk, the first Master's training at the Faculty of Physics began at ASU. From 2009 to 2018, S.A. Beznosyuk supervised the Master's training in physical chemistry and nanoengineering of functional and biomimetic materials at the Faculty of Chemistry of the Altai State University. About 50 people received master's degrees under those programs. In 2018, S.A. Beznosyuk developed the first in Russia innovative master's program "Quantum technologies, computer nanoengineering, physical chemistry and examination of materials" with the aim of training personnel for quantum nanotechnologies in Russia. Twenty masters of Chemistry defended their dissertations under this program.

Sergey Alexandrovich's fruitful scientific activity is reflected in about 300 scientific papers, including 67 scientific articles in 15 highly rated international journals included in the Web of Science (Hirsch index — 8) and Scopus (Hirsch index — 8) databases. He is a co-author of 7 scientific monographs and 6 textbooks (2 with a stamp), received 6 patents and 4 certificates for computer programs. The relevance of scientific results of Professor S.A. Beznosyuk is confirmed by dozens of oral and invited presentations at prestigious International conferences in the UK, France, USA, China, Italy, Russia and other world scientific centers. Due to his high level of professional excellence, he is a member of many scientific communities, such as the Federal Register of Experts in the Scientific and Technical Sphere of the Ministry of Education and Science of RF, the Central Board of the Nanotechnological Society of Russia, the Russian Professorial Assembly and others.

The merits of the celebrant were repeatedly recognized at the highest level. In 2001, S.A. Beznosyuk became an Award Winner of the Altai Territory Prize in Science and Technology. In 2005, he was awarded the Breastplate of the Honorary Worker of Higher Professional Education of the Russian Federation. He was also awarded Honorary Diploma of the International Organizing Committee of the conference "Hydrogen materials science and chemistry of carbon nanomaterials" (2009) and Honorary Diploma of the Government of the Altai Territory for many years of conscientious work and high professionalism (2018). In 2022,

S.A. Beznosyuk was awarded The Diploma of the Winner of the National Prize of Russia "Professor of the Year" in the nomination "Chemical Sciences".

On behalf of his scientific school, all his colleagues, students and friends, we congratulate Professor S.A. Beznosyuk with his 70th birthday and express our deep gratitude for his many years of work in our team! We wish Sergey Aleksandrovich good health, creative longevity, new scientific achievements, grateful students and followers!

References

1   Beznosyuk, S.A., Khon, Y.A., Kuznetsov, V.M. & Fadin, V.P. (1978). Kinetic energy of an inhomogeneous electron gas. *Soviet Physics Journal, 20, 7*. 937–940. https://doi.org//10.1007/BF00893143

2   Beznosyuk, S.A., Khon, Y.A., Kuznetsov, V.M. & Fadin, V.P. (1978). The exchange energy of a non-uniform electron gas. *Soviet Physics Journal, 20, 6*. 770–773. https://doi.org//10.1007/BF00892764

3   Beznosyuk, S.A., Khon, Y.A., Kuznetsov, V.M. & Fadin, V.P. (1978). Method of the spin density functional and the ground state of solids. *Soviet Physics Journal, 20, 10*. 1318–1322. https://doi.org//10.1007/BF00898907

4   Beznosyuk, S.A. & Fadin, V.P. (1981). Method of the spin density functional and the ground state of solids. *Soviet Physics Journal, 23, 11*. 980–983. https://doi.org//10.1007/BF00896173

5   Beznosjuk, S.A., Lytkin, V.N., Kim, L.A. & Zhanabaev, B.Z. (1983). Electronic "phase" transition of hydrogen molecules in the electron density functional method. *Soviet Physics Journal, 25, 10*. 890–892. https://doi.org//10.1007/BF00891658

6   Beznosjuk, S.A. & Kryachko, E.S. (1984). Density functional theory: approximating quasiparticle density functional. *International Journal of Quantum Chemistry, 25, 4*. 645–651. https://doi.org//10.1002/qua.560250403

7   Beznosjuk, S.A., Minaev, B.F., Dajanov, R.D. & Muldachmetov, Z.M. (1990). Approximating quasiparticle density functional calculations of small active clusters: strong electron correlation effects. *International Journal of Quantum Chemistry, 38, 6*. 779–797. https://doi.org//10.1002/qua.560380510

8   Beznosjuk, S.A., Dajanov, R.D. & Kuljanov, A.T. (1990). Density functional calculation of transition metal cluster energy surfaces. *International Journal of Quantum Chemistry*, *38*, 5. 691–698. https://doi.org//10.1002/qua.560380510

9   Beznosjuk, S. A., Minaev, B.F. & Muldachmetov, Z.M. (1991). Informative energetic structure and electronic multistability of condensed state. *Journal of Molecular Structure: THEOCHEM, 227*. 125–129. https://doi.org//10.1016/0166-1280(91)85278-F

10 Beznosyuk, S.A. (1995). Quantum rheology and the confinement of electrons in condensed-state nanostructures. *Russian Physics Journal, 37, 8*. 750–756. https://doi.org/10.1007/BF00559870

11 Beznosyuk, S.A. (1996). Concept of quantum topology of nanostructures in the condensed state. *Russian Physics Journal, 39, 5*. 492–503. https://doi.org/10.1007/BF02436791

12 Beznosjuk, S.A., Beznosjuk, M.S. & Mezentsev, D.A. (1998). Electron swarming in carbon nanostructures. *Carbon, 36, 5-6*. 717–719. https://doi.org/10.1016/S0008-6223(98)00016-5

13 Beznosjuk, S.A., Beznosjuk, M.S. & Mezentsev, D.A. (1998). Electron swarming in nanostructures. *Computational Materials Science, 14, 1-4*. 209–214. https://doi.org/10.1016/s0927-0256(98)00109-8

14 Beznosyuk, S.A., Zhukovskii, M.S. & Zhukovskaya, T.M. (2000). Effect of quantum topology of kinematic bonds on the mechanism of nanostructurtng in materials. *Russian Physics Journal, 43, 12*, 988–993. http://dx.doi.org/10.1023/A:1011395311872

15 Beznosyuk, S.A., Zhukovskii, M.S., Zhukovskaya, T.M., Kolesnikov, A.V. & Mezentsev, D.A. (2001). Characteristic topological and energy features of the positioning and transport potentials in nanosystems. *Russian Physics Journal, 44, 2*, 124–130. http://dx.doi.org/10.1023/A:1011326617732

16 Beznosyuk, S.A., Kolesnikov, A.V., Mezentsev, D.A., Zhukovsky, M.S. & Zhukovsky, T.M. (2002). Dissipative processes of information dynamics in nanosystems. *Materials Science and Engineering: C, 19, 1-2*. 91–94. https://doi.org/10.1016/S0928-4931(01)00448-9

17 Beznosyuk, S.A. (2002). Dissipative processes of information dynamics in nanosystems. *Materials Science and Engineering: C, 19, 1-2*. 369–372. https://doi.org/10.1016/S0928-4931(01)00417-9

18 Beznosyuk, S.A., Fomina, L.V., Perezhogin, A.A. & Zhukovsky, M.S. (2007). Computer modeling of hydrogen and methane transport in cellular nanostructures of amorphous ice. *Materials Science and Engineering: C, 27, 5-8*. 1390–1392. https://doi.org/10.1016/j.msec.2006.09.024

19 Beznosyuk, S.A., Lerh, Y.V., Zhukovsky, T.M. & Zhukovsky, M.S. (2007). Computer simulation of growing fractal nanodendrites by using of the multi-directed cellular automatic device. *Materials Science and Engineering: C, 27, 5-8*. 1270–1272. https://doi.org/10.1016/j.msec.2006.08.013

20 Beznosyuk, S.A., Lerh, Y.V., Vazhenin, S.V., Zhukovsky, M.S. & Zhukovsky, T.M. (2009). Self-assembling growth of fractal catalysts on fuel cell's electrode. *Journal of Nanoscience and Nanotechnology, 9, 2*. 1582–1584. https://doi.org/10.1166/jnn.2009.C207

21 Beznosyuk, S.A., Lerh, Y.V., Zhukovsky, T.M. & Zhukovsky, M.S. (2009). Informational approach to self-assembling aggregation of colloidal nanoparticles. *Materials Science and Engineering: C, 29, 3.* 884–888. https://doi.org/10.1016/j.msec.2006.08.013

22 Beznosyuk S.A., Maslova O.A., Shtobbe I.A., Zhukovsky M.S. & Zhukovsky T.M. (2009). Self-assembling growth of fractal catalysts on fuel cell's electrode. *Journal of Nanoscience and Nanotechnology, 9, 2.* 1408–1411. https://doi.org/10.1166/jnn.2009.C167

23 Beznosyuk, S.A., Maslova, O.A., Fomina, L.V. & Zhukovsky, M.S. (2009). Self-assembling of hydrogen superadsorbate in single-walled carbon nanotubes. *Superlattices and Microstructures, 46, 1-2.* 384–386. https://doi.org/10.1016/j.spmi.2008.10.006

24 Maslova, O.A., Vazhenin, S.V., Beznosyuk, S.A., Zhukovsky, T.M. & Zhukovsky, M.S. (2011). Nanosystem accumulators of hydrogen: quantum polycondensates of hydrogen biradicals in carbon nanotubes. *International Journal of Hydrogen Energy, 36, 1.* 1287–1291. https://doi.org/10.1016/j.ijhydene.2010.06.132

25 Zhukovsky, M.S., Fomina, L.V. & Beznosyuk, S.A. (2011). Computer modeling of hydrogen fuel cell subsystems: carbon nanogel electrodes and fractal nanoparticle catalysts. *International Journal of Hydrogen Energy, 36, 1.* 1212–1216. https://doi.org/10.1016/j.ijhydene.2010.06.128

26 Beznosyuk, S.A., Maslova, O.A. & Zhukovsky, M.S. (2015). Attosecond nanotechnology: NEMS of energy storage and nanostructural transformations in materials. *AIP Conference Proceedings. Advanced Materials with Hierarchical Structure for New Technologies and Reliable Structures.* 020024-28. https://doi.org/10.1063/1.4932714

27 Beznosyuk, S.A., Zhukovsky, M.S. & Zhukovsky, T.M. (2015). Theory and computer simulation of quantum NEMS energy storage in materials. *International Journal of Nanoscience, 14, 1-2.* 1460023-28. https://doi.org/10.1142/S0219581X14600230

28 Beznosyuk, S.A. & Zhukovsky, M.S. (2017). Multiscale space-time dissipative structures in materials: Two-electron genesis of nonequilibrium electromechanical interfaces. *Physical Mesomechanics, 20*, 1. 102–110. https://doi.org/10.1134/S102995991701009X

29 Beznosyuk, S.A., Maslova, O.A., Terenteva, Yu.V., Maksimov, D.Yu. & Zhukovsky, M.S. (2017). Computer simulation of attosecond nanotechnologies based on quantum NEMS in materials. *International Journal of Nanotechnology, 14, 7-8.* 590–603. https://doi.org/10.1504/IJNT.2017.083434

30 Beznosyuk, S.A., Maslova, O.A., Maksimov, D.Y. & Zhukovsky M.S. (2018). Attosecond nanotechnology: from subatomic electrostatic strings entangling electron pairs to supra-atomic quantum nanoelectromechanical systems energy storage in materials. *International Journal of Nanotechnology, 15, 4-5.* 245–257 https://doi.org/10.1504/IJNT.2018.094783

31 Beznosyuk, S.A., Maslova, O.A., Maksimov, D.Yu. & Zhukovsky, M.S. (2019). Computer simulation of hybrid quantum technologies of energy accumulation, storage, transformation and transfer in nanoenergy materials. *International Journal of Nanotechnology, 16, 6-10.* 322–333. https://doi.org/10.1504/IJNT.2019.106608

32 Beznosyuk S.A., Maslova O.A. & Zhukovsky M.S. (2019). Computer simulation of hybrid quantum technologies of energy accumulation, storage, transformation and transfer in nanoenergy materials. *International Journal of Nanotechnology, 16, 1-3.* 22–33. https://doi.org/10.1504/IJNT.2019.102389

33 Beznosyuk, S.A., Maslova, O.A. & Zhukovsky, M.S. (2019). Quantum infrastructure of attosecond sensors and actuators of nonequilibrium physical media in smart materials. *Physical Mesomechanics, 22, 5.* 432–438. https://doi.org10.1134/S1029959919050096

34 Beznosyuk S.A., Maslova O.A. & Zhukovsky M.S. (2020). Subatomic technology of quantum materials. *AIP Conference Proceedings. Physical Mesomechanics. Materials with Multilevel Hierarchical Structure and Intelligent Manufacturing Technology Advanced Materials with Hierarchical Structure for New Technologies and Reliable Structures.* 020030-34. https://doi.org/10.1063/5.0034343

35 Maslova, O.A., Ryabykh, A.V. & Beznosyuk, S.A. (2020). Computer simulation of sod interaction with reactive oxygen species in low-sized membrane cell nanostructures. *AIP Conference Proceedings. Physical Mesomechanics. Materials with Multilevel Hierarchical Structure and Intelligent Manufacturing Technology*. 020196-199. https://doi.org/10.1063/5.0034337

36 Ryabykh, A.V. Maslova, O.A. Beznosyuk, S.A. & Chikina, M.V. (2022). Quantum-Chemical Calculation of Reimination of 1,2-Ditert-Butylethanediimine with Aminoacetic Acid. *Technical Physics Letters, 48, 4.* 220–224. https://doi.org/10.1134/S1063785022070082

37 Maslova, O.A., Ryabykh, A.V. & Beznosyuk, S.A. (2022). On the Problem of the Proton Permeability of Graphene and Borophene in Different Dielectric Media. *Technical Physics Letters, 48, 316–321.* https://doi.org/10.1134/S1063785022110049

Information about addressee and authors*

Beznosyuk, Sergey Alexandrovich — Doctor of Physical and Mathematical Sciences, Professor, Head of the Physical and Inorganic Chemistry Department, Altai State University, Lenin avenue, 61, 656049, Barnaul, Russia; e-mail: bsa1953@mail.ru; https://orcid.org/0000-0002-4945-7197

Zhukovsky, Mark Sergeevich — Candidate of Chemistry, Associate Professor, Department of Information Systems in Economics, Altai State Technical University of the name of I.I. Polzunov, Russia, 656038, Barnaul, Lenin avenue, 46, Barnaul, Russia; e-mail: zhukovsky@list.ru; https://orcid.org/0000-0002-0524-9548

Maslova, Olga Andreevna (*corresponding author*) — Candidate of Physical and Mathematical Sciences, Associate Professor, Physical and Inorganic Chemistry Department, Altai State University, Lenin avenue, 61, 656049, Barnaul, Russia; e-mail: maslova_o.a@mail.ru; https://orcid.org/0000-0003-3862-3687

_____

*The author's name is presented in the order: *Last Name, First and Middle Names*

QUANTUM CHEMISTRY
AND QUANTUM NANOTECHNOLOGIES
OF MATERIALS

Dedicated to the 90th anniversary
of Zainulla M. Muldakhmetov

Boris F. Minaev[1, 2] ID

[1]Department of Physics and Astronomy, Uppsala University, Sweden;
[2]Department of Chemistry and Nanomaterials Science, Bohdan Khmelnytsky National University, Cherkasy, Ukraine
(Author′s e-mail: bfmin43@ukr.net)

Spin Catalysis in Photochemical Reactions and Its Applications to Quantum Information Nanotechnology

Chemistry as a science about spin and electric charge of micro particles which provide driving forces of atomic interactions and molecular structure transformations fits pretty well to the modern Quantum Information Science (QIS) requirements. Today's computers operate only electric current signals in the semiconductor networks but the electron-spin properties are not exploited in a large extend. Spintronics provides spin-polarized currents and manipulates magnetic spin interactions; it uses mostly solid state chemistry of heavy elements. But a rich organic chemistry of solvents and fin films offers a great potential for molecular electronics and quantum computing. Photo-excited organic complexes of the "chromophore–radical" type provide good promise for many technological applications in molecular spintronics and electronics, including QIS technology. The doublet state photo excitation of stable organic radical being delocalized onto the linked anthracene molecule within picoseconds and subsequently evolved into a quartet state for big radicals (a pure high spin state) of the mixed radical-triplet character presents a sensible spin-optical interface for qubit in quantum computing. This high-spin state is coherently addressable with EPR microwaves even at room temperature, with the optical read-out induced by intersystem crossing (ISC) to emissive triplet state. Such integration of radical luminescence and high-spin states EPR provides the organic materials involvement into emerging QIS technologies.

Keywords: spin catalysis, quantum information science, high-spin states, radical luminescence, quantum nanotechnology, spintronics.

Introduction

Molecular electronics and nano-photonics represent versatile platforms for information storage, sensing, encryption, including quantum bit science applications [1–15]. Quantum information science researches are the leading technology forces of XXI century. Quantum teleportation, quantum entanglement and quantum computer manufacturing strongly depend on the comprehensive knowledge and understanding of quantum physics and chemical nano-engineering of particular functional materials. Some IT companies (like Google and IBM) have invested great money since 2010 into hardware research of quantum computer (QC) and recently reached significant progress in the QC manufacturing and quantum cryptography [1] (the late devices are now commercially available). Quantum cipherization will substitute the widely used ciphers like RSA and ECC [6]. New functional materials based on π–conjugation of organic π–radical and chromophore repre-

sent sensible spin-optical interface to utilize unique quantum resources of organic materials. Eighty years ago, academic A.N. Terenin had opened the door to utilize such quantum resources of the triplet excited state of organic chromophores explaining their phosphorescence in solid solvents [15]. Almost simultaneously, academic E.K. Zavoisky had discovered another fundamental physical phenomenon — electron paramagnetic resonance (EPR) for studies of electron spin distribution in radicals [2]. Both discoveries provided a deep background for the spin chemistry and molecular spintronics development for the next century [1–15].

Main Part

Radicals with non-paired spins can be generated by photochemical reactions in organic solvents. Their recombination is a spin-sensitive process which depends on diffusion, concentration, intermolecular exchange and magnetic interactions [2, 3]. These radical pairs (RP) were exploited in chemically induced dynamic nuclear polarization (CIDNP) phenomena, electron spin polarization in EPR spectroscopy and in the external magnetic field effects (MFE) in radical recombination reactions [2–4] including O_2 activation by enzymes [5].

Academic Kev Minullinovich Salikhov, Director of the Zavoisky Physical-Technical Institute (who visited Karaganda State University many times and is a good friend of Zainulla Muldakhmetov) has proposed [3] that the third spin in the time-resolved ESR spectra of the light-induced radical pair (RP) can play an important role of the third observer and spin driver in the luminescent response of the whole three-radicals system. And such third observer could provide potential application in the so-called quantum teleportation, which is one of the modern technologies in the information transfer, cipherization, encryption, and in other researches of the quantum information science [6–14]. The authors of Ref. [11] synthesized the first organic system which displays simultaneously both strong luminescence and the near-unity generation quantum yield of the quartet (and quintet) excited states of high-spin multiplicity (HSM) produced by a link of radical with chromophore.

Though many stable radicals are non-luminescent [8], a new class of emissive radicals was synthesized recently that provides intense emission by spin-allowed electric dipole transitions within the doublet state manifold [15]. This class of available radicals quite rapidly expands their molecular structures and spans the whole visible region including a near IR wavelength range [15]. The best record efficiencies for organic light emitting diodes working in the deep-red and IR regions were recently obtained with the tris(2,4,6-trichlorophenyl)methyl radicals conjugated with carbazole moiety as an electron donor (Fig. 1A) [11, 15].

A   *B*   *C*
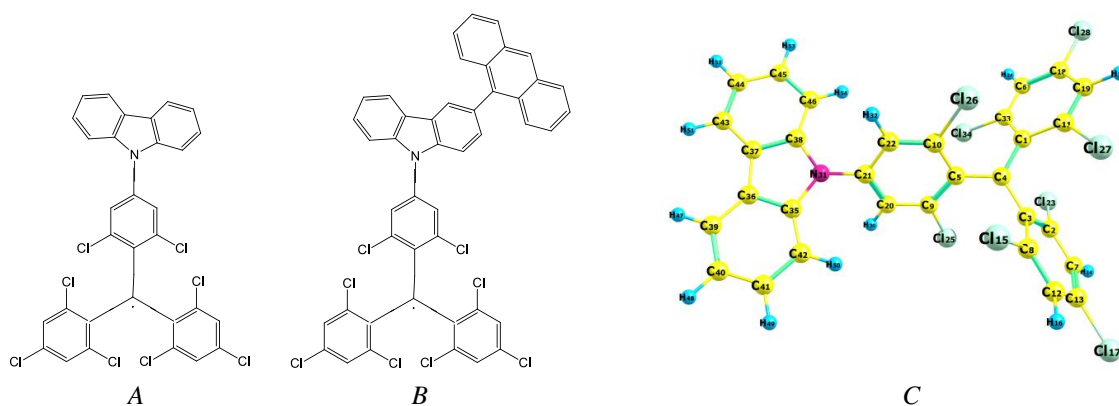
Figure 1. Chemical structure of the tris(2,4,6-trichlorophenyl)methyl radical (TTM) linked to carbazole: TTM-Cz (*A*); the common radical produced by TTM-Cz conjugation with the antracene chromophore (*B*) synthesized by Gorgon at el. [11]; the DFT optimized TTM-Cz radical (*C*)

Gorgon at el. [11] designed the energy resonance between emissive doublet and triplet levels, by covalently coupled tris(trichlorophenyl)methyl-carbazole (TTM-Cz) radical and anthracene (An) molecule (Fig. 1B); they observed the doublet excitation (D) delocalised to the linked anthracene within a picosecond lifetime being evolved subsequently to the pure HSM state of the mixed radical-triplet type at low energy (near 1.8 eV). These are quartet HSM state for the monoradical+acene system (TTM-Cz+An), and subsequently — quintet HSM state for the biradicaloid combination (TTM-Cz)$_2$+An [11]. The authors used impulse EPR scanning of these HSM states by microwaves at room temperature [11]. Presence of radical in

combination with acene enhances the rate of intersystem crossing (ISC), which leads to the high An chromophore triplet states population. Gorgon et al. [11] were succeeding in experiments with coherently addressable by EPR signal of TTM-Cz radical with an optical phosphorescent read-out of anthracene 1B molecule in a dilute toluene solution (even at 295 K) being enabled by ISC to transfer into the emissive states [11]. In the biradical complex system (TTM-Cz)$_2$+An, on return to the ground singlet S$_0$ state the radical spins on either side of the anthracene molecule show strong spin correlation (though they were uncorrelated initially). This approach supports a high efficiency of initialisation, spin manipulations and simultaneously light-based read-out in the radical-An system at room temperature in dilute toluene solution [11]. Such integration of luminescence and HSM states [16] creates a robust chemical synthetic platform based on organic functional materials for emerging modern quantum computation technologies [10–14]. Further QIS technology development of HSM systems strongly depends on the capability to control the spin-magnetic properties of such materials, and requires comprehensive understanding of spin-orbit coupling impact on excited-state dynamics. Quantum chemical treatments of various spin effects based on radical interactions with the triplet excited states were considered in Karaganda State University as early as 45 years ago in the context of spin alignment and microwave induced optical phosphorescence detection [16, 18]. Combinations of the anthracene core with various carbazole moieties in fused heteroacenes were utilized in recent fabrication of highly luminous sky-blue organic light-emitting diodes [17] and their linking with radicals could be potentially interesting for HSM states generation [11–14]. Zainulla Muldakhmetov, as a founder of modern spectroscopy in the Central Kazakhstan region put forward new kinetics photochemical methods of optical-magnetic resonance, EPR, flash-photolysis and quantum-chemical approaches [18] which provide essential fundamental backgrounds for contemporary quantum cipherization, information transfer, integration of luminescence and high-spin states dynamics. All these efforts created an organic materials platform for emerging quantum information technologies [9–12, 18–21].

In the present work an attempt is made to illustrate the quantum chemical feature of the new systems on the ground of time dependent (TD) density functional theory (DFT) with the spin-UB3LYP functional. The results provide an assignment of the electronic absorption UV-vis spectrum of the common radical produced by TTM-Cz conjugation with the anthracene chrmophore synthesized by Gorgon et al. Figure 1B [11]. They are shown in Table. Figure 2 presents the frontier molecular orbitals (MOs) of this TTM-Cz-An radical.

All radicals (TTM, TTM-Cz and TTM-Cz-An) structures are optimized by DFT UB3LYP method and their IR spectra are analyzed in terms of normal vibrations; all frequencies of vibrational modes were found to be real. One can see in Figure 2 that the antracene chrmophore's MOs are almost independent from the electronic system of the TTM-Cz radical. Only the highest doubly occupied molecular orbitals (HOMO) (217β and 218α) and the next to the lowest unoccupied molecular orbital (LUMO+1) 219β have small admixtures at the place of conjugation between antracene chrmophore and the radical electronic system (Fig. 2).

T a b l e

TD DFT calculation of the electronic absorption spectrum of the TTM-Cz-An radical and rotatory strengths (R) in CGS (10^{-40} erg esu cm/Gauss); λ — wavelength, f — oscillator strength

State	E (eV)	λ (nm)	f	Configuration state function	R_{XX}	R_{YY}	R_{ZZ}	R length
CT	1.570	790.9	0.0051	(217β→218β)	0.46	0.15	0.05	0.19
D$_0$T$_1$	1.769	700.1	10^{-6}	0.70(217β→219β)- -0.69(218α→219α)	0	0	0	0
D$_1$S$_0$	1.897	653.7	0.1030	0.98(216β→218β)	−7.81	4.43	−6.54	−3.30
D$_3$	2.284	542.8	0	(215β →218β)	0	0	0	0
D$_4$	2.660	466.1	0.0174	0.81(212β→218β)	−5.78	−22.3	−7.11	−11.5
D$_5$	2.764	448.4	0.0062	0.75 (210β→218β)	4.28	0	0	1.42
D$_6$	2.848	435.4	0	0.91(214β→218β)	0.36	0.12	0	0.14
D$_7$	2.899	427.6	0.0031	0.71(209β→218β) +0.44(208β→218β)	2.15	7.14	−26.3	−5.36
D$_8$	2.949	420.6	0.0027	0.68(207β→218β)- -0.28(217α→-220α)	−42.4	0.99	−11.8	−17.7
D$_9$	2.950	420.2	0.0039	+0.71(208β→218β)- 0.50(209β→218β)	−1.32	13.98	−53.3	−13.4

217 β

218 β

219 β

216 β

215 β

212 β

209 β

208 β
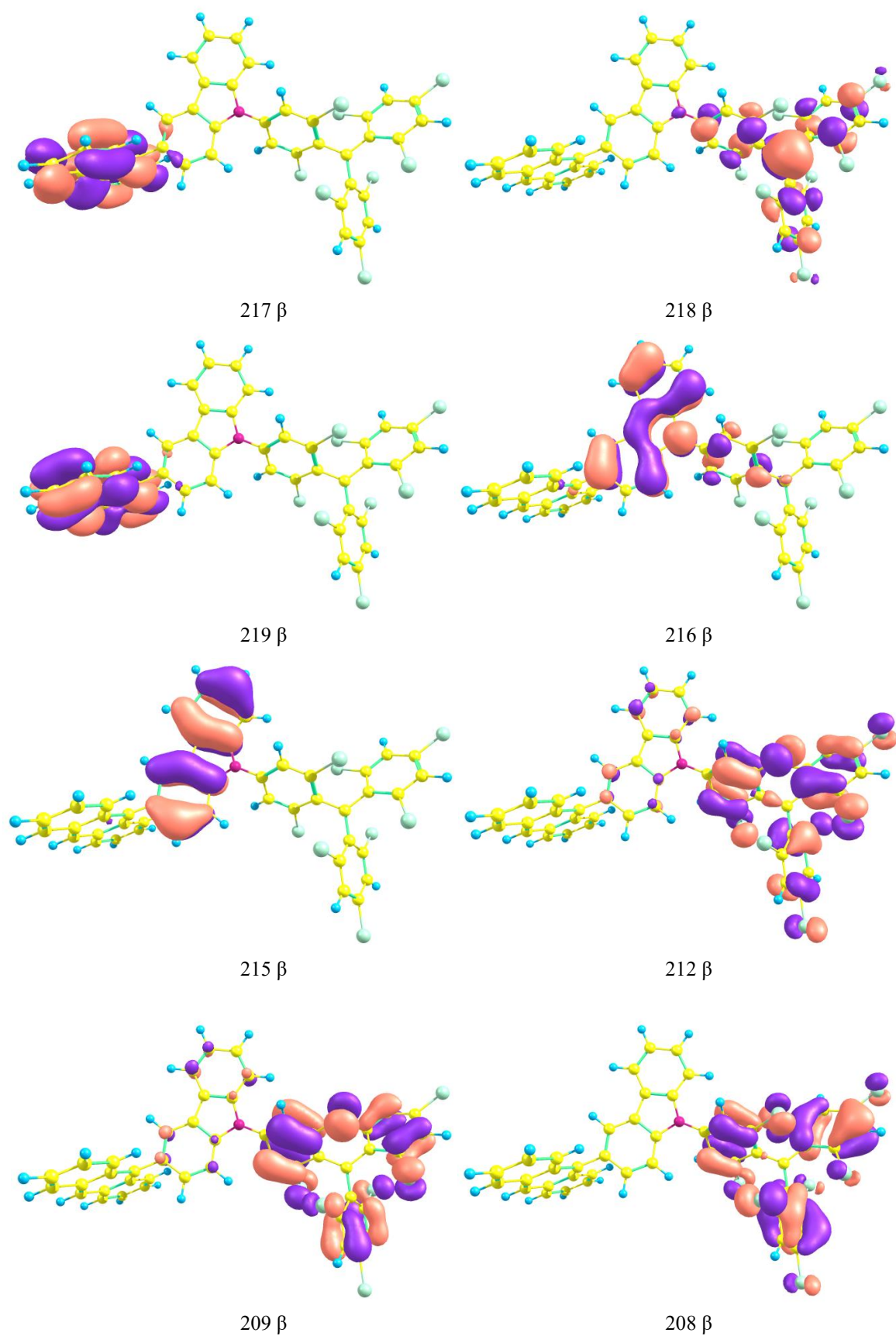
Figure 2*a*. Frontier molecular orbitals for β spins of the radical TTM-Cz-Anthracene depicted in Figure 1B

218 HOMO α

219 LUMO α

217 α

220 α
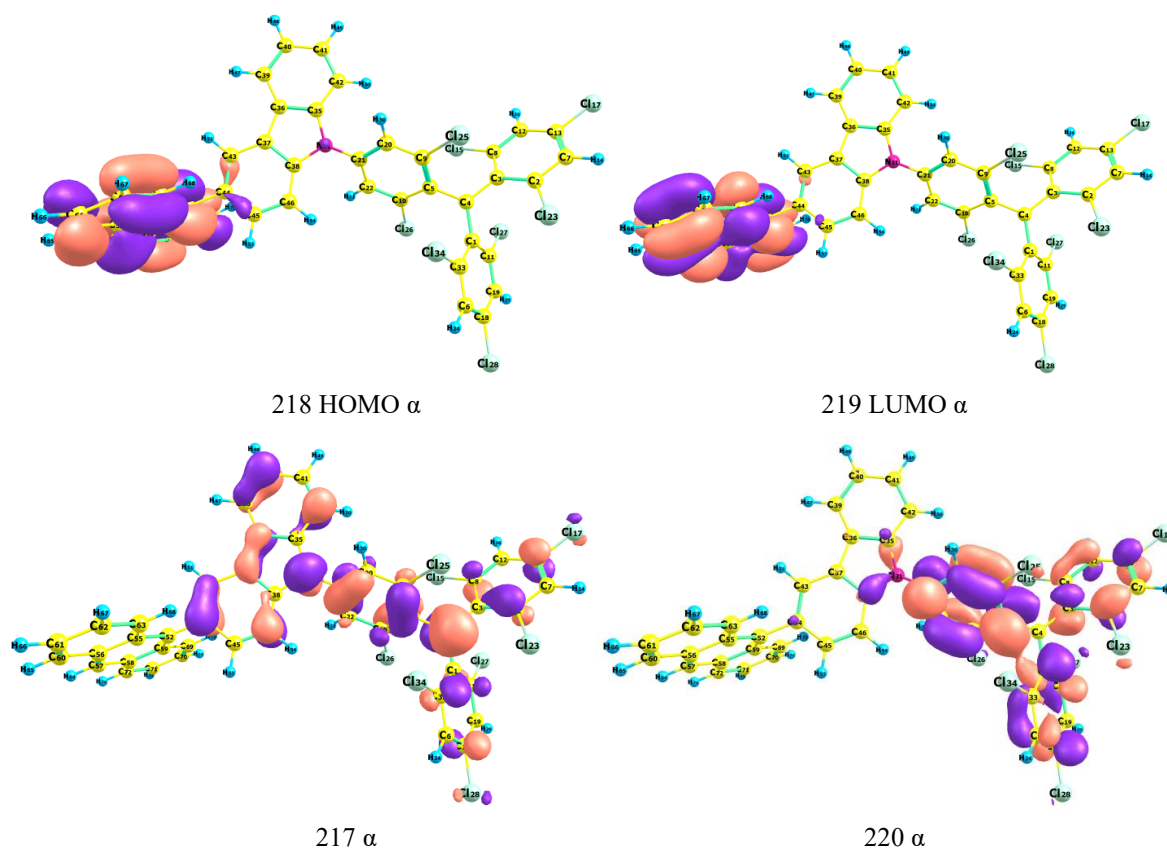
Figure 2*b*. Frontier molecular orbitals for α spins of the radical

According to our calculation, the first excited state of the whole radical corresponds to a pure charge transfer (CT) transition from anthracene to the TTM radical moiety 217β→218β (Fig. 2*a*). It produces a moderately intense absorption band ($f = 0.005$) with a maximum at 790 nm (Table). This result does not coincide with interpretation of Gorgon at el. [11], who believe that CT state is higher in energy than the first excited state of the TTM-Cz radical. Probably, our TD DFT calculation underestimates the CT state energy, but the rest assignments are in agreement with experiment [11]. The D_0S_0-D_0T_1 excitation in anthracene (1.769 eV) occurs below the first excited state in the TTM-Cz radical (1.897 eV); the late represents (216β→218β) transition with the largest intensity ($f = 0.103$; Table). This is almost pure doublet state (S^2 expectation value is 0.81 instead of 0.75 for S=1/2). The ground state D_0 has the S^2 expectation value equal to 0.77 and after spin annihilation we get 0.7504 value. The $D_0 – D_1$ transition represents a single electron excitation 216β→218β, that is an excitation in the TTM-Cz radical with a large portion of charge transfer from the carbazole moiety to the TTM radical (Fig. 2*a*). At the same time, the singly occupied molecular orbital (SOMO) 217α in the ground radical state D_0 represents the whole TTM-Cz radical (Fig. 2*b*), it is bearing one nonpaired α electron. It should be noted that the 218 β MO (which is a virtual analogous of SOMO) does not include contribution from the carbazole moiety (Fig. 2*a*). The spin density in the excited CT state (1.57 eV) represents mostly the An$^+$ cation radical of anthracene (217β) and minimal contribution from the carbazole moiety. The whole TTM-Cz-An radical is now transferred into the (TTM)$^-$ anion (218β) with an almost closed-shell electronic structure that is linked with the anthracene cation radical.

In order to understand comparison with the experimental spectra [11] we have to analyze absorption and luminescence of both radicals A and B shown in Figure 1. The TD DFT calculation results for the electronic absorption spectrum of the A radical (TTM-Cz) are presented in Table S1 **Supplementary Materials**. First, we need to compare $D_0→D_1$ transition in radical A with the $D_0S_0→ D_1S_0$ absorption band in the composed B radical (TTM-Cz-An). The band $D_0 – D_1$ includes transition from the doubly occupied 171 MO (Fig. S1) to the singly occupied molecular orbital (SOMO) 172. This is the allowed long-axis polarized transition which embraces the whole TTM-Cz species; this is mostly π→π* type excitation. Its analogous in the composed B radical (TTM-Cz-An) could be the 216α →217α transition (Fig. S1). In fact, the D_1S_0 state in the late radical B is presented by 216β→ 218β configuration and bears some CT character inside the A radi-

cal (Figure 1; TTM-Cz). The third excited state at 1.897 eV (654 nm) in the TTM-Cz-An radical represents the doublet state (Table). In the TTM-Cz radical (Fig. 1A) calculated by the same TD DFT method the first excited doublet state is at 1.875 eV (661 nm); thus, it is shifted to the red region in comparison with 1.897 eV excitation energy of the radical B. The second transition in the A radical is a charge transfer excitation from the carbazole moiety to the TTM radical.

In experiment [11] the light absorption with the wavelength higher than that for the first singlet-singlet S_0–S_1 transition in anthracene corresponds to the D_0S_0-D_1S_0 absorption band. This radical-excited state is close to the doublet D_0T_1 anthracene (T_1) excited state (Table). According to [11] a rapid doublet-doublet relaxation of radical excitation D_1S_0 to the coupled anthracene D_0T_1 state proceeds within a few picoseconds. This fast rate is possible since the total spin is conserved during such "doublet radical → triplet molecule" energy transfer. Subsequently, the doublet $^2[D_0T_1]$ exciton undergoes intersystem crossing (ISC) transition to the anthracene–excited quartet state $^4[D_0T_1]$. The rate of such ISC depends on spin-orbit coupling (SOC) matrix element (ME). The spatial (orbital) part of the doublet $^2[D_0T_1]$ and quartet $^4[D_0T_1]$ wave functions are very close; thus, the SOC ME is expected to be negligible [11]. In fact, account of all α and β MOs differences leads to prediction that this direct SOC matrix element is not small. We have estimated it within the PM3 approximation accounting the spin-restricted Hartree-Foch method with the limited configuration interaction [16–19] to be equal 0.237 cm^{-1}. Nevertheless, the square of SOC ME which determines the ISC rate is really small and cannot compete with other $^2[D_0T_1]$ doublet state relaxation processes. Thus, the direct ISC seems impossible to generate high yields of the quartet $^4[D_0T_1]$ state at the nanoseconds timescales in agreement with the observed dynamics of the composed TTM-Cz-An radical luminescence.

The authors of [11] proposed that the CT state (in Table it corresponds to 217β→218β excitation) could be close in energy to both $^{4,2}[D_0T_1]$ states of the anthracene-excitonic type. Though our TD DFT calculation puts the CT state too low in energy, in reality it still could be an intermediate in the $^2[D_0T_1]$ -$^4[D_0T_1]$ relaxation. The CT state accessibility could assist ISC process to the quartet state via SOC, which must be definitely higher for the states of different orbital character (Table, Fig. 2). The CT state can be easily produced (according to [11]) from the $^2[D_0T_1]$ doublet following spin-conserving electron transfer from locally excited anthracene into the single vacancy of radical; that is, from the LUMO 219α of anthracene to the SOMO 217α of TTN-Cz radical (Fig. 2b). If the ISC transition occurs during the reverse electron-transfer, then the spin flip and the quartet $^4[D_0T_1]$ state can be formed. The authors of [11] have proposed that such forward mechanism could be near-barrierless and could explain their experimental observation of a high quantum yield of the quartet state at all studied conditions in a great interval from 20 K till room temperatures. The late was measured from the $D_1 \rightarrow D_0$ luminescence quantum efficiency of radical B (Fig. 1) together with the triplet $^2[D_0T_1]$ state yield extracted from the measured transient optical absorption. For the TTM-Cz-An radical in the toluene solutions at room temperature the quartet state yield was about 73 %. [11]. Thus, combining PL spectroscopy, EPR, and optical detection of magnetic resonance, the authors of [11] show a possibility to generate the pure high-spin states in organic molecules, to manipulate them, and then to read them out by radical luminescence at ambient condition. Taking into account the correction for the low CT state energy, we try here to support this discovery, which is quite important for the modern quantum information science.

Conclusions

It was shown recently [11] that synthetic chemical tuning of poly-radical molecular structures opens new ways to design the coupled high-multiplicity spin systems, which could be addressed by light of chosen wavelengths range. The tria(trichlorophenyl)methyl-carbazole (TTM-Cz) radical covalently coupled with anthracene was studied in the present work in order to explain how the doublet excitation delocalized to the linked anthracene during a picosecond lifetime can be evolved into the high-multiplicity (quartet) spin state of the mixed radical-triplet type at low excitation energy in the visible region. High-spin quartet (and quintet) states are able to produce the dense architecture with multiple qubits distributed within the single manifold of spin sublevels. These multilevel qubits offer great advantages in the quantum information science and quantum computing.

References

1   Shiba, K., Sakamoto, K., Yamaguchi, K., Malla, D. B. & Sogabe, T. (2019). Convolution filter embedded quantum gate autoencoder. *arXiv preprint arXiv:1906.01196*. https://doi.org/10.48550/arXiv.1906.01196

2   Salikhov, K.M. (2019). Current state of the spin exchange theory in dilute solutions of paramagnetic particles. New paradigm of spin exchange and its manifestations in EPR spectroscopy. *Physics-Uspekhi*, *62*(10), 951–975. https://doi.org/10.3367/ufne.2018.08.038421

3   Salikhov, K.M., Golbeck, J.H. & Stehlik, D. (2007). Quantum teleportation across a biological membrane by means of correlated spin pair dynamics in photosynthetic reaction centers. *Applied Magnetic Resonance*, *31*(1–2), 237–252. https://doi.org/10.1007/bf03166259

4   Minaev, B. (2022). The spin of dioxygen as the main factor in pulmonology and respiratory care. *Archives of Pulmonology and Respiratory Care*, *8*(1), 028–033. https://doi.org/10.17352/aprc.000081

5   Minaev, B.F. (2019). How cofactor-free oxygenases can overcome spin prohibition in substrates oxygenation by dioxygen. *Chemical Physics*, *521*, 61–68. https://doi.org/10.1016/j.chemphys.2019.01.021

6   Nielsen, M.A. & Chuang, I.L. (2010). Quantum Computation and Quantum Information. Cambridge University Press, Cambridge, 676.

7   Salikhov, K.M., Zech, S.G. & Stehlik, D. (2002). Light induced radical pair intermediates in photosynthetic reaction centres in contact with an observer spin label: spin dynamics and effects on transient EPR spectra. *Molecular Physics, 100*(9), 1311–1321. https://doi.org/10.1080/00268970110112336

8   Kandrashkin, Y.E. & Salikhov, K.M. (2009). Numerical Simulation of Quantum Teleportation Across Biological Membrane in Photosynthetic Reaction Centers. Applied Magnetic Resonance, *37*(1–4), 549–566. https://doi.org/10.1007/s00723-009-0081-8

9   Wu, Y., Zhou, J., Nelson, J.N., Young, R.M., Krzyaniak, M.D. & Wasielewski, M.R. (2018). Covalent Radical Pairs as Spin Qubits: Influence of Rapid Electron Motion between Two Equivalent Sites on Spin Coherence. *Journal of the American Chemical Society, 140*(40), 13011–13021. https://doi.org/10.1021/jacs.8b08105

10   Olshansky, J.H., Krzyaniak, M.D., Young, R.M. & Wasielewski, M.R. (2019). Photogenerated Spin-Entangled Qubit (Radical) Pairs in DNA Hairpins: Observation of Spin Delocalization and Coherence. *Journal of the American Chemical Society, 141*(5), 2152–2160. https://doi.org/10.1021/jacs.8b13155

11   Gorgon, S., Lv, K., Grüne, J., Drummond, B. H., Myers, W. K., Londi, G., ... & Evans, E. W. (2023). Reversible spin-optical interface in luminescent organic radicals. *arXiv preprint arXiv:2303.13934*. https://doi.org/10.48550/arXiv.2303.13934

12   Wasielewski, M.R., Forbes, M.D.E., Frank, N.L., Kowalski, K., Scholes, G.D., Yuen-Zhou, J., Baldo, M.A., Freedman, D.E., Goldsmith, R.H., Goodson, T., Kirk, M.L., McCusker, J.K., Ogilvie, J.P., Shultz, D.A., Stoll, S. & Whaley, K.B. (2020). Exploiting chemistry and molecular systems for quantum information science. *Nature Reviews Chemistry*, *4*(9), 490–504. https://doi.org/10.1038/s41570-020-0200-5

13   Quintes, T., Mayländer, M. & Richert, S. (2023). Properties and applications of photoexcited chromophore–radical systems. *Nature Reviews Chemistry*, *7*(2), 75–90. https://doi.org/10.1038/s41570-022-00453-y

14   Peng, Q., Obolda, A., Zhang, M. & Li, F. (2015). Organic Light-Emitting Diodes Using a Neutral π-Radical as Emitter: The Emission from a Doublet. *Angewandte Chemie*, *127*(24), 7197–7201. https://doi.org/10.1002/ange.201500242

15   Terenin, A.N. (1943). Photochemical processes in aromatic compounds. *Acta physicochim. URSS*, *18*(4), 210-241.

16   Minaev, B.F. (1979). Spin allignement of the triplet state and new methods of the phosphorescence study. *Fizika Molecul, Naukova Dumka, Kiev*, *7*, 34.

17   Ivaniuk, K., Cherpak, V., Stakhira, P., Hotra, Z., Minaev, B., Baryshnikov, G. & Luszczynska, B. (2016). Highly luminous sky-blue organic light-emitting diodes based on the bis[(1,2)(5,6)] indoloanthracene emissive layer. *The Journal of Physical Chemistry C*, *120*(11), 6206-6217. https://doi.org/10.1021/acs.jpcc.6b00696

18   Muldahmetov, Z. M., Minaev, B. F. & Ketsle, G. A. (1983). Optical and magnetic properties of the triplet state. *Alma Ata*.

19   Minaev, B., Baryshnikov, G., Ågren, H. (2014). Principles of phosphorescent organic light emitting devices. *Physical Chemistry Chemical Physics*, *16*(5), 1719-1758. https://doi.org/10.1039/c3cp53806k

20   Skuodis, E., Leitonas, K., Panchenko, A., Volyniuk, L., Simokaitienė, J., Keruckień, R., Volyniuk, D., Minaev, B.F., & Graˇzuleviˇcius, J.V. (2022). Very sensitive probes for quantitative and organoleptic detection of oxygen based on conformer-induced room-temperature phosphorescence enhancement of the derivative of triazatruxene and phenothiazine. *Sensors & Actuators: B. Chemical*, *373*, 132727. https://doi.org/10.1016/j.snb.2022.132727

21   Karaush, N.N., Baryshnikov, G.V. & Minaev, B.F. (2014). DFT characterization of a new possible graphene allotrope. *Chemical Physics Letters*, *612*, 229-233. https://doi.org/10.1016/j.cplett.2014.08.025

22   Frisch, M.J., Trucks, G.W., Schlegel, H.B. et al. (2016). Gaussian 16, Revision C.01. *Wallingford: CT*.

Information about author*

Minaev, Boris Filippovich (*corresponding author*) — Doctor Of Chemical Sciences, Professor, Department of Physics and Astronomy, Uppsala University, SE-752 37, Uppsala, Sweden; Department of Chemistry and Nanomaterials Science, Bohdan Khmelnytsky National University, 18031, Cherkasy, Ukraine; e-mail: bfmin43@ukr.net; https://orcid.org/0000-0002-9165-9649;

_____

*The author's name is presented in the order: *Last Name, First and Middle Names*

Sergey A. Beznosyuk*

Department of Physical and Inorganic Chemistry, Altai State University, Barnaul, Russia
*(*Corresponding author's e-mail: bsa1953@mail.ru)*

The Second Quantum Revolution: Development of Subatomic Quantum Nanotechnologies of Intelligent Materials

The article analyzes the future development of quantum nanotechnology based on attosecond physics of the subatomic level of the condensed state. The ways of realizing the main achievements of the second quantum revolution in subatomic nanotechnologies of materials, namely quantum entanglement, quantum contextuality and quantum dissipativity are considered. The theoretical analysis of the prospects for this direction in the development of quantum subatomic nanotechnologies has been carried out within the framework of the well-known theory of thermal field dynamics of the condensed state. The analysis shows that subatomic entanglement of electron pairs is realized by attosecond single-cycle photons. The entangled electron pairs form the interfaces of supra-atomic capsules — quantum nanoelectromechanical systems (NEMS) of the condensed state of the material. The Coulomb blockade of quantum NEMS interfaces is complemented by the fact that they are controlled by the infrastructure of subatomic two-electron sensors and actuators located at the interface boundaries. When the primary subatomic interfaces of NEMS function, secondary supra-atomic scale entangled pairs of electrons are generated, which dissipate the NEMS energy and form a dissipative multilevel hierarchy of condensed state interfaces at higher spatio-temporal scales of intelligent materials.

Keywords: the second quantum revolution, subatomic attosecond physics, thermo-field dynamics, quantum entanglement, quantum contextuality, quantum dissipativity, quantum nanotechnology, intelligent materials.

Contents

Introduction
    1. Attosecond quantum entanglement of subatomic electrons
    2. Quantum contextuality of measurement and control of hybrid NEMS
    3. Quantum dissipative infrastructure of hybrid electronic and bielectronic systems
Conclusions

Introduction

In the coming years, production based on quantum technology of the so-called second quantum revolution will expand rapidly, covering high-tech industries [1]. One of the main areas of research is subatomic quantum technologies. Their specificity is determined by quantum effects on the space-time scales of the subatomic level of matter, limited from below by the size of the inner electron shells closest to the nucleus, and from above — by the length of the outer electron shells of the atom. It is assumed that individual attosecond electromagnetic pulses are key tools for manipulating quantum effects in the subatomic region of matter. The solution to these questions is the main problem of attophysics, which has been rapidly developing in the last decade [2–5]. There is no doubt that attosecond subatomic technologies will play a key role in the second quantum revolution and become one of the breakthrough directions of its development.

At the supra-atomic level, there are many combinations of the dynamics of various one-electron excitations with vibrational-rotational-translational modes of excitation of the nuclear subsystem and the pathways of chemical reactions. All these femtosecond processes in different atomic-molecular systems have been well studied over the last quarter of a century in the framework of femtochemistry [6].

At present, the attosecond quantum dynamics of an electron at the subatomic level is intensively studied in attophysics [7–10]. Attosecond pulses are an ideal tool for studying the effects of electron correlation with time resolution in the subatomic region Electronic strong correlation, which is determined by the interaction of electrons in a many-electron system at subatomic areas, plays a fundamental role in several physical processes and characterizes several nonequilibrium processes, for example, the relaxation of excited states of atoms and molecules irradiated with XUV pulses. The dynamics of these states can lead to various phenom-

ena at the supra-atomic level, such as Auger decay in atoms, interatomic Coulomb decay, or charge migration in atomic-molecular systems.

Although a complete characterization of the time-dependent correlated motion of two electrons can only be obtained using the attosecond pumping method and the attosecond probe, so far only alternative methods based on a combination of attosecond XUV and femtosecond IR pulses have been used. In this regard, the effects of the appearance of entangled pairs of electrons generated by an attosecond pulse in the subatomic region cannot be experimentally studied yet. The problems of the second quantum revolution indicate the prospects of studying the attosecond pulsed entanglement of subatomic electron pairs, which can appear at the next supra-atomic scale level — the basic one for quantum nanotechnology [11–14]. The purpose of this article is to provide a theoretical analysis of the possibilities for the development of the second quantum revolution in this direction.

The layout of the article is as follows. This article discusses three aspects of the second quantum revolution in the development of a fundamentally new quantum subatomic nanotechnology using the effects of quantum entanglement, contextuality and dissipativity. Section 1 analyzes the mechanism of implementation of pulsed attosecond quantum entanglement of subatomic electron pairs. In Section 2, we will consider the mechanism of the quantum contextuality of measuring and controlling electron-nuclear systems at the supra-atomic level using subatomic entangled electron pairs. The final Section 3 discusses the role of the quantum dissipativity of secondary supra-atomic entangled electron pairs in the formation of the infrastructure of quantum smart materials.

1. Attosecond quantum entanglement of subatomic electrons

To fully understand the influence of the interrelated motion of electrons on the course of nonequilibrium processes in matter, it is necessary to study in detail the effects of the rearrangement of the correlated motion of electron pairs at the subatomic scale level caused by a separate attosecond pulse. It is known that the quantum mechanics of an electron in the matter is determined by its two Coulomb electrostatic interactions with nuclei and other electrons. There is one-electron interaction with protons of nuclei (e^-–p), as well as two-electron interactions (e^-–e^-). Under the adiabatic approximation of quantum mechanics, electron-nuclear particles of matter endow it in stationary states with an atomic-molecular structure. This structure is specified by the topology of the electron density distribution $n(r)$ in the physical space R^3. Due to the identity of N-electrons in a quantum system, the distribution $n(r)$ is only a function of the probability density $n_1(r)$ of finding a single electron at the point r: $n(r) = N \cdot n_1(r)$. The one-electron interaction (e^-–p) establishes the supra-atomic scale level of atomic-molecular systems in materials. It was shown [11] that restrictions from below on the fundamental supra-atomic scale length is specified by the (e^-–p) atomic Bohr radius $a_0 = \dfrac{\hbar^2}{m_0 e^2}$.

In quantum field electrodynamics of a condensed state at the subatomic level, in addition to two above-mentioned electrostatic interactions of an electron, its gauge kinematic relationship (e^-~χ) with the electromagnetic γ-field begins to play an important role [15]. This relationship imposes restrictions from below on the subatomic scale of the quantum dynamics by the Compton length of the electron $\lambda_e = \dfrac{\hbar}{m_0 c}$.

The fundamental scales of the subatomic and supra-atomic dynamics of an individual electron in a condensed state are related by the fine structure constant of the physical vacuum $\alpha = \dfrac{e^2}{\hbar c}$ as follows [11]:

$$a_0 = \lambda_e / \alpha . \qquad (1)$$

It is known that the interaction of two electrons in physical space is not reduced only to instantaneous electrostatic interaction (e^-–e^-) due to the finite velocity of propagation of perturbations of the gauge electromagnetic field. Within the framework of the concept of the thermofield dynamics, it has been shown that in the subatomic region of the nonequilibrium condensed state, the attosecond χ-mode of the kinematic density wave of the gauge electromagnetic field is capable of entangling a pair of electrons like a string (e^-~χ~e^-) [12]. The mechanism of quantum entanglement is that a strongly correlated motion is established inside an entangled pair of electrons as a result of spontaneous condensation χ-Goldstone mode of a static kinematic density wave, according to the formula: $\chi_0(x) \rightarrow \chi_0(x) + \chi$ [11, 15]. As a result, for an entangled pair of electrons, the distance between them does not change, and their lifetime in the pair is synchronized.

The quantum state $\Psi(r_1, t_1; r_2, t_2)$ of an entangled electron pair with the space-time coordinates of the first (r_1, t_1) and second (r_2, t_2) electrons synchronized in the pair lifetime $t = (t_1 + t_2) / 2$ and at a fixed electron displacement in the pair $R = (r_1 - r_2)$ is described by a kinematic density wave $\phi_R(r|t)$ of their center of mass with spatial coordinate $r = (r_1 + r_2) / 2$:

$$\Psi(r_1, t_1; r_2, t_2) = \phi_R(r|t). \qquad (2)$$

The kinematic density wave $\phi_R(r|t)$ of the bielectron is enclosed in a compact spatial loggia in the material [11]. The characteristic length of the loggia L is determined by the limiting distance of propagation of the quantum kinematic density wave $\phi_R(r|t)$ during the existence of a subatomic entangled pair of electrons. If we denote by $|R|$ the fixed distance between the entangled electrons of the pair ($a_0 \geq |R| \geq \lambda_e$), then the length L will be determined by the ratio: $L = |R|/\alpha$, where α is the fine structure constant. The L parameter sets the next supra-atomic scale level of the material: $a_0 / \alpha \geq L \geq a_0$.

The restructuring effects of the correlated motion of electron pairs at the subatomic level caused by a single attosecond pulse are presented in Figure 1. The diagram shows the main stages of the generation of an entangled electron pair in the subatomic region of one of the atoms and further propagation of its kinematic density wave to neighboring atoms inside a compact spatial loggia at the supra-atomic scale level of the material.
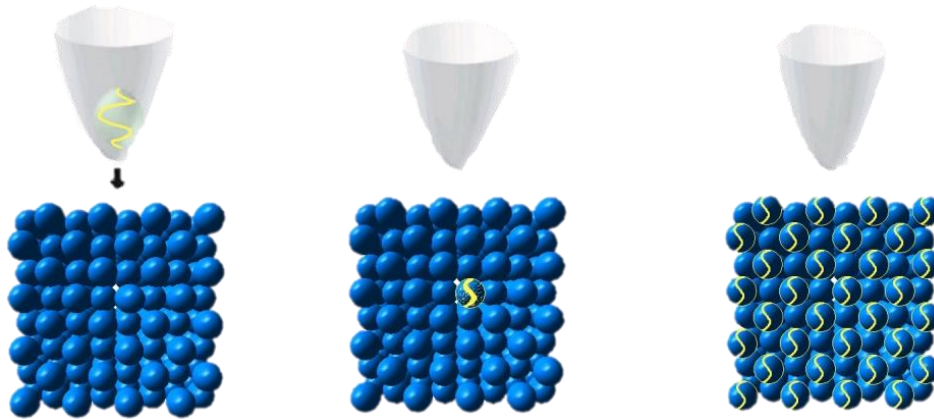
Figure 1. Attosecond impulse mechanism of subatomic formation of an entangled pair
of electrons ($e^- \sim \chi \sim e^-$) and propagation of a kinematic wave of bielectron density
inside a spatial loggia at the supra-atomic scale level of materials

As can be seen from Figure 1, during the attosecond propagation time $\delta\tau$ of the kinematic density wave of a subatomic entangled pair of electrons, a topologically closed interface of separated electron charges appears at the boundary of the supra-atomic loggia. The interface creates a Coulomb electrostatic blockade of the nuclear-electronic subsystem inside the topological capsule, forming a composite quantum nanoelectromechanical system (NEMS). Thus, the quantum-dimensional NEMS is a hybrid comprising a capsule of the boundary kinematic density wave of a subatomic entangled electron pair with a thickness $|R|$ less than 0.1 nm, inside which the electron-nuclear subsystem is enclosed. The NEMS capsule has a supra-atomic length of 0.1 to 10 nanometers, containing from one to a thousand atoms.

2. Quantum contextuality of measurement and control of hybrid NEMS

Let us turn now on the example of hybrid NEMSs to consideration of application in the most promising quantum technologies of another cornerstone idea of the second quantum revolution — the effect of contextuality perception and control of quantum objects in materials. This question is a special case of a more general problem of the quantum contextuality. Currently, this most "quantum" of all quantum phenomena has developed a sharp controversy [16]. Quantum contextuality is a feature of the phenomenology of quantum mechanics, according to which measurements of observables of a quantum object cannot be regarded simply as revealing pre-existing values. Firstly, because at the moment of measurement, a multi-wave reduction of the quantum state of the object occurs and, secondly, the result of measuring the quantum observable de-

pends on switching properties of measuring devices taking part in the measurement. In connection with the above remarks, below we will consider the quantum mechanism of the contextuality process of the stepwise unfolding in time of the NEMS motion in the material.

In fact, in the case of a hybrid quantum NEMS, the capsule interface acts as a measuring device in the attosecond pulsed mode and a control device in the femtosecond pulsed mode for the internal electron-nuclear component of the NEMS. Let us show it.

It has been shown earlier [11–14] that after the completion of the propagation of the kinematic density wave, the electronic state Φ_1 of a subatomic entangled pair has the following expression:

$$\Phi_1 = 2^{-1/2}(\Phi_{-1} + \Phi_{+1})_.$$

(3)

Diagram in the Figure 2 shows the charge separation scheme on the supercapacitor interface for two quantum entangled bipolar charge states Φ_{+1} and Φ_{-1}. The charge distribution of two entangled excitons at the capsule interface is shown as two separate entangled electric dipoles: open circles represent hole excitations and dark circles represent electronic excitations. As a result, the charge density distribution of the entangled pair of electrons has a topological boundary with separated charges in the physical space of the material.
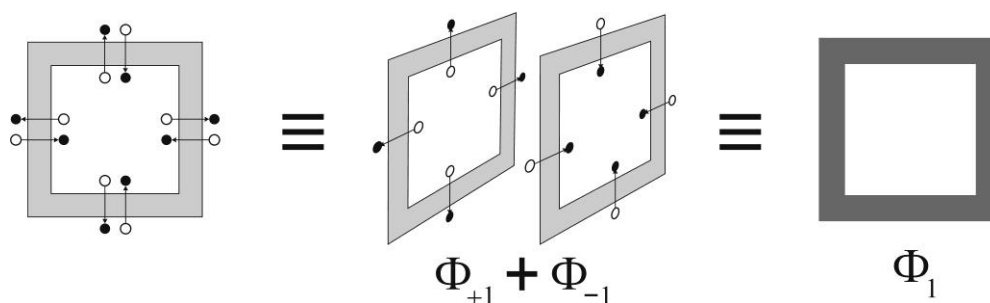
Figure 2. Diagrams of the interface capsule of NEMS in the quantum state Φ_1

During the attosecond lifetime $\delta\tau_1$, the quantum state Φ_1 of the interface capsule and the quantum state Θ_1 of its locked subsystem of nuclei and electrons are in the untangled quantum state of NEMS:

$$\Psi_1 = \Theta_1\Phi_1.$$

(4)

In the process of interaction of the electromechanical interface of the capsule with the electron-nuclear subsystem, secondary low energy entangled electron pair arise, which has dimensions on the order of the length of the supraatomic loggia of the capsule. Figure 3 shows that in comparison with the primary excited state Φ_1 in the excited quantum state Φ_2 a supplementary low-energy excitation of the tangled electron pair with small electron ionization I_2 and electron affinity A_2 is emerged.
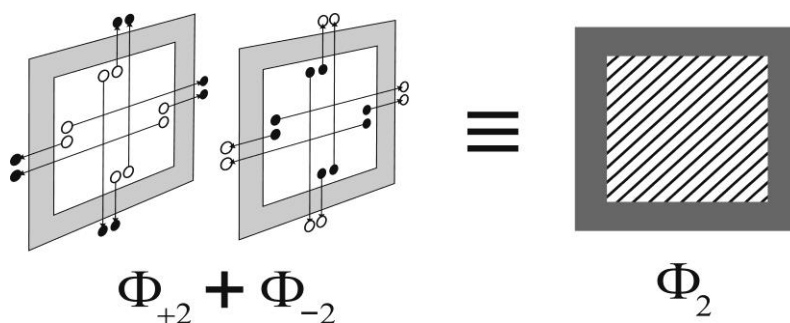
Figure 3. Diagrams of the electromechanical capsule of NEMS in the quantum state Φ_2

As it was shown in [11], the source of the excitation energy of a supplementary pair of entangled excitons on the interface is the mechanical work δA performed inside the capsule by confined nuclear-electron subsystem of the NEMS when its quantum state changes from Θ_1 to $\Theta_1 + \Theta_2$. The excitation energies of

secondary electron pairs lie in the region of electronic-vibrational-rotational excitations energies of the electron-nuclear subsystem.

As a result, entanglement of the electromechanical capsule with the electronic-nuclear subsystem NEMS occurs as follows:

$$\Psi_2 = \Theta_1 \Phi_1 + \Theta_2 \Phi_2 . \tag{5}$$

The lifetime τ_1 of the entangled state Ψ_2 of NEMS is limited by the action of quantum thermofield fluctuations of the condensed state. As a result of such fluctuations, the NEMS spontaneously dissipates the energy of the secondary entangled pair of electrons into the medium, passing from an entangled state Ψ_2 to an untangled state $\Psi_{1'}$. Reduction occurs into the wave function Φ_1 of the capsule and a wave function $\Theta_{1'} = \Theta_1 + \Theta_2$ of the confined nuclear-electron subsystem NEMS:

$$\Psi_2 = \Theta_1 \Phi_1 + \Theta_2 \Phi_2 \Rightarrow \Theta_1 \Phi_1 + \Theta_2 \Phi_1 = (\Theta_1 + \Theta_2)\Phi_1 = \Theta_{1'} \Phi_1 = \Psi_{1'} . \tag{6}$$

The transition in time from the initial untangled state of the NEMS through the entangled state to the new untangled state, and so on, can be represented as a cycle of two-step processes:

$$\Psi_1 \overset{\delta\tau_1}{\Rightarrow} \Psi_2 \overset{\tau_1}{\Rightarrow} \Psi_{1'} \overset{\delta\tau_2}{\Rightarrow} \Psi_{2'} \overset{\tau_2}{\Rightarrow} \Psi_{1''} ..... \tag{7}$$

Thus, a contextual stepwise motion of the electron-nuclear subsystem of the NEMS appears in the material. At the supra-atomic scale level, it is encapsulated in the NEMS electromechanical interface capsule formed by a subatomic entangled pair of electrons. The processes of measurement and control of the electronic-nuclear subsystem NEMS are carried out by the sensor and actuator subsystem of low-energy secondary entangled pairs of electrons. The sensory stages of pulsed attosecond measurements alternate with stages of pulsed femtosecond control.

3. Quantum dissipative infrastructure of hybrid electronic and bielectronic systems

In measurement processes, secondary low-energy entangled electron pairs dissipate the energy of the electron-nuclear subsystem of the NEMS. As a result, the process of multiplication of the subsystem of low-energy secondary entangled pairs of electrons in the surrounding dissipative medium of a condensed state occurs. They form the dissipative infrastructure of electromechanical interfaces at higher hierarchical scale levels of new quantum smart-materials [11, 13].

In view of the above, in the thermofield quantum dynamics of a condensed state, it is assumed that the material, in addition to the system of electrons, contains a subsystem of short living entangled pairs of electrons. The generalized Hilbert space of states H^{NP} of the unified electronic system is constructed by the direct product of the Hilbert space of states of N electrons and the Hilbert space of states of P entangled bielectrons:

$$H^{NP} = H^{Ne} \otimes H^{P(2e)} . \tag{8}$$

In equation (8) the Hilbert space of states H^{Ne} of N electrons is represented as an antisymmetric direct product of the spaces of individual single electrons:

$$H^{Ne} = Asym(H_1^{1e} \otimes H_2^{1e} \otimes ... \otimes H_N^{1e}) . \tag{9}$$

Similarly, the Hilbert space of states $H^{P(2e)}$ of P entangled bielectrons is represented as an antisymmetric direct product of the spaces of individual entangled electron pairs:

$$H^{P(2e)} = Asym(H_1^{2e} \otimes H_2^{2e} \otimes ... \otimes H_P^{2e}) . \tag{10}$$

The general Fock space of states H_{OES} of an open unified electronic system consisting of electrons and bielectrons is constructed as a direct sum of Hilbert spaces of states $\{ H^{NP} \}$ with a variable number of electrons $N = 1, 2, ...$ and a variable number of the entangled electron pairs $P = 1, 2, ... $.

$$H_{OES} = \oplus_N \oplus_P H^{NP} . \tag{11}$$

Let us note the special status of the subatomic level of attosecond pulsed quantum processes. It is only at this basic level of the multiscale structure of the nonequilibrium condensed state that high-energy entangled electron pairs are formed. They are able to accumulate quantum electromechanical energy at the inter-

faces of the NEMS capsules without competing for the absorption of the energy of attosecond hard ultraviolet and soft X-ray pulses from femtochemical electronic-vibrational-rotational excitations in the material.

The uniqueness of the supra-atomic sublevel of the material structure lies in the fact that atomic-molecular processes of quantum femtochemistry and processes of quantum attophysics of nanoelectromechanical systems take place in it. There are two types of nanoscale condensed matter objects here, namely quantum nanoelectromechanical systems and quantum nanomolecular systems. They coexist "in parallel" on two-time scale sublevels: attosecond and femtosecond, respectively.

It should be taken into account that in secondary electromechanical interfaces on a scale from ten nanometers to a micrometer, the energy of tertiary entangled two-electron excitations lies within the excitation bands of conventional electronic femtochemical processes of materials and can dissipate over the degrees of freedom of electronic-vibrational-rotational excitations of the material.

Conclusions

Currently, applications of the effects of quantum entanglement, quantum contextuality and quantum dissipativity form the basis of the second quantum revolution in high technology development. This article discusses the quantum effects of entanglement, contextuality and dissipativity of subatomic and supra-atomic entangled electron pairs in a nonequilibrium condensed state. We have considered their use for the development of fundamentally new quantum subatomic nanotechnologies. In Section 1, we analyzed the prospects for the implementation of the mechanism of attosecond pulsed entanglement of pairs of subatomic electrons. In Section 2, we considered the organization of the quantum contextuality of measurement and control of nonequilibrium femtosecond electron-nuclear systems at the supra-atomic level of the condensed state of matter using subatomic entangled electron pairs. Finally, in Section 3, we discussed the prospects for applying the quantum dissipativity of the combined bosonic subsystem of primary high-energy subatomic and secondary low-energy supra-atomic entangled electron pairs in the formation of the infrastructure of new quantum smart materials.

Modern developments of quantum NEMS complement the approaches and methods for creating atomic-molecular devices. Molecular nanomachines are created by femtochemical processes using picosecond infrared and femtosecond pulsed optical radiation. The development of the direction of quantum NEMS as hybrid binary two-level quantum devices should be based on the attosecond pulsed action of hard ultraviolet radiation or soft X-ray radiation on a material. The breakthrough in this field of quantum subatomic nanotechnology of materials is delayed not only due to the lack of developed theoretical concepts and adequate computer models, but also because of the lack of precision experiments. Further research is needed.

References

1   Jaeger, L. (2018). The Second Quantum Revolution: From Entanglement to Quantum Computing and Other Super-Technologies. *Springer Nature Switzerland AG*, 331. https://doi.org/10.1007/978-3-319-98824-5

2   Levesque, J. & Corkum, P.B. (2006). Attosecond science and technology. *Canadian Journal of Physics*, *84*, 1, 1–18. https://doi.org/10.1139/p05-068

3   Corkum, P.B. & Krausz, F. (2007). Attosecond science. *Nature Physics*, *3*, 6, 381–387. https://doi.org/10.1038/nphys620

4   Krausz, F. & Ivanov, M. (2009). Attosecond physics. *Reviews of Modern Physics*, *81*, 1, 163–234. https://doi.org/10.1103/RevModPhys.81.163

5   Gallmann, L., Cirelli, C. & Keller, U. (2012). Attosecond Science: Recent Highlights and Future Trends. *Annual Review of Physical Chemistry*, *63*, 447–469. https://doi.org/10.1146/annurev-physchem-032511-143702

6   Zewail, A.H. (2000). Femtochemistry. Past, present, and future. *Pure and Applied Chemistry*, *72*, 12, 2219–2231. https://doi.org//10910.1351/pac200072122219

7   Morishita, T., Watanabe, S. & Lin, C.D. (2007). Attosecond light pulses for probing two-electron dynamics of helium in the time domain. *Physical Review Letters*, *98*, 8, 083003. https://doi.org/10.1103/PhysRevLett.98.083003

8   Ott, C., Kaldun, A., Argenti, L., Raith, P., Mayer, K., Laux, M., Zhang, Y., Blättermann, A., Hagstotz, S., Ding, T., Heck, R., Madroñero, J., Martín, F. & Pfeifer, T. (2014). Reconstruction and control of a time-dependent two-electron wave packet. *Nature*, *516*, 374–378. https://doi.org/10.1038/nature14026

9   Ranitovic, P., Hogle, C.W., Riviere, P., Palacios, A., Tong, X.M., Toshima, N., Gonzalez-Castrillo, A., Martin, L., Martin, F., Murnane, M. & Kapteyn, H. (2014). Attosecond VUV coherent control of molecular dynamics. *Proceedings of the National Academy of Sciences USA*, *111*, 3, 912–917. https://jila.colorado.edu/bibcite/reference/3356

10   Calegari F., Sansone, G., Stagira, S., Vozzi, C. & Nisoli, M. (2016). Advances in attosecond science. *Journal of Physics B*: *Atomic, Molecular and Optical Physics*, *49*, 062001, 1–27. http://dx.doi.org/10.1088/0953-4075/49/6/062001

11 Beznosyuk, S.A. & Zhukovsky, M.S. (2017). Multiscale space-time dissipative structures in materials: Two-electron genesis of nonequilibrium electromechanical interfaces. *Physical Mesomechanics*, *20*, 102–110 https://doi.org/10.1134/S102995991701009X

12 Beznosyuk, S.A., Maslova, O.A., Maksimov, D.Yu. & Zhukovsky, M.S. (2018). Attosecond nanotechnology: from subatomic electrostatic strings entangling electron pairs to supra-atomic quantum nanoelectromechanical systems energy storage in materials. *International Journal of Nanotechnology*, *15*, 4/5, 245-257. https://doi.org/10.1504/IJNT.2018.094783

13 Beznosyuk, S.A., Maslova, O.A. & Zhukovsky, M.S. (2019). Quantum infrastructure of attosecond sensors and actuators of nonequilibrium physical media in smart materials. *Physical Mesomechanics*, *22*, 432–438 https://doi.org/10.1134/S1029959919050096

14 Beznosyuk, S.A., Maslova, O.A. & Zhukovsky, M.S. (2019). Hybrid quantum technologies of intellectual nanomaterials. *International Journal of Nanotechnology*, *16*, 1-2-3, 22–33. http://dx.doi.org/10.1504/IJNT.2019.102389

15 Umezawa, H., Matsumoto, H. & Tachiki, M. (1982). Thermo Field Dynamics and Condensed States. North-Holland; Amsterdam (Netherlands); ISBN 0 444 86361, 607 pp.

16 Dzhafarov E.N. (2019). Contextuality and probability in quantum mechanics and beyond: a preface. Philosophical Transactions of the Royal Society A Mathematical Physical and Engineering Sciences, *377*(2157), 20190371. https://doi.org/10.1098/rsta.2019.0371

Information about author*

Beznosyuk, Sergey Alexandrovich (*corresponding author*) — Doctor of Physical and Mathematical Sciences, Professor, Head of the Physical and Inorganic Chemistry Department, Altai State University, Lenin avenue, 61, 656049, Barnaul, Russia; e-mail: bsa1953@mail.ru; https://orcid.org/0000-0002-4945-7197

_____

*The author's name is presented in the order: *Last Name, First and Middle Names*

Michael G. Kucherenko [ID], Tatiana M. Chmereva [ID]

Center of Laser and Informational Biophysics, Orenburg State University, Orenburg, Russia
(*Corresponding author's e-mail: clibph@yandex.ru)

Quantum Kinetics of the Electronic Energy Transformation in Molecular Nanostructures

A quantum theory of electronic energy transfer in a layered nanostructure with molecular J-aggregates of polymethine dyes was proposed. An expression for the exciton-plasmon bond energy depending on various parameters of the system was given. The rate of non-radiative Förster resonance energy transfer (FRET) from surface plasmon polaritons (SPPs) of a metal substrate to Frenkel excitons of J-aggregates was determined and dispersion dependences for hybrid states were obtained. It was established that the energy transfer rate can reach values of 10^{12}–10^{13} s^{-1}, and the value of the Rabi splitting is up to 100 MeV. The kinetics of the process under strong exciton-plasmon interaction was investigated. The time dependence of the energy exchange between the system components had the form of damped oscillations depending on the relaxation parameters, the Rabi frequency, and the response to resonance. In addition, the exciton FRET between two parallel monolayers of J-aggregates of polymethine dyes separated by a nanometer-thick metal film was investigated. It was found that the presence of the metal layer increases the FRET rate. The spin evolution of a pair of two triplet (T) molecules localized in the nano-cell region under the over-barrier jumps regime in a magnetic field was studied. The influence of the parameters of the two-dimensional potential on the frequency of inter-dimensional motions and the population of triplets was considered. The spin dynamics of molecular T-T pairs in the magnetic field of a ferromagnetic globular nanoparticle under free surface diffusion of a spin-carrying molecule was investigated.

Keywords: non-radiative energy transfer, surface plasmon, J-aggregate, Frenkel exciton, triplet-triplet annihilation, dispersion curves, spin dynamics, globular nanoparticle, Rabi splitting.

Contents

1. Plasmon-exciton dynamics and relaxation in a planar system with a monolayer of J-aggregates of polymethine dyes

A number of papers [1–3] consider the strong coupling of exciton and plasmon states in nanostructures with J–aggregates, which leads to the formation of hybrid quasiparticles. In [3], the plasmon-exciton interaction was studied in a nanostructure of parallel layers: a metal substrate and two non-conducting layers with different electrical constants. In a dielectric medium, a monolayer of J-aggregates of polymethine dye molecules is located at the interface. Upon photoexcitation of the sandwich structure, Frenkel excitons appear in the quasi-two-dimensional layer of molecular J-aggregates that interact with surface plasmon polaritons (SPPs) of the metal base.

The configuration of the system under study is shown in Figure 1. In the case of weak coupling of exciton and plasmon (EP) states, calculations of the energy transfer rate from the surface plasmon polariton to molecular J-aggregates were carried out within the framework of quantum mechanical perturbation theory. In the case of a strong coupling of excitons and plasmons, the effect of the dielectric medium and the thickness of the layer *l* on the Rabi splitting (EP interaction energy) at strict resonance was investigated.

The hybrid EP state occurs at the intersection of the dispersion curves in Figure 2, and its energy is [3] as

$$E(\mathbf{k}) = \frac{1}{2}\left(E_{ex}(\mathbf{k}) + \hbar\omega(k) \pm \sqrt{\left(E_{ex}(\mathbf{k}) - \hbar\omega(k) \right)^2 + 4\left| V_{10,01}(\mathbf{k}) \right|^2} \right),$$ (1)

where $E_{ex}(\mathbf{k})$ is the energy of the 2d exciton, $\hbar\omega(k)$ is the energy of the 2d polariton, $V_{10,01}(\mathbf{k})$ is the matrix element of the EP-coupling, $\mathbf{k}$ is the wave vector of the EP hybrid, $k = |\mathbf{k}|$.
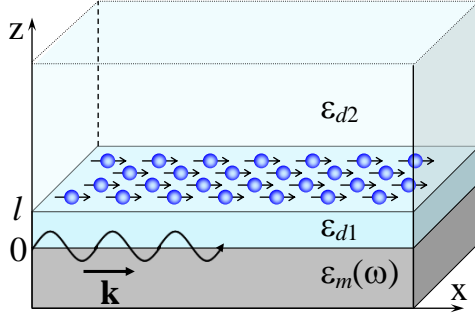
Figure 1. Mutual arrangement of the layers of the hybrid JDM system
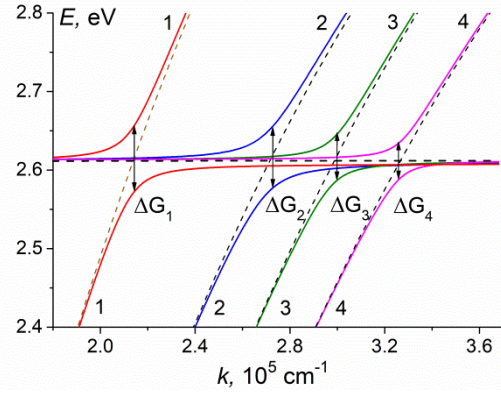
Figure 2. Dispersion curves of hybrid exciton-plasmon quasiparticles for different permittivity values ε_{d2}

It is convenient to represent the EP-interaction in the formalism of secondary quantization. In [4, 5] the quasi-static approximation was used, in which the potential of the SPP field was determined on the basis of the Laplace equation. But already in [3] the intensity of the field created by the SPP was determined from Maxwell's equations. In the approach [6] the time-average field energy of the SPP was quantized by replacing the field strengths with the operators of destruction and generation of SPP with the wave vector $\mathbf{k}$.

The electric field strength operators of the SPP in metal $z < 0$

$$\hat{\mathbf{E}}_m(\mathbf{r}, z, t) = \sum_{\mathbf{k}} \sqrt{\frac{2\pi\hbar\omega}{SL(k)}} \left(\mathbf{e}_{\mathbf{k}} - i\frac{k}{k_z^m}\mathbf{e}_z \right) e^{k_z^m z} e^{i(\mathbf{kr} - \omega t)} a_{\mathbf{k}} + H.c.$$ (2)

in the dielectric layer $0 \leq z \leq l$

$$\hat{\mathbf{E}}_{d1}(\mathbf{r}, z, t) = \sum_{\mathbf{k}} \sqrt{\frac{2\pi\hbar\omega}{SL(k)}} \left\{ \left(\mathbf{e}_{\mathbf{k}} + i\frac{k}{k_z^{d1}}\frac{f}{d}\mathbf{e}_z \right) \mathrm{ch}\left(k_z^{d1} z \right) - \left(\frac{f}{d}\mathbf{e}_{\mathbf{k}} + i\frac{k}{k_z^{d1}}\mathbf{e}_z \right) \mathrm{sh}\left(k_z^{d1} z \right) \right\} e^{i(\mathbf{kr} - \omega t)} a_{\mathbf{k}} + H.c.$$ (3)

in a half — space $z > l$, filled with a dielectric

$$\hat{\mathbf{E}}_{d2}(\mathbf{r}, z, t) = \sum_{\mathbf{k}} \sqrt{\frac{2\pi\hbar\omega}{SL(k)}} \frac{a}{d} e^{k_z^{d2} l} \left(\mathbf{e}_{\mathbf{k}} + i\frac{k}{k_z^{d2}}\mathbf{e}_z \right) e^{-k_z^{d2} z} e^{i(\mathbf{kr} - \omega t)} a_{\mathbf{k}} + H.c.,$$ (4)

where S is the surface area of the metal-dielectric interface, $L(k)$ is the area of localization of the surface plasmon along the normal to the substrate surface. Here $\mathbf{e}_{\mathbf{k}}$ and $\mathbf{e}_z$ are unit vectors directed respectively along and perpendicular to the surface; $k = |\mathbf{k}|$ is the longitudinal wave number through which the real coefficients are expressed $k_z^m = \sqrt{k^2 - \varepsilon_m(\omega) \cdot \omega^2/c^2}$, $k_z^{d1(2)} = \sqrt{k^2 - \varepsilon_{d1(2)} \cdot \omega^2/c^2}$, characterizing the rate of decay of fields at a distance from the metal surface; c is the speed of light, Also in formulas (3)–(5) the notation is introduced: l is the thickness of the intermediate layer; $a = \varepsilon_{d1}k_z^{d2}$, $b = \varepsilon_{d2}k_z^{d1}$, $d = a\,\mathrm{ch}\left(k_z^{d1}l \right) + b\,\mathrm{sh}\left(k_z^{d1}l \right)$ and $f = b\,\mathrm{ch}\left(k_z^{d1}l \right) + a\,\mathrm{sh}\left(k_z^{d1}l \right)$. An expression for the localization region $L(k)$ of the surface plasmon has been obtained, from which it follows that the function $L(k)$ decreases monotonically with an increase in the longitudinal wave number k.

The frequency $\omega(k)$ of the surface plasmon-polariton is the solution of the dispersion equation

$$\frac{\varepsilon_m(\omega)k_z^{d1}}{\varepsilon_{d1}k_z^m} = -\frac{\varepsilon_{d2}k_z^{d1}\text{ch}(k_z^{d1}l) + \varepsilon_{d1}k_z^{d2}\text{sh}(k_z^{d1}l)}{\varepsilon_{d2}k_z^{d1}\text{sh}(k_z^{d1}l) + \varepsilon_{d1}k_z^{d2}\text{ch}(k_z^{d1}l)}. \tag{5}$$

The operator describing the interaction of molecular aggregates with a metal substrate is written as [7]

$$\hat{V} = -\sum_{\mathbf{n}} \hat{\mathbf{p}}_{10} \cdot \hat{\mathbf{E}}(\mathbf{n}),$$

where $\hat{\mathbf{p}}_{10} = N^{-1/2}\sum_{\mathbf{Q}}\left(\mathbf{p}_{10}B_{\mathbf{Q}}^+ e^{-i\mathbf{Qn}} + \mathbf{p}_{01}^* B_{\mathbf{Q}} e^{i\mathbf{Qn}}\right)$ is the operator of the dipole moment of transition in a J-aggregate molecule located at a node with a radius vector $\mathbf{n}$ [8], $\mathbf{p}_{10}$ is the electric dipole moment of the quantum transition of the molecule from the ground to the first excited state; N is the number of molecules in a two-dimensional lattice, $B_{\mathbf{Q}}^+$ and $B_{\mathbf{Q}}$ are the operators of the generation and destruction of excitons with the wave vector $\mathbf{Q}$.

The matrix element of the EP-interaction operator between the state of a system with one exciton $\left|1_{ex}, 0_{pl}\right\rangle$ (without a plasmon), and the state with one plasmon (without an exciton) $\left|0_{ex}, 1_{pl}\right\rangle$ has the following form:

$$V_{10,01}(\mathbf{k}) = -\sqrt{\frac{2\pi\hbar\omega}{s \cdot L(k)}}\frac{a}{d}\exp\left[-k_z^{(d2)}(z-l)\right](\mathbf{e_k} \cdot \mathbf{p}_{10}), \tag{6}$$

where s is the area of the unit cell of a two-dimensional monolayer, z is the distance from the metal surface to the monolayer.

In the case of weak EP-coupling, the rate of transition from state $\left|0_{ex,}1_{pl}\right\rangle$ to state $\left|1_{ex,}0_{pl}\right\rangle$ is written as

$$U(\mathbf{k}) = \frac{2\pi}{\hbar}\left|V_{10,01}(\mathbf{k})\right|^2 \delta\left(E_{ex}(\mathbf{k}) - \hbar\omega(k)\right). \tag{7}$$

As can be seen from (7), the dependence of the transition rate on the wave number has a delta-like peak when the exciton energy and the SPP coincide $E_{ex}(\mathbf{k}) = \hbar\omega(k)$.

If $U^{-1} < \tau_{ex}$, this is effectively the quenching of excitons, i.e. the energy transfer from the Frenkel excitons of the J-aggregate to the metal substrate. According to the calculations performed, the quenching rate is at a maximum of $\sim 10^{13}$ s^{-1} with a layer thickness of 15 nm, which is significantly higher than the rates of other processes leading to the death of excitons.

A numerical study of the dependence of the Rabi splitting on the system parameters was carried out for a strong EP-coupling. Figure 2 shows the dispersion laws (1) of hybrid plasmon-exciton states for different values of the dielectric constant of the second medium at fixed values of thickness $l = 10$ nm and the dielectric constant $\varepsilon_{d1} = 2$ of the first medium. The dotted lines correspond to unrelated excitonic and SPP-modes. With increasing permeability ε_{d2}, the intersection point of the exciton and SPP dispersion curves shifts towards large k, and the value of the Rabi splitting decreases from $\Delta G_1 = 84$ meV at $\varepsilon_{d2} = 2$ to $\Delta G_4 = 46$ meV at $\varepsilon_{d2} = 5$.

Thus, the study carried out in [3] showed that the geometric and dielectric characteristics of the considered three-layer structure significantly affect the magnitude of the plasmon-exciton interaction energy. Therefore, depending on the system parameters, the value of Rabi splitting can reach $\sim$100 MeV, which is consistent with the experimental data of other authors [8–9]. In addition, varying the permeability and thickness of the interlayer between the metal substrate and the film of J-aggregates, it is possible to change the rate of energy exchange between surface plasmons and Frenkel excitons and achieve unilateral energy transfer to J-aggregates, which is necessary for the development of new organic light emitters.

With a strong exciton-plasmon interaction, it is necessary to describe the energy transformation on the basis of a more general quantum mechanical formalism using a paired density matrix $\hat{\rho}(t)$ of quantum subsystems interacting both with each other and with a thermostat [10–11].

In [11], the kinetics of energy exchange between plasma and exciton subsystems in a planar composite nanostructure with strong exciton-plasmon interaction was investigated. It was shown that the energy trans-

fer between the system components occurs non-monotonically in time, but has the form of damped oscillations depending on the relaxation parameters, the Rabi frequency and the detuning from resonance.

The density operator $\hat{\rho}(t)$ of a multilayer system satisfies a kinetic equation written on the basis of the Neumann equation with a relaxation term — drain

$$\frac{d}{dt}\hat{\rho} = \frac{1}{i\hbar}\left[\hat{H}_0 + \hat{V}, \hat{\rho}\right] - \hat{R}^\dagger \hat{\rho} .\tag{8}$$

Operator $\hat{H}_0$ in eq. (8) is the Hamiltonian of the combined 1+2 system (exciton + plasmon subsystems) in the absence of exciton-plasmon interaction; $\hat{R}^\dagger$ is a relaxation superoperator. In the simplest case of equality of the exciton and plasmon lifetimes $\tau_{pl} = \tau_{exc} = \tau$, an autonomous equation for inversion $\Delta\rho(t) = \rho_{11}(t) - \rho_{22}(t)$ was obtained on the basis of (8) at an arbitrary phase relaxation time T_2 and under conditions of zero detuning from resonance $\Delta E = 0$

$$\Delta\ddot{\rho}(t) + \left(\frac{1}{\tau} + \frac{1}{T_2}\right)\Delta\dot{\rho}(t) + \left(\Omega^2 + \frac{1}{\tau T_2}\right)\Delta\rho(t) = 0 , \quad \Omega = 2|V_{12}|/\hbar .\tag{9}$$

Calculations based on equation (9) at equal times $\tau_{pl} = \tau_{exc} \sim 10^{-12}$ c and zero detuning from resonance $\Delta E = 0$ showed that with a decrease in the transverse relaxation time T_2 from $0.8\tau_{exc}$ to $0.05\tau_{exc}$ at the Rabi frequency of $\Omega = 15 \div 20 \cdot 10^{12}$ s^{-1}, a decrease in the depth of population modulation was observed $\rho_{11}(t)$ and $\rho_{22}(t)$ up to its almost complete disappearance. When increased to Ω to $30 \cdot 10^{12}$ s^{-1}, the modulation became clearly pronounced again.

In the general case of arbitrary relations between times $\tau_{pl}, \tau_{exc}, T_2$ and non-zero detuning ΔE from resonance, the kinetics of populations of states 1 and 2 is analyzed on the basis of the modified Johnson-Merrifield equation [12] proposed to describe spin-selective exciton annihilation

$$\frac{d}{dt}\hat{\rho} = -\frac{i}{\hbar}\left[(\hat{H}_0 + \hat{V}), \hat{\rho}\right] - \frac{1}{2}\tilde{k}_1\{\hat{P}_1, \hat{\rho}\}_+ - \frac{1}{2}\tilde{k}_2\{\hat{P}_2, \hat{\rho}\}_+ - T_2^{-1}\hat{\rho} ,\tag{10}$$

where $\{\hat{P}_j, \hat{\rho}\}_+ = \hat{P}_j \cdot \hat{\rho} + \hat{\rho} \cdot \hat{P}_j$ is the anti-commutator, $\hat{P}_j = |j\rangle\langle j|$ is the projection operator on state j, $\tilde{k}_1, \tilde{k}_2$ are additives to scalar rates of deactivation of the system through plasmon and exciton decay channels. The solution of the operator equation (10) can be represented using matrix exponentials $\hat{\rho}(t) = \exp(-t/T_2) \cdot \exp(\hat{K}^{(-)}t)\hat{\rho}(0)\exp(\hat{K}^{(+)}t)$, and the kinetic matrix $K_{ij}^{(\mp)}$ is

$$K_{ij}^{(\mp)} = \begin{pmatrix} \mp\dfrac{i}{\hbar}(\hbar\omega(k) + V_{11}) - \dfrac{1}{2}\tilde{k}_1 & \mp\dfrac{i}{\hbar}V_{12} \\[2ex] \mp\dfrac{i}{\hbar}V_{21} & \mp\dfrac{i}{\hbar}(E_{exc} + V_{22}) - \dfrac{1}{2}\tilde{k}_2 \end{pmatrix} ,\tag{11}$$

with eigenvalues of matrices $K_{ij}^{(\mp)}$ in the form of

$$\kappa_{1,2}^{(\mp)} = (\mp)\frac{i}{2}\left[\omega(k) + E_{exc}/\hbar\right] - \frac{1}{4}(\tilde{k}_1 + \tilde{k}_2) \mp \frac{1}{2}\left\{\left[i(\mp)\Delta E/\hbar + (\tilde{k}_1 - \tilde{k}_2)/2\right]^2 - \Omega^2\right\}^{1/2} .$$

In particular, the population kinetics of the exciton state $|2\rangle = |1_{ex}, 0_{pl}\rangle$ is determined by the following set of exponents with complex-valued indicators as combinations of the $\kappa_{1,2}^{(\mp)}$ eigenvalues

$$\rho_{22}(t) = \langle 2|\hat{\rho}(t)|2\rangle = \frac{K_{21}^{(-)}K_{12}^{(+)}}{(\kappa_1^{(-)} - \kappa_2^{(-)})(\kappa_1^{(+)} - \kappa_2^{(+)})} \times$$
$$\times\left[\exp\left((\kappa_1^{(-)} + \kappa_1^{(+)})t\right) + \exp\left((\kappa_2^{(-)} + \kappa_2^{(+)})t\right) - \exp\left((\kappa_1^{(-)} + \kappa_2^{(+)})t\right) - \exp\left((\kappa_2^{(-)} + \kappa_1^{(+)})t\right)\right] .\tag{12}$$

Based on models (9) and (10)–(12), the parametric dependences of population kinetics $\rho_{11}(t)$ and $\rho_{22}(t)$ an activated planar system with an exciton-bearing J-aggregate layer on a conductive substrate were investigated.

Figures 3 and 4 show the time dependences of the populations of the plasmon and exciton subsystems calculated on the basis of model (10)–(12). At significant differences (up to the order of magnitude and high-

er) in the proper lifetimes of excitons and plasmons τ_{exc}, τ_{pl}, characteristic modulations with the Rabi frequency Ω not only of partial densities $\rho_{11}(t)$ and $\rho_{22}(t)$ quasiparticles, but also of the total excitation density $n(t) = \rho_{11}(t) + \rho_{22}(t)$, with noticeable deviations from the trend exponent, were observed. Increasing the Rabi frequency from $20 \cdot 10^{12}$ to $80 \cdot 10^{12}$ s^{-1} resulted in a significant increase in the depth of modulation of the plasmon density $\rho_{11}(t)$ at the ratio of relaxation rates $\tilde{k}_1 = 5.5 \cdot T_2^{-1}$, $\tilde{k}_2 = 0.1 \cdot T_2^{-1}$. At the same time, the modulation of the exciton density $\rho_{22}(t)$ at the Rabi frequency was carried out almost to zero values over time $t \sim \Omega^{-1}$.
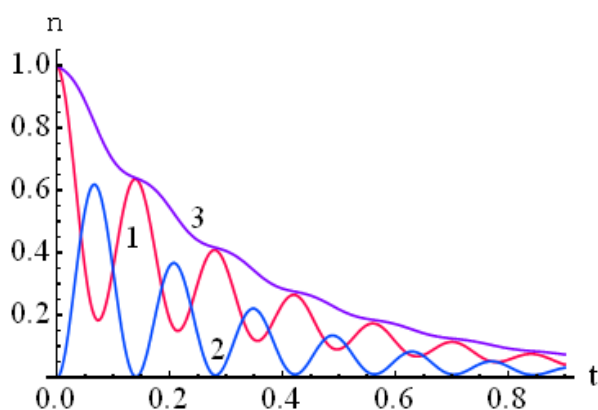
Figure 3. Kinetics of partial populations of plasmon $\rho_{11}(t)$ — (1) and exciton $\rho_{22}(t)$ — (2) subsystems, as well as the total population $n(t) = \rho_{11} + \rho_{22}$ (envelope curve 3) of the excited state of the system, at various additional decay rates $\tilde{k}_1 = 5.5 \cdot T_2^{-1}$, $\tilde{k}_2 = 0.1 \cdot T_2^{-1}$, transverse relaxation time $T_2 = 1$ ps and Rabi frequency $\Omega = 40 \cdot T_2^{-1}$. Time t is expressed in ps. The amount of detuning from the resonance $\Delta E / \hbar = 20 \cdot T_2^{-1}$
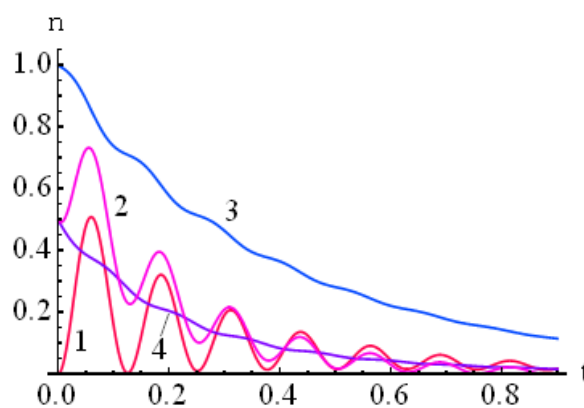
Figure 4. Population kinetics of the exciton $\rho_{22}(t)$ subsystem at the initial settlement of the partial plasmon state $\rho_{11}(0) = 1$ — (1), the pure initial state of the equal-amplitude superposition — (2); the mixed initial state with the same weight coefficients — (4), as well as the total population $n(t) = \rho_{11} + \rho_{22}$ (envelope curve 3) of the excited state of the system. The parameter values are the same as for Figure 3

1.1 Transfer of exciton excitation energy between two monolayers of J-aggregates

In addition to the energy transfer to the plasmon resurvoir in the system of Figure 1, the non-radiative transfer of exciton excitation energy between monolayers A and B of molecules of polymetine dyes forming J-aggregates was investigated (Fig. 5). It was assumed that such a distant transfer could be carried out by means of surface plasmons of a nanometer-thick metal film located between the monolayers. The study of multilayered systems containing J-aggregates (JA) of two varieties is important for understanding the processes of energy transfer in biological light-harvesting complexes, as well as for the creation of artificial photosynthesis systems [13].

A number of experimental papers report on the registration of this process. Thus, the authors of [14-15] observed energy transfer between JA layers formed by molecules of various polymethine dyes in a polymer film. As a result of the EP interaction, non-radiative energy transfer J→SPP→J occurs with the appearance of the Frenkel exciton in the initially inactive molecular layer. At weak PE-coupling, the energy transfer rate PP→J can be calculated on the basis of quantum mechanical perturbation theory [16].
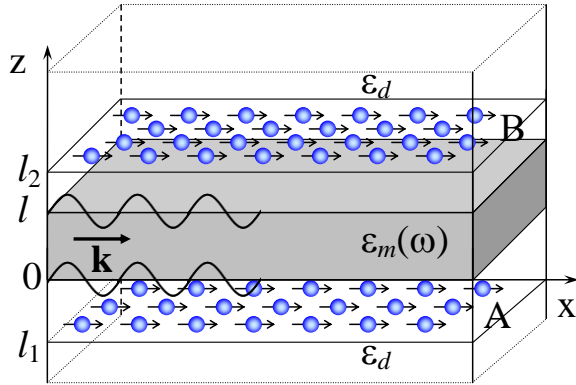
Figure 5. Location of the metal film
between two monolayers of J-aggregates
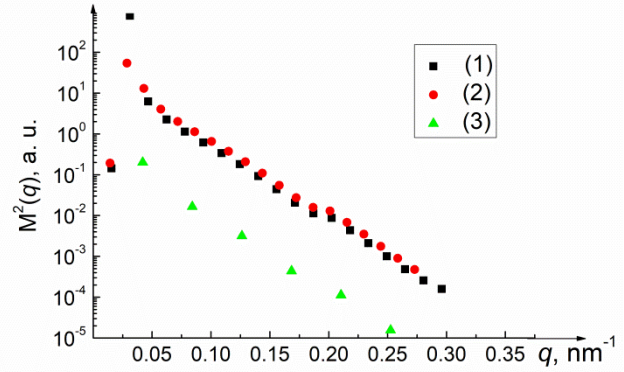
Figure 6. Dependence of the square of a composite
matrix element on the wave number for different wave
vectors: 1 — $\mathbf{q} \parallel \mathbf{q}_a$, 2 — $\mathbf{q} \parallel \mathbf{q}_a + \mathbf{q}_b$, 3 — $\mathbf{q} \parallel \mathbf{q}_a$ — $\mathbf{q}_b$

The exciton excitation energy transfer rate from one monolayer to another using surface plasmons of the metal film can be determined in the second order of quantum mechanical perturbation theory

$$U_{AB} = \frac{2\pi}{\hbar} \sum_{\mathbf{q},\mathbf{q}'} P_{\mathbf{q}} \left| M\left(\mathbf{q},\mathbf{q}'\right) \right|^2 \delta\left(E_A\left(\mathbf{q}\right) - E_B\left(\mathbf{q}'\right)\right), \tag{13}$$

where $M(\mathbf{q}, \mathbf{q}')$ is a composite matrix element of EP-interaction defined by the expression

$$M\left(\mathbf{q},\mathbf{q}'\right) = \sum_{\mathbf{k},j} \left[\frac{\langle \mathbf{q}' | \hat{V}_{pl-exB}^{(j)} | \mathbf{k}\rangle \langle \mathbf{k} | \hat{V}_{pl-exA}^{(j)} | \mathbf{q}\rangle}{E_A(\mathbf{q}) - \hbar\omega_k^{(j)}} \right]. \tag{14}$$

The following designations are introduced in formulas (13) and (14): the initial state of the system $|\mathbf{q}\rangle = |1_{ex}^A, 0_{ex}^B, 0_{pl}\rangle$ is the exciton state of monolayer A, the final state $|\mathbf{q}'\rangle = |0_{ex}^A, 1_{ex}^B, 0_{pl}\rangle$ is the exciton state of monolayer B, $|\mathbf{k}\rangle = |0_{ex}^A, 0_{ex}^B, 1_{pl}\rangle$ is an intermediate plasmon state characterized by a wave vector $\mathbf{k}$. Summation by j takes into account the possibility of excitation in a thin film of two types of surface plasmons: antisymmetric (high-frequency $\omega_k^{(1)}$) and symmetric ($\omega_k^{(2)}$ low-frequency), $E_A(\mathbf{q})$ and $E_B(\mathbf{q}')$ are exciton excitation energies in monolayers A and B, $P_{\mathbf{q}}$ is the population of exciton states described by the Boltzmann distribution.

To calculate the matrix elements of the plasmon-exciton interaction operator $\hat{V}_{pl-ex}^{(j)} = -\sum_{\mathbf{n}} \mathbf{d}(\mathbf{n}) \cdot \mathbf{E}^{(j)}(\mathbf{n})$ included in (14), it is convenient to use the secondary quantization formalism. The operator $\mathbf{d}(\mathbf{n})$ of the dipole moment of transition JA to the exciton state is written in this formalism as

$$\mathbf{d}(\mathbf{n}) = \frac{1}{\sqrt{N}} \sum_{\mathbf{q}} \left(\mathbf{d}_{01} e^{i\mathbf{q}\mathbf{n}} B_{\mathbf{q}} + \mathbf{d}_{10} e^{-i\mathbf{q}\mathbf{n}} B_{\mathbf{q}}^+ \right), \tag{15}$$

where $\mathbf{d}_{10}$ is the dipole moment of transition in a J-aggregate molecule between its ground and first excited states, $\mathbf{n}$ is the vector specifying the position of the molecule in JA, N is the number of molecules in JA, $B_{\mathbf{q}}$ and $B_{\mathbf{q}}^+$ are the exciton destruction and generation operators. The electric field strength operators of the surface plasmon mode j can be found in the same way as in [3]. In a dielectric medium at $z < 0$ (Fig. 5), the intensity decreases exponentially with distance from the metal film

$$\mathbf{E}_d^{(j)}(\mathbf{n}, z, t) = \sum_{\mathbf{k}} \sqrt{\frac{2\pi\hbar\omega_k^{(j)}}{S L^{(j)}(k)}} \left(1 \mp e^{-k_{mz}^{(j)}l}\right) e^{k_{dz}^{(j)}z} \left(\mathbf{e}_{\mathbf{k}} - i\frac{k}{k_{dz}^{(j)}} \mathbf{e}_z \right) e^{i\left(\mathbf{kn} - \omega_k^{(j)}t\right)} a_{\mathbf{k}} + H.c. \tag{16}$$

In the area of metal $0 \le z \le l$, the tension has the complicated form

$$\mathbf{E}_m^{(j)}(\mathbf{n}, z, t) = \sum_{\mathbf{k}} \sqrt{\frac{2\pi\hbar\omega_k^{(j)}}{S L^{(j)}(k)}} \left[\left(\mathbf{e}_{\mathbf{k}} + i\frac{k}{k_{mz}^{(j)}} \mathbf{e}_z \right) e^{-k_{mz}^{(j)}z} \mp \left(\mathbf{e}_{\mathbf{k}} - i\frac{k}{k_{mz}^{(j)}} \mathbf{e}_z \right) e^{k_{mz}^{(j)}(z-l)} \right] e^{i\left(\mathbf{kn} - \omega_k^{(j)}t\right)} a_{\mathbf{k}} + H.c. \tag{17}$$

At the same time $z > l$, an exponential decrease of field strength with distance is observed

$$\mathbf{E}_d^{(j)}\left(\mathbf{n}, z, t\right) = \mp \sum_{\mathbf{k}} \sqrt{\frac{2\pi\hbar\omega_k^{(j)}}{S\,L^{(j)}\left(k\right)}} \left(1 \mp e^{-k_{mz}^{(j)}l}\right) e^{-k_{dz}^{(j)}(z-l)} \left(\mathbf{e_k} + i\frac{k}{k_{dz}^{(j)}}\mathbf{e}_z\right) e^{i\left(\mathbf{kn} - \omega_k^{(j)}t\right)} a_\mathbf{k} + H.c., \tag{18}$$

where the "$-$" sign refers to the antisymmetric, the "$+$" sign refers to the symmetric plasmon. In formulas (16)–(18), the surface area of the film is indicated by S; $a_\mathbf{k}$ is the plasmon destruction operator. The frequency $\omega_k^{(j)}$ of the surface plasmon is the solution of the following dispersion equation [16]

$$e^{k_{mz}l} = \mp \frac{\varepsilon_m\left(\omega\right)k_{dz} - \varepsilon_d k_{mz}}{\varepsilon_m\left(\omega\right)k_{dz} + \varepsilon_d k_{mz}}, \tag{19}$$

where are the coefficients $k_{dz} = \sqrt{k^2 - \varepsilon_d\,\omega^2/c^2}$, and $k_{mz} = \sqrt{k^2 - \varepsilon_m\left(\omega\right)\omega^2/c^2}$ as in the single-layer case, the rate of decrease in the field strength of the surface plasmon is determined as it moves away from the metal-dielectric interface; $\varepsilon_m\left(\omega\right) = \varepsilon_\infty - \omega_{pl}^2/\omega^2$ is the dielectric constant of the metal in the generalized Drude model, ε_d is the frequency–independent dielectric constant of the medium surrounding the metal film, ε_∞ is the high-frequency dielectric constant of the metal, ω_{pl} is the plasma frequency of the metal.

The function $L^{(j)}\left(k\right)$, as in the single-layer case, has a length dimension and characterizes the width of the localization region of the surface plasmon in the direction normal to the surface of the metal film [16]. In the quasi-static approximation, when $c \to \infty$, $k_{mz}, k_{dz} \to k$, the coefficient $L^{(j)}\left(k\right)$ is greatly simplified

$$L^{(j)}\left(k\right) = \frac{2}{k}\frac{\omega_{pl}^2}{\omega_k^{(j)2}}\left(1 - e^{-2kl}\right)$$

and the frequencies of antisymmetric and symmetric plasmons can be written explicitly

$$\omega_k^{(1)2} = \frac{\omega_p^2\left(1 + e^{kl}\right)}{\varepsilon_\infty\left(1 + e^{kl}\right) - \varepsilon_d\left(1 - e^{kl}\right)}, \quad \omega_k^{(2)2} = \frac{\omega_p^2\left(1 - e^{kl}\right)}{\varepsilon_\infty\left(1 - e^{kl}\right) - \varepsilon_d\left(1 + e^{kl}\right)}. \tag{20}$$

Formulas (16)–(18) for the electric field strengths of the surface plasmon pass into the expressions obtained and used in [4].

Matrix elements of the EP interaction operator $\hat{V}_{pl-ex}^{(j)}$ have the following form:

$$\left\langle\mathbf{k}\left|\hat{V}_{pl-ex}^{(j)}\right|\mathbf{q}\right\rangle = \sqrt{\frac{2\pi\hbar\omega_k^{(j)}}{s_\mathrm{A}\,L^{(j)}\left(k\right)}}\left(\mathbf{d}_{10}^\mathrm{A}\cdot\mathbf{e_k}\right)\left(1 \mp e^{-k_{mz}^{(j)}l}\right) e^{-k_{dz}^{(j)}l_1}\delta_{\mathbf{k},\mathbf{q}}, \tag{21}$$

$$\left\langle\mathbf{q}'\left|\hat{V}_{pl-ex}^{(j)}\right|\mathbf{k}\right\rangle = \mp\sqrt{\frac{2\pi\hbar\omega_k^{(j)}}{s_\mathrm{B}\,L^{(j)}\left(k\right)}}\left(\mathbf{d}_{01}^\mathrm{B}\cdot\mathbf{e_k}\right)\left(1 \mp e^{-k_{mz}^{(j)}l}\right) e^{-k_{dz}^{(j)}(l_2-l)}\delta_{\mathbf{k},\mathbf{q}'}, \tag{22}$$

where $s_\mathrm{A(B)}$ is the unit cell area of monolayer A(B), $l_1(l_2)$ is the distance from the lower surface of the film to monolayer A(B). The Kronecker symbol $\hat{V}_{pl-ex}^{(j)}$ in the operator expresses the equality of the exciton wave vectors and the intermediate surface plasmon, which, in turn, leads to the equality of the exciton wave vectors $\mathbf{q}$ and $\mathbf{q}'$ in monolayers A and B.

Substitution (21), (22) in (14) gives the following expression for a composite matrix element:

$$M\left(\mathbf{q}, \mathbf{q}\right) = \frac{2\pi}{\sqrt{s_\mathrm{A}s_\mathrm{B}}}d_{01}^\mathrm{A}d_{10}^\mathrm{B}\cos\alpha\cos\beta\sum_j\left(\mp\right)\frac{\hbar\omega_q^{(j)}}{L^{(j)}\left(q\right)}\frac{\left(1 \mp e^{-k_{mz}^{(j)}l}\right)^2 e^{-k_{dz}^{(j)}(l_1+l_2-l)}}{E_A\left(\mathbf{q}\right) - \hbar\omega_q^{(j)}}, \tag{23}$$

where α and β are the angles between the exciton wave vector and the dipole transition moments in the molecules of J-aggregates A and B.

It should be noted that the rate of direct transfer of exciton excitation energy from monolayer A to monolayer B due to the dipole-dipole interaction between monolayer molecules can also be found by formula (13), in which the matrix element $M_1(\mathbf{q}, \mathbf{q}')$ of the dipole-dipole interaction energy operator is used instead of a composite matrix element, taking into account delocalization molecular excitation

$$M_1(\mathbf{q},\mathbf{q}') = \sum_{\mathbf{n},\mathbf{m}} \left[\frac{\mathbf{d}_{01}^{A}\mathbf{d}_{10}^{B}}{\varepsilon_d\, r_{\mathbf{nm}}^3} - 3\frac{\left(\mathbf{r_{mn}}\mathbf{d}_{01}^{A}\right)\left(\mathbf{r_{mn}}\mathbf{d}_{10}^{B}\right)}{\varepsilon_d\, r_{\mathbf{nm}}^5} \right] e^{i\mathbf{qn}} e^{-i\mathbf{q'm}} \; ,$$

where $r_{\mathbf{nm}}$ is the distance between molecules position of which is given by the vector $\mathbf{n}$ in one monolayer and the vector $\mathbf{m}$ in the other. If we consider the number of molecules forming each monolayer $N \to \infty$, then the matrix element $M_1(\mathbf{q}, \mathbf{q}')$ will be diagonal. Also in this case, a continuum approximation can be used, in which summation is replaced by integration. Then, provided that $\mathbf{d}_{01}^{A} = \mathbf{d}_{10}^{B} = \mathbf{d}_{10}$, the following expression for a matrix element is obtained [16].

$$M_1(\mathbf{q},\mathbf{q}) = \frac{2\pi}{\varepsilon_d\sqrt{s_A s_B}} d_{10}^2\, q\, e^{-q\, l_{AB}} \cos^2\alpha \; , \tag{24}$$

where l_{AB} is the distance between monolayers.

To make the energy transfer efficient, monolayers of J-aggregates with the closest possible positions of absorption and luminescence spectra were selected as energy donors and acceptors. In particular, J-aggregates of pseudoisocyanine (PIC) and the dye 5,5',6,6'-tetrachloro-1,1'-diethyl-3,3'-bis(4-sulfopropyl)-benzimidazolocarbocyanine (TDBC), absorption spectra maxima of which are located at ~590 nm (2.1 eV), satisfy this condition [16]. In another variant, the same JA can be considered as an energy donor and acceptor. During the calculations, it was assumed that both the donor and the acceptor were J-aggregates of the TDBC dye, and in both monolayers there were $N = 500$ molecules in each direction of the elementary vectors. The dipole moment of the transition in the TDBC molecule is co-directional with the elementary vector $\boldsymbol{a}$ and is equal to $|d_{10}| \approx 10\,\mathrm{D}$. The width of the Lorentz contour at half the height was assumed to be equal to $\Gamma = 0.05$ eV. In all calculations, the temperature was considered equal to $T = 300$ K. Silver was chosen as the material of the conductive film, for which the plasma frequency is $\hbar\omega_{pl} = 9.1$ eV and the high-frequency dielectric permittivity is $\varepsilon_\infty = 3.7$. The dielectric constant of the medium surrounding the film was $\varepsilon_d = 2$.

Figure 6 shows the results of calculations of the square of a composite matrix element according to formula (23) for different values and directions of the wave vector q. Calculations were carried out for a film with a thickness of $l = 10$ nm and the distances from the donor monolayer A and the acceptor monolayer B to the lower surface of the film $l_1 = 5$ nm and $l_2 = 20$ nm, respectively. It should be noted that the distance l_1 remained unchanged in all calculations. As can be seen from the figure, the matrix element reaches the highest values in the region of small quantum numbers $q \sim 10^5$ cm^{-1}, since the energy difference between exciton and plasmon is minimal in this region. In addition, the values of the matrix element are small (points 3) if the exciton propagates almost perpendicular to the direction of the dipole moment of transition, which follows from formula (23).

T a b l e

Dependence of the energy transfer rate on the distance between monolayers

Distance between surfactant monolayers l_{AB}, nm	The rate of energy transfer through the film U_{AB}, s^{-1}	The rate of energy transfer in the dielectric U'_{AB}, s^{-1}
15	$3.85 \cdot 10^{12}$	$3.98 \cdot 10^9$
20	$2.19 \cdot 10^{12}$	$1.70 \cdot 10^9$
25	$1.24 \cdot 10^{12}$	$8.32 \cdot 10^8$
30	$7.07 \cdot 10^{11}$	$4.52 \cdot 10^8$

The dependences of the rate of non-radiative energy transfer on the distance h between the monolayer B and the film surface at different film thicknesses were determined. Calculations showed that energy transfer occurs mainly due to symmetric plasmons. The field strength of plasmons of this type decreases with increasing film thickness.

Table presents data illustrating the effect of a 5 nm thick conductive film on the energy transfer rate between JA monolayers. The distance from monolayer B to the surface of the film varied. The table shows that in the presence of a metal film, energy transfer is more efficient than directly in a dielectric at the same distance.

Thus, in [16] there was constructed and numerically implemented a mathematical model of the energy transfer of a two-dimensional Frenkel exciton from one JA monolayer to another by means of surface plas-

mons of a metal film placed between the monolayers. It was shown that the presence of a conductive film significantly increases the rate of non-radiative energy transfer. In addition, the distance over which the energy can be efficiently transmitted increases several times compared to transmission in a dielectric. This circumstance may be useful in the development of modern optoelectronic devices based on new physical principles of operation.

1.2 Energy transfer in a cylindrical nanostructure consisting of a metal core and a coaxial shell with phosphor molecules

Light absorption and non-radiative exchange of electron excitation energy between a circular metal nanowire and phosphor molecules surrounding it were investigated on the basis of the above concepts [17]. In the case of molecules not interacting with each other, calculations of the energy transfer rate from a single excited molecule to a nanowire and the decay kinetics of the excited state of the phosphor were carried out. For molecules combined in J-aggregate complexes, the energy transfer rate from a coaxial monolayer formed by J-aggregates to a nanowire was calculated and the possibility of a hybrid exciton-plasmon state was shown. A significant influence of the geometric characteristics of the considered systems on the rate of transformation of the energy of electronic excitation was revealed.

For the rate of energy transfer from the excited phosphor molecule to the nanowire, it is possible to obtain

$$\bar{U}(r) = \frac{4|\mathbf{p}_{01}|^2}{3\hbar} \int_0^\infty \left\{ \frac{\omega_0(k)}{S_0(k)} \frac{I_0^2(q_m R)}{K_0^2(q_d R)} \left[\frac{k^2}{q_d^2} K_0'^2(q_d r) + K_0^2(q_d r) \right] G(\omega_0(k)) + 2\sum_{n=1}^\infty \frac{\omega_n(k)}{S_n(k)} \frac{I_n^2(q_m R)}{K_n^2(q_d R)} G(\omega_n(k)) \times \right.$$
$$\left. \times \left[\left(\frac{k}{q_d} K_n'(q_d r) + \frac{\omega_n(k) nf}{q_d^2 r} K_n(q_d r) \right)^2 + \left(\frac{nk}{q_d^2 r} K_n(q_d r) + \frac{\omega_n(k) f}{q_d} K_n'(q_d r) \right)^2 + K_n^2(q_d r) \right] \right\} dk, \tag{25}$$

where $\mathbf{p}_{01}$ is the matrix element of the electric dipole moment of the quantum transition of the molecule from the first excited state to the ground state, r is the distance between the molecule and the axis of the nanowire, $G(\omega)$ is the emission spectrum of the phosphor molecule. In formula (25), the averaging is performed along the directions of the dipole moment of the transition of the molecule. In the case when the nanowire is surrounded by a monolayer of organic molecules in the J-aggregate state, an energy exchange between the Frenkel excitons of the monolayer and the surface plasmons of the nanowire is possible. The matrix element $V_{10,01}$ of the operator $\hat{V} = -\sum_{\mathbf{n}} \hat{\mathbf{p}}_{01} \cdot \hat{\mathbf{E}}(\mathbf{n})$ of interaction of J-aggregate molecules with the electric field of a surface plasmon between the states $|1_{ex}, 0_{pl}\rangle$ of the system under consideration (with one exciton and without plasmons) and $|0_{ex}, 1_{pl}\rangle$ (with one plasmon and without excitons) takes the form

$$V_{10,01}^{(n)} = -\sqrt{\frac{4\pi\hbar r \omega_n(k)}{s S_n(k)}} \frac{I_n(q_m R)}{K_n(q_d R)} \times \left[\left(\frac{nk_z}{q_d^2 r} K_n(q_d r) + \frac{\omega_n(k) f}{q_d} K_n'(q_d r) \right)(\mathbf{p}_{01})_\phi + K_n(q_d r)(\mathbf{p}_{01})_z \right] \delta_{k_z, q_1} \delta_{n, q_2 r}, \tag{26}$$

where s is the area of the unit cell of the monolayer. As can be seen from the obtained formula, axisymmetric ($n = 0$) surface plasmons interact only with excitons propagating along the axis of the nanowire ($q_2 = 0$). In other cases, the exciton wave vector has a component along the circumference of the cylinder. $I_n(q_m R), K_n(q_d R)$ are Bessel functions of an imaginary argument.

In the case of strong plasmon-exciton coupling, the conditions for the applicability of the perturbation theory are not fulfilled, and it is necessary to use the density matrix formalism to describe the kinetics of energy exchange as in papers [10-11].

2. Magnetic field modulation of the rate of triplet-triplet annihilation of electronic excitations in nanostructures

The course of spin-selective reactions involving the annihilation of triplet (T) excitons or T-electron excitations localized on molecules is carried out in different ways, depending on how the migration of reagents occurs in a coherent T-T pair [18–20]. In nanostructured systems, the mobility of molecules involved in the reaction depends significantly on the structural features of such systems, and the mechanism of spatial movement of reagent particles reflects either the dynamics of conformational rearrangements of structural

subunits (in the case of "soft-systems") [18], or the shape of the potential field [19] formed by the system, or both together.

In nanostructures with bistable spatial states, depending on which spatial configuration the T-T pair is in (in a "dense" or "loose" state), we introduce the corresponding density operators $\rho_1(t)$ and $\rho_2(t)$. Thus, the subscript will indicate that the mobile T-molecule belongs to a potential well 1 or 2. The frequencies of jumps Γ_1 and Γ_2 between the pits will be assumed to be different and constant. Then we can write the following system of equations [19]:

$$\begin{cases} \dfrac{d}{dt}\rho_1(t) = -\dfrac{i}{\hbar}\big[H,\rho_1(t)\big] - \dfrac{1}{2}\big\{\rho_1\Lambda + \Lambda\rho_1\big\} - K_{-1}\rho_1(t) - \Gamma_1\rho_1(t) + \Gamma_2\rho_2(t) \\[2mm] \dfrac{d}{dt}\rho_2(t) = -\dfrac{i}{\hbar}\big[H_0,\rho_2(t)\big] - K_{-2}\rho_2(t) + \Gamma_1\rho_1(t) - \Gamma_2\rho_2(t) \end{cases}, \tag{27}$$

where the spin-Hamiltonian H_0 of a "loose" T-T-pair does not contain an exchange interaction. The annihilation operator Λ in (27) is determined through the projector on the singlet state of the T-T-pair: $\Lambda = K_S|00\rangle\langle 00|$ and a fixed rate $U(r_{ann}) = K_S$. For the density operator $\rho_1(t)$ we obtain ($U(t) = \exp(Kt)$, $K = -iH/\hbar - \Lambda/2$)

$$\rho_1(t) = \exp(-\alpha_1 t)U(t)\left[\rho_1(0) + \Gamma_2\left(\int_0^t \exp(-\alpha_1 t')U(-t')\rho_2(t')U^*(-t')dt'\right)\right]U^*(t). \tag{28}$$

We can write a similar equation for the density operator $\rho_2(t)$

$$\rho_2(t) = \exp(-\alpha_2 t)U_0(t)\left[\rho_2(0) + \Gamma_1\left(\int_0^t \exp(-\alpha_2 t')U_0^+(t')\rho_1(t')U_0(t')dt'\right)\right]U_0^+(t). \tag{29}$$

The unitary operators $U_0(t) = \exp(-iH_0 t/\hbar)$ and $U_0^+(t) = \exp(iH_0 t/\hbar)$ introduced in (29) are related to the Hamiltonian H_0 determining the evolution of the T-T pair in its "loose" configuration (coherent T excitations are spaced in different pits 1 and 2).

Substituting (29) into (28) we obtain an exact integral equation for the density operator $\rho_1(t)$ ($\Delta\alpha = \alpha_1 - \alpha_2$)

$$U(-t)\rho_1(t)U^*(-t) = \exp(-\alpha_1 t)\left[\rho_1(0) + \Gamma_2\left(\int_0^t \exp(\Delta\alpha t')U(-t')U_0(t')\rho_2(0)U_0^+(t')U^*(-t')dt'\right) + \right.$$

$$\left. + \Gamma_1\Gamma_2\left(\int_0^t \exp(\Delta\alpha t')U(-t')U_0(t')\left(\int_0^{t'} \exp(\alpha_2 t'')U_0^+(t'')\rho_1(t'')U_0(t'')dt''\right)U_0^+(t')U^*(-t')dt'\right)\right] \tag{30}$$

To construct approximations of solutions of the basic integral equation (30), an iterative procedure can be organized following one of two paths:

1) For the integral term, the first term $\rho_1^{(0)}(t)$ of the right part (30) can be used as the zero approximation operator

$$\rho_1^{(0)}(t) = \exp(-\alpha_1 t)U(t)\rho_1(0)U^*(t). \tag{31}$$

2) The sum of the first two terms of the right part (30) can be used as the zero approximation operator $\rho_1^{(0)}(t)$.

In another typical variant of the initial condition $\rho_2(0) = 0$, in the approximation of one-time returns to pit 1, we obtain a closed solution. The matrix element $\rho_{SS}(t) = \langle 00|\rho_1(t)|00\rangle$ determining the population dynamics of a paired singlet state can be calculated based on Sylvester's theorem for matrix exponentials.

It can be seen from the matrix $\langle J|K|J'\rangle$ structure that the mixing of spin states $|00\rangle$ and $|10\rangle$ is a consequence of the difference in the g-factors of excitations and, in addition, the relationship between spin states $|00\rangle$ and $|20\rangle$ appears as a result of intramolecular spin-spin interaction.

In [20] the effect of a magnetic field generated by a ferromagnetic nanoparticle on the annihilation of triplet-excited organic molecules or triplet excitons in a near-surface particle layer was studied. A detailed mathematical model has been presented that accounts for electron excitation diffusive mobility and geometry of the system.

We define the coordinate-spin density operator $\hat{\rho}\left(\mathbf{r}_1,\mathbf{r}_2,t\,|\,\mathbf{r}_1',\mathbf{r}_2',\mathbf{B}(\mathbf{r}_1),\mathbf{B}(\mathbf{r}_2)\right)$ determining the population growth rate of the state $\left|JM\right\rangle$ optimal for the reaction (here J, M are the total spin moment and its z-projection correspondingly). For the rate constant $K\left(\mathbf{r}_1',\mathbf{r}_2'\right)$ of the spin-selective triplet (T) states annihilation the following holds

$$K(\mathbf{r}_1',\mathbf{r}_2') = \int_0^\infty dt \iint_{\Delta V_R} U(|\,\mathbf{r}_1 - \mathbf{r}_2\,|)\frac{1}{2}\mathrm{Tr}\left\{P_S, \hat{\rho}(\mathbf{r}_1,\mathbf{r}_2,t\,|\,\mathbf{r}_1',\mathbf{r}_2',\mathbf{B}(\mathbf{r}_1),\mathbf{B}(\mathbf{r}_2))\right\}_+ d^3r_1 d^3r_2, \qquad (32)$$

where $\mathrm{Tr}\left\{P_S,\hat{\rho}\right\}_+ = \sum_{J,M}\left\langle JM\left|\left(P_S\hat{\rho} + \hat{\rho}P_S\right)\right|JM\right\rangle = \left\langle 00|\hat{\rho}|00\right\rangle$, because $P_S = \left|00\right\rangle\left\langle 00\right|$ is the operator performing a projection of the T-T pair singlet state; $\mathbf{r}_1',\mathbf{r}_2'$ are the initial positions of the mobile particles. ΔV_R is integration volume (volume of the layer between the ferromagnetic particle and the inner surface of the nanoreactor); $U(r)$ is the distance-dependent rate of an annihilation act. The kinetic operator is given in the complete 9x9 basis of triplet- triplet pair spin states. Time dependencies of the singlet spin state population of the triplet-triplet pair and the dependence of the triplet-triplet annihilation magnetic response profile (magnetic reaction effect) from the magnetic field induction were obtained. It was found that the influence of a magnetic field gradient on the reaction yield dominates over the other known mechanisms of spin-dynamics in triplet-triplet pairs.

Conclusions

A series of works by the authors [3–5, 10, 11 and 16-20] laid the foundations for a general quantum description of the features of exciton-plasmon and exciton-exciton interaction in hybrid organometallic nanosystems, as well as the kinetics of photo-transformations of quasiparticles, taking into account the mesoscopic specificity inherent in such nanosystems.

Acknowledgments

References

1   Zayats, A.V. & Richards, D. (2009). *Nanooptics and near-field optical microscopy*. Boston, Boston: Artech House.

2   Gonzalez-Tudela, A., Huidobro, P.A., Martın-Moreno, L., Tejedor, C. & Garcıa-Vidal, F.J. (2013). Theory of Strong Coupling between Quantum Emitters and Propagating Surface Plasmons. *Phys. Rev. Lett.*, *110*, 126801. https://doi.org/10.1103/PhysRevLett.110.126801

3   Chmereva, T.M., Kucherenko, M.G. & Kurmangaleev, K.S. (2016). The plasmon-exciton interaction in layered nanostructures with two-dimensional J-aggregates. *Optics and Spectroscopy*, *120*(6), 881–887. https://doi.org/10.1134/S0030400X16060060

4   Chmereva, T.M. & Kucherenko, M.G. (2015). Intermolecular radiationless electronic excitation energy transfer near a conductive film. *Russian Physics Journal*., *57*(10), 1428–1435. https://doi.org/10.1007/s11182-015-0399-7

5   Chmereva, T.M., Kucherenko, M.G. & Dmitriev, A.D. (2015). Quenching of excited electronic states of quantum dots by a metallic nanowire. *Optics and Spectroscopy*, *118*(2), 284–289. https://doi.org/10.1134/S0030400X15020058

6   Archambault, A., Marquier, F., Greffet, J.-J. & Arnold, C. (2010). Quantum theory of spontaneous and stimulated emission of surface plasmons. *Phys. Rev B*, *82*, 035411. https://doi.org/10.1103/PhysRevB.82.035411

7   Goliney, I.Yu., Sugakov, V.I., Valkunas, L. & Vertsimakha, G.V. (2012). Effect of metal nanoparticles on energy spectra and optical properties of peripheral light-harvesting LH2 complexes from photosynthetic bacteria. *Chem. Phys.*, *404*, 116–122. http://dx.doi.org/10.1016/j.chemphys.2012.03.011

8   Balci, S., Kocabas, C., Ates, S., Karademir, E., Salihoglu, O. & Aydinli, A. (2012). Tuning surface plasmon-exciton coupling via thickness dependent plasmon damping. *Phys. Rev B*, *86*, 235402. https://doi.org/10.1103/PhysRevB.86.235402

9   Bellessa, J., Symonds, C., Laverdant, J., Benoit, J. -M., Plenet, J.C. & Vignoli, S. (2014). Strong Coupling between Plasmons and Organic Semiconductors. *Electronics*, *3*, 303-313. https://doi.org/10.3390/electronics3020303

10 Kucherenko, M.G. & Chmereva, T.M. (Eds.). (2016). Proceedings from BPO 2016: *IX International Conference «Basic Problems of Optics-2016»*. St. Petersburg: ITMO University.

11 Kucherenko, M.G. & Chmereva, T.M. (2018). Energy exchange dynamics and relaxation of excitations upon strong exciton–plasmon interaction in a planar nanostructure of molecular J-aggregates on a metal substrate. *Optics and Spectroscopy, 125*(2), 173–183. https://doi.org/10.1134/S0030400X18080179

12 Johnson, R.C. & Merrifield, R.E. (1970). Effects of Magnetic Fields on the Mutual Annihilation of Triplet Excitons in Anthracene Crystals. *Phys. Rev. B., 1*(2), 896–902. https://doi.org/10.1103/PhysRevB.1.896

13 Coles, D.M., Somaschi, N., Michetti, P. et.al. (2014). Polariton-mediated energy transfer between organic dyes in a strongly coupled optical microcavity. *Nature Materials*, *13*, 712–719. https://doi.org/10.1038/nmat3950

14 Nakajima, H., Kometani, N., Asami, K. & Yonezawa, Y. (2001). Excitation energy transfer between J-aggregates in layer-by-layer alternate assemblies. *J. Photochem. Photobiol. A: Chemistry*, *143*, 161–167. https://doi.org/10.1016/S1010-6030(01)00491-9

15 Petrenko, V.Yu., Dmitriev, O.P., Slominskii, Yu.L. & Smirnova, A.L. (2015). Efficient energy transfer between J-aggregates of thiamonomethinecyanine dyes. *Chem. Phys. Lett.*, *621*, 22–28. https://doi.org/10.1016/j.cplett.2014.12.054

16 Chmereva, T.M. & Kucherenko, M.G. (2018). Radiationless Electronic Excitation Energy Transfer Between Monolayers of *J*-aggregates. *Russian Physics Journal, 61,* 304–311. https://doi.org/10.1007/s11182-018-1402-x

17 Kucherenko, M.G. & Chmereva, T.M. (2017). Energy Transfer in a Cylindrical Nanostructure Consisting of a Metal Wire and a Coaxial Covering with Luminophore Molecules. *Journal of Applied Spectroscopy*, *84*, 382–390. https://doi.org/10.1007/s10812-017-0480-9

18 Kucherenko, M.G. & Dusembaev, R.N. (2010).Positive magnetic field effect on mutual triplet triplet annihilation of mixed molecular pairs: Magnetosensitive geterofusion induced by difference of g-factors. *Chem. Phys. Lett., 487,* 58-61. https://doi.org/10.1016/j.cplett.2010.01.016

19 Kucherenko, M.G. & Pen'kov, S.A. (2014) External magnetic field effect on the rate of mutual annihilation of triplet electronic excitations in nanostructures with bistable spatial states. *Chemical Physics and Mesoscopy*, *16*(4), 574–587. https://www.elibrary.ru/contents.asp? id=34040736

20 Kucherenko, M.G. & Neyasov, P.P. (2022). Spin-selective interaction of triplet-excited molecules on the surface of a ferromagnetic nanoparticle. *Eurasian Physical Technical Journal, 19*(4), 5–16. https://doi.org/10.31489/2022No4/5-16

Information about authors*

Kucherenko, Michael Gennad'evich (*corresponding author*) — Doctor of Physical and Mathematical Sciences, Professor, Leading researcher, Professor, Orenburg State University, 460018, Orenburg, Russia; e-mail: clibph@yandex.ru; https://orcid.org/0000-0001-8821-2427

Chmereva, Tatiana Mihajlovna — Doctor of Physical and Mathematical Sciences, Associate Professor, Senior researcher, Professor, Orenburg State University, 460018, Orenburg, Russia; e-mail: chmereva@yandex.ru; https://orcid.org/0000-0003-3111-7853

_____

*The author's name is presented in the order: *Last Name, First and Middle Names*

Lenara I. Valiulina ⓘD, Victor N. Cherepanov ⓘD, Rashid R. Valiev* ⓘD

National Research Tomsk State University, Tomsk, Russia
(Corresponding author's e-mail: valievrashid@mail.ru)

Relationship between the Electric Polarizability and Aromaticity of Metallocene-Containing Macrocycles

Magnetically induced ring currents, aromaticity, as well as polarizability and second hyperpolarizability of the metallocenothiaporphyrins with transition metals of group VIII (Fe, Ru) and isoelectronic cations of group IX (Co^+, Rh^+) and metallocene-containing annulenes ((C_5H_5)$_2$M[$n = 18–24$], where M is Fe, Co^+) have been studied computationally at Density Functional level of Theory (DFT). The calculations show that the value of average polarizability of the studied compounds depends on their character of the aromaticity. Aromatic structures are characterized by larger polarizability than their corresponding antiaromatic congeners. The average polarizability of metallocenothiaporphyrins also depends on the magnitude of magnetically induced ring currents, which quantify the degree of electron delocalization. An increase in the number of π-electrons in conjugation pathway plays a key role in the growth of polarizability. Aromaticity also influences on the second hyperpolarizability of metallocene-containing annulenes. In the case of compounds with the same number of conjugated electrons, the second hyperpolarizability is larger for more aromatic systems. To conclude, our results pinpoint the importance of electron delocalization on the polarizability and second hyperpolarizability of the studied metallocene-containg macrocycles.

Keywords: magnetically induced ring currents, aromaticity, polarizability, hyperpolarizability, metallocenothiaporphyrins, optical properties, metallocenes, electron delocalization.

Introduction

The polarizability as well as the first and second hyperpolarizabilities are important optical quantities in the field of chemistry and physics. These characteristics describe the responses of a molecular system when it interacts with an external electric field. Polarizability plays an important role in determining intramolecular and intermolecular interactions, reactivity, and optical properties of materials [1–3]. The values of the first and second hyperpolarizabilities describe nonlinear processes occurring in compounds under the action of intense laser radiation. These processes include second and third harmonic generations, two-photon absorption, the Kerr effect, spontaneous and stimulated Raman scattering [4–7]. The search for molecules with a large nonlinear response is an urgent task, since they are used as molecular electronic, optical limiting devices, molecular switches, as well as sensitizers for photodynamic therapy [8–11].

The polarizability is strongly affected by the presence of conjugated bonds in the molecule [12]. When bond conjugation forms a closed circuit, the electron delocalization occurs, which causes the aromaticity. Aromaticity and electron delocalization determine the specific structural, magnetic, energetic and electronic properties of conjugated systems, which in turn affect the optical and nonlinear optical properties of molecules [13–15]. Thus, macrocyclic aromatic compounds with well-defined electron delocalization present the greatest interest in the study of optical and nonlinear optical properties. Among macrocyclic aromatic systems, metal porphyrin complexes have attracted considerable attention in the last decade due to their exceptional properties [16, 17]. Recent studies have shown that metallocene fragments with Fe and Ru incorporated in the porphyrin circuit are able to transfer π-conjugation [18, 19]. The transmission of π-electron conjugation across a *d*-electron metallocene contributes to three-dimensional metallomacrocyclic aromaticity [20]. The metallocene fragment in the porphyrin leads to a unique electronic structure, which can be reflected in special photophysical and electronic properties, aromaticity, conformational flexibility, as well as non-linear optical properties.

In this regard, the purpose of this work was a quantum-chemical study of the optical properties of metallocene-containing macrocyclic molecules, an assessment of the effect of conjugation and electron delocalization on optical and nonlinear optical properties. It is important to understand the role of the electronic

structure and electron delocalization in determining optical and nonlinear optical properties for the development of new promising materials.

Computational Details

The molecular structures of the studied metallocenothiaporphyrins are shown in Figure 1. We have investigated metallocenothiaporphyrins with transition metals of group VIII (Fe, Ru) and isoelectronic cations of group IX (Co$^+$, Rh$^+$). We denote the studied molecules as $(C_5H_5)_2MP$ for metallocenothiaporphyrins and H_2-$(C_5H_5)_2MP$ for dihydrometallocenothiaporphyrins (Fig. 1). In this notation, M is a metal atom or ion and P is a porphyrin ring.

$(C_5H_5)_2MP$ **H_2-$(C_5H_5)_2MP$**
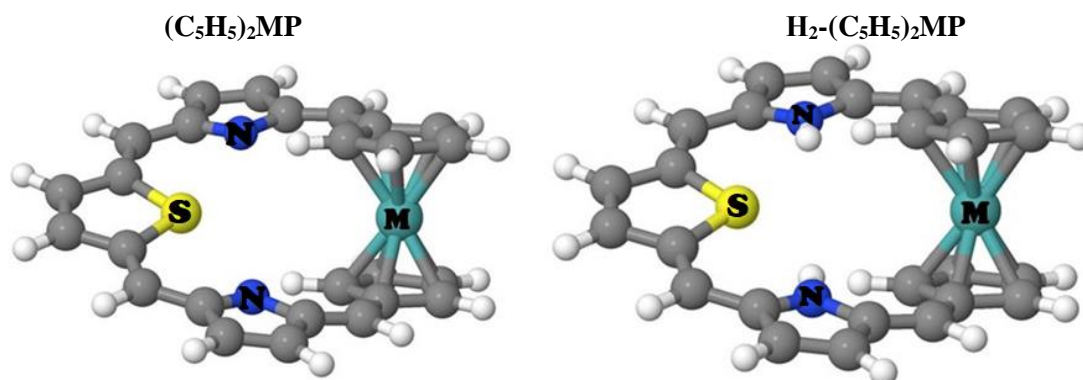
Figure 1. The molecular structures of metallocenothiaporphyrins, where M = Fe, Co$^+$, Ru, Rh$^+$

To unravel the effect of conjugation on the optical properties we have considered the hypothetical structures of annulenes with an incorporated metallocene fragment: $(C_5H_5)_2M[n = 18–24]$ (M = Fe, Co$^+$). The molecular structure of these compounds is shown in Figure 2.

$(C_5H_5)_2M[n = 18–24]$
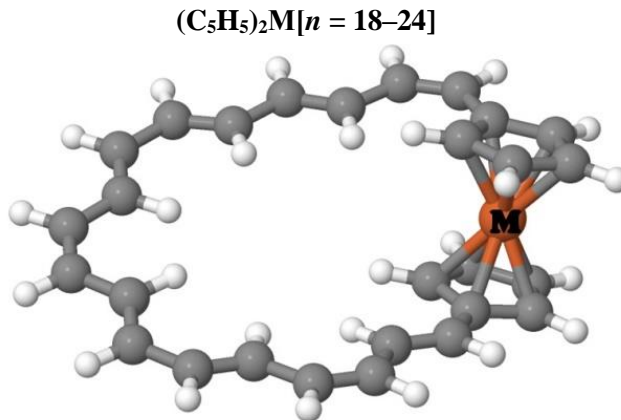
Figure 2. The molecular structure of metalloceno[*n*]anullenes (*n* = 18-24), where M = Fe, Co$^+$

The optimized structures of the studied molecules were obtained at the density functional theory (DFT) level using the Becke, Lee, Yang, Parr (B3LYP) [21, 22] functional and the Karlsruhe def2-TZVP basis set [23]. The vibrational frequency calculations indicate that all structures are minima on the potential energy surface. The nuclear magnetic shielding tensors, as well as the polarizabilities, and the second hyperpolarizabilities were calculated at the same level of theory. Time-dependent DFT (TD-DFT) calculations were carried out at the B3LYP/def2-TZVP level of theory to evaluate excitation energies and the corresponding oscillator strengths (f) of main low-energy electronic transitions. All calculations were carried out in the quantum-chemical software package GAUSSIAN 9 [24] on the SKIF Cyberia computing cluster.

Calculations of magnetically induced current densities were carried out using the GIMIC method [25], which uses the first-order magnetically perturbed density matrices, unperturbed density matrices and information on the basis set. To get detailed information about the GIMIC program and its capabilities we refer

the reader to [25, 26]. The ring-current strengths (nA/T) were obtained by numerically integrating the current density flux passing through the plane placed perpendicularly to the chemical bond.

The average polarizability $\bar{\alpha}$ was obtained by the trace of the polarizability tensor:

$$\bar{\alpha} = \frac{1}{3} tr(\alpha_{ii}) = \frac{1}{3} \sum_{i=x,y,z} \alpha_{ii} \qquad (1)$$

and its anisotropy $\Delta\alpha$, defined as:

$$\Delta\alpha^2 = \frac{1}{2}\left[(\alpha_{xx} - \alpha_{yy})^2 + (\alpha_{xx} - \alpha_{zz})^2 + (\alpha_{yy} - \alpha_{zz})^2 + +6\alpha_{xz}^2 + 6\alpha_{xy}^2 + 6\alpha_{yz}^2 \right]. \qquad (2)$$

The parallel component of average second hyperpolarizability $\gamma_{//}$ was defined as:

$$\gamma_{//}(-2\omega; \omega, \omega, 0) = \frac{1}{15} \sum_{i,j=x,y,z} (\gamma_{iijj} + \gamma_{ijij} + \gamma_{ijji}). \qquad (3)$$

Results and Discussion

Polarizability of metallocenothiaporphyrins

The ring-current strengths, aromaticity and the average polarizabilities of the studied metalloceno-thiaporphyrins are summarized in Table 1. The results of the ring-current strengths were taken from our previous works [20].

T a b l e   1

Magnetically induced ring-current strength I, aromaticity and the average polarizability $\bar{\alpha}$ and its anisotropy $\Delta\alpha$ computed at different frequencies (ω, eV) of the studied metallocenothiaporphyrins

Molecule	I, nA/T	$\Delta E_{HOMO-LUMO}$, eV	$\bar{\alpha}$, a.u./$\Delta\alpha$, a.u.			
			0, eV	0.544, eV	0.653, eV	1.034, eV
$(C_5H_5)_2FeP$	−10.4 (ant.)	1.97	419/292	424/299	427/302	444/325
H_2-$(C_5H_5)_2FeP$	13.8 (ar.)	2.19	447/331	454/339	456/343	473/366
$(C_5H_5)_2RuP$	−10.8 (ant.)	1.96	428/284	433/290	435/294	451/315
H_2-$(C_5H_5)_2RuP$	15.3 (ar.)	2.21	460/331	466/339	469/343	485/366
$(C_5H_5)_2Co^+P$	−21.3 (ant.)	1.66	410/285	417/294	420/298	-932/3939*
H_2-$(C_5H_5)_2Co^+P$	21.8 (ar.)	2.22	455/349	461/358	464/362	483/387
$(C_5H_5)_2Rh^+P$	−20.5 (ant.)	1.71	420/279	426/287	430/291	482/386
H_2-$(C_5H_5)_2Rh^+P$	23.2 (ar.)	2.24	466/348	473/357	476/361	493/384

* The negative value of polarizability indicates that the field frequency is higher than the frequency corresponding to the transition to the first excited state ($\Delta E(S_0 \rightarrow S_1)$ = 1.03 eV)

The result of the calculations showed that antiaromatic systems are characterized by a smaller energy gap between the frontier molecular orbitals $\Delta E_{HOMO-LUMO}$ compared to their aromatic counterparts. The value of energy gap determines the chemical stability of the compounds, so the low $\Delta E_{HOMO-LUMO}$ values for anti-aromatic molecules explain their high reactivity [27]. The energy gap also affects the optical properties. So, molecules must have a small energy gap to obtain high values of polarizability [28]. In simple perturbation theory when the two-level model is used polarizability can be obtained by [2]:

$$\alpha \approx \frac{\mu_t^2}{E_{HOMO-LUMO}}, \qquad (4)$$

where μ_t —the transition dipole moment from the ground state to the first dipole-allowed excited state. $\alpha \sim \frac{1}{\Delta E_{HOMO-LUMO}}$

However, the analysis of Table 1 shows that the average polarizability of aromatic systems, despite the large energy gap, is larger than for corresponding antiaromatic congeners both in the static and dynamic regimes (Fig. 3). The average polarizability increases in the following order: $(C_5H_5)_2Co^+P < (C_5H_5)_2FeP < (C_5H_5)_2Rh^+P < (C_5H_5)_2RuP$ for antiaromatic metallocenothiaporphyrins and H_2-$(C_5H_5)_2FeP < H_2$-$(C_5H_5)_2Co^+P < H_2$-$(C_5H_5)_2RuP < H_2$-$(C_5H_5)_2Rh^+P$ for aromatic metallocenothiaporphyrins. Compounds with $3d$ metals (Fe, Co$^+$) have lower average polarizability values, which is caused by the stronger binding of electrons to the nucleus.
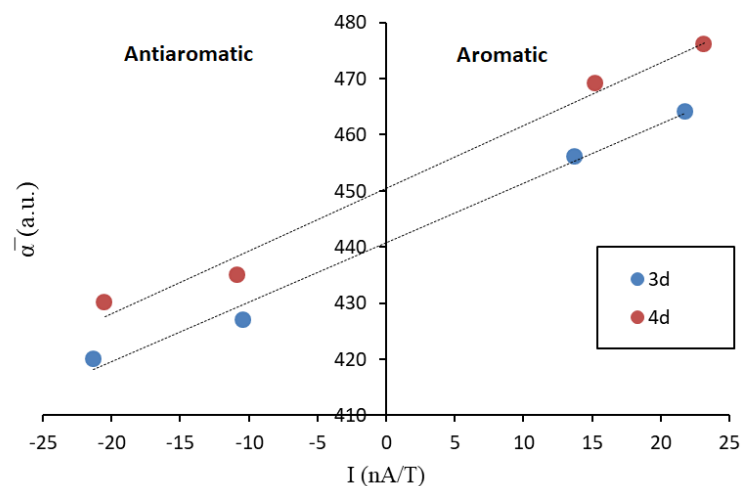
Figure 3. Average polarizability $\bar{\alpha}$ ($\omega = 0.653$ eV) as a function of ring-current strength
for the studied metallocenothiaporphyrins

Eq. (4) can be modified in terms of oscillator strength to [29]:

$$\alpha = \frac{\hbar^2 e^2}{m_e} \sum_{l \neq k} \frac{f_{kl}}{\Delta E_{kl}^2} , \qquad (5)$$

where the summation runs over all integrals including the continuum.

Eq. (5) implies that the large contributions to the polarizability come from low-lying high intensity electronic transitions. In general, aromatic compounds characterized by distinctive absorption, whereas antiaromatic species show smeared and attenuated absorption bands [30]. Moreover, the low-lying electronic transition ($S_0 \rightarrow S_1$) corresponding to HOMO→LUMO transition in antiaromatic porphyrinoids is optically forbidden while in aromatic molecules this transition forms Q-bands in the absorption spectra [31]. Table 2 presents the characteristic properties of the first and the main optically-allowed electronic transitions ($f > 0.01$) of the studied metallocenothiaporphyrins.

T a b l e 2

Vertical excitation energies of the first and the main electronic transitions of the studied metallocenothiaporphyrins

Antiaromatic			Aromatic			Antiaromatic			Aromatic		
$S_0 \rightarrow S_n$	E, eV	f	$S_0 \rightarrow S_n$	E, eV	f	$S_0 \rightarrow S_n$	E, eV	f	$S_0 \rightarrow S_n$	E, eV	f
$(C_5H_5)_2FeP$			H_2-$(C_5H_5)_2FeP$			$(C_5H_5)_2Co^+P$			H_2-$(C_5H_5)_2Co^+P$		
S_1	1.24	0.004	S_1	1.77	0.050	S_1	1.03	0.008	S_1	1.51	0.020
S_3	1.68	0.030	S_3	2.07	0.070	S_2	1.95	0.014	S_4	2.28	0.013
S_{10}	2.93	0.014	S_5	2.30	0.020	S_3	2.27	0.012	S_5	2.32	0.040
			S_7	2.64	0.014	S_4	2.32	0.020	S_6	2.59	0.110
			S_9	2.74	0.030	S_7	2.55	0.030	S_7	2.63	0.060
			S_{10}	2.91	0.028	S_{10}	2.68	0.040	S_9	2.86	0.270
									S_{10}	2.96	0.300
$(C_5H_5)_2RuP$			H_2-$(C_5H_5)_2RuP$			$(C_5H_5)_2Rh^+P$			H_2-$(C_5H_5)_2Rh^+P$		
S_1	1.39	0.016	S_1	1.92	0.110	S_1	1.11	0.010	S_1	1.78	0.043
S_3	2.07	0.020	S_5	2.89	0.200	S_2	2.24	0.030	S_4	2.78	0.200
S_4	2.12	0.010	S_6	3.05	0.250	S_8	2.83	0.100	S_5	2.93	0.500
S_5	2.60	0.050	S_7	3.07	0.300	S_9	3.05	0.010	S_6	2.97	0.400
S_6	2.88	0.020	S_8	3.29	0.060	S_{10}	3.08	0.350	S_7	3.40	0.400
S_7	2.92	0.050	S_9	3.31	0.500				S_8	3.52	0.030
S_{10}	3.03	0.200	S_{10}	3.39	0.020				S_9	3.61	0.020

As can be seen from the Table 2 the number of optically allowed transitions in the aromatic structures of metallocenothiaporphyrins in general is greater than in antiaromatic ones. Moreover, these transitions are

more intense. This explains why aromatic metallocenothiaporphyrins have larger polarizability than antiaromatic metallocenothiaporphyrins.

Figure 3 illustrates that, beside the aromaticity effect, the average polarizability in metallocenothiaporphyrins depends on the magnetically induced ring-currents strength I (nA/T), which determines the degree of electron delocalization.

It should be noted that we calculated the magnetic susceptibility for the $(C_5H_5)_2Co^+P$ molecule. The result shows that $(C_5H_5)_2Co^+P$ is diamagnetic ($\chi = -13.2$ a.u.). The diamagnetic character as well as the negative average polarizability at 1.034 eV ($\overline{\alpha} = -932$ a.u.), indicate that $(C_5H_5)_2Co^+P$ can potentially be used as a building block for advanced optical materials with a negative refractive index [32].

Polarizability and Second hyperpolarizability of metallocene-containing annulenes

The ring-current strengths, aromaticity and the average polarizabilities of the studied metallocene-containing annulenes are presented on Table 3.

T a b l e 3

Magnetically induced ring-current strength *I*, aromaticity and the average polarizability $\overline{\alpha}$ and its anisotropy $\Delta\alpha$ computed at different frequencies (ω, eV) of the studied metalloceno[*n*]anullenes (*n* = 18–24)

Molecule	*I*, *n*A/T	$\Delta E_{HOMO-LUMO}$, eV	$\overline{\alpha}$, a.u./$\Delta\alpha$, a.u.			
			0, eV	0.544, eV	0.653, eV	1.034, eV
$(C_5H_5)_2Fe[18]$	−5.5(ant.)	2.13	493/423	500/434	504/439	523/466
$(C_5H_5)_2Fe[20]$	5.3(ar.)	2.16	577/503	587/519	593/526	622/566
$(C_5H_5)_2Fe[22]$	−2.8 (non.)	1.97	635/586	649/605	656/614	696/669
$(C_5H_5)_2Fe[24]$	2.8 (non.)	1.98	757/730	781/763	793/780	879/898
$(C_5H_5)_2Co^+[18]$	−16.1(ant.)	1.62	511/463	520/477	524/484	524/517
$(C_5H_5)_2Co^+[20]$	17.6(ar.)	1.92	628/591	644/614	652/626	698/696
$(C_5H_5)_2Co^+[22]$	−18.4(ant.)	1.43	658/622	673/644	680/654	711/706
$(C_5H_5)_2Co^+[24]$	16.8(ar.)	1.72	798/801	827/846	842/869	943/1029

The ring current calculations reveals that metalloceno[*n*]anullenes (*n* = 18–24) with Fe, in contrast to Co+, have less effective conjugation and weakly pronounced electron delocalization, which is confirmed by weak ring-current strengths. This indicates that the charge in the system is involved in the electron delocalization, leading to its enhancement. Molecules $(C_5H_5)_2Fe[n = 22]$ and $(C_5H_5)_2Fe[n = 24]$ are non-aromatic ($|I|<3$ *n*A/T). The nonaromatic character of these systems is also confirmed by the energy gap $\Delta E_{HOMO-LUMO}$. For compounds with Fe, $\Delta E_{HOMO-LUMO}$ does not change significantly with a change in the number of π-electrons, while for compounds with Co+, the energy gap increases for aromatic systems and decreases for antiaromatic ones.
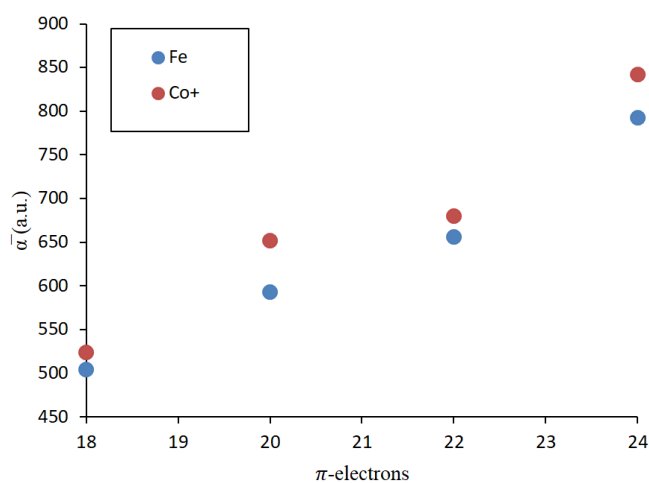

Figure 4. Average polarizability $\overline{\alpha}$ (ω = 0.653 eV) as a function of π- electrons
for the studied metalloceno[*n*]anullenes (*n* = 18–24)

The polarizability of the investigated metalloceno[n]anullenes ($n = 18$–24) increases with an increase in the number of π-electrons (Fig. 4). Structures with Co^+ have the larger average polarizabilities. The greater difference in values between metalloceno[18–24]anullenes with Co^+ and Fe is observed for the aromatic systems $(C_5H_5)_2Co^+[n = 20]$ and $(C_5H_5)_2Co^+[n = 24]$. Thus, for isoelectronic systems the aromatic properties lead to increase the polarizability values.

The results of the parallel component of average second hyperpolarizability calculations for the investigated metalloceno[n]anullenes ($n = 18$–24) are presented in Table 4.

T a b l e 4

Second Hyperpolarizabilities $\gamma_{//}$ at ω=0.653 eV of the studied metalloceno[18–24]anullenes

Molecule	I, nA/T	$\gamma_{//}$, 10^3 a.u.
$(C_5H_5)_2Fe[n = 18]$	−5.5(ant.)	1150
$(C_5H_5)_2Fe[n = 20]$	5.3(ar.)	1860
$(C_5H_5)_2Co^+[n = 18]$	−16.1(ant.)	1488
$(C_5H_5)_2Co^+[n = 20]$	17.6(ar.)	17053

Table 4 shows that the second hyperpolarizability $\gamma_{//}$ is greater for aromatic systems. Moreover, the character of the aromaticity, as well as its degree plays an important role, which is expressed through the strength of magnetically induced currents. Thus, the more aromatic structure $(C_5H_5)_2Co^+[n = 20]$ has the second hyperpolarizability in order of magnitude higher than the one for the less aromatic structure $(C_5H_5)_2Fe[n = 20]$.

Conclusions

Magnetically induced ring currents, polarizability and second hyperpolarizability for metallocene-containing macrocyclic molecules were studied by means of density functional theory (B3LYP/def2-TZVP) calculations. The calculations results showed that the aromatic character and the number of conjugated electrons in the structure are the key factors leading to an increase in the polarizability of the studied molecules. Moreover, the average polarizability of metallocenothiaporphyrins also depends on the magnetically induced ring-current strengths, which determines the degree of electron delocalization and aromaticity. It was also shown that the average polarizability grows linearly on going from antiaromatic to aromatic metallocenothiaporphyrins molecules. The obtained results demonstrate that the studied metallocene-containing macrocycles are promising molecules with special structure, aromatic and optical properties. Thus, they can be used as nonlinear optical materials.

Acknowledgments

References

1 Hunter, C.A. (2004). Quantifying Intermolecular Interactions: Guidelines for the Molecular Recognition Toolbox. *Angew. Chem. Int. Ed.*, *43*, 5310–5324. https://doi.org/10.1002/anie.200301739

2 Li, X.-D., Wang, H.-Y., Lv, R., Wu, W.-D., Luo, J.-Sh. & Tang, Y.-J. (2009). Correlations of the Stability, Static Dipole Polarizabilities, and Electronic Properties of Yttrium Clusters. *J. Phys. Chem. A*, *113*, 10335–10342. https://doi.org/10.1021/jp904420z

3 Kuznetsova, O.V., Egorochkin, A.N., Khamaletdinova, N.M. & Domratcheva-Lvova, L.G. (2015). Reactivity of Organometallic Compounds and Polarizability Effect. *Journal of Organometallic Chemistry, 779*, 73-80. https://doi.org/10.1016/j.jorganchem.2014.12.004

4 Torres-Torres, C. & García-Beltrán, G. (2022). Study on Second- and Third-Order Nonlinear Optical Properties in Nanostructured Systems: Nanocrystals and Complex Geometries. *Optical Nonlinearities in Nanostructured Systems. Springer Tracts in Modern Physics, 287*, 125–151. https://doi.org/10.1007/978-3-031-10824-2_6

5 Béjot, P., Cormier, E., Hertz, E., Lavorel, B., Kasparian, J., Wolf, J.P. & Faucher, O. (2013). High-field Quantum Calculation Reveals Time-Dependent Negative Kerr Contribution. *Phys. Rev. Lett., 110*, 043902. DOI: 10.1103/PhysRevLett.110.043902

6   Prince, R.C., Frontiera, R.R. & Potma, O. (2017). Stimulated Raman Scattering: From Bulk to Nano. *Chem. Rev., 117*, 5070−5094. https://doi.org/10.1021/acs.chemrev.6b00545

7   Pawlicki, M., Collins, H.A., Denning, R.G. & Anderson, H.L. (2009). Two-Photon Absorption and the Design of Two-Photon Dyes. *Angew. Chem. Int. Ed., 48,* 3244–3266. https://doi.org/10.1002/anie.200805257

8   Lacroix, P.G., Malfant, I. & Lepetit, C. (2016). Second-Order Nonlinear Optics in Coordination Chemistry: an Open Door Towards Multifunctional Materials and Molecular Switches. *Coord. Chem. Rev., 308*, 381−394. https://doi.org/10.1016/j.ccr.2015.05.015

9   Okuno, K., Shigeta, Y., Kishi, R. & Nakano, M. (2013). Photochromic Switching of Diradical Character: Design of Efficient Nonlinear Optical Switches. *J. Phys. Chem. Lett., 4*, 2418−2422. https://doi.org/10.1021/jz401228c

10   Jurow, M., Schuckman, A.E., Batteas, J.D. & Drain, C.M. (2010). Porphyrins as molecular electronic components of functional devices. *Coord. Chem. Rev., 254*, 2297–2310. doi: 10.1016/j.ccr.2010.05.014

11   Collins, H.A., Khurana, M., Moriyama, E.H., Mariampillai, A., Dahlstedt, E., Balaz, M., Kuimova, M.K., Drobizhev, M., Yang, V.X.D., Phillips, D., Rebane, A., Wilson, B.C. & Anderson, H.L. (2008). Blood-Vessel Closure Using Photosensitizers Engineered for Two-Photon Excitation. *Nat. Photonics, 2*, 420–424. doi:10.1038/nphoton.2008.100

12   Smith, S.M., Markevitch, A.N., Romanov, D.A., Li, X., Levis, R.J. & Schlegel, H.B. (2004). Static and Dynamic Polarizabilities of Conjugated Molecules and Their Cations. *J. Phys. Chem. A, 108*, 11063–11072. https://doi.org/10.1021/jp048864k

13   Woller, T., Geerlings, P., De Proft, F., Champagne, B. & Alonso, M. (2019). Fingerprint of Aromaticity and Molecular Topology on the Photophysical Properties of Octaphyrins. *J. Phys. Chem., 123*, 7318–7335. https://doi.org/10.1021/acs.jpcc.8b10908

14   Woller, T., Geerlings, P., De Proft, F., Champagne, B. & Alonso, M. (2018). Aromaticity as a Guiding Concept for Spectroscopic Features and Nonlinear Optical Properties of Porphyrinoids. *Molecules, 23*, 1333. DOI: 10.3390/molecules23061333

15   Lim, J.M., Yoon, Z.S., Shin, J.-Y., Kim, K.S., Yoon, M.-Ch. & Kim, D. (2008). The Photophysical Properties of Expanded Porphyrins: Relationships Between Aromaticity, Molecular Geometry and Non-linear Optical Properties. *Chem. Commun., 45*, 261–273. https://doi.org/10.1039/B810718A

16   Schulz, S., Wong, R.J., Vreman, H.J. & Stevenson, D.K. (2012). Metalloporphyrins — an Update. *Front Pharmacol, 3*, 36. DOI: 10.3389/fphar.2012.00068

17   Strianese, M., Pappalardo, D., Mazzeo, M., Lamberti, M. & Pellecchia, C. (2021). The Contribution of Metalloporphyrin Complexes in Molecular Sensing and in Sustainable Polymerization Processes: a New and Unique Perspective. *Dalton Trans., 50*, 7898–7916. https://doi.org/10.1039/D1DT00841B

18   Simkowa, I., Latos-Grażyn´ski, L. & Stępień, M. (2010). π Conjugation Transmitted across a d-Electron Metallocene in Ferrocenothiaporphyrin Macrocycles. *Angew Chem Int Ed Engl., 49*, 7665–7669. https://doi.org/10.1002/anie.201004015

19   Simkowa, I., Latos-Grażyn´ski, L. & Stępień, M. (2013). Ruthenocenoporphyrinoids: Conformation Determines Macrocyclic π-Conjugation Transmitted Across a d-Electron Metallocene. *Angew Chem Int Ed Engl., 52*, 1044–1048. https://doi.org/10.1002/anie.201208289

20   Valiev, R.R., Kurten, T., Valiulina, L.I., Ketkov, S.Yu., Cherepanov, V.N., Dimitrova, M. & Sundholm, D. (2022). Magnetically Induced Ring Currents in Metallocenothiaporphyrins. *Phys. Chem. Chem. Phys., 24*, 1666–1674. https://doi.org/10.1039/D1CP04779E

21   Becke, A.D. (1988). Density-Functional Exchange-Energy Approximation with Correct Asymptotic Behavior. *Physical Review A., 38*, 3098–3100. https://doi.org/10.1103/PhysRevA.38.3098

22   Lee, C., Yang, W. & Parr, R.G. (1988). Development of the Colle-Salvetti Correlation-Energy Formula into a Functional of the Electron Density. *Phys. Rev. B: Condens. Matter Mater. Phys., 37*, 785–789. https://doi.org/10.1103/PhysRevB.37.785

23   Weigend, F. & Ahlrichs, R. (2005). Balanced Basis Sets of Split Valence, Triple Zeta Valence and Quadruple Zeta Valence Quality for H to Rn: Design and Assessment of Accuracy. *Phys. Chem. Chem. Phys., 7*, 3297–3305. https://doi.org/10.1039/B508541A

24   Gaussian 09, Revision A.02, Frisch, M.J., Trucks, G.W., Schlegel, H.B., Scuseria, G.E., Robb, M.A., Cheeseman, J.R. et al. (2016). Gaussian, Inc., Wallingford CT.

25   Fliegl, H., Taubert, S., Lehtonen, O. & Sundholm, D. (2011). The Gauge Including Magnetically Induced Current Method. *Phys. Chem. Chem. Phys., 13*, 20500–20518. https://doi.org/10.1039/C1CP21812C

26   Sundholm, D., Fliegl, H. & Berger, R. (2016). Calculations of Magnetically Induced Current Densities: Theory and Applications. *Wiley Interdiscip. Rev.: Comput. Mol. Sci., 6*, 639–678. https://doi.org/10.1002/wcms.1270

27   Gershoni-Poranne, R., Rahalkar, A.P. & Stanger, A. (2018). The Predictive Power of Aromaticity: Quantitative Correlation Between Aromaticity and Ionization Potentials and HOMO–LUMO Gaps in Oligomers of Benzene, Pyrrole, Furan, and Thiophene. *Phys. Chem. Chem. Phys., 20*, 14808–14817. https://doi.org/10.1039/C8CP02162G

28   Ashraf Janjua, M.R.S., Mahmood, A., Nazar, M.F., Yang, Z. & Pan, Sh. (2014). Electronic Absorption Spectra and Nonlinear Optical Properties of Ruthenium Acetylide Complexes: A DFT Study Toward the Designing of New High NLO Response Compounds. *Acta Chim Slov, 61*, 382–390.

29   Lim, I.S. (2004). Static Electric Dipole Polarizabilities of Atoms and Molecules (Doctoral dissertation). Retrieved from Massey University. (2010-09-27T00:15:35Z) http://hdl.handle.net/10179/1694

30   Cho, S., Yoon, Z.S., Kim, K.S., Yoon, M.-Ch., Cho, D.-G., Sessler, J.L. & Kim, D. (2010). Defining Spectroscopic Features of Heteroannulenic Antiaromatic Porphyrinoids, *J. Phys. Chem. Lett., 1*, 895–900. https://doi.org/10.1021/jz100039n

31 Valiev R.R., Fliegl, H. & Sundholm, D. (2017). Optical and Magnetic Properties of Antiaromatic Porphyrinoids. *Phys. Chem. Chem. Phys., 19*, 25979–25988. https://doi.org/10.1039/C7CP05460B

32 Padilla, W.J., Basov, D.N. & Smith, D.R. (2006). Negative refractive index metamaterials, *Materials Today, 9*, 28–35. https://doi.org/10.1016/S1369-7021(06)71573-5

Information about authors*

Valiulina, Lenara Ilmirovna — 1st year PhD student, Department of Optics and Spectroscopy, National Research Tomsk State University, Lenin Avenue, 36, 634050, Tomsk, Russia; e-mail: valiulina-lenara@mail.ru; https://orcid.org/0000-0002-3364-0448

Cherepanov, Victor Nikolaevich — Doctor of Physics and Mathematics, Head of Department of Optics and Spectroscopy National Research Tomsk State University, Lenin Avenue, 36, 634050, Tomsk, Russia; e-mail: vnch1626@mail.ru; https://orcid.org/0000-0002-5952-5202

Valiev, Rashid Rinatovich (*corresponding author*) — Doctor of Chemical Sciences, Assistant professor, National Research Tomsk State University, Lenin Avenue, 36, 634050, Tomsk, Russia; e-mail: valiev-rashid@mail.ru; http://orcid.org/0000-0002-2088-2608

_____

*The author's name is presented in the order: *Last Name, First and Middle Names*

Niyazbek Kh. Ibrayev[*] ⓘ, Evgeniya V. Seliverstova ⓘ

Institute of Molecular Nanophotonics, Karaganda University of the name of academician E.A. Buketov, Karaganda, Kazakhstan
(*Corresponding author's e-mail: niazibrayev@mail.ru)

Interaction of the Excited Electronic States
of Carbon Quantum Dots and Molecular Oxygen

The S,N-doped carbon quantum dots based on citric acid and L-cysteine were synthesized. The sizes of the synthesized carbon dots vary from 4 to 10 nm. The absorption spectrum exhibits a band with a maximum at 360 nm, as well as a shoulder at about 240–250 nm. The fluorescence band of the studied carbon dots is located in the region of 370–600 nm with a maximum at ~430 nm. The properties of the long-lived luminescence of carbon quantum dots solutions were studied. It was established that the decay of triplet states occurs as a result of a radiative phosphorescent transition and triplet–triplet annihilation. The synthesized carbon quantum dots are reviled to be the singlet oxygen sensitizers, as evidenced by the observed luminescence of molecular oxygen upon excitation of solutions in the absorption band of the carbon quantum dots. It was shown that when $O_2(^3\Sigma_g^-)$ was added to the solution, the process of singlet–triplet annihilation develops, the efficiency of which depends on the concentrations ratio of triplet carbon quantum dots and singlet $O_2(^1\Delta_g)$ molecules. In the presence of plasmonic Ag nanoparticles, the phosphorescence of singlet oxygen is enhanced.

Keywords: carbon quantum dots, singlet oxygen, excited states, delayed fluorescence, phosphorescence, Ag nanoparticles, plasmons.

Introduction

Molecular oxygen (O_2) is an oxidizing agent that is involved in metabolic pathways that are fundamental to aerobic life. However, the oxidizing power of O_2 at room temperature is low due to the strong oxygen-oxygen chemical bond, as well as its triplet nature of the ground state. These difficulties can be overcome by transferring oxygen to the singlet state $O_2(^1\Delta_g)$ [1]. Oxygen activation is a very interesting task for biology, chemistry and industry. A great contribution to the development of electronic mechanisms for the activation of molecular oxygen was made by Minaev B.F. *et al.* [2–5].

To overcome the spin forbidding rule for the transition of O_2 to $O_2(^1\Delta_g)$, photosensitizers with a high yield to the triplet state are required. Photosensitization-generated reactive oxygen species $O_2(^1\Delta_g)$ can be used for various photodynamic applications, such as photodynamic therapy (PDT) [6–8], light deactivation of proteins [9], oxidative processes in biological objects [10, 11] and photodegradation of organic pollution [12].

Therefore, the photophysical properties of photosensitizers (spin-catalysts) have a great importance for the photosensitized activation of oxygen, especially the population of triplet states by intersystem crossing.

Carbon quantum dots (CQDs) are a promising type of photosensitizer. The CQDs refers to quasi-spherical or spherical particles with a diameter of less than 10 nm. They could be represented as a core/shell structure consisting of a carbon core with graphite fragments and a shell of various surface functional groups [13]. CQDs have attracted attention due to their unique properties and some advantages over organic molecules and traditional semiconductor quantum dots [14]. CQDs particles have chemical resistance and photo-stability, high luminescence efficiency, good biocompatibility, and low toxicity. This causes their wide application in such areas as bioimaging [15], protective coatings [16], LEDs, solar cells [17], lasers [18] and sensors [19].

CQDs along with fluorescence exhibit an additional afterglow that is also an undoubted advantage. Moreover, the efficiency and position of the bands of both types of CQDs luminescence on the wavelength scale can be controlled by the directed synthesis [13, 16]. In this regard, CQDs particles are an attractive agent for PDT in deep tissues with controlled optical properties through chemical functionalization [16–19]. CQDs were shown as effective PDT agents in antibiotic therapy and wound healing, despite of low optical absorption and emission in the IR and near IR ranges [20, 21].

In view of extensive research of the CQDs exhibiting photodynamic effects inducing cytotoxicity in cancer cells and tumors, the fundamental understanding of parameters that allow CQDs to be useful PDT agents remains unclear. In [22], the role of oxygen-containing chemical groups in the catalytic generation of OH radicals, one of the common types of reactive oxygen species, was illustrated. However, the detailed mechanism of the photodynamic activity of CQDs has rarely been reported [23, 24].

The plasmonic effect is currently actively used to increase the efficiency of photo-processes both in organic molecules [25–28] and in semiconductor quantum dots [29], since the rates of photo-physical reactions could be changed near the plasmonic nanoparticles (NPs) surface [25, 30–31].

For CQDs, the plasmonic effect was used to enhance fast fluorescence [32–36]. The authors of [36] demonstrated that, by chemically binding CQDs to gold NPs, it is possible to achieve a fivefold enhancement of the orange emission of carbon dots. The observed intensity grow is due to the ultrafast resonant energy transfer from the gold NP to the carbon dot. Composites based on CQDs and plasmonic metal NPs were used to detect mercury ions [37], chlorophyll [38], bioimaging [39], anticancer drug [40], etc.

This paper presents the results of our study of the singlet oxygen photosensitization by CQDs, as well as the plasmon effect of NPs on these processes. The both electronic mechanisms of intermolecular interactions between the triplet CQDs and also — CQDs species with molecular oxygen are considered.

Experimental

For the CQDs synthesis the citric acid (CA, Sigma Aldrich) was used as a carbon source, and L-cysteine (Sigma Aldrich) was chosen as a source of N- and S-containing groups. All reagents were of analytical grade and used without further purification. The microwave reactor Monowave 200 (Anton Paar) was used for the preparation of CQDs. To do this, CA and L-cysteine were diluted with deionized water (5 mL) in a borosilicate glass tube and sonicated for 30 minutes. Next, the tube was placed in a microwave reactor and heated at 200 °C for an hour with vigorous stirring. The molar ratio of citric acid:L-cysteine was 1:2. After that solutions with different concentrations of ethanol were prepared. Its volume fraction was 25, 50, or 75 %. In the CQDs+Ag NPs solutions the concentration of CQDs was constant, and the concentration of plasmonic NPs was 10^{-14}, 10^{-13} or 10^{-12} mol/L.

Silver NPs were obtained in solution by ablation of a silver target by high-intensity laser radiation from a Nd:YAG laser with a generation wavelength (λ_{gen}) of 532 nm, a pulse duration $\tau_{pulse}=8$ ns, and a pulse energy E~90 mJ. The laser beam was focused by a converging lens onto a target immersed in ethanol. The diameter of the laser spot on the target was 0.01 cm^2. The height of the solvent above the target was 0.8 cm. The diameter of the resulting NPs was 46±12 nm (Zetasizer S90, Malvern). SEM images (Mira 3LMU, Tescan) showed that the NPs have a spherical shape (Fig. 1).
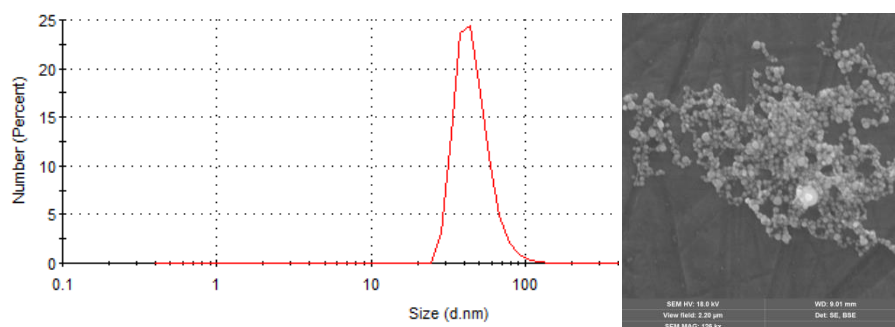
Figure 1. Size distribution and SEM image of Ag NPs

Absorption spectra were obtained using a Cary 300 spectrophotometer (Agilent Techn.). Fast and long-lived luminescence spectra were recorded using a Cary Eclipse spectrometer (Agilent Techn.).

Fluorescence decay kinetics was measured on a spectrofluorometer with picosecond resolution and registration in the time-correlated single photon counting mode from Becker&Hickl. The excitation of the samples was carried out using a diode laser with $\lambda_{gen}=375$ nm, $\tau_{pulse}=120$ ps. Fluorescence lifetimes were estimated with SPCImage software (Becker&Hickl).

Long-lived luminescence was recorded with an FLS1000 luminescence spectrometer (Edinburgh Instr.) equipped with highly sensitive UV-Vis (R13456, Hamamatsu) and IR (H10330C-75, Hamamatsu) photodetectors. Photoexcitation of samples at $\lambda_{exc}=360.8$ nm was carried out using a laser system based on Nd:YAG

laser LQ529, parametric light generator LP604 and second harmonic generator LG305. For the long-lived luminescence registration the cuvette with the CQDs solution was evacuated to a pressure of P = 10^{-5} mm Hg.

Results and Discussion

The absorption spectra of the studied CQDs are shown in Figure 2. The spectrum exhibits a weak band with a maximum at 360 nm, as well as a strong shoulder at about 240–250 nm. The long-wavelength absorption band is associated with $\pi \rightarrow \pi^*$ transitions in aromatic compounds of the CQD, while the absorption at 200 nm and the shoulder at 250 nm are associated with $n \rightarrow \sigma^*$ and $n \rightarrow \pi^*$ transitions, respectively. As shown in [41], the intensity and position of the maximum of the CQD fluorescence band depend on the excitation wavelength (λ_{exc}). The most intense emission was registered for λ_{exc}=350 nm. Under these conditions, the fluorescence band is located in the region of 370–600 nm with a maximum at ~430 nm.
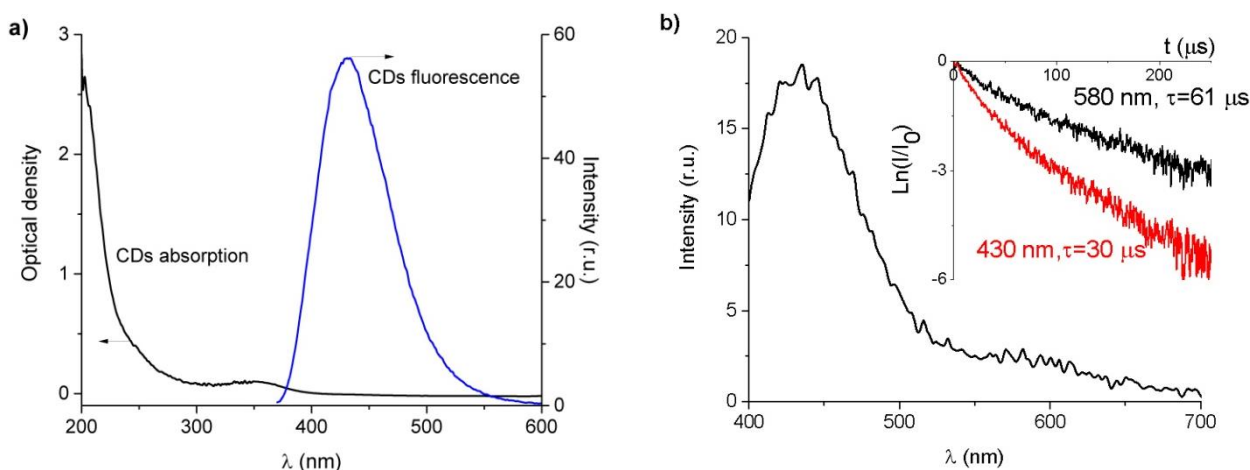
Figure 2. (*a*) Absorption (black curve) and fluorescence (blue curve, λ_{exc}=350 nm) spectra of CQDs and (*b*) long-lived luminescence of CQD in a solution with 25 % of ethanol. The inset shows decay kinetics of long-lived luminescence detected at 430 nm and 580 nm. E_{exc}= 5.5 mJ

A broad band with two maxima at 430 and 580 nm was recorded in the long-lived luminescence spectrum (Fig. 2b). Since the short-wavelength band coincides in position and shape with the fast fluorescence spectrum, it can be concluded that it belongs to the delayed fluorescence (DF) of CQDs. The long wavelength band can be interpreted as phosphorescence. This is confirmed by the times estimated from the decay kinetics of the long-lived luminescence recorded at 430 and 580 nm. The duration of phosphorescence is almost 2 times longer than that for DF. Therefore, the DF can be of the triplet-triplet (T-T) annihilation nature. According to [42, 43], the presence of oxygen groups induces a decrease in ΔE_{ST} and an increase in the spin-orbit interaction in the CQD, which contributes to the population of triplet states.

It is known that the annihilation-type DF is a magnetically sensitive process [44], and its intensity depends quadratically on the intensity of the exciting light. To study the influence of the magnetic field on the DF of the CQDs species, we used the N35 neodymium magnet with a magnetic induction of ~1 T. The magnitude of the magnetic effect $g(B)$ was estimated from the relative change in the luminescence intensity in the presence and in the absence of a magnetic field using the following formula:

$$g(B) = \frac{I(B) - I(0)}{I(B)} \times 100 \% , \qquad (1)$$

where I_B and I_0 are the luminescence intensities in the field and without the field, respectively.

As shown by the results (Table 1), in the presence of a magnetic field, the DF intensity decreases by ~33 %. The magnitude of the magnetic-field effect $g(B)$ decreases with increasing time of registration, which is apparently associated with a decrease in the number of triplet-excited particles. The intensity of the long-lived luminescence at λ_{reg}=580 nm is not significantly affected by the magnetic field.

Values of magnetic effect *g(B)* on DF of the CQDs at various times of registration

№	Time of registration, μs	$g(B)$, % λ_{reg}= 430 nm
1	0	-33.2±3
2	5	-31.2±3
3	15	-28.6±3

The data presented in Figure 3 were obtained upon excitation of the CQDs solutions by laser pulses of various intensities. At a wavelength of 580 nm, the luminescence intensity linearly depends on the excitation energy, which is typical for phosphorescence. At λ_{reg}= 430 nm, the dependence $I_{DF} \sim I_{exc}^2$ indicates that the DF signal is a result of the T-T annhilation of the triplet carbon dots.
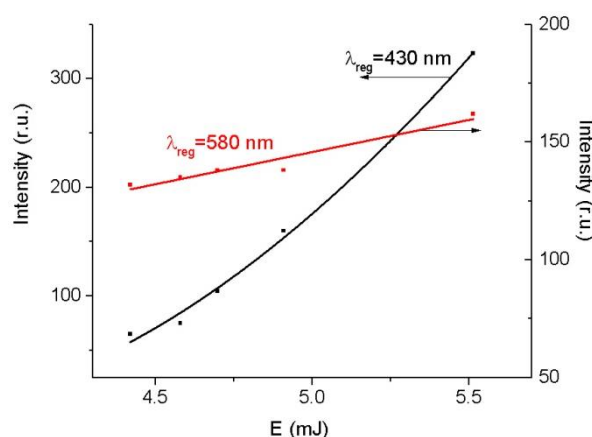
Figure 3. Dependence of the DF and phosphorescence intensity of CQDs
on the energy (intensity) of the exciting light

Thus, the data obtained indicate that the photoexcitation of the CQDs solutions leads to formation of the excited CQDs triplet states (T_{CD}), as a result of singlet-triplet interconversion. These T_{CD} decay occurs as a result of the following processes:

$$T_{CD} \rightarrow S_0 + Phos., \tag{2}$$
$$T_{CD} + T_{CD} \rightarrow (T_{CD} \ldots T_{CD}) \rightarrow S_1 + S_0 \rightarrow 2S_0 + ADF, \tag{3}$$
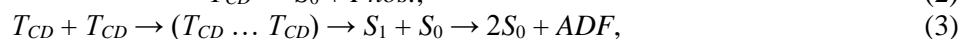
where S_0, S_1, T_{CD} are the singlet and triplet electronic states of CQDs.

Reaction (2) is phosphorescence and expression (3) represents the reactions of triplet-triplet annihilation generating the delayed fluorescence (ADF).

CQDs are good sensitizers of singlet oxygen [22–24]. The efficiency of sensitization will be determined not only by the concentration of triplet CQDs, but also by the solvent [2, 3, 45–48]. Figure 4*a* shows the decay kinetics of the phosphorescence of singlet oxygen $O_2(^1\Delta_g)$ in water–ethanol solutions with different ethanol contents, measured at atmospheric pressure. With an increase in the proportion of ethanol, the intensity and lifetime of $O_2(^1\Delta_g)$ phosphorescence increase, since the oxygen concentration and the $O_2(^1\Delta_g)$ lifetime in ethanol are higher than in water [3, 45–48].

The results of experiments on the oxygen concentration effect on photo-processes in a water–ethanol solutions of CQDs are presented in Figure 4*b*. Before the start of measurements, the cuvette with the solution was evacuated to a pressure of $P = 10^{-5}$ mm Hg. In this case, there was no signal of oxygen phosphorescence at a wavelength of 1270 nm. With an increase in the concentration of $O_2(^3\Sigma_g^-)$ in the cell, the intensity of phosphorescence of $O_2(^1\Delta_g)$ increases (red curve). The lifetime within the measurement error remains constant and equal to $\tau_\Delta = 9.2$ μs. The DF signal of CQDs (black curve) was grew up with the addition of oxygen and reaches a maximum at $C(O_2) = 0.05$ mL and then quenches. The DF lifetime of CQDs decreases with increasing $O_2(^3\Sigma_g^-)$ concentration (blue curve). The CQD's phosphorescence was quenched when initial oxygen concentrations were added to the solution, and we could not follow its dynamics, since water strongly scattered the exciting light.
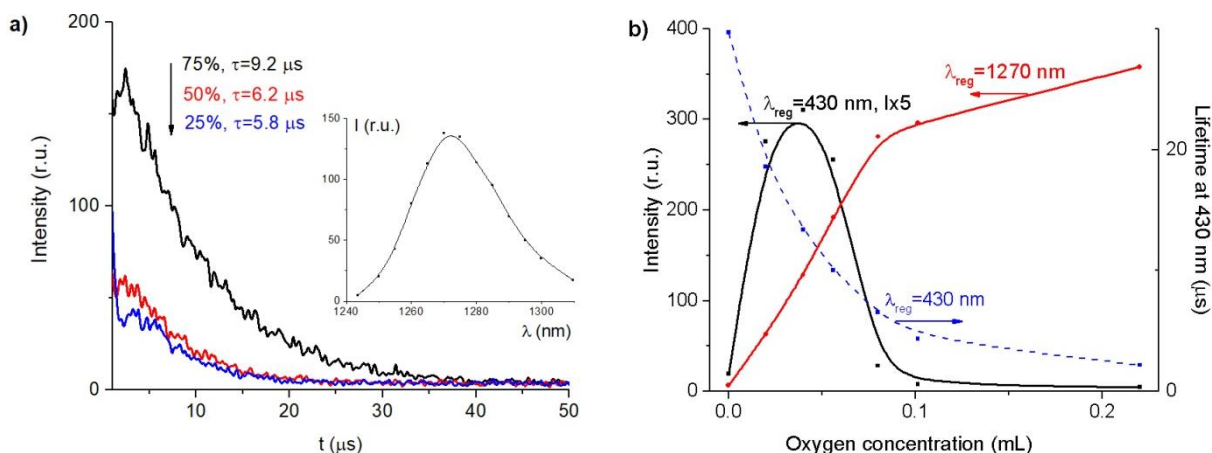
Figure 4. (*a*) Decay kinetics of $^1O_2$ phosphorescence ($\lambda_{reg} = 1270$ nm) sensitized by CQDs in solutions with different concentrations of ethanol at atmospheric pressure. The inset — the phosphorescence spectrum of $^1O_2$ ($\lambda_{exc} = 350$ nm) in a CQDs solution with 75 % ethanol. (*b*) Dependence of the intensity and lifetime of DF of CQDs (75 % ethanol) and $^1O_2$ phosphorescence ($\lambda_{exc} = 350$ nm) on the concentration of the oxygen

According to [1–3], the following processes can occur in collision complexes of molecular oxygen and CQD:

$$T_{CD} + (^3\Sigma_g^-) \rightarrow (T_{CD}\ ^3\Sigma_g^-)^{1,3,5} \rightarrow S_0 + {}^1\Delta_g \qquad (4)$$

$$T_{CD} + {}^1\Delta_g \rightarrow (T_{CD}\ ^1\Delta_g)^3 \rightarrow S_1 + {}^3\Sigma_g^- \rightarrow S_0 + {}^3\Sigma_g^- + h\upsilon_{DF} \qquad (5)$$

$${}^1\Delta_g \rightarrow {}^3\Sigma_g^- + h\upsilon_{Phos}, \qquad (6)$$
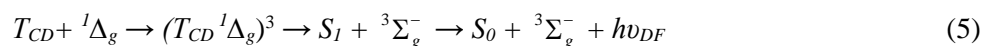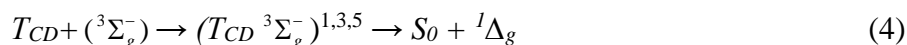
where formula 4 — the reaction of singlet oxygen sensitization; formula 5 — the singlet–triplet annihilation reaction; formula 6 — the generation of singlet oxygen phosphorescence.

In accordance with reactions (4–6), the dependence of I_{DF} on the $O_2(^3\Sigma_g^-)$ concentration (Fig. 4*b*, black curve) is due to reaction 5. At low oxygen concentrations, the number of triplet CQDs is still sufficient to form pairs $(T_{CD}\ ^3\Sigma_g^-)^{1,3,5}$ which, decaying with the formation of S_1 states of CQDs, additionally generate DF. Under conditions of strong quenching of CQD triplets, the efficiency of the processes of both singlet–triplet (5) and intrinsic (3) annihilation decreases, which leads to a decrease in the CQD luminescence intensity.

In the presence of plasmonic NPs, the sensitization of singlet oxygen by organic dyes is enhanced [49, 50]. The next we consider the effect of Ag NPs on the activation of $O_2(^3\Sigma_g^-)$ molecules. The maximum absorption spectrum of silver NPs exhibits at 420 nm. At 250–270 nm, the absorption band of *d*-electrons of Ag appears. In the presence of plasmonic NPs, no change in the shape of the CQD absorption spectrum was observed. In this case, the optical density also practically did not change, both in the long-wavelength and short-wavelength absorption bands of the CQD.

At atmospheric pressure, the highest quenching of CQD's fluorescence was observed at $C_{Ag} = 10^{-12}$ mol/L. The decrease in intensity was about 11 % (Table 2). The fluorescence lifetime also decreases by 8–10 % on average. The observed decrease in the intensity and lifetime of CQD fluorescence in the presence of Ag NPs is associated both with the effect of plasmonic NPs on the radiative decay rate of CQDs and with nonradiative energy transfer (FRET) from CQDs to metal NPs [25, 30].

The measurements showed that, in the presence of plasmonic NPs, the intensity of the CQDs DF decreases almost twice. Its duration was also reduced (Table 2).

Registration of the oxygen phosphorescence kinetics showed that in the presence of plasmonic NPs, its intensity in solutions of carbon particles increases by almost 2 times (Fig. 5). The greatest enhancement was recorded at a silver concentration of 10^{-13} mol/L. The lifetime did not change and amounted to 9.3±0.2 μs.

T a b l e 2

Ag NPs effect on optical density, intensity and lifetime of fluorescence and DF of CQDs (75 % of ethanol) and phosphorescence of O$_2$($^1\Delta_g$) at atmospheric pressure

C_{Ag}, mol/L	D	I_{fl}, r.u.	$\tau_{fl}\pm0.1$, ns	I_{DF}, r.u. 430 nm	$\tau_{DF}\pm0.2$, µs 430 nm	I, r.u. 1270 nm	$\tau\pm0.2$, µs 1270 nm
0	0.17	52.90	8.70	480.00	29.7	111.5	9.35
10^{-15}	0.17	50.86	8.14	380.50	24.5	163.3	9.34
10^{-14}	0.17	50.10	8.10	360.50	24.4	168.0	9.26
10^{-13}	0.17	49.90	7.85	324.00	24.2	202.0	9.35
10^{-12}	0.17	47.10	8.00	354.50	25.8	176.0	9.44
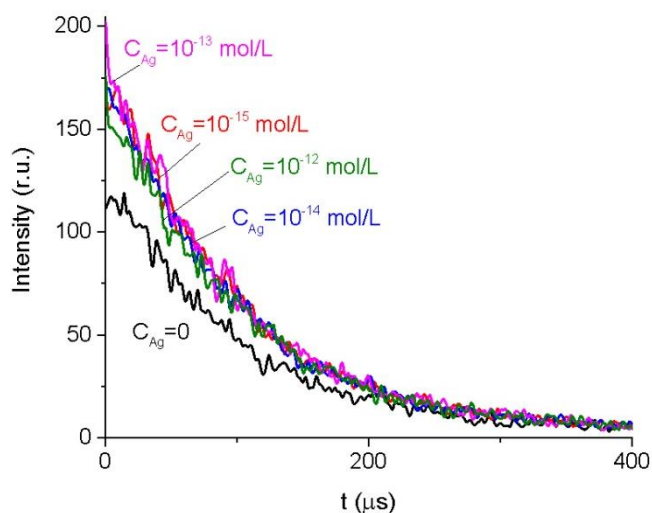
Figure 5. Decay kinetics of sensitized phosphorescence of O$_2$($^1\Delta_g$) (λ_{reg}=1270 nm) at different concentrations of Ag NPs in solution

Possible reasons for the enhancement of oxygen phosphorescence may be the following. The plasmonic effect can increase the population of the CQDs triplet state, which will lead to an increase in the concentration of singlet oxygen. The effect of Ag NPs on the exchange of energy between CQDs species and O$_2$($^3\Sigma_g^-$) triplet molecules is also possible [49]. In addition, the plasmon effect can directly enhance the rate of radiative decay of singlet oxygen. Our further work will be devoted to a detailed establishment of the mechanisms of the influence of the plasmon effect of metal NPs on the photo-physics of molecular oxygen and CQDs.

Conclusions

The properties of the long-lived luminescence of CQDs solutions were studied. It was established that the decay of the CQDs triplet states occurs as a result of a radiative phosphorescent transition and triplet–triplet annihilation. The synthesized CQDs species are the singlet oxygen sensitizers, as evidenced by the observed luminescence of molecular oxygen upon excitation of solutions in the CQDs absorption band. It was shown that the addition of aerated O$_2$($^3\Sigma_g^-$) to the solution leads to the development of the process of singlet–triplet annihilation, the efficiency of which depends on the concentrations ratio of triplet CQDs and the singlet O$_2$($^1\Delta_g$) molecules. In the presence of plasmonic Ag NPs, the phosphorescence of singlet oxygen is enhanced.

Acknowledgments

References

1 Pibiri, I., Buscemi, S., Palumbo Piccionello, A. & Pace, A. (2017). Photochemically produced singlet oxygen: applications and perspectives. *ChemPhotoChem*, *2*(7), 535–547. https://doi.org/10.1002/cptc.201800076

2 Bregnhøj, M., Westberg, M., Minaev, B. F. & Ogilby, P. R. (2017). Singlet oxygen photophysics in liquid solvents: converging on a unified picture. *Acc. Chem. Res., 50,* 1920–1927. https://doi.org//10.1021/acs.accounts.7b00169.

3 Minaev, B. F. (2007). Electronic mechanisms of activation of molecular oxygen. *Russ. Chem. Rev., 76*(1), 989. https://doi.org/10.1070/RC2007v076n11ABEH003720

4 Minaev, B. F., Minaeva, V. A. & Evtuhov, Y. V. (2009). Quantum chemical study of the singlet oxygen emission. *Int. J. Quantum Chem., 109*, 500–515. https://doi.org/10.1002/qua.21783

5 Minaev, B. F., Murugan, N. A. & Ågren, H. (2013). Dioxygen spectra and bioactivation. *Int. J. Quantum Chem., 113*, 1847–1867. https://doi.org/10.1002/qua.24390

6 Minaev, B.F. (2022). The spin of dioxygen as the main factor in pulmonology and respiratory care. *Arch. Pulmonol. Respir. Care, 8(1)*, 028–033. https://dx.doi.org/10.17352/aprc.000081

7 Maharjan, P. S. & Bhattarai, H. K. (2022). Singlet oxygen, photodynamic therapy, and mechanisms of cancer cell death. J. Oncology, 2022, 7211485. https://doi.org/10.1155/2022/7211485

8 Ishchenko, A. A. & Syniugina, A. T. (2023). Structure and photosensitaizer ability of polymethine dyes in photodynamic therapy: a Review. *Theor. Exp. Chem., 58*, 373–401. https://doi.org/10.1021/acs.bioconjchem.9b00482

9 Jiang, Y., Fu, Y., Xu, X., Guo, X., Wang, F., Xu, X., Yao-Wei, Huang, Shi, J. & Shen, C. (2023). Production of singlet oxygen from photosensitizer erythrosine for facile inactivation of coronavirus on mask. *Environment Int., 177*, 107994. https://doi.org/10.1016/j.envint.2023.107994

10 Schmidt, R. Photosensitized generation of singlet oxygen. (2006). *Photochem Photobiol., 82*(5), 1161–1177. https://dx.doi.org/10.1562/2006-03-03-IR-833.

11 Aerssens, D., Cadoni, E., Tack, L. & Madder, A. (2022). A Photosensitized singlet oxygen ($^1O_2$) toolbox for bio-organic applications: tailoring $^1O_2$ generation for DNA and protein labelling, targeting and biosensing. *Molecules, 27(3)*, 778. https://www.mdpi.com/1420-3049/27/3/778

12 Sheng, F., Ling, J., Hong, R., Jin, X., Wang, C., Zhong, H., Gu, X. & Gu, C. (2019). A new pathway of monomethylmercury photodegradation mediated by singlet oxygen on the interface of sediment soil and water. Environ. Pollut., *248*, 667–675. https://doi.org/10.1016/j.envpol.2019.02.047

13 Wan, B. & Lu, S. (2022). The light of carbon dots: From mechanism to application. *Matter, 5*, 110–149. https://doi.org/10.1016/j.matt.2021.10.016.

14 Song, S. H., Jang, M. H., Chung, J., Jin, S. H., Kim, B. H., Hur, S. H., Yoo, S., Cho, Y. & Jeon, S. (2014). Highly efficient light-emitting diode of graphene quantum dots fabricated from graphite intercalation compounds. *Adv. Opt. Mater., 11*, 1016–1023. https://doi.org/10.1002/adom.201400184

15 Sun, Q. C., Dinga, Y. C., Sagara, D. M. & Nagpal, P. (2017). Photon upconversion towards applications in energy conversion and bioimaging. *Prog. Surf. Sci., 92*, 281–316. https://doi.org/10.1016/j.progsurf.2017.09.003

16 Kang, H., Zheng, J., Liu, X. & Yang, Y. (2021). Phosphorescent carbon dots: microstructure design, synthesis and applications. *New Carbon Mater., 36*, 649–664. https://doi.org/10.1016/s1872-5805(21)60083-5

17 Kim, A., Dash, J. K., Kumar, P. & Patel, R. (2022). Carbon-based quantum dots for photovoltaic devices: a review. *ACS Appl. Electron. Mater., 4*, 27–58. https://doi.org/10.1021/acsaelm.1c00783

18 Sciortino, A., Mauro, N., Buscarino, G., Sciortino, L., Popescu, R., Schneider, R., Giammona, G., Gerthsen, D., Cannas, M. & Messina, F. (2018). β-C$_3$N$_4$ nanocrystals: carbon dots with extraordinary morphological, structural, and optical homogeneity. *Chem. Mater., 30*, 1695–1700. https://doi.org/10.1021/acs.chemmater.7b05178

19 Nur Afifah, A. N., Nur Hidayah, A., Mohd Hafiz, A. B., Nadhratun, N. M., Yunhan, L., Norhana, A., Hasnan Tg, A. A., Ahmad Rifqi, Md Z. & Ahmad Ashrif, A. B. (2022). Localized surface plasmon resonance decorated with carbon quantum dots and triangular Ag nanoparticles for chlorophyll detection. *Nanomaterials, 12*, 35. https://doi.org/10.3390/nano12010035

20 Sun, H., Gao, N., Dong, K., Ren, J. & Qu, X. (2014). Graphene quantum dots-band-aids used for wound disinfection. *ACS Nano, 8*, 6202-6210. https://doi.org/10.1021/nn501640q

21 Fowley, C., Nomikou, N., McHale, A.P., McCaughan, B. & Callan, J.F. (2013). Extending the tissue penetration capability of conventional photosensitisers: a carbon quantum dotprotoporphyrin IX conjugate for use in two-photon excited photodynamic therapy. *Chem. Commun., 49*, 8934-8936. https://doi.org/10.1039/C3CC45181J

22 Zhou, Y., Sun, H., Wang, F., Ren, J. & Qu, X. (2017). How functional groups influence ROS generation and cytotoxicity of graphene quantum dots. *Chem. Comm., 53*, 10588-10591. https://doi.org/10.1039/C7CC04831A

23 Pillar-Little, T. J., Wanninayake, N., Nease, L., Heidary, D. K., Glazer, E. C. & Kim, D. Y. (2018). Superior photodynamic effect of carbon quantum dots through both type I and type II pathways: detailed comparison study of top-down-synthesized and bottom-up-synthesized carbon quantum dots. *Carbon, 140*, 616-623. https://doi.org/10.1016/j.carbon.2018.09.004

24 Wu, S., Zhou, R., Chen, H., Zhang, J. & Wu, P. (2020). Highly efficient oxygen photosensitization of carbon dots: the role of nitrogen doping. *Nanoscale, 12*, 5543–5553. https://doi.org/10.1039/C9NR10986B

25 Seliverstova, E., Ibrayev, N., Omarova, G., Ishchenko, A. & Kucherenko, M. (2021). Competitive influence of the plasmon effect and energy transfer between chromophores and Ag nanoparticles on the fluorescent properties of indopolycarbocyanine dyes. *J. Lumin., 235*, 118000. https://doi: 10.1016/j.jlumin.2021.118000

26 Ibrayev, N., Afanasyev, D., Ishchenko, A. & Kanapina, A. (2021). Influence of silver nanoparticles on the spectral-luminescent and lasing properties of merocyanine dyes solutions. *Laser Phys. Lett., 18*, 085001. https://doi.org/10.1088/1612-202X/ac0e3f

27 Yu, H., Peng, Y., Yang, Y. & Li, Z. (2019). Plasmon-enhanced light–matter interactions and applications. *NpjComput. Mater., 5*, 45. https://doi:10.1038/s41524-019-0184-1

28 Seliverstova, E. V., Ibrayev N. K. & Zhumabekov, A. Zh. (2020). The effect of silver nanoparticles on the photodetecting properties of the TiO_2/graphene oxide nanocomposite. *Opt. Spectrosc., 128*, 1449–1457. https://doi:10.1134/S0030400X20090192

29 Bitton, O., Gupta, S. & Haran, G. (2019). Quantum dot plasmonics: from weak to strong coupling. *Nanophotonics, 8*, 559–575. https://doi:10.1515/nanoph-2018-0218

30 Temirbayeva, D., Ibrayev, N. & Kucherenko, M. (2022). Distance dependence of plasmon-enhanced fluorescence and delayed luminescence of molecular planar nanostructures. *J. Lumin., 243*, 118642. https://doi:10.1016/j.jlumin.2021.118642

31 Lakowicz, J. R. (2006). Principles of Fluorescence Spectroscopy, N.Y.: Kluwer Plenum Publishers.

32 Anger, P., Bharadwaj, P. & Novotny, L. (2006). Enhancement and quenching of single–molecule fluorescence. *Phys. Rev. Lett., 96*, 113002. https://doi.org/10.1103/PhysRevLett.96.113002

33 Yuan, K., Qin, R., Yu, J., Li, X., Li, L., Yang, X. & Liu H. (2019). Effects of localized surface plasmon resonance of Ag nanoparticles on luminescence of carbon dots with blue, green and yellow emission. *Appl. Surf. Sci., 502*, 144277. https://doi:10.1016/j.apsusc.2019.144277

34 Bagra, B., Zhang, W., Zeng, Z., Mabe, T. & Wei, J. (2019). Plasmon enhanced fluorescence of carbon nanodots in gold nanoslit cavities. *Langmuir, 35*, 8903-8909. https://doi:10.1021/acs.langmuir.9b00448

35 Kamura, Y. & Imura, K. (2020). Photoluminescence from carbon dot-gold nanoparticle composites enhanced by photonic and plasmonic double-resonant effects. *ACS Omega, 5*, 29068-29072. https://doi.org/10.1021/acsomega.0c03588

36 Sciortino, A., Panniello, A., Minervini, G., Mauro, N, Giammona, G., Buscarino, G., Cannas, M., Striccoli, M. & Messina, F. (2022). Enhancing carbon dots fluorescence via plasmonic resonance energy transfer. *Mater. Res. Bull. 149*, 111746. https://doi.org/10.1016/j.materresbull.2022.111746

37 Abdolmohammad-Zadeh, H., Azari, Z. & Pourbasheer, E. (2020). Fluorescence resonance energy transfer between carbon quantum dots and silver nanoparticles: Application to mercuric ion sensing. *Spectrochim. Acta A., 245*, 118924. https://doi.org/10.1016/j.saa.2020.118924

38 Nazri, N., Azeman, N., Bakar, M., Mobarak, N., Luo, Y., Arsad, N., Aziz, T., Zain, A. & Bakar, A. (2022). Localized surface plasmon resonance decorated with carbon quantum dots and triangular Ag nanoparticles for chlorophyll detection. *Nanomaterials, 12*, 35. https://doi.org/10.3390/nano12010035

39 Bukasov, R., Filchakova, O., Gudun, K. & Bouhrara, M. (2017). Strong surface enhanced florescence of carbon dot labeled bacteria cells observed with high contrast on gold film. *J. Fluoresc, 28*, 1–4. https://doi.org/10.1007/s10895-017-2194-z

40 Amjadi, M., Shokri, R. & Hallaj, T. (2016). Interaction of glucose-derived carbon quantum dots with silver and gold nanoparticles and its application for the fluorescence detection of 6-thioguanine. *Luminescence, 32*, 292–297. https://doi.org/10.1002/bio.3177

41 Ibrayev, N., Dzhanabekova, R., Seliverstova, E. & Amanzholova, G. (2021). Optical properties of N- and S-doped carbon dots based on citric acid and L-cysteine. *Fullerenes, Nanotubes, Carbon Nanostruct., 30(1)*, 22-26. https://doi.org/10.1080/1536383X.2021.1999933

42 Liu, J., Zhang, H., Wang, N., Yu, Y., Cui, Y., Li, J. & Yu, J. (2019). Template-modulated afterglow of carbon dots in zeolites: room-temperature phosphorescence and thermally activated delayed fluorescence. *ACS Materials Lett., 1*, 58–63. https://doi.org/10.1021/acsmaterialslett.9b00073

43 Zhang, H., Wang, B., Yu, X., Li, J., Shang, J. & Yu, J. (2020). Carbon dots in porous materials: host–guest synergy for enhanced performance. *Angew. Chemie Inernat. Ed., 59(44)*, 19390-19402. https://doi.org/10.1002/anie.202006545

44 Buchachenko, A. L., Sagdeev, R. Z. & Salikhov K. M. (1978). Magnitniye spinovye effekty v khimicheskikh reaktsiiakh [Magnetic spin effects in chemical reactions]. Novosibirsk: Nauka [in Russian].

45 Bregnhøj, M., Westberg, M., Jensen, F. & Ogilby, P. R. (2016). Solvent-dependent singlet oxygen lifetimes: temperature effects implicate tunneling and charge-transfer interactions. *Phys. Chem. Chem. Phys., 18*, 22946-22961. https://doi.org/10.1039/C6CP01635A

46 Salokhiddinov, K. I., Byteva, I. M. & Gurinovich, G. P. (1981). Lifetime of singlet oxygen in various solvents. *J. Appl. Spectrosc., 34*, 561–564. https://doi.org/10.1007/BF00613067

47 Minaev, B. F. (1985). Quantum-chemical investigation of the mechanisms of the photosensitization, luminescence, and quenching of singlet $^1\Delta_g$ oxygen in solutions. *J. Appl. Spectrosc., 42(5)*, 518-523. https://doi.org/10.1007/BF00661398

48 Minaev, B. F., Lunell, S. & Kobzev, G. I. (1994). Collision-induced intensity of the $b^1\Sigma_g^+ - a^1\Delta_g$ transition in molecular oxygen: Model calculations for the collision complex $O_2 + H_2$. *Int. J. Quantum Chem., 50(4)*, 279-292. https://doi.org/10.1002/qua.560500405

49 Bryukhanov, V. V., Minaev, B. F., Tsibul'nikova, A. V. & Slezhkin V. A. (2015). The Effect of gold nanoparticles on exchange processes in collision complexes of triplet and singlet oxygen molecules with excited eosin molecules. *Optics Spectrosc., 119(1),* 29–38. https://doi.org/10.1134/S0030400X15070061

50 Konstantinova, E. I., Minaev, B. F., Tsibul'nikova, A. V., Borkunov, Yu. R., Tsar'kov, M. V., Antipov, Yu., Samusev, I. G. & Bryukhanov, V. V. (2018). Dynamics of thermoluminescence under dual-wavelength vis–ir laser excitation of eosin molecules in a polyvinyl butyral film containing oxygen and silver nanoparticles. *Optics Spectrosc., 125(6),* 874–881. https://doi.org/10.1134/S0030400X19020152

Information about authors*

Ibrayev, Niyazbek Khamzauly (*corresponding author*) — Doctor of Physical-Mathematical Sciences, Institute of Molecular Nanophotonics, Karaganda University of the name of academician E.A. Buketov, Universitetskaya street, 28, 100024, Karaganda, Kazakhstan; e-mail: niazibrayev@mail.ru; https://orcid.org/0000-0002-5156-5015

Seliverstova, Evgeniya Vladimirovna — Doctor PhD, Institute of Molecular Nanophotonics, Karaganda University of the name of academician E.A. Buketov, Universitetskaya street, 28, 100024, Karaganda, Kazakhstan; e-mail: genia_sv@mail.ru; https://orcid.org/0000-0002-9507-8825

_____

*The author's name is presented in the order: *Last Name, First and Middle Names*

Article

UDC 544.18   https://doi.org/10.31489/2959-0663/3-23-9

Gabriel K. Obiyenwa[1] iD, Banjo Semire[1, 2]* iD, Abel K. Oyebamiji[3] iD, Ibrahim O. Abdulsalami[4] iD, Dayo F. Latona[5] iD, Moriam D. Adeoye [6] iD, Olusegun A. Odunola[2,7] iD

[1]Department of Chemistry, Federal University, Lokoja, Kogi State, Nigeria;
[2]Computational Chemistry Laboratory, Department of Pure and Applied Chemistry,
Ladoke Akintola University of Technology, Ogbomoso, Nigeria;
[3]Industrial Chemistry Programme, Bowen University, Iwo, Osun State, Nigeria;
[4]Department of Chemistry, Nigerian Army University, Biu, Bornu State, Nigeria;
[5]Department of Pure and Applied Chemistry, Osun State University, Osogbo, Nigeria;
[6]Department of Chemistry, Fountain University, Osogbo, Osun State, Nigeria;
[7]Department of Chemistry, Faculty of Natural and Applied sciences, Hallmark University, Ijebu-Itele, Ogun state, Nigeria
(*Corresponding author′s e-mail: bsemire@lautech.edu.ng)

TD-DFT and DFT Investigation on Electrons Transporting Efficiency of 2-Cyano-2-Pyran-4-Ylidene-Acetic Acid and 2-Cyanoprop-2-Enoic Acid as Acceptors for Thiophene-Based π-Linkers Dye-Sensitized Solar Cells

Great attention is being shifted to Dye-sensitized solar cells because of their structural and electronic tunability, high performance, and low cost compared to conservative photovoltaic devices. In this work, B3LYP/6-31G** level of theory was used to study the molecular architecture of the donor-π-acceptor (D-π-A) type. This architecture contains a series of dyes with the 2-cyano-2-pyran-4-ylidene-acetic acid (PLTP-dye) and 2-cyanoprop-2-enoic acid (CLTP-dye) units as acceptors; donor groups and thiophene-based π-linkers. The molecular and electronic properties, light harvesting efficiency, open circuit voltage (V_{OC}), injection force (ΔG^{inject}), regeneration force (ΔG^{regen}) and excitation state lifetime (τ_{esl}) were calculated. CLTP-dyes showed lower band gap, chemical hardness (η), chemical potential (μ), higher electrophilicity (ω) and electron denoting power (ω^-) than the corresponding PLTP-dyes. The ω^- demonstrated that PLTP-1, PLTP-2 and PLTP-3, CLTP-1, CLTP-2 and CLTP-3 should readily push electrons to the π-linker, which can lead to high intra-molecular charge transfer and photocurrent for the dyes. The Voc and ΔG^{inject} parameters favoured the CLTP-dyes over corresponding PLTP-dyes, and also dyes with the N,N-diphenylaniline donor have higher Voc, ΔG^{inject} values and longer wavelengths (λ_{max}) than the dyes with carbazole unit (N,N-diphenylaniline dyes > Carbazole dyes) in accordance with the calculated ω^-, although all the dyes have good regeneration and injection abilities.

Keywords: frontier orbitals, photoelectric properties, reactivity indices, TD-DFT, DFT, B3LYP, D-π-A type, dye-sensitized solar cells (DSSC).

Introduction

Increasing energy consumptions coupled with the global warming effect determined by energy supply from fossil resources has caused significant interest in renewable energy research. The energy released by the Sun to the Earth per hour exceeds the current world energy consumption per year; therefore, there is a daily growing in the development and use of solar renewable energy [1]. Consequently, efficient solar energy conversion devices or methods are required to provide a promising technology that can counterbalance the ever-growing energy demand needed for fast industrial development [2, 3]. However, solar photovoltaic cell has been considered to be one of the foremost prospective to cover a higher percentage of the future energy needs among other available renewable energy sources. In order to exploit this great benefit, a safe, cost-effective, efficient and ecofriendly method of harvesting solar energy are needed, and dye-sensitized solar cells (DSSCs) which belong to the third-generation solar cell technologies have the potential to meet these requirements. DSSCs invented by O'Regan and Grätzel in 1991, gave the broad view of using molecular components-based devices for the construction of a large-scale solar facility for electricity production, and thus put the solid-state technology to challenge by operating photovoltaic devices at molecular or nanoscale levels [4]. Although research is still ongoing, as well as pre-industrial technology in DSSCs is still low com-

pared to the performance of silicon devices; the efficiency is still below 13 % for DSSC [5]. Over the years, the applications of DSSCs have been intensively studied as a result of its potentially low cost of production, despite its current low efficiency and stability [6]. Designing of dye-sensitizers for DSSC have inform of donor (D)-π spacer-acceptor (A) to ensure intra-molecular charge transfer, usually from donor unit through π spacer to the acceptor unit [7, 8]. In an attempt to improve the dye-sensitizers importance, different types of dyes combinations have been developed, such as D–π–D–π–A, (D–π–A)₂, D–A–π–A, D–D–π–A, D–π–A–A and A–π–D–π–A [9–13].

Organic dyes with triphenylamine-based donor groups and the cyanoacrylic dyes as an acceptor/anchoring group are known for their outstanding properties, which have attracted much attention in DSSC technology [14–16]. Triphenyl moiety containing organic dyes possess unique characteristics such as the tunable frontier orbital energies, low dye aggregation, high molar absorption coefficients and non-planarity. These notable properties have made the triphenylamine (TPA) based sensitizers highly suitable for the DSSCs application [17]. However, these properties have led to a low recombination and back-reaction rate in the solar energy conversion process. Though, π-conjugated systems of the sensitizing dyes can be easily modified to obtain desired absorption wavelengths by adjusting the band gap of dyes [14, 15].

The cyanoprop-2-enoic acid has been a popular acceptor moiety for anchoring dye-sensitizers to TiO₂ surface in dye sensitized solar cells [16, 5]. However, other acceptor moieties used such dyes like the rhodamine-3-acetic acid in which the photovoltaic results were compared with those of the cyanoprop-2-enoic acid acceptor. The results revealed that dye with the rhodamine-3-acetic acid as an acceptor unit had the shorter wavelength, lower molar extinction coefficients and lower light capturing ability due to the weaker intra-molecular charge transfer ability [18]. Also, in some of our recent works, a series of dyes with the cyano-2-pyran-4-ylidene-acetic acid as acceptor were computationally modeled and studied. The results predicted very good optical properties, light harvesting efficiency and high circuit voltage, which were improved by the presence of fluorine atoms in the cyano-2-pyran-4-ylidene-acetic acid [19, 20]. Besides, several dyes of pyran derivatives have been investigated for absorption, light harvesting, intra-molecular charge transfer, regeneration and recombination properties using computational methods [21]; the results predict their applications as organic light emitting diode (OLED), bulk-heterojunction solar cells, and sensors [21–25].

Density functional theory (DFT) methods continue to play a leading role in the design and research of the electronic structure, photocurrent and electron transport properties of dye-sensitizers for photovoltaic applications such as DSSCs development [26–31]. Therefore, in this present study, density functional theory was used to explore the electron transporting efficiency of the 2-cyano-2-pyran-4-ylidene-acetic acid (type A dyes) and the 2-cyanoprop-2-enoic acid (type B dyes) as the acceptor anchoring units for thiophene-based π-linkers for dye-sensitized solar cells as shown in Table 1. The effects of these acceptor units on intra-molecular charge transfer, electrons regenerating, electrons injecting and light harvesting efficiency of the dye sensitizers were studied. The roles of thiophene derivatives (bisthioeno[3,2-b,3-b]thiophene, 4H-cyclopenta[1,2-b,5,4-b]bisthiophene and terthiophene) as the π-linkers have thoroughly investigated and discussed.

Computational Details

The accuracy of DFT calculations depends on the selected functional and basis sets. It has been established that the polarized split-valence 6-31G(d, p) basis sets is sufficiently accurate for calculating the electronic excitation properties of organic dyes without extension of the basis sets [32, 33]; thus the designed D-π-A dyes were optimized using DFT of the three-parameter density functional, with Becke's gradient exchange correction [34] and the Lee, Yang, Parr correlation functional (i.e. B3LYP) [35] accounting the 6-31G(d, p) basis set. Frequency calculations were performed on the optimized structures of the dyes at the same levels of theory to reveal the stationary points as local minima, and none of the optimized structures of the dyes exhibited imaginary frequencies. The frontier orbital energies, reactivity indices, natural density analysis, photo-electronics properties, intra-molecular charge transfer properties, and injection and regeneration driving forces were calculated. All calculations were carried out using Spartan 14 software from Wavefunction Inc. (Spartan, 2014) [36], implemented on an Intel® Core TM i7-4520M CPU, 2.50 GHz computer.

Schematic structure of the studied molecules: Type A is the 2-cyano-2-pyran-4-ylidene-acetic acid and Type B is the 2-cyanoprop-2-enoic acid as acceptor anchor, respectively

Type A

PLTP-1

Type B

CLTP-1

PLTP-2

CLTP-2

PLTP-3

CLTP-3

PLTP-4

CLTP-4

PLTP-5

CLTP-5
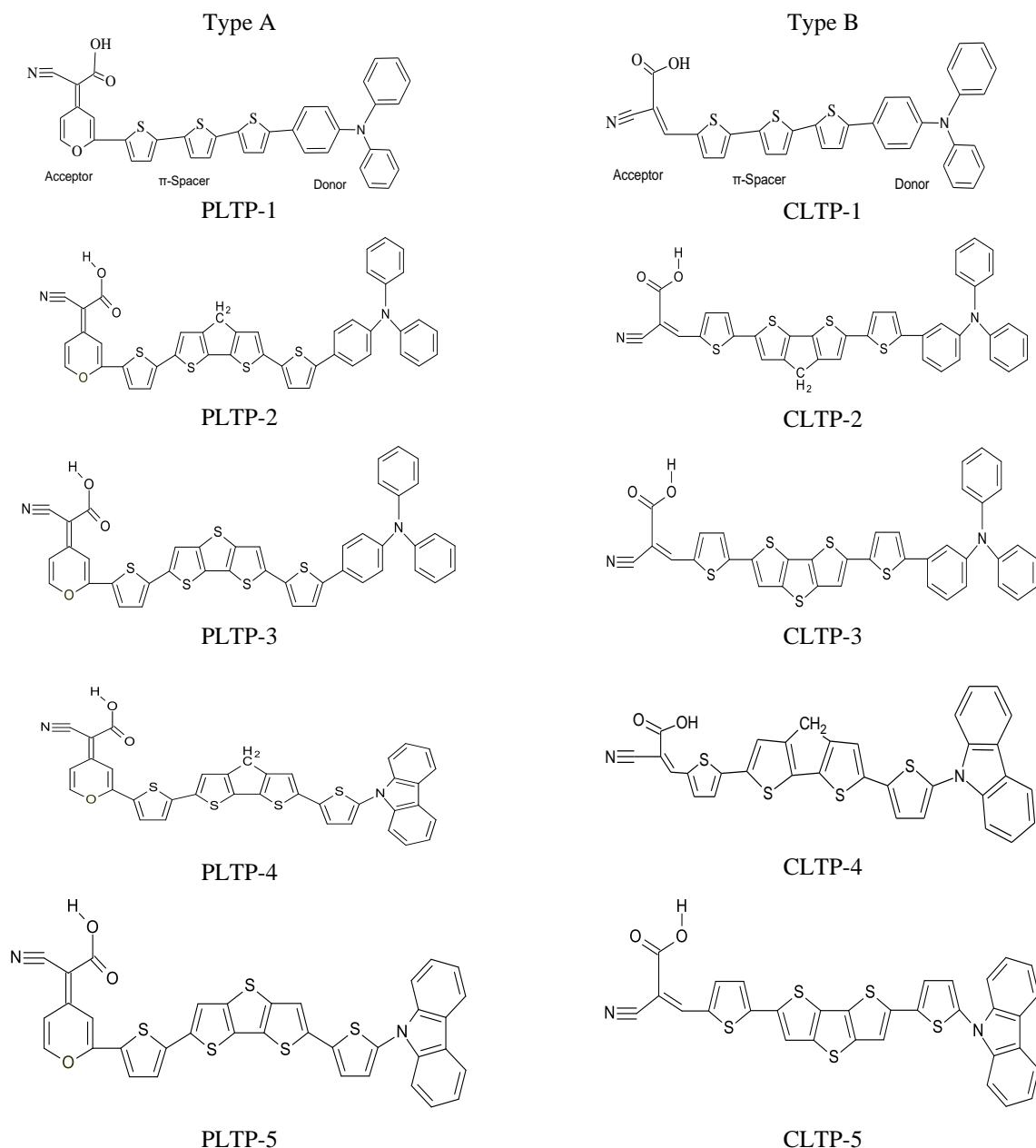
Results and Discussion

Frontier Molecular Orbital energies and reactivity indices

The frontier orbital energies, such as the HOMO and LUMO energies of dye sensitizers, are vital for modification the redox potential of the electrolyte and conduction-band edge of the semiconductor in DSSCs to achieve high harvesting and desired capability of the dye [37]. Designing low-molecular weight D–π–A dye sensitizers require fine tuning the properties of frontier orbitals because they are qualitative characteristics of organic dyes excitation properties [38, 26, 27, 29]. The frontier orbitals contour overlay is displayed in Figure 1 shows that the HOMOs overlaid are localized on the donor subunit extended over π-linker, and also the LUMOs overlaid are mainly on acceptor subunit with extension over π-linker. This means that there is a good interaction between the donor and acceptor groups through π-linker, which could facilitate intramolecular charge transfer from donor to acceptor unit [39].

Mol	Optimized Structure	HOMO	LUMO
PLTP-1			
PLTP-2			
PLTP-3			
PLTP-4			
PLTP-5			
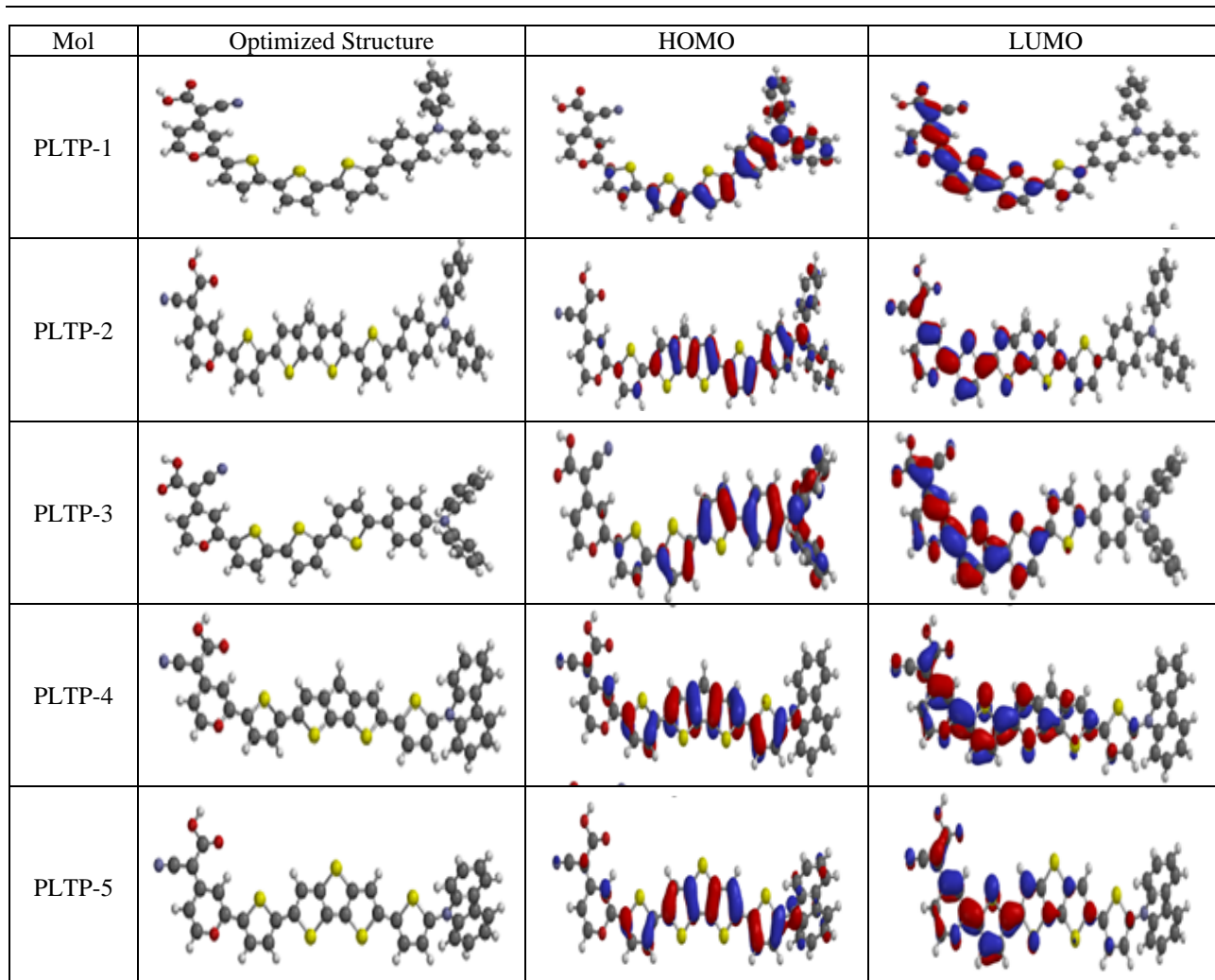
Figure 1*a*. The Contour Plots of the frontier orbitals of PLTPs dyes

Mol	Optimized Structure	HOMO	LUMO
CLTP-1			
CLTP-2			
CLTP-3			

| CLTP-4 | | | |
| CLTP-5 | | | |
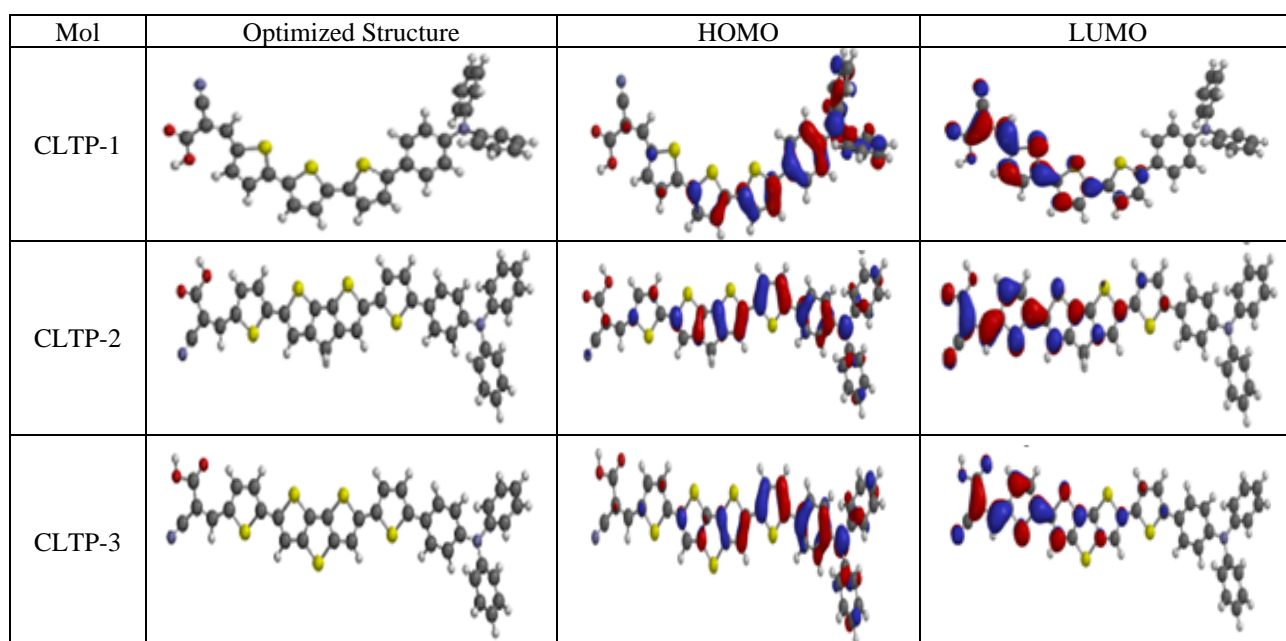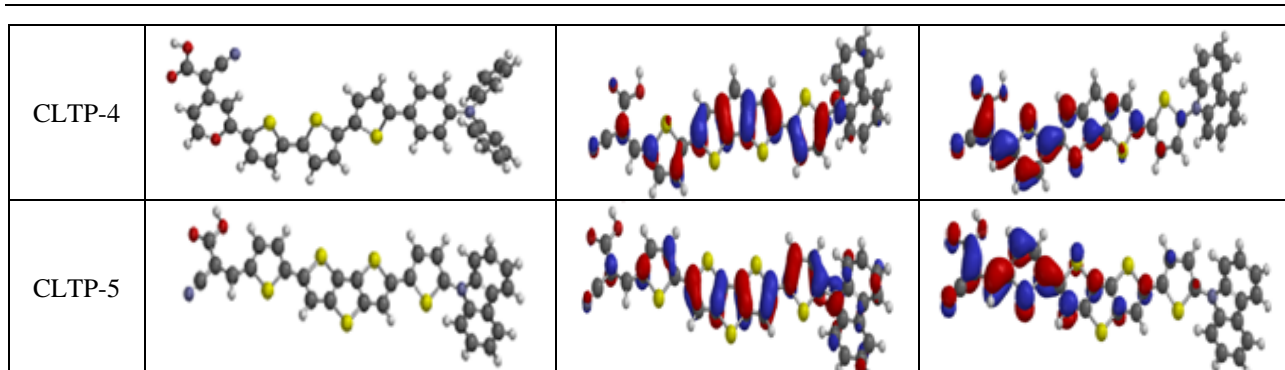
Figure 1*b*. The Contour Plots of frontier orbitals of CLTPs dyes

The electron accepting efficiency of the dye acceptors (types A and B) were examined by considering dyes with similar donors and π-conjugated linkers such as CLTP-1 and PLTP-1, CLTP-2 and PLTP-2, CLTP-3 and PLTP-3, CLTP-4 and PLTP-4, CLTP-5 and PLTP-5 (Lu et al., 2011 [40]). The HOMO, LUMO, and HOMO–LUMO energy gap (E_g) for the dyes were calculated as –4.92, –2.57 and 2.35 eV for PLTP-1; –5.04, –2.84 and 2.20 eV for CLTP-1, respectively. The CLTP-1 dye (Type B) with the 2-cyanoprop-2-enoic acid as acceptor unit showed a decrease in both the HOMO and LUMO energies by 0.12 and 0.27 eV, respectively, which resulted into lowering of Eg by 0.15 eV for CLTP-1 compare to PLTP-1. The calculated HOMO, LUMO, and Eg values for PLTP-2 were –4.82, –2.60, 2.22eV; and –4.91, –2.83 and 2.08 for CLTP-2, which also showed a reduction of the HOMO/LUMO by 0.09/0.23 eV resulting in a decrease of Eg by 0.14 eV for CLTP-2 over PLTP-2. Moreover, the HOMO, LUMO, and Eg for PLTP-3 were –4.94, –2.67, and 2.27 eV; and –4.99, –2.88 and 2.11 eV for CLTP-3; this led to a relative decrease in the HOMO/LUMO by 0.05/0.21 eV resulting in a reduction of Eg by 0.16 eV for CLTP-3 compare to PLTP-3 (Fig. 2).

Similarly, the HOMO, LUMO and Eg for CLTP-4 was lowered by 0.12 eV as compare to PLTP-4 due to a decrease in the HOMO/LUMO by 0.01/0.22 eV. This observation revealed that both the HOMO and LUMO of type B dye's orbitals are delocalized leading relative ease of π-electrons flow, thus lowering of Eg in CLTP dyes. The Eg values of the studied dyes can be ordered as PLTP-2 < PLTP-1 < PLTP-3 < PLTP-4 < < PLTP-5 for type A, and CLTP-2 < CLTP-3 < CLTP-1 < CLTP-4 < CLTP-5 for type B (Fig. 2). Generally, type B presented lower band gap than the corresponding type A; however, all the dyes are good photosensitized prospects, since their HOMO energy levels are lower than the redox potential of the I^-/I_3^- electrolyte (–4.8 eV) and LUMO energy levels are higher than the conduction band (CB) of the TiO_2 semiconductor (–4.0 eV) which ensures the injection of the electron from the dye to TiO_2 as well as dye renaissance [40; 41].
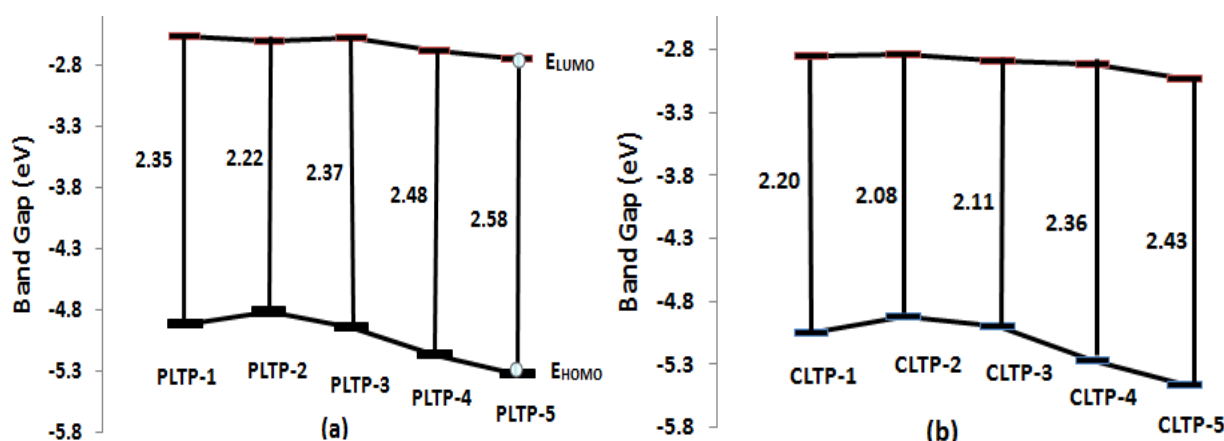
a — 2-cyano-2-pyran-4-ylidene-acetic acid; *b* — 2-cyanoprop-2-enoic acid as acceptor anchor, respectively

Figure 2. Energy band gap for the studied D–π–A dye sensitizers

Furthermore, the effect of π-linkers on the intramolecular charge transfer was investigated in the two-dye series; PLTP-1, PLTP-2 and PLTP-3 for type A, and CLTP-1, CLTP-2 and CLTP-3 for type B. The frontier energies (HOMO, LUMO and E_g) for PLTP-1, PLTP-2 and PLTP-3 were (–4.92, –2.57 and 2.35 eV), (–4.82, –2.60, 2.22 eV) and (–4.95, –2.58 and 2.37 eV), respectively. Therefore, the use of 4H-cyclopenta[1,2-b,5,4-b]bisthiophene as π-linker in PLTP-2 increases/decreases the HOMO/LUMO energy by 0.10/0.03 eV compare to PLTP-1 with terthiophene as π-linker, thereby causing delocalization of the LUMO orbital leading to reduction in the E_g by 0.13 eV. However, with bisthioeno[3,2-b,3-b]thiophene as π-linker in PLTP-3, the HOMO/LUMO was slightly decreased by 0.04/0.01 eV, thus PLTP-3 only increased in Eg by 0.02 eV. Also, similarly, the frontier orbital energies (HOMO, LUMO and Eg) for CLTP-1, CLTP-2 and CLTP-3 were (–5.04, –2.84, 2.20 eV), (–4.91, –2.83, 2.08 eV) and (–4.99, –2.88 and 2.11 eV), respectively. The electronic properties revealed that the HOMO/LUMO energies of CLTP-2 (with 4H-cyclopenta[1,2-b,5,4-b]bisthiophene as π-linker) increases by 0.13/0.01 eV, leading to lowering of Eg by 0.12 eV compare to CLTP-1. At the same time, with bisthioeno[3,2-b,3-b]thiophene as π-linker in CLTP-3, the HOMO/LUMO energies increases/decreases by 0.05/0.04 eV, which leads to reduction in Eg by 0.09 eV compare to CLTP-1 (Fig. 2). This suggests that dyes with 4H-cyclopenta[1,2-b,5,4-b]bisthiophene as linker could have superior photocurrent and charge transfer (CT) than dyes with terthiophene and bisthioeno[3,2-b,3-b]thiophene as π-linkers (Semire et al., 2017 [48]), It can be argued that higher HOMO energy together with the lower LUMO energy favors excitation of electrons in D–π–A organic dyes [21].

In addition, the efficiency of the donor subunits was also investigated by considering CLTP-2 and CLTP-4, PLTP-2 and PLTP-4 dyes. Comparing CLTP-2 and CLTP-4, the HOMO, LUMO energies, and Eg were –5.27, –2.91, 2.36 eV for CTP-4; and –4.91, –2.83 and 2.08 eV for CLTP-2. There is a stabilization of both the HOMO and LUMO orbitals by 0.36 and 0.08 eV, respectively leading to enhancement of Eg by 0.28 eV in CLTP-2 dyes compare to CLTP-4. Also, comparing PLTP-4 and PLTP-2, it can be noted that Eg enhanced by 0.26 eV as a result of stabilization of both the HOMO/LUMO by 0.35/0.09 eV. Therefore, N,N-diphenylaniline donor group donors/pushes more electrons readily towards π-linker than carbazole donor group, thus dyes bearing N,N-diphenylaniline donor group should have better intramolecular charge transfer and good photocurrent ability [20].

The natural bond orbital (NBO) analysis was performed on the optimized structure in the ground state in order to study the electron transfer mechanism as well as charge distribution of the studied D-π-A dyes. The calculated NBOs at the B3LYP/6-31G (d, p) level are listed in Table 2. The positive charges on the N,N-diphenylaniline moiety reveals an efficacious electron-donor unit and the large negative NBO charges on 2-cyano-2-pyran-4-ylidene-acetic acid/2-cyanoprop-2-enoic acid are evidence that electrons are enthralled in the acceptor unit. The NBO analysis, N-diphenylaniline donor group shows that the cyano-substituent attached to the acceptor unit of the dyes increases/decreases the natural bond orbital charges on both the acceptor and donor units. The trapping of electrons in the acceptor unit denotes that the NBO charges in the dye sensitizers are subjugated by acceptor moieties [42].

The dyes electronegativity (χ), chemical hardness (η), electrophilicity index (ω) and electron donating power (ω$^-$) were estimated from the ground state geometries of the optimized dyes at B3LYp/6-31G** level of theory for an N-electron system with total energy E as described in equations 1–4 [42, 43].

$$\chi = -\mu = \left(\frac{\delta E}{\delta N}\right)_{v(r)} \cong \frac{IP + EA}{2} \tag{1}$$

$$\eta = \left(\frac{\delta^2 E}{\delta N^2}\right)_{v(r)} \cong \frac{IP - EA}{2} \tag{2}$$

$$\omega = \frac{\mu^2}{2\eta} = \frac{(IP + EA)^2}{4(IP - EA)} \tag{3}$$

$$\omega^- = \frac{(3IP - EA)^2}{16(IP - EA)}, \tag{4}$$

where IP (vertical ionization potential) and EA (vertical electron affinity) are approximated to $-E_{HOMO}$ and $-E_{LUMO}$, respectively [45].

Global Molecular Descriptors and Light Harvesting Efficiency (LHE)

MOL	q_{Donor}	π-linker	$q_{Acceptor}$	Δq(D-A)	μ (eV)	η (eV)	ω (eV)	ω^- (eV)
PLTP-1	0.126	–0.006	–0.120	0.246	–3.745	1.175	5.968	3.952
PLTP-2	0.142	–0.008	–0.138	0.280	–3.710	1.110	6.200	3.960
PLTP-3	0.141	–0.002	–0.140	0.281	–3.765	1.185	5.981	3.970
PLTP-4	0.152	0.019	–0.153	0.305	–3.930	1.240	6.227	4.142
PLTP-5	0.130	–0.004	–0.133	0.263	–4.040	1.290	6.325	4.247
CLTP-1	0.127	0.001	–0.125	0.252	–3.940	1.100	7.055	4.284
CLTP-2	0.033	–0.036	–0.172	0.205	–3.870	1.040	7.200	4.255
CLTP-3	0.135	–0.024	–0.164	0.299	–3.935	1.055	7.338	4.330
CLTP-4	0.143	–0.013	–0.132	0.275	–4.090	1.180	7.088	4.407
CLTP-5	0.142	–0.009	–0.136	0.278	–4.245	1.215	7.415	4.584

a — PLTPs; *b* — CLTPs
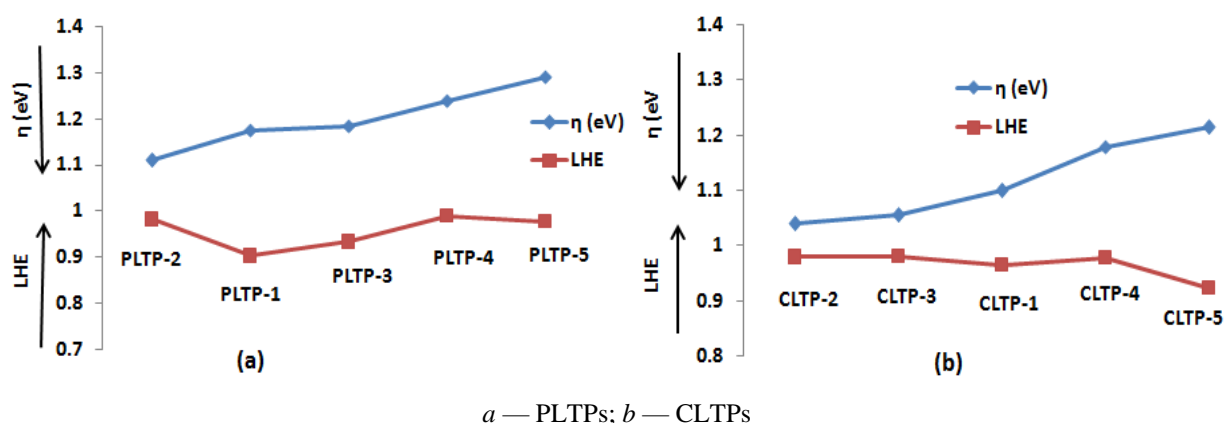
Figure 3: Relationship between light harvesting efficiency (LHE) and chemical hardness (η):

The thermodynamic stability of dye-sensitizers, a crucial parameter was adjudged by reactivity indices. Chemical hardness (η) is a parameter associated with molecular resistance to charge transfer with the surrounding [19]. According to [48] (Semire et al., 2017) it has a very close relation to intra-molecular charge transfer is favoured by low η for good dye-sensitizers. The η shows that type B (CLTP dyes) have lower chemical hardness compare to type A (PLTP dyes). The relationship between η and LHE has been described as a graph funnel-like shape [46]. Thus, as shown in Figure 3, low η and high LHE enhance good photocurrent in DSSCs [46] leading to a better short circuit current density (J_{SC}). Chemical potential (μ) is a parameter relating to charge transfer ability of a dye in its ground state, this is enhanced by high negative value of μ (Table 2). The electrophilicity (ω) describes the stabilization energy of a dye when an electronic charge is added to the dye from the surrounding, therefore, a high ω is desirable for good energy stabilization. All the dyes exhibit very good stabilization energy; however, type B (CLTP dyes) is more stabilized than type A (PLTP dyes). The electron denoting power (ω^-) is related to the ability of the dye to donate/push electrons through the linker/spacer to the acceptor unit of a dye. So, low value of ω^- corresponds to a better ability of donating/pushing electron density towards acceptor [46, 47]. Therefore, PLTP-1, PLTP-2 and PLTP-3 of type A and CLTP-1, CLTP-2 and CLTP-3 of type B will readily push electrons to the π-linker, leading to high intramolecular charge transfer and thus high photocurrent in DSSCs [48], suggesting higher electron-donating ability of dyes with N, N-diphenylaniline donor unit.

Theoretical view of the dye's efficiency

The light harvesting efficiency (LHE) is expected to be as high as possible for the dye sensitizers to have good performance in DSSC, also to enhance the photocurrent if the excited processes have a CT character. Therefore, the LHEs of the studied dyes are calculated as [49]:

$$LHE = 1 - 10^{-A} = 1 - 10^{-f}, \tag{5}$$

where f is the oscillator strength of the excited state associated to the λ_{max} and A is the absorption coefficient.

The LHE values reveal that PLTP-2, PLTP-4 and PLTP-5 for type A dyes, and CLTP-3, CLTP-2 and CLTP-4 for type B dyes are favoured for higher photocurrent (Table 3). Also, another key parameter of molecular global descriptors of solar cells is the open circuit voltage (V_{oc}) [35]. It is well known that the larger value V_{oc} corresponds to the better performance of solar cells [50]. V_{oc} is interrelated by the difference between the LUMO energy of the dye-sensitizer and the conduction band (the LUMO) of the electron acceptor (TiO$_2$; –4.0 eV), taking into account the energy lost during the photo-charge generation [51; 52]. The V_{oc} of the studied solar cell can be estimated by Equation (6) [44]:

$$V_{OC} = E_{LUMO} - E_{CB}^{TiO_2}.$$ (6)

The calculated V_{oc} values were 1.43, 1.40, 1.42, 1.31 and 1.25 for PLTP-1 to PLTP-5; and 1.16, 1.17, 1.12, 1.09 and 0.97 for CLTP-1 to CLTP-5, respectively (Table 3). This shows that V_{oc} values for type A dyes are higher than for the corresponding type B dyes; therefore, they are expected to present higher injection driving force and power conversion efficiency than type B. This also reveals that dyes with N,N-diphenylaniline donor unit have a higher V_{oc} value than dyes with carbazole unit (N,N-diphenylaniline dyes > Carbazole dyes) in line with calculated ω^- (Table 2).

The electron injecting ability (ΔG^{inject}) of the dyes were estimated for the two dyes series of dye-sensitizers (i.e. PLTPs and CLTPs) from the oxidation potential of the excited dye (E_{ox}^{dye*}) and the redox potential of the dye-TiO$_2$ couples [47]:

$$\Delta G^{inject} = E_{ox}^{dye*} - E_{CB}^{TiO_2}.$$ (7)

However, E_{ox}^{dye*} was calculated as the difference in the ground state oxidation potential of the dye and vertical electronic transition energy (λ_{max}^{ICT}) [14].

$$E_{ox}^{dye*} = E_{ox}^{dye} - \lambda_{max}^{ICT}$$ (8)

and the driving force of the dye regeneration known as regeneration efficiency (ΔG^{regen}) was estimated using Equation 9 [15].

$$\Delta G^{regen} = E_{ox}^{dye} - E_{redox}^{electrolyte},$$ (9)

where 4.70 eV was taken as the value of $E_{redox}^{electrolyte}$ [44].

The negative values of injection driving force (ΔG^{inject}) show the ability of the dyes to inject electrons readily into TiO$_2$ surface as shown in Table 3. The ΔG^{inject} values show that PLTP-1, PLTP-3 for type A dyes, and CLTP-1, CLTP-2 and CLTP-3 for type B dyes are considered the best dyes, for they presented higher ΔG^{inject} values than PLTP-2, PLTP-4, PLTP-5, CLTP-4 and CLTP-5 (Table 3), signifying easy electrons injection into TiO$_2$. The positive values of dye regeneration drive force (ΔG^{regen}) suggest fast electrons transfer and thus ability to regenerate. However, it is necessary for ΔG^{regen} be as low as possible, making PLTP-2, CLTP-2, PLTP-1, PLTP-3 and CLTP-3 to be the candidate dyes for greater power conversion efficiency [53]. Another parameter to adjudge the suitability of a dye-sensitizer is the excitation state lifetime (τ_{esl}), a critical parameter for the charge-transport characteristics of a dye. It was predicted using Equation 10 [53; 54]:

$$\tau_{esl} = \frac{1.499}{fE^2},$$ (10)

where E is the excitation energy of different electronic states in cm^{-1}, and f is the oscillator strength corresponding to the electronic state.

The τ_{esl} values reveal that CLPT-4 (2.576 ns), CLTP-5 (2.479 ns), PLTP-2 (2.998 ns) and PLTP-1 (1.647 ns) could be more stable in the cationic state, leading to long-lived excited state, higher charge transfer efficiency and improved efficiency of the dye-sensitizers than dyes with lower τ_{esl} [54].

Table 3

Calculated driving force of electron rejection and dye regeneration, LHE, Voc and excited state lifetimes (τ)

MOL	λ_{max}^{ICT}	f	E_{ox}^{dye*}	ΔG_{inj}	ΔG_{reg}	Voc	LHE	$\tau(ns)$
PLTP-1	2.714	1.0117	2.206	−1.794	0.22	1.43	0.9026	1.932
PLTP-2	2.041	1.7299	2.779	−1.221	0.12	1.40	0.9813	2.998
PLTP-3	2.731	1.1766	2.219	−1.781	0.25	1.42	0.9334	1.647
PLTP-4	2.319	1.9851	2.851	−1.149	0.47	1.31	0.9896	1.349

MOL	λ_{max}^{ICT}	f	E_{ox}^{dye*}	ΔG_{inj}	ΔG_{reg}	Voc	LHE	$\tau(ns)$
PLTP-5	2.368	1.6574	2.962	−1.038	0.63	1.25	0.9779	1.550
CLTP-1	2.701	1.4629	2.339	−1.661	0.34	1.16	0.9655	1.350
CLTP-2	2.465	1.6913	2.445	−1.555	0.21	1.17	0.9796	1.401
CLTP-3	2.502	1.7410	2.488	−1.512	0.29	1.12	0.9818	1.322
CLTP-4	2.279	1.0761	2.991	−1.010	0.57	1.09	0.9776	2.576
CLTP-5	2.284	1.1136	3.176	−0.824	0.76	0.97	0.9230	2.479

Photo-electronic Properties

The Beer–Lambert law states that absorbance at higher level denotes higher dye application. The study of the correlation between the DSSC photocurrent and the number of dye molecules has become trendy. In view of this, larger photocurrent can be attributed to increased adsorbed dye, ensuing in the increased harvesting of incident light [55–60]. Atomic information with reference to the electronic transitions can be obtained by investigating the molecular orbitals associated with each electronic transition, as calculated at TD-DFT/6-31G(d, p) level of theory (Tables 4). Absorptions in the visible and near-ultraviolet (UV) regions of the spectrum are the most important for photo to current conversion, so only the singlet → singlet transitions of the absorption bands with the wavelength longer than 300 nm are listed in the Table 4. The maximum absorbent wavelengths (λ_{max}) with probability of electron transition (oscillating strength, f) for the type A; PLTP-1, PLTP-2, PLTP-3, PLTP-4 and PLTP-5 were 579.02 (0.7881), 600.75 (1.7299), 570.36 (1.009), 528.81 (1.951) and 517.87 nm (1.6574), respectively, all arising from H→L orbital transitions. It is interesting to note that two major electronic transitions with highest f are arisen from the H→L and H-1→L orbitals' transitions (Table 4a). The maximum absorption transitions for type A dyes decreases in the following order: PLTP-2 > PLTP-1 > PLTP-3 > PLTP-4 > PLTP-5. Furthermore, the λ_{max} with oscillating strength, f for CLTP-1, CLTP-2, CLTP-3, CLTP-4 and CLTP-5 were 609.58 (0.7484), 626.50 (1.4056), 631.16 (1.0761), 537.94 (1.6503) and 536.83 (1.1136) nm, respectively, all arising from H→L orbitals' transitions as observed for type A. Similarly, the two major electronic transitions with highest f are arisen from the H→L and H-1→L orbitals' transitions (Table 4b), and the maximum absorption transitions for type B dyes decreases as follows: CLTP-3 > CLTP-2 > CLTP-1 > CLTP-4 > CLTP-5.

To compare the effect of π-linkers of electronic transitions as it relates to intramolecular charge transfer, PLTP-2 (CLTP-2) and PLTP-3 (CLTP-3) were considered. The 4H-cyclopenta[1,2-b,5,4-b]bisthiophene π-linker was changed in PLTP-2 (CLTP-2) to bisthioeno[3,2-b,3-b]thiophene as presented in PLTP-3 (CLTP-3). There was a shift in λ_{max} to shorter wavelength (blue-shift) by 30 and 4 nm, respectively; which may be due to easier delocalization of π-electrons for 4H-cyclopenta[1,2-b,5,4-b]bisthiophene π-linker than bisthioeno[3,2-b,3-b]thiophene leading to extension of π-conjugation [48]. To adjudge the effect of donor groups on intra-crossing charge transfer as it reflected in electronic transitions, PLTP-2 (CLTP-2) and PLTP-4 (CLTP-4) were considered. Replacement of N,N-diphenyalamine in PLTP-2 (CLTP-2) with carbazole in PLTP-4 (CLTP-4) shifted the λ_{max} to shorter wavelength (blue shift) of about 72 (90) nm, indicating that N,N-diphenylaniline pushes electrons more readily towards the linker than carbazole donor which is in line with the frontier orbital interactions and Eg energy earlier observed. Generally, **type B** dyes present lower energy energies and longer λ_{max} than the corresponding **type A** dyes, which may be linked to effective delocalization of π-electrons for 2-cyanoprop-2-enoic acid acceptor bearing dyes, and so enhance longer wavelength**.**

Table 4a

Absorption peaks, oscillation strength and molecular orbital's (MOs) involved in transitions calculated for PLTPs using B3LYP/6-31G (d, p)

λ, nm	OS	MOs involved in transition
		PLTP-1
350.57	0.2312	H-1 → L+1 (63 %)
367.83	0.2710	H → L +2 (81 %)
394.99	0.1113	H-2 → L (63 %), H-1 → L+1 (20 %),
428.85	0.2152	H → L+1 (81 %)
451.85	1.0117	H-1 → L (86 %)
579.02	0.7861	H → L (96 %)

λ, nm	OS	MOs involved in transition
		PLTP-2
378.42	0.0970	H-1 → L+1 (54 %), H-2 → L (20 %)
392.12	0.0840	H → L+2 (66 %), H-3 → L (22 %)
409.36	0.0486	H-2 → L (49 %), H-1 → L+1 (35 %).
457.61	0.4318	H → L+1 (81 %)
486.49	1.2276	H-1 → L (89 %)
600.75	1.7299	H → L (97 %)
		PLTP-3
350.13	0.2415	H-1 → L+1 (66 %)
367.00	0.1481	H → L+2 (83 %)
394.57	0.0732	H-2 → L (64 %), H-1 → L+1 (18 %).
427.09	0.1730	H → L+1 (81 %)
449.08	1.1766	H-1 → L (88 %)
570.36	1.0098	H → L (98 %)
		PLTP-4
369.57	0.0049	H → L+2 (65 %), H-4 → L (29 %)
388.72	0.2378	H-3 → L (42 %), H → L+1 (26 %), H-1 →L+1 (17 %).
428.53	0.3541	H → L+1 (58 %), H-3 → L (38 %).
450.32	0.3635	H-1 → L (94 %)
528.81	1.9851	H→ L (94 %).
PLTP-5		
366.12	0.0335	H-4 → L (85 %)
389.08	0.2185	H-3 → L (36 %), H → L+1 (28 %), H-1 → L+1 (23 %)
419.26	0.2816	H → L+1 (53 %), H-3 → L (42 %)
444.03	0.5918	H-1 → L (95 %)
517.87	1.6574	H → L (96 %)

**Absorption peaks, oscillation strength and molecular orbital's (MOs)
involved in transition calculated for CLTPs using B3LYP/6-31G (d, p)**

λ, nm	OS	MOs involved in transition
		CLTP-1
326.99	0.0694	H → L+4 (40 %), H-4 → L (18 %), H → L+3 (16 %)
339.04	0.0680	H → L+2 (45 %), H → L+3 (36 %).
361.61	0.2603	H-1 → L+1 (55 %), H-2 → L (32 %)
412.25	0.2996	H → L+1 (77 %)
454.06	1.4629	H-1 → L (83 %)
609.58	0.7484	H → L (97 %)
		CLTP-2
356.84	0.0086	H → L+2 (50 %), H-3 → L (20 %), H-1 → L+1 (14 %)
357.91	0.0060	H-2 → L (40 %), H → L+2 (29 %)
395.70	0.1449	H-1 → L+1 (63 %), H-2 → L (22 %)
449.92	0.5089	H → L+1 (77 %), H-2 → L (18 %)
497.36	1.6913	H-1 → L (86 %)
627.50	1.4056	H → L (94 %)
CLTP-3		
353.83	0.0073	H-2→ L (31 %), H-1 → L+1 (22 %), H → L+2 (13 %)
384.95	0.0672	H-3 → L (69 %), H-1 → L+1 (26 %)
390.88	0.2129	H-2→ L (40 %), H-1 → L+1 (30 %), H-3 → L (19 %)
442.01	0.6049	H → L+1 (79 %)
490.18	1.7410	H-1 → L (88 %)
631.16	1.0761	H → L (97 %)

λ, nm	OS	MOs involved in transition
		CLTP-4
367.84	0.0226	H-1 → L+1 (81 %).
415.32	0.4898	H → L+1 (69 %), H-3 → L (28 %)
461.19	0.9159	H-1 → L (86 %)
537.94	1.6503	H → L (86 %)
		CLTP-5
370.99	0.1496	H-1 → L+1 (74 %)
382.82	0.0147	H-4 → L (68 %), H-3 → L (27 %).
405.72	0.6982	H → L+1 (72 %), H-3 → L (21 %).
462.95	1.1122	H-1 → L (88 %)
536.83	1.1136	H → L (89 %)

Conclusions

This paper reports a comprehensive computational investigations on the efficiency of the 2-cyano-2-pyran-4-ylidene-acetic acid and the 2-cyanoprop-2-enoic acid units as acceptor units connected through the thiophene-based π-linker dyes for the improvement of dye-sensitizers for DSSCs using the DFT(B3LYP/6-31G(d, p) method. The results revealed the following:

(1) Dyes with 4*H*-cyclopenta[1,2-b,5,4-b]bis-thiophene as a π-linker exhibit narrower band gap, and the longer absorption wavelength than others dyes in each dye series, indicating better intra-molecular charge transfer;

(2) Dyes with N,N-diphenyalamine as a donor unit presents lower band gaps, better the open circuit current (V_{oc}) and longer λ_{max} wavelength than dyes with the carbazole donor unit, indicating that N,N-diphenylaniline pushes electrons readily towards the π-linker than the carbazole donor; thus represents the better donor group;

(3) **Type B** dyes present lower band gaps and longer λ_{max} wavelength than the corresponding **type A** dyes, indicating effective delocalization of π-electrons in dyes with the 2-cyanoprop-2-enoic acid acceptor anchoring unit. This leads to better intra-molecular charge transfer, enhanced longer wavelength, higher V_{oc} value and injection force**.**

References

1   Park, SH, Leclerc, M, Heeger AJ & Lee K (2006). High Efficiency Polymer Solar Cells with Internal Quantum Efficiency Approaching 100 %. *Proc SPIE,* 74160. https://doi.org/10.1117/12.825836

2   Kammen, D.M. (2006). The rise of renewable energy. *Sci Am., 295*, 84–93. https://doi.org/10.1038/scientificamerican0906-84

3   Chiba, Y., Islam, A., Watanabe, Y., Komiya, R., Koide, N. & Han L (2006). Dye-Sensitized Solar Cells with Conversion Efficiency of 11.1 %. *Japanese J Appl Phys L 638*–L640. https://doi.org/10.1143/JJAP.45.L638

4   Regan, B.O. & Grätzel, M., (1991) A low-cost, high-efficiency solar cell based on dye-sensitized colloidal TiO₂ films. *Nature 353*, 737–740. https://doi.org/10.1038/353737a0

5   Yella, A, Lee, H.W., Tsao, H.N., Yi, C., Chandiran, A.K., Nazeeruddin, M.K., Diau,.W., Yeh, C.Y., Zakeeruddin, S.M. & Grätzel, M. (2011). Porphyrin sensitized solar cells with cobalt(II/III)-based redox electrolyte exceed 12 percent efficiency. *Science 334*, 629–634. https://doi.org/10.1126/science.1209688

6   Hagfeldt, H., Boschloo, G., Sun, L., Kloo, L. & Pettersson, H. (2010). Dye-sensitized solar cells. *Chem Rev 110*, 6595–6663. https://doi.org/10.1021/cr900356p

7   Qian, X., Gao, H-H, Zhu, Y-Z, Pan, B. & Zheng, J-Y, (2015). Tetraindole-based saddle-shaped organic dyes for efficient dye-sensitized solar cells. *Dyes Pigments. 121*, 152–158. https://doi.org/10.1016/j.dyepig.2015.05.015

8   Jia, J., Chen, Y., Duan, L., Sun, Z., Liang, M. & Xue S. (2017). New D–π–A dyes incorporating dithieno[3,2-b:2′,3′-d]pyrrole (DTP)-based π-spacers for efficient dye-sensitized solar cells. *RSC Adv. 7*, 45807–45817. https://doi.org/10.1039/C7RA08965A

9   Semire, B., Odunola, O.A., Adejoro, I.A. (2012). Structural and electronic properties of 4H-Cyclopenta [2, 1-b, 3; 4-b'] dithiophene S-oxide (BTO) With S, S= O, O, SiH₂ and BH₂ bridge: semi-empirical and DFT study. *J mol Model 18*, 2755–2760. https://doi.org/10.1007/s00894-011-1291-1

10 Zhang, C.R. Liu, L., Zhe, J.W., Jin, N.Z., Ma, Y., Yuan, L.H., Zhang, M.L., Wu, Y.Z., Liu, Z.J. & Chen, H.S. (2013). The Role of the Conjugate Bridge in Electronic Structures and Related Properties of Tetrahydroquinoline for Dye Sensitized Solar Cells. *Int J Mol Sci 14*, 5461-5481. https://doi.org/10.3390/ijms14035461

11 Ahn, H.J., Thogiti, S., Cho, J.M., Jang, B.Y. & Kim, J.H. (2015). Comparison of triphenylamine based single and double branched organic dyes in dye-sensitized solar cells. *Electronic Mater Lett 11*, 822–827. https://doi.org/10.1007/s13391-015-4501-7

12 Dindorkar, S.S. & Yadav, A., (2022). Insights from Density Functional Theory on the Feasibility of Modified Reactive Dyes as Dye Sensitizers in Dye-Sensitized Solar Cell Applications. *Solar 2*, 12–31. https://doi.org/10.3390/solar2010002

13 Roohi, H. & Mohtamadifar, N. (2022). The role of the donor group and electron-accepting substitutions inserted in π-linkers in tuning the optoelectronic properties of D–π–A dye-sensitized solar cells: a DFT/TDDFT study. *RSC Adv.*, *121*, 1557–11573. https://doi.org/10.1039/D2RA00906D

14 Hagberg, D., Marinado, T., Karlsson, K., Nonomura, K., Qin, P. & Boschloo, G. (2007). Tuning the HOMO and LUMO energy levels of organic chromophores for dye sensitized solar cells. *J Org Chem. 72*, 9550-9556. https://doi.org/10.1021/jo701592x

15 Marszalek, M., Nagane, S., Ichake, A., Baker, R., Paul, V. & Zakeeruddin, S. (2012). Tuning spectral properties of phenothiazine based donor-π-acceptor dyes for efficient dye-sensitized solar cells. *J Mater Chem 22*, 889-894. https://doi.org/10.1039/C1JM14024H

16 Tan, L., Huang, J., Shen, Y., Xiao, L., Liu, J. & Kuang D. (2014). Highly efficient and stable organic sensitizers with duplex starburst triphenylamine and carbazole donors for liquid and quasi-solid-state dye-sensitized solar cells. *J Mater Chem A 2*, 8988-8994. https://doi.org/10.1039/C4TA01351D

17 Cheng, Y.J., Yang, S.H., Hsu, C.S. (2009). Synthesis of conjugated polymers for organic solar cell applications. *Chem Rev 109*, 5868–5923. https://doi.org/10.1021/cr900182s

18 Wang, X., Bolag, A., Yun, W., Zhang, X., Bao, T., Ning, J., Alata, H. & Ojiyed, T. (2020). Synthesis, Characterization and Dye-Sensitized Solar Cell Application of a Novel Symmetric Diphenylpyran Dye with Dual Rhodamine-3-acetic Acid Anchors. *J Phys: Conf Series 1549,* 032072. https://doi.org/10.1088/1742-6596/1549/3/032072

19 Semire, B., Oyebamiji, A. & Odunola, O.A. (2016). Design of (2Z)-2-cyano-2-[2-[(E)-2-[5-[(E)-2-(4-dimethylamino-phenyl)vinyl]-2-thienyl]vinyl]pyran-4-ylidene]acetic acid derivatives as D-π-A dye sensitizers in molecular photovoltaics: a density functional theory approach. *Res Chem Intermed 42*, 4605-4619. https://doi.org/10.1007/s11164-015-2303-z

20 Semire, B., Oyebamiji, A.K. & Odunola, O.A. (2020). Electronic properties' modulation of D–A–A via fluorination of 2-cyano-2-pyran-4-ylidene-acetic acid acceptor unit for efficient DSSCs: DFT-TDDFT approach. *Scientific African 7*, e00287. https://doi.org/10.1016/j.sciaf.2020.e00287

21 Joo, H.K. & Hoosung, L. (2002). Synthesis, electrochemistry, and electroluminescence of novel red-emitting poly(p-phenylenevinylene) derivative with 2-pyran-4-ylidenemalononitrile obtained by the heck reaction. *Chem Mater 14*, 2270–2275. https://doi.org/10.1021/cm011553r

22 Peng, Q., Lu, Z.Y., Huang, Y., Xie, M.G., Han, S.H., Peng, J.B. & Cao, Y. (2004). Synthesis and characterization of new red-emitting polyfluorene derivatives containing electron-deficient 2-pyran-4-ylidene- malononitrile moieties, *Macromolecules 37*, 260–266. https://doi.org/10.1021/ma0355397

23 Cui, Y., Jiancan, Y., Gao, J., Wang, Z. & Qian, G. (2009). Synthesis and luminescence behavior of inorganic–organic hybrid materials covalently bound with pyran-containing dyes. *Sci Technol 52*, 362–369. https://doi.org/10.1007/s10971-009-2037-8

24 Xue, J., Gu, X., Yang, Z., Xu, B. & Tian W. (2009). Efficient bulk hetero-junction solar cells based on a symmetrical D-pi-A-pi-D organic dye molecule. *J Phys Chem C 113*, 12911– 12917. https://doi.org/10.1021/jp902976w

25 Son, Y.A., Gwon, S.Y., Lee, S.Y. & Kim, S.H. (2010). Synthesis and property of solvatochromic fluorophore based on D-pi-A molecular system: 2-{[3-Cyano-4-(N-ethyl-N-(2-hydroxyethyl)amino)styryl]-5,5-dimethylfuran 2(5H)lidene}malononitrile dye. *Spectrochim Acta, A: Mol Biomol Spectrosc 75*, 225–229. https://doi.org/10.1016/j.saa.2009.10.015

26 Megala, M. & Rajkumar, B.J. (2018). Molecular design of vinyl-functionalized quercetin dyes with different acceptors for dye-sensitized solar cells: theoretical investigation. J Comput Electro *17*, 1153–1166. https://doi.org/10.1007/s10825-018-1195-8

27 Wang, H., Liu, Q., Liu, D., Su, R., Liu, J. & Li, Y. (2018). Computational Prediction of Electronic and Photovoltaic Properties of Anthracene-Based Organic Dyes for Dye-Sensitized Solar Cells. *Int J Photoenergy 17*, 4764830, https://doi.org/10.1155/2018/4764830

28 Pounraj, P., Mohankumar, V., Senthil Pandian, M. & Ramasamy, P. (2019). Donor substituted triphenylamine based sensitizers for dye sensitized solar cells (DSSC) application — DFT and TD-DFT approach. *AIP Conf Proc 2115*, 030345. https://doi.org/10.1063/1.5113184

29 Prabu, K.M., Agalya, P., Akila, K. & Suresh, S. (2019). Non-linear optical properties of carbazole based dyes modified with diverse spacer units for dye-sensitized solar cells: A first principle study. *AIP Conf Proc 2177*, 020072. https://doi.org/10.1063/1.5135247

30 Bonomo, M., Carella, A., Borbone, F., Rosato, L., Dini, D. & Gontrani, L. (2020). New pyran-based molecules as both n- and p-type sensitizers in semi-transparent Dye Sensitized Solar Cells, *Dyes and Pigments*. *175*, 108140. https://doi.org/10.1016/j.dyepig.2019.108140

31 Lin, C., Liu, Y., Shao, D., Wang, W., Xu, H., Shao, C., Zhang, W. & Yang, Z. (2012). Density functional theory design of double donor dyes and electron transfer on dye/TiO2(101) composite systems for dye-sensitized solar cells. *RSC Adv 11*, 3071-3078. https://doi.org/10.1039/D0RA08815C

32 Pastore, M., Mosconi, E., de Angelis, F. & Gratzel, M. (2010). A computational investigation of organic dyes for dye-sensitized solar cells: Benchmark, strategies, and open issues. *J Phys Chem C 114*, 7205–7212. https://doi.org/10.1021/jp100713r

33 Estrella, L.L., Balanay, M.P. & Kim, D.H. (2016). The effect of donor group rigidification on the electronic and optical properties of arylamine-based metal-free dyes for dye-sensitized solar cells: a computational study. *J Phys Chem A*, 120, 5917-5927. https://doi.org/10.1021/acs.jpca.6b03271

34 Becke, A.D. (1993). Density functional thermo-chemistry. III. The role of exact exchange. *Journal of Physical Chemistry, 98*, 5648–5652. https://doi.org/10.1063/1.464913

35 Lee, C., Yang, W. & Parr, P.G. (1988). Development of the colle-salvetti correlation-energy formula into a functional of the electron density. *Phys Rev B 37*,785-789. https://doi.org/10.1103/PhysRevB.37.785

36 Spartan '14 wavefunction Inc. Irvine, USA (2014).

37 Delgado-Montiel, T., Baldenebro-López, J., Soto-Rojo, R. & Glossman-Mitnik D. (2020). Theoretical Study of the Effect of π-Bridge on Optical and Electronic Properties of Carbazole-Based Sensitizers for DSSCs. *Molecules 25*, 3670. https://doi.org/10.3390/molecules25163670

38 El-Shishtawy, R.M., Elroby, S.A., Asiri, A.M. & Müllen, K. (2016). Optical Absorption Spectra and Electronic Properties of Symmetric and Asymmetric Squaraine Dyes for Use in DSSC Solar Cells: DFT and TD-DFT Studies. *Int J Mol Sci 17*, 487. https://doi.org/10.3390/ijms17040487

39 Wazzan, N.A. (2019). A DFT/TDDFT investigation on the efciency of novel dyes with ortho‑fuorophenyl units (A1) and incorporating bnzotriazole/benzothiadiazole /phthalimide units (A2) as organic photosensitizers with D–A2–π–A1 configuration for solar cell applications. *J Comput Electron 8*, 375-395. https://doi.org/10.1007/s10825-019-01308-4

40 Lu, X., Wei, S., Wu, C. -M.L., Li, S. & Guo, W. (2011). Can Polypyridyl Cu(I)-based Complexes Provide Promising Sensitizers for Dye-Sensitized Solar Cells? A Theoretical Insight into Cu(I) versus Ru(II) Sensitizers. *J Phys Chem C 115*, 3753–3761. https://doi.org/10.1021/jp111325y

41 Soto-Rojo, R., Baldenebro-Lopez, J. & Glossman-Mitnik, D. (2015). Study of chemical reactivity in relation to experimental parameters of efficiency in coumarin derivatives for dye sensitized solar cells using DFT. *Phys Chem Chem Phys 17*, 14122-14129. https://doi.org/10.1039/C5CP01387A

42 Zhang, M-D, Xie, H-X, Ju, X-H, Qin, L., Yang, Q-X, Zheng, H-G & Zhou, X-F (2013). D-D-π-A organic dyes containing 4,4′-di(2-thienyl)triphenylamine moiety for efficient dye-sensitized solar cells. *Phys Chem Chem Phys, 15*, 634–641. https://doi.org/10.1039/C2CP42993D

43 Parr, R.G., Szentpaly, L. & Liu, S. (1999). Electrophilicity Index. *Journal of American. Chemistry. Society 121*, 1922-1924. https://doi.org/10.1021/cr040109f

44 Afolabi, S.O., Semire, B., Akiode, O.K. & Idowu, M.A. (2022). Quantum study on the optoelectronic properties and chemical reactivity of phenoxazine-based organic photosensitizer for solar cell purposes. *Theo Chem Acc 141*, 22. https://doi.org/10.1007/s00214-022-02882-w

45 Koopmans, T. (1934). Ordering of Wave Functions and Eigenenergies to the Individual Electrons of an Atom. *Physica*, *1*, 104-113. https://doi.org/10.1016/S0031-8914(34)90011-2

46 Afolabi, S.O., Semire, B., Akiode, O.K., Afolabi, T.A., Adebayo, G.A. & Idowu, M.A. (2020). Design and theoretical study of phenothiazine-based low bandgap dye derivatives as sensitizers in molecular photovoltaics. *Opt Quant Electronics 52*, 476. https://doi.org/10.1007/s11082-020-02600-5

47 Afolabi, S.O., Semire, B. & Idowu, M.A. (2021). Electronic and optical properties' tuning of phenoxazine-based D-A2-π-A1 organic dyes for dye-sensitized solar cells. DFT/TDDFT investigations. *Heliyon, 7*, e06827. https://doi.org/10.1016/j.heliyon.2021.e06827

48 Semire, B., Oyebamiji, A.K. & Odunola, O.A. (2017). Tailoring of energy levels in (2Z)-2-cyano-2-[2-[(E)-2-[2-[(E)-2-(p-tolyl)vinyl]thieno[3,2-b]thiophen-5-yl]vinyl]pyran-4-ylidene]acetic acid derivatives via conjugate bridge and fluorination of acceptor units for effective D–π–A dye-sensitized solar cells: DFT–TDDFT approach. *Res Chem Intermed 43*, 1863–1879. https://doi.org/10.1007/s11164-016-2735-0

49 Preat, J., Michaux, C., Jacquemin, D. & Perpete, E.A. (2009). Enhanced Efficiency of Organic Dye-Sensitized Solar Cells: Triphenylamine Derivatives. *J Phys Chem C 113*, 16821-16833. https://doi.org/10.1021/jp904946a

50 Rand, B.P., Genoe, J., Heremans, P., Poortmans, J. (2007). Solar cells utilizing small molecular weight organic semiconductors. *Progress in Photovoltaics: Res Appl 15*, 659-676. https://doi.org/10.1002/pip.788

51 Chou, C.T., Lin, C.H., Wu, M.H., Cheng, T.W., Lee, J.H., Liu, C.H., Tai, Y., Chattopadhyay, S., Wang, J.K., Chen, K.H., Chen, L.C. (2011). Tuning open-circuit voltage in organic solar cells by magnesium modified Alq(3). *J Appl Phys, 110*, 83104-831045. https://doi.org/10.1063/1.3653259

52 Zgou, H., Boussaidi, S., Eddiouane, A., Chaib, H., Tripathi, R.P., Ben, Hadda, T., Bouachrine, M. & Hamidi, M. (2016). New low band-gap conjugated organic materials based on fluorene, thiophene and phenylene for photovoltaic applications: Theoretical study. *Mates Today: Proc 3*(7), 2578-2586. https://doi.org/10.1016/j.matpr.2016.04.005

53 Ren, P., Sun, C., Shi, Y., Song, P., Yang, Y., Li, Y. (2019). Global performance evaluation of solar cells using two models: from charge-transfer and recombination mechanisms to photoelectric properties. *J Mater Chem* C 7, 1934–1947. https://doi.org/10.1039/C8TC05660A

54 Kacimi, R., Raftani, M., Abram, T., Azaid, A., Ziyat, H., Bejjit, L., Bennani, M.N., Bouachrine M. (2021). Theoretical design of D-π-A system new dyes candidate for DSSC application. *Heliyon. 7*, e07171: https://doi.org/10.1016/j.heliyon.2021.e07171

55 Wang, H., Wang, B., Yu, J., Hu, Y., Xia, C., Zhang, J. & Liu, R. (2015). Significant enhancement of power conversion efficiency for dye sensitized solar cell using 1D/3D network nanostructures as photoanodes. *Scientific Reports 5*, 305. https://doi.org/10.1038/srep09305

56 Minaev, B.F., Baryshnikov, G.V. & Minaeva, V.A. (2012). Electronic structure and spectral properties of the triarylamine-dithienosilole dyes for efficient organic solar cells. *Dyes and Pigments*, *92*(1), 531-536. https://doi.org/10.1016/j.dyepig.2011.06.012

57 Baryshnikov, G.V., Minaev, B.F., Myshenko, E.V. & Minaeva, V.A. (2013). Structure and electronic absorption spectra of isotruxene dyes for dye-sensitized solar cells: investigation by the DFT, TDDFT, and QTAIM methods. *Optics and spectroscopy, 115*, 484-490. https://doi.org/10.1134/S0030400X13100020

58 Oprea, C.I., Frecuş, B., Minaev, B.F. & Gîrţu, M.A. (2011). DFT study of electronic structure and optical properties of some Ru-and Rh-based complexes for dye-sensitized solar cells. *Molecular Physics, 109* (21), 2511-2523. https://doi.org/10.1080/00268976.2011.621454

59 Minaev, B.F., Khomenko, E.M. & Yashchuk, L.B. (2009). Modeling the structure and spectral properties of sensitizing black dye for nanocrystalline TiO$_2$ solar cells. *Journal of Applied Spectroscopy*, *76* (6), 772-776. https://doi.org/10.1007/s10812-010-9264-1

60 Minaev, B., Li, X., Ning, Z., Tian, H. & Ågren, H. (2011). Organometallic materials for electroluminescent and photovoltaic devices. *Organic Light Emitting Diode—Material, Process and Devices, In Tech, Rieka*, 61-100. https://doi.org/10.5772/21145

Information about authors*

Obiyenwa, Gabriel Kehinde — PhD, Assistant Professor, Department of Chemistry, Federal University, P.M.B 1154, Lokoja, Kogi State, Nigeria; e-mail: gabriel.obiyenwa@fulokoja.edu.ng; https://orcid.org/0000-0003-0184-8807

Semire, Banjo (*corresponding author*) — PhD, Professor, Candidate of Computational Chemistry Laboratory, Department of Pure and Applied Chemistry, Ladoke Akintola University of Technology, PMB 4000, Ogbomoso, Nigeria; e-mail: bsemire@lautech.edu.ng; https://orcid.org/0000-0002-4173-9165

Oyebamiji, Abel Kolawole — PhD, Assistant Professor, Industrial Chemistry Programme, Bowen University, PMB 284, Iwo, Osun State, Nigeria; e-mail: abel.oyebamiji@bowen.edu.ng; https://orcid.org/0000-0002-8932-6327

Abdulsalami, Ibrahim Olasegun — PhD, Senior Lecturer, Department of Chemistry, Nigerian Army University, PMB 1500, Biu, Bornu State, Nigeria; e-mail: aiboldkip@gmail.com; https://orcid.org/0000-0001-5154-6407

Latona, Dayo Felix — PhD, Associate Professor, Department of Pure and Applied Chemistry, Osun State University, 210001, Osogbo, Nigeria; e-mail: dayo.latona@uniosun.edu.ng; https://orcid.org/0000-0002-2722-6734

Adeoye, Moriam Dasola — PhD, Professor, Department of Chemistry, Fountain University, Osogbo, P.M.B. 4491, Osun State, Nigeria; e-mail: dasoladeoye@yahoo.com; https://orcid.org/0000-0002-1274-9452

Odunola, Olusegun Ayobami — PhD, Professor, Department of Chemistry, Faculty of Natural and Applied sciences, Hallmark University, 122101, Ijebu-Itele, Ogun state, Nigeria; e-mail: oaodunola@lautech.edu.ng; https://orcid.org/0000-0001-6385-1257

_____
*The author's name is presented in the order: *Last Name, First and Middle Names*

Article

UDC 541.65/.654+535.372

https://doi.org/10.31489/2959-0663/3-23-8

Dmitry A. Sunchugashev[*] iD, Victor N. Cherepanov iD

National Research Tomsk State University, Tomsk, Russia
(*Corresponding author's e-mail: dsunchugashev@gmail.com)

Vibronic Emission Spectra of Dithiophene and Terthiophene and Their Complexes with H_2S and $(H_2S)_2$

In this work, the vibronic emission spectra of dithiophene (T2) and terthiophene (T3) molecules and their complexes with hydrogen sulfide and its dimmer were calculated at the TD-DFT / CAM-B3LYP / 6-31G(d) theory level. The solvent was taken into account within the PCM model. Vibronic spectra were calculated considering both the Herzberg-Teller and Duschinsky effects. Good agreement between the computed and experimental spectra was obtained. The vibration promoting modes forming vibronic progressions were found. Vibronic bands for bithiophene and terthiophene were formed by their low-frequency modes (≤ 370 cm^{-1}), combinations of low-frequency modes with high-frequency modes (1497 and 1672 cm^{-1} for T2 and 1516 and 1573 cm^{-1} for T3), and with their composite high-frequency modes. The intensities of vibronic lines for the emission spectra of T2···H2S, T3···H2S and T2···(H2S)2, T3···(H2S)2 complexes were shown to decrease 3.7, 2.6 and 5.5, 3.6 times compared to T2 and T3, respectively. The bathochromic shifts of the vibronic bands of dithiophene and terthiophene complexes with H2S and (H2S)2 did not exceed 130 cm^{-1} for all bands.

Keywords: oligothiophenes, hydrogen sulfide, vibronic spectra, emission, complexes, vibration modes, Herzberg-Teller effect, Duschinsky effect.

Introduction

At present, many conjugated organic molecules are being actively studied for their use as light-emitting diodes [1–2]. Molecules based on polythiophenes and their derivatives are promising for implementation in organic electronics devices. This is due to their efficient charge transfer, low cost, high chemical stability [3–4], and compatibility with a flexible substrate in a technological process at a low operating voltage [5]. Shorter structures of such compounds, in particular oligothiophene molecules, are also promising as materials for organic electronics [6–7]. The possibility of modifying oligothiophene structures with different functional groups makes it possible to improve their chemical and radiation properties [8–9]. For example, the photoluminescence quantum yield for a dioctylphenyl-substituted polythiophene derivative is 24 % [10]. The photoluminescence efficiency of materials based on oxygen-containing benzothiophene is 21 %, and the electroluminescence brightness is 10500 cd/m^2 [11]. Recently, the thiazole-centered oligothiophene donor has provided the efficiency of 15.4 % [12]. In addition, such compounds in the crystal packing are prone to formation of intermolecular bonds [5]. It should be noted that thiophenes can be extracted from medium sulfur oil refining products [13]. Other reactions are also possible during this treatment, such as thermal cleavage of hydrocarbons to lighter hydrocarbons, complete sulfurization of some products to carbon disulfide, secondary reaction of some products with sulfur or hydrogen sulfide, leading to the formation of high sulfur content resin.

It is well-known that oligothiophenes have a pronounced vibronic structure of the emission spectra and a weak vibronic structure of the absorption spectra [14]. To interpret the spectral bands, it is necessary to determine the promoting vibration modes that form these vibronic spectra. Note that the quantum-chemical calculations of vibronic spectra for oligothiophenes were carried out in [15-17] using the FCclasses [18] and MidasCpp [19] codes. However, an analysis of promoting vibration modes is missing in this works. In the present work, such an analysis was performed on the example of oligothiophene compounds with 2 (dithiophene) and 3 (terthiophene) thiophene fragments. The influence of H2S and (H2S)2 on vibronic spectra of dithiophene and terthiophene complexes with these molecules, which can be formed during the technological processes, were also studied.

Computational Details

The equilibrium geometries of bithiophene and terthiophene molecules and their complexes with hydrogen sulfide molecules were optimized at the DFT level for the singlet state S_0 and at the TD-DFT level for the first excited state S_1 using the hybrid exchange-correlation functional CAM-B3LYP [23] with the basis set 6-31G(d) [24]. The choice of the method is due to its effectiveness for application to such compounds [15, 18]. The solvent (ethanol) used in the experiment [14] was taken into account within the PCM to compare the computational and experimental results. In this study, all vibronic spectra of the considered compounds were calculated using the Gaussian code [20] taking into account the Herzberg-Teller [21] and Duschinsky [22] effects.

Results and Discussion

Molecule structures. For all found equilibrium structures of molecules studied in the work, the calculated vibration frequencies turned out to be positive. It should be noted that the obtained equilibrium geometries of dithiophene (T2) and terthiophene (T3) molecules both in the ground and excited electronic states agree well with the results of [15-16]. Analysis shows that these compounds have a non-planar structure in the ground electronic state. The torsion angles calculated between the monomeric thiophene rings are 20º (the experimental value is 21º [25]). As a result, the conjugations between these fragments are disrupted. At the same time, oligothiophene molecules are practically planar in the excited electronic state.

The structures of the complexes for their ground electronic states formed from T2 and T3 molecules and H₂S and (H₂S)₂ are shown in Figure 1. The coordinates of atoms, bond lengths and angles of T2···H₂S, T2···(H₂S)₂, T3···H₂S, T3···(H₂S)₂ are given in Supplementary Materials. The calculations showed that for these complexes the bond lengths change by less than 0.016 Å and the angles change by less than 0.41º compared to the free T2 and T3 molecules. For excited states, the structures of these complexes also change very slightly (for bond lengths < 0.018 Å, and for angles < 0.65º). Thus, dithiophene and terthiophene molecules forming complexes with H₂S and (H₂S)₂ retain practically their non-planar structures in the ground electronic state and planar structures in the first excited states.
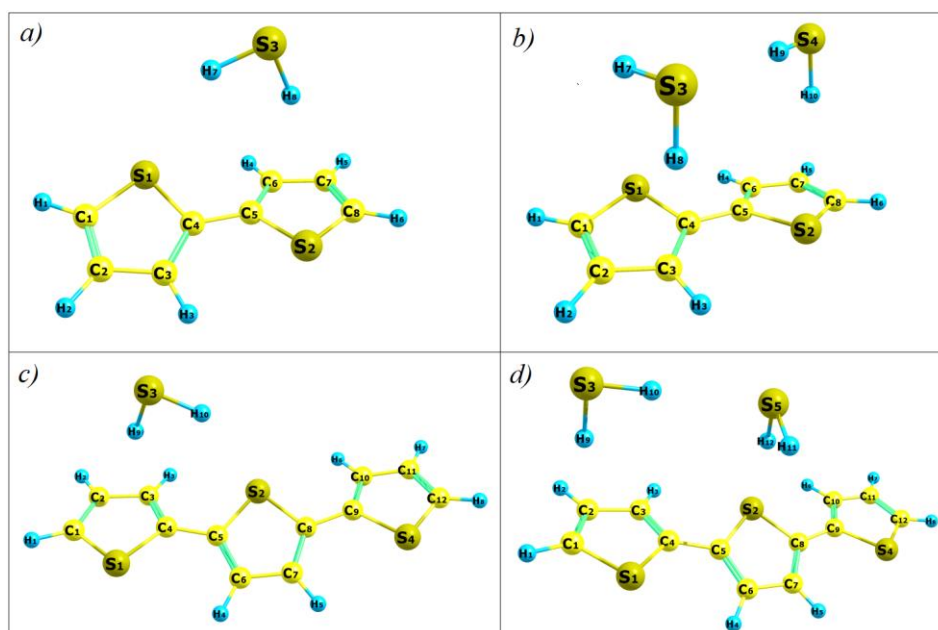
a — T2···H₂S; *b* — T2···(H₂S)₂; *c* — T3···H₂S; *d* — T3···(H₂S)₂

Figure 1. The equilibrium geometries optimized for the ground electronic states of the complexes

Vibronic spectra. The calculation results of vibronic spectra for bithiophene and terthiophene molecules and their complexes with H₂S and (H₂S)₂ in comparison with experimental spectra are shown in Figure 2 and Table. A half-width of ~ 600 cm⁻¹ estimated from the experimental spectra [14] was used to simulate the vibronic spectra.
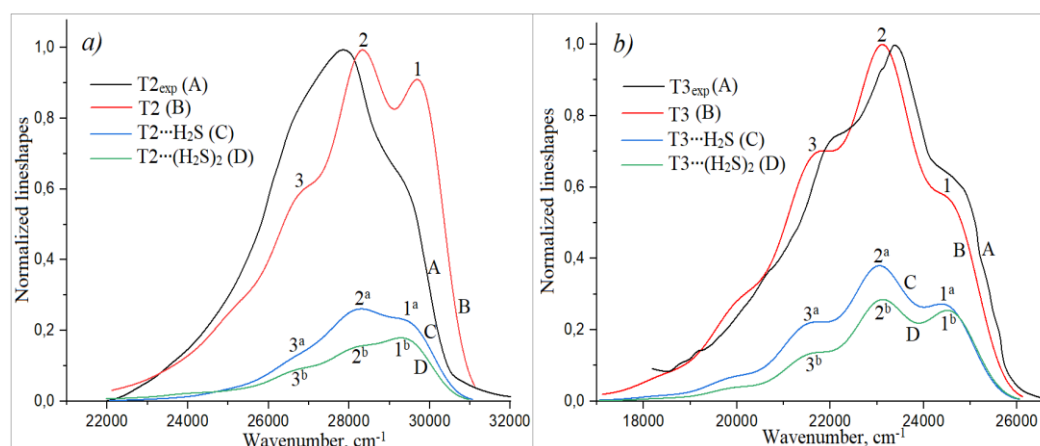
a — T2, T2···H$_2$S, T2···(H$_2$S)$_2$; b — T3, T3···H$_2$S, T3···(H$_2$S)$_2$

Figure 2. Experimental (A) (Reprinted with permission from [14]. Copyright 1996 American Chemical Society) and calculated (B, C, D) vibronic emission spectra at room temperature

T a b l e

Parameters (harmonic frequencies $\omega_i+\omega_j+\cdots$, square of the dipole moment of transitions μ^2) for vibronic spectra of bithiophene, terthiophene and their complexes with H$_2$S and (H$_2$S)$_2$

Peak number	$\omega_i + \cdots + \omega_j$ cm^{-1}	μ^2, a.u.	$\omega_i + \cdots + \omega_j$ cm^{-1}	μ^2, a.u	$\omega_i + \cdots + \omega_j$ cm^{-1}	μ^2, a.u
	T2		T2···H$_2$S		T2···(H$_2$S)$_2$	
1	87+66	$0.54 \cdot 10^{-3}$	62+21	$0.24 \cdot 10^{-2}$	54+16	$0.11 \cdot 10^{-3}$
	290+66	$0.65 \cdot 10^{-2}$	75+62+21	$0.49 \cdot 10^{-2}$	69+16	$0.13 \cdot 10^{-3}$
	370+87+66	$0.24 \cdot 10^{-3}$	291+75+62+21	$0.18 \cdot 10^{-3}$	69+54+16	$0.18 \cdot 10^{-3}$
2	1497+66	$0.14 \cdot 10^{-1}$	1495+62+21	$0.10 \cdot 10^{-3}$	1494+69+16	$0.70 \cdot 10^{-4}$
	1672+66	$0.16 \cdot 10^{-1}$	1670+62+21	$0.13 \cdot 10^{-3}$	1670+69+16	$0.67 \cdot 10^{-4}$
	1497+290+66	$0.27 \cdot 10^{-2}$	1670+75+62+21	$0.23 \cdot 10^{-3}$	1494+69+54+16	$0.82 \cdot 10^{-4}$
	1497+370+66	$0.14 \cdot 10^{-2}$	1495+75+62+21	$0.17 \cdot 10^{-3}$	1670+69+54+16	$0.83 \cdot 10^{-4}$
	1672+370+66	$0.12 \cdot 10^{-2}$	1670+291+75+62+21	$0.96 \cdot 10^{-4}$	1670+69+54+32+16	$0.36 \cdot 10^{-4}$
			1495+291+75+62+21	$0.81 \cdot 10^{-4}$	1494+69+54+32+16	$0.41 \cdot 10^{-4}$
3	1672+1497 +66	$0.22 \cdot 10^{-2}$	1670+1105+75+62+21	$0.59 \cdot 10^{-4}$	1670+1494+69+32+16	$0.14 \cdot 10^{-4}$
	1672+1497+370+66	$0.14 \cdot 10^{-2}$	1670+1495+75+62+21	$0.91 \cdot 10^{-4}$	1670+1494+69+54+16	$0.11 \cdot 10^{-4}$
	T3		T3···H$_2$S		T3···(H$_2$S)$_2$	
1	71+53	$0.28 \cdot 10^{-3}$	204+70+51+20	$0.16 \cdot 10^{-4}$	57+52+19+10	$0.86 \cdot 10^{-5}$
	174+53	$0.16 \cdot 10^{-3}$	204+70+51+35	$0.12 \cdot 10^{-4}$	57+52+29+10	$0.12 \cdot 10^{-4}$
	174+70+53	$0.22 \cdot 10^{-3}$	204+70+51+35+20	$0.25 \cdot 10^{-4}$	57+52+29+19+10	$0.11 \cdot 10^{-4}$
2	1516+53	$0.11 \cdot 10^{-4}$	1517+70+51+20	$0.13 \cdot 10^{-4}$	1513+57+52+29+10	$0.11 \cdot 10^{-5}$
	1573+53	$0.84 \cdot 10^{-4}$	1572+70+51+20	$0.14 \cdot 10^{-4}$	1571+57+52+19+10	$0.61 \cdot 10^{-5}$
	1516+71+53	$0.51 \cdot 10^{-3}$	1517+70+51+35+20	$0.23 \cdot 10^{-4}$	1571+57+52+29+10	$0.62 \cdot 10^{-5}$
	1573+71+53	$0.53 \cdot 10^{-3}$	1572+70+51+35+20	$0.31 \cdot 10^{-4}$	1513+57+52+29+19+10	$0.12 \cdot 10^{-4}$
	1516+174+71+53	$0.40 \cdot 10^{-3}$	1517+70+51+35+20	$0.11 \cdot 10^{-4}$	1513+204+57+52+29+10	$0.77 \cdot 10^{-5}$
	1573+174+71+53	$0.35 \cdot 10^{-3}$	1572+70+51+35+20	$0.14 \cdot 10^{-4}$	1571+204+57+52+29+10	$0.62 \cdot 10^{-5}$
			1517+204+70+51+35+20	$0.16 \cdot 10^{-4}$	1513+204+57+52+29+10	$0.67 \cdot 10^{-5}$
			1572+204+70+51+35+20	$0.12 \cdot 10^{-4}$	1571+204+57+52+29+19+10	$0.59 \cdot 10^{-5}$
3	1573+1516+53	$0.16 \cdot 10^{-3}$	1572+1517+61+59+70+51+20	$0{,}17 \cdot 10^{-4}$	1513+1571+57+52+29+10	$0.71 \cdot 10^{-5}$
	1573+1516+71+53	$0.46 \cdot 10^{-3}$	1572+1517+61+59+70+51+35+20	$0{,}19 \cdot 10^{-4}$	1513+1571+57+52+29+19+10	$0.69 \cdot 10^{-5}$
	1573+1516+174+71+53	$0.28 \cdot 10^{-3}$				

Figure 2 shows the calculated and experimental emission spectra of the molecules and complexes in question. It is well visible that the spectra contain a vibronic structure. Here, the intensity was normalized to the maximum peak 2 for T2 and T3 molecules, respectively, for comparison with experimental work [14]. The calculated absolute values of these peaks are 0.23×10^3 µJ/mol for T2 and 0.26×10^2 µJ/mol for T3. It should be noted that a good agreement between the experimental and calculated positions of the spectral peaks was obtained when the solvent (ethanol) was taken into account in the PCM model. In particular, for the maximum peaks 2 of T2 and T3 molecules, the difference between these positions is about 533 cm^{-1} and 246 cm^{-1}, respectively. Analysis of Figure 2 also shows that the shifts (bathochromic) of the vibronic bands of dithiophene and terthiophene complexes with H$_2$S and (H$_2$S)$_2$ do not exceed 130 cm^{-1} for all bands. In addition, the purely electronic transition (0-0) in the complexes is also slightly shifted. Indeed, the calculated frequencies of the electronic transition (0-0) are 30112 cm^{-1}, 30059 cm^{-1}, 29977 cm^{-1} for T2, T2···H$_2$S,

T2···(H$_2$S)$_2$ and 25119 cm^{-1}, 25056 cm^{-1}, 25053 cm^{-1} for T3, T3···H$_2$S, T3···(H$_2$S)$_2$, respectively. At the same time, a significant decrease of emission line intensity for these complexes as compared to that for individual free molecules of dithiophene and terthiophene is clearly seen in Figure 2: 3.7 and 2.6 times for T2···H$_2$S and T3···H$_2$S and by 5.5 and 3.6 times for T2···(H$_2$S)$_2$ and T3···(H$_2$S)$_2$, respectively. It is also seen that the complexity of the complexes' structures also leads to a decrease in the emission intensity.

Table shows the composite frequencies ($\omega_i + \omega_j + \cdots$) of the harmonic oscillations of the promoting modes, which make the main contributions to the emission spectrum under study, and the squares of the dipole moment (μ^2) of transitions for these modes calculated taking into account the Herzberg-Teller and Duschinsky effects. The calculation results presented in Table and Figure 2 also show that the vibronic bands 1 for bithiophene and terthiophene are formed by their low-frequency modes (≤ 370 cm^{-1}). The band 2 corresponds to combinations of low-frequency modes with high-frequency modes 1497 cm^{-1}, 1672 cm^{-1} for T2 and 1516 cm^{-1}, 1573 cm^{-1} for T3. The band 3 is formed by combinations of low-frequency modes and composite high-frequency modes.

A similar situation is observed for bithiophene and tertiophene complexes with H$_2$S and (H$_2$S)$_2$, where the vibronic structure of bands 1^a and 1^b (the subscripts a and b denote complexes with H$_2$S and (H$_2$S)$_2$, respectively) is a combination of low-frequency modes formed by intramolecular vibrations of bithiophene and terthiophene as well as intermolecular vibrations. The bands 2^a and 2^b correspond to combinations of low-frequency modes with high-frequency modes 1495 cm^{-1}, 1670 cm^{-1} and 1517 cm^{-1}, 1572 cm^{-1} for T2···H$_2$S and T3···H$_2$S, respectively. It can also be seen that the vibronic spectra of the complexes containing (H$_2$S)$_2$ are close to ones of the corresponding complexes with H$_2$S (Fig. 2). At the same time, high-frequency modes are practically unchanged, namely 1494 cm^{-1}, 1670 cm^{-1} for T2···(H$_2$S)$_2$ and 1513 cm^{-1}, 1571 cm^{-1} for T3···(H$_2$S)$_2$.

Figure 3 illustrates the high-frequency promotion modes for bithiophene and terthiophene and their complexes with H$_2$S and (H$_2$S)$_2$. As can be seen, the contribution to the vibronic bands comes from high-frequency vibrations of C–C bonds in the central part of the molecules. The low-frequency modes (Table) correspond to out-of-plane vibrations of bithiophene and terthiophene molecules as well as to intermolecular vibrations of their complexes with H$_2$S and (H$_2$S)$_2$.
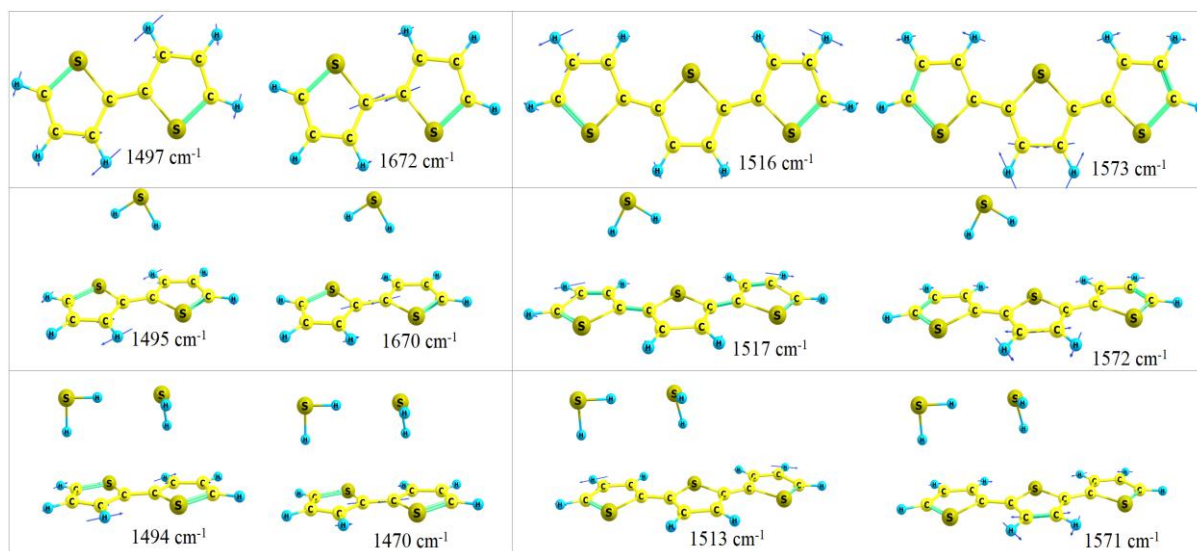
Figure 3. High-frequency promotion modes for T2 and T3 and for their complexes with H$_2$S and (H$_2$S)$_2$

Conclusions

The emission spectra of bithiophene and terthiophene molecules had a clear vibronic structure. As a result of calculations, it was found that the positions of bands (peaks) in the vibronic emission spectra of these compounds agreed well with the experimental data. It was established that vibronic progressions for bithiophene and terthiophene, as well as for oligofluorenes [26], are caused by low-frequency modes and some combinations of low-frequency modes with high-frequency modes and their combinations. A similar situation occurred for complexes of dithiophene and terthiophene molecules with H$_2$S and (H$_2$S)$_2$. The presence

of H_2S and $(H_2S)_2$ molecules in these complexes led to a 2.6–5.5-fold decrease in the vibronic band intensity in the emission spectra and to small bathochromic band shifts (< 130 cm^{-1}).

References

1   Xu, R.-P., Li, Y.-Q. & Tang J.-X. (2016). Recent advances in flexible organic light-emitting diodes. *Journal of Materials Chemistry C*, *4*(39), 9116–9142. https://doi.org/10.1039/C6TC03230C

2   Choi, S., Kwon, S., Kim, H., Kim, W., Kwon, J.H., Lim, M.S., Lee, H.S. & Choi, K.C. (2017). Highly flexible and efficient fabric-based organic light-emitting devices for clothing-shaped wearable displays. *Scientific Reports*, *7*(1). https://doi.org/10.1038/s41598-017-06733-8

3   Barbarella, G., Favaretto, L., Zambianchi, M., Pudova, O., Arbizzani, C., Bongini, A. & Mastragostino, M. (1998). From easily oxidized to easily reduced thiophene-based materials. *Advanced Materials*, *10*(7), 551–554. https://doi.org/10.1002/(SICI)1521-4095(199805)10:7<551::AID-ADMA551>3.0.CO;2-Y

4   Perepichka, I. F., Perepichka, D. F. & Meng, H. (2009). Thiophene-based materials for electroluminescent applications. Handbook of Thiophene-Based Materials, 695–756. https://doi.org/10.1002/9780470745533.ch19

5   Zhang, L., Colella, N.S., Cherniawski, B.P., Mannsfeld, S.C.B. & Briseno, A.L. (2014). Oligothiophene semiconductors: synthesis, characterization, and applications for organic devices. *ACS Applied Materials & Interfaces*, *6*(8), 5327–5343. https://doi.org/10.1021/am4060468

6   Murphy, A.R. & Fréchet, J.M.J. (2007). Organic semiconducting oligomers for use in thin film transistors. *Chemical Reviews*, *107*(4), 1066–1096. https://doi.org/10.1021/cr0501386

7   Zade, S.S., Zamoshchik, N. & Bendikov, M. (2011). From short conjugated oligomers to conjugated polymers. Lessons from studies on long conjugated oligomers. *Accounts of Chemical Research*, *44*(1), 14–24. https://doi.org/10.1021/ar1000555

8   Mishra, A., Ma, C.-Q. & Bäuerle, P. (2009). Functional oligothiophenes: molecular design for multidimensional nanoarchitectures and their applications. *Chemical Reviews*, *109*(3), 1141–1276. https://doi.org/10.1021/cr8004229

9   Lim, S.T., Kwon, M.S. & Shin, D.-M. (2001). Organic light emitting diodes(OLEDs) with oligothiophene and silicon monoxide. *Molecular Crystals and Liquid Crystals Science and Technology. Section A. Molecular Crystals and Liquid Crystals*, *371*(1), 171–176. https://doi.org/10.1080/10587250108024715

10   Granlund, T., Theander, M., Berggren, M., Andersson, M., Ruzeckas, A., Sundström, V., Bjork, G., Granstrom, M. & Inganäs, O. (1998). A polythiophene microcavity laser. *Chemical Physics Letters*, *288*(5-6), 879–884. https://doi.org/10.1016/s0009-2614(98)00320-0

11   Mazzeo, M., Pisignano, D., Favaretto, L., Barbarella, G., Cingolani, R. & Gigli, G. (2003). Bright oligothiophene-based light emitting diodes. *Synthetic Metals*, *139*(3), 671–673. https://doi.org/10.1016/s0379-6779(03)00304-7

12   Duan, T., Chen, Q., Yang, Q. Hu, D., Cai, G., Lu, X., Lv, J., Song, H., Liu, F., Yu, D. & Lu, S. (2021) Simple thiazole-centered oligothiophene donor enables 15.4% efficiency all small molecule organic solar cells. *Journal of Materials Chemistry A*, *10*(6), 3009-3017. https://doi.org/10.1039/D1TA09058E

13   Sharipov, A.K. (2002). Chemistry and technology of fuels and oils, 38(5), 340–344. https://doi.org/10.1023/a:1021294917644

14   Becker, R.S., Seixas de Melo, J., Maçanita, A.L. & Elisei, F. (1996). Comprehensive evaluation of the absorption, photophysical, energy transfer, structural, and theoretical properties of α-oligothiophenes with one to seven rings. *The Journal of Physical Chemistry*, *100*(48), 18683–18695. https://doi.org/10.1021/jp960852e

15   Improta, R., Ferrer, F.J. A., Stendardo, E. & Santoro, F. (2014). Quantum-classical calculation of the absorption and emission spectral shapes of oligothiophenes at low and room temperature by first-principle calculations. *ChemPhysChem*, *15*(15), 3320–3333. https://doi.org/10.1002/cphc.201402323

16   Stendardo, E., Avila Ferrer, F., Santoro, F. & Improta, R. (2012). Vibrationally resolved absorption and emission spectra of dithiophene in the gas phase and in solution by first-principle quantum mechanical calculations. *Journal of Chemical Theory and Computation*, *8*(11), 4483–4493. https://doi.org/10.1021/ct300664d

17   Madsen, D., Christiansen, O., Norman, P. & König, C. (2019). Vibrationally resolved emission spectra of luminescent conjugated oligothiophenes from anharmonic calculations. *Physical Chemistry Chemical Physics*, *21*(31), 17410–17422. https://doi.org/10.1039/C9CP03039E

18   Santoro, F. & Cerezo, J. FCclasses. CNRICCOM, http://www.iccom.cnr.it/en/fcclasses/

19   Christiansen, O., Artiukhin, D. & Godtliebsen, I.H. Midascpp GITLAB, https://gitlab.com/midascpp/midascpp

20   Frisch, M.J., Trucks, G.W., Schlegel, H.B., Scuseria, G.E., Robb, M.A., Cheeseman et. al. (2009). Gaussian, Inc., Wallingford CT. https://gaussian.com/glossary/g09

21   Herzberg, G. & Teller, E. (1933). Schwingungsstruktur der elektronenübergänge bei mehratomigen molekülen. *Zeitschrift Für Physikalische Chemie*, *21B*(1). https://doi.org/10.1515/zpch-1933-2136

22 Duschinsky, F. (1937). The importance of the electron spectrum in multi atomic molecules. Concerning the Franck-Condon principle *Acta Physicochim. URSS* 7. 551–566.

23 Yanai, T., Tew, D.P., & Handy, N.C. (2004). A new hybrid exchange–correlation functional using the Coulomb-attenuating method (CAM-B3LYP). *Chemical Physics Letters*, *393*(1–3), 51–57. https://doi.org/10.1016/j.cplett.2004.06.011

24 Francl, M.M., Pietro, W.J., Hehre, W.J., Binkley, J.S., Gordon, M.S., DeFrees, D.J. & Pople, J.A. (1982). Self-consistent molecular orbital methods. XXIII. A polarization-type basis set for second-row elements. *The Journal of Chemical Physics*, *77*(7), 3654–3665. https://doi.org/10.1063/1.444267

25 Takayanagi, M., Gejo, T. & Hanazaki, I. (1994). Geometry and torsional potential of 2,2'-bithiophene in a supersonic jet. *The Journal of Physical Chemistry*, *98*(49), 12893–12898. https://doi.org/10.1021/j100100a014

26 Valiev, R.R., Sunchugashev, D.A., Gadirov, R.M., Nasibullin, R.T. & Cherepanov, V.N. (2022). Vibronic spectra of bifluorene and terfluorene. *Russian Physics Journal*, *64*(11), 2082–2088. https://doi.org/10.1007/s11182-022-02559-8

Information about authors*

Cherepanov, Victor Nikolaevich — Doctor of Physical and Mathematical Sciences, Head of Optics and Spectroscopy Department, National Research Tomsk State University, Lenin ave., 36, 634050, Tomsk, Russia; e-mail: vnch@phys.tsu.ru; https://orcid.org/0000-0002-5952-5202

Sunchugashev, Dmitry Andreevich (*corresponding author*) - 4th year PhD student, Department of Physics, National Research Tomsk State University, Lenin ave., 36, 634050, Tomsk, Russia; e-mail: dsunchugashev@gmail.com; https://orcid.org/0009-0006-6069-3410

_____

*The author's name is presented in the order: *Last Name, First and Middle Names*

Article

UDC 544.522

https://doi.org/10.31489/2959-0663/3-23-7

Valentina A. Minaeva[1] , Nataliya N. Karaush-Karmazin[1*] , Olexandr O. Panchenko[1] ,
Maryana V. Chernyk[1], Jurate Simokaitiene[2] , Dmytro Yu. Volyniuk[2] ,
Juozas V. Grazulevicius[2] , Boris F. Minaev[1, 3*] , Oleksandr V. Reshetnyak[4]

[1]Department of Chemistry and Nanomaterials Science, Bohdan Khmelnytsky National University, Cherkasy, Ukraine;
[2]Department of Polymer Chemistry and Technology, Kaunas University of Technology, Kaunas, Lithuania;
[3]Department of Physics and Astronomy, Uppsala University, Uppsala, Sweden;
[4]Department of Physical and Colloid Chemistry, Ivan Franko National University of Lviv, Lviv, Ukraine
*(*Corresponding authors' e-mail: karaush22@ukr.net; bfmin43@ukr.net)*

Structure and Spectral Properties of Thianthrene and Its Benzoyl-Containing Derivatives

The IR absorption spectra of the recently synthesized series of benzoyl-containing thianthrene derivatives were studied in the context of their structural identification. Geometry optimization of the ground singlet state by density functional theory (DFT) calculations with the gradient and Hessian search were performed for thianthrene molecule in the framework of the C_{2v} symmetry restriction. The excited singlet and triplet states of thianthrene were found to be distorted along the b_{3u} vibrational mode of the D_{2h} point group, as well as the ground state, which leads to the non-planar butterfly-like structure (C_{2v}). But the excited states require additional symmetry reduction; they are closer to planarity but have no symmetry elements. Optimized ground states structure for the thianthrene-benzoyle molecule and its four derivatives with fluoro-substituents and different substitution positions were analyzed through complete assignment of all their vibrational modes and comparison with experimental infrared absorption spectra. A good agreement between experimental data and DFT calculated IR spectra provides additional structural support to results of the X-ray diffraction analysis of all synthesized compounds. The Hirshfeld surfaces analysis of the crystalline 3-fluorobenzoyl-thianthrene (**T3F**) was performed in order to analyze intermolecular interactions in **T3F** crystal. It indicates the presence of weak CH…F, CH…S and CH…O intermolecular contacts, stabilizing the crystal structure of **T3F**. The CH…O interactions appear in the IR spectrum of **T3F** crystal as two vibrational modes with frequencies 3084 and 3078 cm^{-1}. The intermolecular interactions CH…F and CH…S do not affect the IR spectrum of **T3F**.

Keywords: thianthrene, benzoylthianthrene, DFT calculations; B3LYP/6-31 G(d, p), IR spectra; X-ray analysis, Hirshfeld surface analysis.

Introduction

Organic dyes containing π-conjugated donor (D) and acceptor (A) moieties, which are connected through effective π-bonds, have attracted considerable attention in modern optoelectronic technologies. In addition to the extended π-conjugated chain, such organic luminophores must satisfy many other requirements, including thermal and chemical stability, high external quantum efficiency, correct redox parameters, and good electron-hole transport characteristics. The thianthrene molecule and its derivatives are interesting luminophores for modern OLED technology due to the high yield of triplet excited states and the ability to create thermally activated delayed fluorescence (TADF) [1].

Thianthrene is the anthracene heterocyclic analog with two sulfur atoms substituents at the 9,10-positions (Fig. 1). Its form consists of two benzene rings disposed into two planes intersecting along the S-S axis at a dihedral angle of 128° [1]. Strong inclination of these two planes and the extended π-electronic conjugation system with peculiar lone pairs at sulfur atoms provide interesting chemical, photophysical and electrochemical properties of thianthrene [2]. The bent, non-aromatic structure of the central dithiine ring leads to the strongly pronounced and expressed electron-donor properties of thianthrene, its stable cation and dication species. While the chemistry and electrochemistry of thianthrene are well studied, its luminescence and photophysical constants have not been propery investigated [1–3]. In particular, Arena et al. [1] studied phosphorescence of the thianthrene molecular crystals accompanied by semiempirical calculation of excited states with vertical excitations, but not many studies of its numerous derivatives were published [1, 2].

Recently synthesized thianthrene-benzoyle derivatives with different halogen substituents and substitution positions have been shown as efficient room temperature phosphorescent emitters with large (>90 %) or moderate phosphorescence contribution to the total photoluminescence and electroluminescence [3]. The X-ray diffraction (XRD) analysis of few synthesized compounds does not afford us to distinguish two types of fluoro-substituted isomers; namely (2-fluorophenyl)(thianthren-2-yl)methanone (**T2F**) and (6-fluoro-phenyl)(thianthren-2-yl)methanone **(T6F)** benzoyl-thianthrene derivatives without additional study. To do this, we performed IR absorption measurements and DFT calculations of all vibrational modes of four thianthrene-benzoyle derivatives. Comparison of intensity and frequency of experimental and theoretical IR absorption bands permits us to ensure all structural parameters of new synthesized compounds.

We also performed full interpretation of the thianthrene IR spectrum on the basis of DFT calculation of all 60 normal vibrations. The knowledge of the quite accurate calculated thianthrene force field in the ground state helps us to predict the first excited states structure for the singlet (S) and triplet (T) state manifolds. To do this we applied the pseud-Jahn-Teller effect theory [4] and ideology developed by I.B. Bersuker. First, we shall consider the IR spectra problems and then we shall use and illustrate the vibronic perturbation analysis of the pseudo-JT effect [4, 5] comparing the parent anthracene and relative thianthrene molecules in order to explain the ground and excited states of these two particles.

Computational Details

To analyze IR spectra of thiantrene and its derivatives, it is necessary first to carry out quantum chemical calculations of molecular structure of these compounds by optimizing the geometry. The structures of nuclear positions in the studied molecules were optimized by the electronic density calculation at the DFT level using the B3LYP/6-31 G(d, p) method [6–8] based on the initial molecular geometries obtained by the self-consistent field semiempirical PM3 approach [9, 10]. The optimization of the 3-fluorobenzoylthianthrene (**T3F**) molecule was carried out on the basis of the X-ray diffraction analysis data [11]. On the basis of the optimized geometry the theoretical IR spectra of molecules the studied compounds were calculated and analyzed. Vibrational frequencies, wave numbers with the corresponding IR intensities were evaluated in the framework of the same DFT method through the gradients of total energy, dipole moments and force constants calculations. All frequencies of normal vibrations found to be real, which indicates the achievement of a true minimum of the potential energy hypersurface. The best fitting between the experimental and calculated infrared spectra can be achieved implementing three various scale factors for the different types of vibrations: we use 0.950 scaling parameter for the high frequency region of the C–H stretching modes, 0.97 — for C=C stretching vibrations and 0.98 — for the rest of the IR spectrum; that is mostly the CH bending in-plane and out-of-plane vibrations, ring deformations modes. The scale factors were estimated as the ratio of the experimentally observed and DFT-calculated frequencies averaged for all IR bands in the particular region of the spectra. It should be noted that similar scale factors are often used in other studies for the corresponding IR spectral parts [12].

The finally predicted IR spectra of the studied molecules were produced by the GaussView 6.0 software [13] using the chosen half-width of 10 cm^{-1} and the Lorenzian distribution function. The qualitative vibrational assignment of all normal modes in terms of the natural coordinates were achieved with the help of animation program by the Chemcraft code [14], which provides a visual presentation of the calculated vibrations. The quantum chemical calculations of electronic structure and vibrational movements were performed by the Gaussian16 program package [15].

The results of IR spectra calculations of the studied molecules were compared with experimental data for the synthesized compounds [3].

The Bruker Vertex 70 infrared spectrometer (Vertex 70, Bruker Corporation, Germany) with the samples in the form of KBr pellets was used to record FTIR spectra.

The Hirschfeld surface of the studied crystal of the compound **T3F** was calculated using Crystal Explorer 17.5 software with a very high resolution [16, 17].

Results and Discussion

Structural features and IR spectra of thianthrene and benzoylthianthrene

The crystal and molecular structure of thianthrene was analysed by X-ray diffraction [18]. The chemical structure of thianthrene is shown in Figure 1.
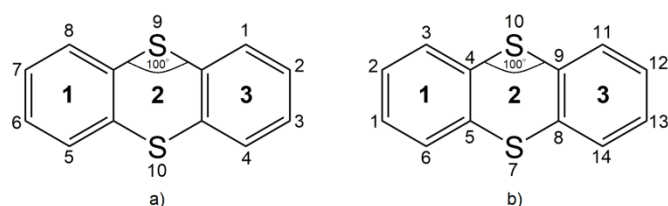
a — chemical numbering of atoms; *b* — numbering of atoms is set by the Gaussian program

Figure 1. Chemical structure of thianthrene

The molecule was found to be folded in respect to the S···S axis so that two benzene rings lie in two planes at an angle of 128°, the bending CSC valence angle is 100° and C−S bond lengths is 1.76±0.01 Å [18].

Chemical structures of benzoylthianthrene and its fluoro-substituted derivatives are shown in Figure 2.
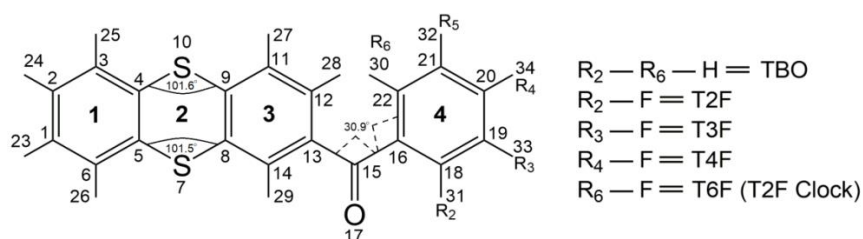
TBO — phenyl(thianthren-2-yl)methanone or benzoylthianthrene; **T2F** — (2-fluorophenyl)(thianthren-2-yl)methanone or 2-fluorobenzoylthianthrene (counter clockwise orientation); **T3F** — (3-fluorophenyl)(thianthren-2-yl)methanone or 3-fluorobenzoylthianthrene; **T4F** — (4-fluorophenyl)(thianthren-2-yl)methanone or 4-fluorobenzoylthianthrene; **T6F** — (6-fluorophenyl)(thianthren-2-yl)methanone or 6-fluorobenzoylthianthrene or **T2F** clock-wise orientation

Figure 2. Chemical structures of benzoylthianthrene and its fluoro-derivatives: the abbreviated names of fluoro-substituted benzoylthianthrenes are given based on the counterclockwise orientation of the substituent on the phenyl ring. The arbitrary atomic numbering generated by the computer program; the same numbers are used for all other fluoro-derivatives for the sake of comparisons

The DFT optimized molecular structures for thianthrene and benzoylthianthrene (**TBO**) are shown in Figures 3 and 4, respectively. Numbering of atoms is set by the program and used in this paper for all other molecules
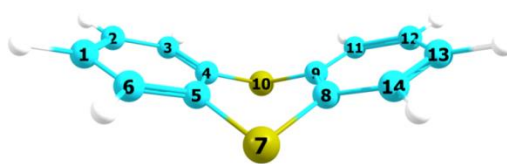
Figure 3. The optimized structure of the thianthrene molecule
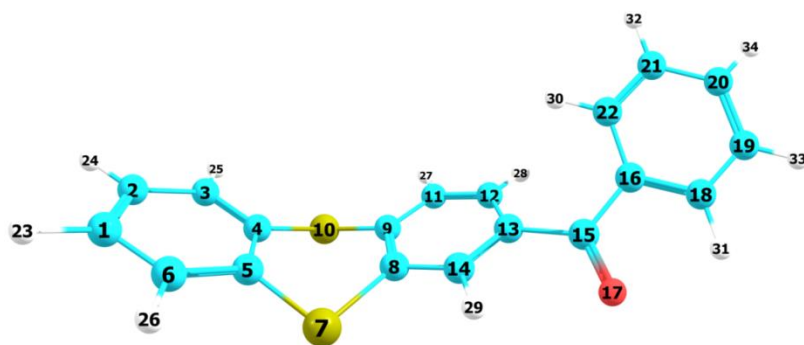
Figure 4. The optimized structure of the benzoylthianthrene (**TBO**) molecule

The calculated atomic charges for all studied molecules are presented in Table; the structural parameters (bond lengths (Å) and angles (deg)) for the thianthrene and **TBO** molecules are given in Table S1 **Supplementary Materials**.

T a b l e

**Calculated atomic charges (according to Mulliken) for thianthrene and its benzoyl derivatives
in the electron charge units**

| Atom	Thianthrene	TBO	T2F	T3F	T4F	T6F (T2F, clock wise)
C1	–0.080	–0.079	–0.079	–0.079	–0.079	–0.079
C2	–0.080	–0.080	–0.080	–0.080	–0.080	–0.080
C3	–0.091	–0.090	–0.090	–0.090	–0.090	–0.090
C4	–0.107	–0.110	–0.111	–0.111	–0.111	–0.110
C5	–0.107	–0.108	–0.109	–0.109	–0.109	–0.108
C6	–0.091	–0.091	–0.091	–0.091	–0.091	–0.091
S7	0.157	0.173	0.175	0.174	0.174	0.172
C8	–0.107	–0.117	–0.117	–0.118	–0.118	–0.118
C9	–0. 107	–0.099	–0.099	–0.099	–0.099	–0.098
S10	0.157	0.169	0.171	0.170	0.170	0.169
C11	–0.091	–0.103	–0.102	–0.103	–0.102	–0.105
C12	–0.080	–0.108	–0.109	–0.107	–0.109	–0.109
C13	0.080	0.044	0.044	0.044	0.044	0.057
C14	–0.091	–0.098	–0.100	–0.098	–0.098	–0.099
C15	–	0.329	0.346	0.333	0.330	0.339
C16	–	0.041	–0.037	0.035	0.039	–0.024
O17	–	–0.464	–0.447	–0.460	–0.465	–0.458
C18	–	–0.090	0.341	–0.146	–0.092	–0.092
C19	–	–0.092	–0.138	0.351	–0.143	–0.090
C20	–	–0.075	–0.079	–0.127	0.364	–0.080
C21	–	–0.094	–0.090–	–0.096	–0.147	–0.136
C22	–	–0.116	–0.107	–0.115	–0.117	0.320
H28	0.094	0.109	0.109	0.109	0.108	0.101
H29	0.105	0.131	0.135	0.132	0.132	0.133
H30	–	0.103	0.108	0.106	0.111	–0.287 (F)
H31	–	0.116	–0.272 (F)	0.130	0.125	0.120
H32	–	0.093	0.096	0.102	0.110	0.109
H33	–	0.095	0.109	–0.293 (F)	0.112	0.098
H34	–	0.094	0.101	0.110	–0.289 (F)	0.102

As can be seen from Table S1, the calculated bond angles CSC and bond lengths C–S for thianthrene are close to the experimental values [18]. The calculated C=C bond lengths in thianthrene and benzoylthianthrene are in the range of 1.394÷1.404 Å, which are typical for aromatic C=C bonds. The addition of a benzoyl moiety into the benzene ring number **3** enriches the electron density on the carbon atoms of this ring and pulls the electron density from the sulfur atoms (increases the positive charge) (Table). The calculated dipole moments of the thianthrene and **TBO** molecules are equal 1.6472 and 3.8659 D, respectively.

The benzoyl moiety provides structural distortions in the benzene rings of thiantrene; it mostly affects the length of C=C bonds within the benzene ring number **3** (changes are up to 0.008 Å), the bond angles (up to 1°) and the dihedral angles (changes up to 1.8°) (Table S1). These changes are also observed in the dithiine moiety (thianthrene ring number **2**), but to a less extent. The noted changes should affect the vibration frequencies and absorption intensities in IR spectra of these compounds. Twisting is observed between the thianthrene and benzoyl groups (Fig. 4), the torsion angle C13-C15-C16-C22 is 30.87° (Table S1).

On the background of the gradient derivatives (Hessian) for the optimized geometry the theoretical IR spectra of the studied molecules were calculated and analyzed; the normal vibration frequencies and their IR intensity for the thianthrene and **TBO** molecules are presented in Table S2 and Table S3, respectively. Theoretically predicted IR spectra of both molecules are compared with experimental results of thianthrene [19] and benzoylthianthrene in the Tables S2, S3 and in Figures 5, 6, respectively.

There are 60 normal vibrations in the thianthrene molecule. For the C_{2V} point group symmetry, they can be classified as follows: $15A_1$, $15A_2$, $14B_1$ and $16B_2$. According to the IR vibrational selection rules only A_1, B_1 and B_2 vibrations are allowed in the IR spectrum. All vibrational modes in the thianthrene molecule IR spectrum are presented and assigned in Table S2. Figure S5 illustrates the high-frequency IR absorption region of the thianthrene and **TBO** molecules, Figure S6 shows the finger print parts of IR spectra of those molecules.
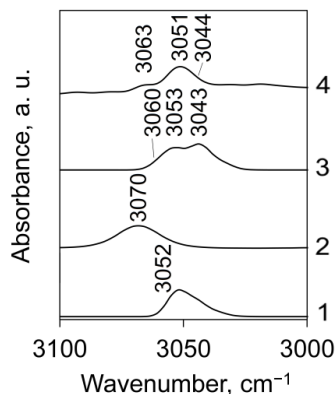
Curve 1 — calculated IR spectrum for thianthrene;
curve 2 — experimental IR spectrum for solid-state thianthrene sample of the studied compound [19];
curve 3 — calculated IR spectrum for the **TBO** molecule;
curve 4 — experimental IR spectrum for the solid-state **TBO** sample

Figure 5. IR spectra of thianthrene and **TBO** in the high-frequency range (3100–3000 cm^{-1})
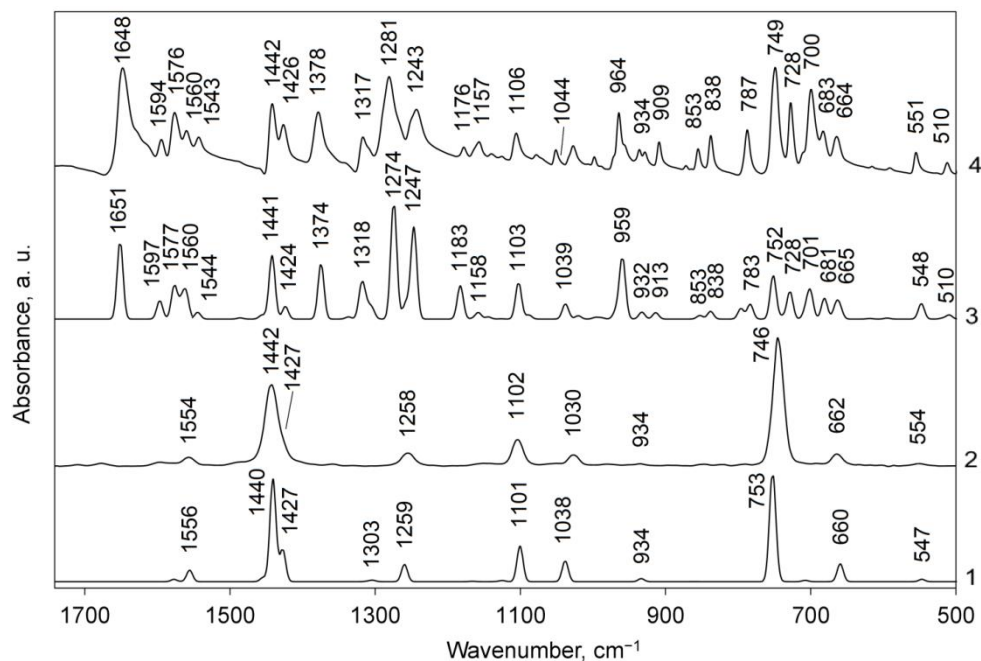
Curve 1 — calculated IR spectrum for the thianthrene molecule;
curve 2 — experimental IR spectrum for the solid-state thianthrene sample [19];
curve 3 — calculated IR spectrum for the **TBO** molecule;
curve 4 — experimental IR spectrum for the solid-state **TBO** sample

Figure 6. IR spectra of thianthrene and **TBO** in the 1700–500 cm^{-1} range

According to the characteristic group frequencies analysis [20], the C–H stretching vibrations in aromatic compounds can be found in the range 3080–3030 cm^{-1}, the CH bending in-plane deformation modes — in the

range 1225–950 cm^{-1} and CH bending out-of-plane deformation vibrations — below 900 cm^{-1}. The IR absorption bands of the aromatic C=C stretching vibrations are usually observed in the region 1650–1430 cm^{-1}. The assignment of all normal modes with the help of animation program of the Chemcraft code [21], which provides a visual presentation of the calculated vibrations, indicates that in the thianthrene IR spectrum the C–H stretching vibrations should be observed in the range 3053–3028 cm^{-1} (calc.: 3052 cm^{-1}, exp.: 3070 cm^{-1}), the planar CH bending deformation — in the range 1259–1101 cm^{-1} (calc.: 1259, 1101 cm^{-1}, exp.: 1258, 1102 cm^{-1}), the bending out-of-plane deformation vibrations — 970–750 cm^{-1} (calc.: 934, 753 cm^{-1}, exp.: 934, 746 cm^{-1}), the C=C stretching vibrations of aromatic rings at in the region 1577–1427 cm^{-1} (calc.: 1556, 1440, 1427 cm^{-1}, exp.: 1554, 1442, 1427 cm^{-1}). Most of the bands in the calculated and experimental spectra of thianthrene have a weak absorption intensity (Table S2, Fig. 6, curves 1, 2). The most intense absorption bands in the thianthrene IR spectrum are connected with the out-of-phase asymmetric C=C stretching vibrations (calc.: 1440 cm^{-1}, exp.: 1442 cm^{-1}) and symmetric CH bending out-of-plane vibrations (calc.: 753 cm^{-1}, exp.: 746 cm^{-1}). The C–S stretching and CSC bending modes are mixed with other type of vibrations and contribute to the experimental bands 1443, 1427, 1102, 662 and 554 cm^{-1} (Table S2). We conclude, that the calculated vibration frequencies in the thianthrene molecule are in a good agreement with the experimental spectrum (Table S2, Fig. 6, curves 1, 2).

We attribute the high-frequency shift of the experimental band of stretching C–H vibrations (in the left part of Fig. 5 curve 2) to intermolecular S···H interactions. The noncovalent π–π stacking interactions in the crystal thianthrene structure are unlikely, since the thiantrene molecules are not planar.

The C–H stretching vibrations in the phenyl ring of the benzoyl fragment at 3051 (v_{92}), 3043 (v_{90}), 3033 (v_{87}) cm^{-1} as well as occurring simultaneously C-H modes in the benzene ring (number **3**) at 3060 (v_{96}) 3059 (v_{95}) cm^{-1} (Table S3) change the shape of the spectral curve in the high-frequency region of the IR spectrum of **TBO** (Fig. 5, curves 3, 4) compared to thiantrene. The ring number **3** associated with the benzoyl fragment provides total distortion of the **TBO** spectrum (Fig. 5, curves 3, 4).

The addition of the benzoyl moiety to the benzene ring (number **3**) enriches the finger-print IR spectrum with strong absorption bands of C=O stretching vibration (calc.: 1651 cm^{-1}, v_{84}, exp.: 1648 cm^{-1}, Fug. 6). There are asymmetric C=C stretching vibrations in the benzene ring (number **3**) (calc.: 1374 cm^{-1}, v_{72}, exp.: 1378 cm^{-1}), asymmetric =C–C(O)–C= stretching vibrations (calc.: 1274 cm^{-1}, v_{67}, and 1247 cm^{-1}, v_{65}, exp.: 1281 and 1243 cm^{-1}), asymmetric ring deformation. in-plane, in the aromatic rings number **3** and **4** (calc.: 959 cm^{-1}, v_{47}, exp.: 964 cm^{-1}, Table S2, Fig. 6, curves 3, 4). Strong differences between **TBO** and thianthrene IR absorption is also determined by the normal vibrations v_{83}, v_{70}, v_{64}, v_{44}, v_{34}, v_{33}, with frequencies 1597, 1318, 1183, 932, 707, 701 cm^{-1} in the phenyl ring of the benzoyl fragment as well as the normal vibrations v_{41}, v_{40}, v_{39}, v_{38}, v_{35}, v_{31} and v_{30}, with calculated frequencies 853, 838, 796, 783, 728, 681 and 665 cm^{-1} occurring simultaneously in the phenyl ring of the benzoyl fragment and in the benzene ring (number **3**) associated with the benzoyl fragment form in the IR spectrum absorption bands with medium and medium-to-weak intensities (Fig. 6, curves 3, 4). The assignment of these bands is given in Table S3. Thus, a change in the charges on atoms, bond lengths, and bond angles in the benzene ring of thianthrene (ring number 3) upon addition of a benzoyl fragment leads to a change in vibration frequencies and their intensities, and to the appearance of new vibrations (Fig. 6).

The effect of the fluoro-substituent in the benzoyl fragment on the IR spectrum of benzoylthianthrenes

Due to the fact that the phenyl ring in the **TBO** molecule is not conjugated with the thiantrene fragment, the substitution of a hydrogen atom by a fluorine atom in the phenyl ring does not significantly affect the electron density redistribution in the thiantrene fragment, but it has a significant effect on the electronic properties of the phenyl ring itself. Because of the strongly electron-withdrawing nature of the fluorine atom, a slight polarization of the benzene ring of the thiantrene fragment associated with the benzoyl fragment and the carbonyl link through the hyperconjugation system between this ring and the corresponding benzoyl substituent is observed. Thus, in the molecules of **T2F** counter clock-wise orientation and **T2F** clock-wise orientation, a decrease in the electron density is observed on the C15 and O17 atoms, and in the **T2F** clock-wise orientation molecule and on the C13 atom (Table).

The substitution of hydrogen atom by fluorine atom in phenyl ring also does not cause a visible change in bond lengths and bond angles within the thiantrene fragment, but affects the length of C=C bonds within the phenyl group (changes are up to 0.006 Å), bond angles (up to 3°) and the dihedral angles change significantly (up to 16°) (Table S1). These changes are calculated for molecules **T2F** and **T6F**. The dipole mo-

ments of the **TBO**, **T2F**, **T3F**, **T4F** and **T6F** molecules are equal 3.87, 4.79, 4.66, 3.39, and 3.25 D, respectively. The **T2F** and **T3F** are more polar molecules which agree with the slow cooling of the melting samples.

The noted changes should affect the vibration frequencies and absorption intensities in the IR spectra of these compounds.

The calculated normal vibration frequencies and their intensity in IR spectra of the **T2F** and **T6F** molecules are presented in Tables S4 and S5 of **Supplementary Materials**, respectively. Theoretical predicted IR spectra of both molecules are compared with experimental spectrum of **T2F** compound in Figure 7.
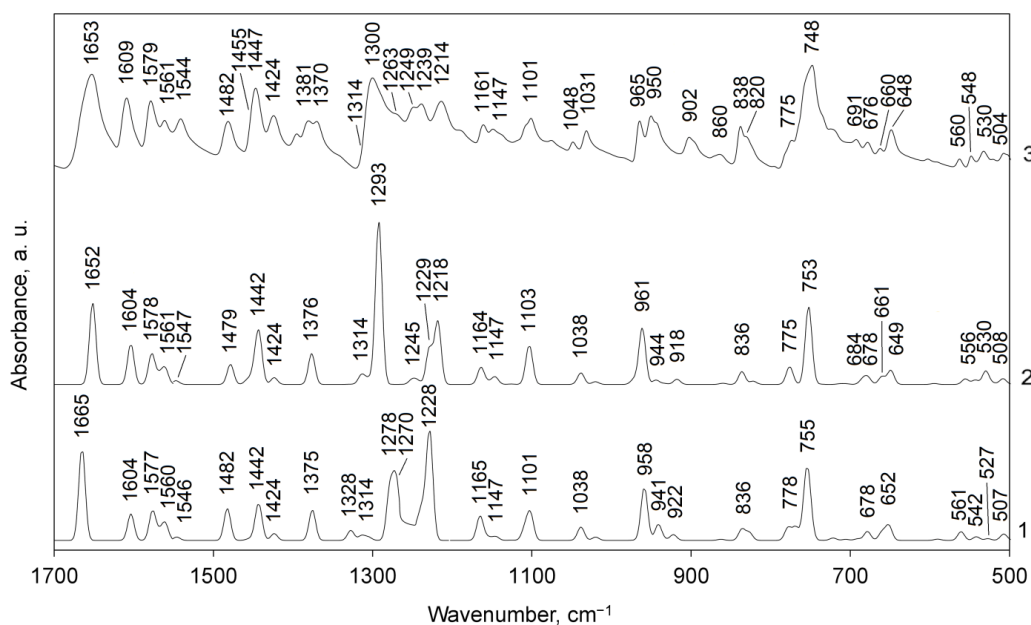
Curve 1 — IR spectrum for the **T2F** molecule calculated in vacuum;
curve 2 — IR spectrum for **T6F** molecule, calculated in vacuum;
curve 3 — experimental IR spectrum for **T2F** compound

Figure 7. Absorption IR spectra of the 2-fluorobenzoylthianthrene derivatives in the 1700–500 cm^{-1} range

Comparison of theoretical IR spectra of both molecules with the experimental spectrum compound **T2F** indicates that calculated IR spectrum of molecule **T2F** clock-wise orientation **(T6F)** fits better the observed IR bands profile. For example, the strong absorption bands C=O stretching vibration at 1652 cm^{-1} in the DFT-calculated IR spectrum of molecule **T6F** coincides with the similar band in the experimental IR spectrum of the **T2F** species (Fig. 7, curve 2 and 3; Table S5, ν_{85}) while in the calculated spectrum of the molecule **T2F** such IR band is shifted by 12 cm^{-1} to the region of high frequencies (Fig. 7, curve 1 and 3; Table S4, ν_{85}, calc.: 1665 cm^{-1}). The calculated frequency 1293 cm^{-1} very strong band asymmetric =C–C(O)–C= stretching vibrations with contribution from C–F stretching vibrations in the IR spectrum of molecule **T6F** (ν_{69}, I = 335 km/mole) close in value to the experimental frequency of 1300 cm^{-1} in the IR spectrum of the **T2F** species while in the calculated spectrum of the molecule **T2F** such IR band but with a lower intensity is formed by two normal vibrations (ν_{69} and ν_{68}) and only in one of them (ν_{69}) there is a contribution from C–F stretching vibrations. It should be noted that all calculated vibrational modes in the IR spectrum of **T6F** in the frequency range 1298–1214 cm^{-1} have a contribution from C–F stretching vibrations, while in the calculated IR spectrum of molecule **T2F** in this frequency range only two modes (ν_{69} and ν_{66}, Table S4) have a contribution from C–F stretching vibrations, which also has an influence on the frequency and intensity of normal vibrations in this region. Based on the calculation of the IR spectrum of the **T6F** molecule, we assign experimental band at 1214 cm^{-1} of the middle intensity (Fig. 7, curve 3) to the =C–C(O)–C= stretching vibrations with contribution from C–F stretching and CH bending in-plane vibrations (calc.: 1218 cm^{-1}). In the IR spectrum of **T2F** molecule this normal vibrations, having lost the contribution of C–F stretching vibrations, formed a strong band shifted towards higher frequencies up to 1228 cm^{-1} (Fig. 7, curve 1, Table S4). These differences can be used to discern the **T2F** and **T6F** isomers with different positions fluorine atom in the phenyl ring.

The total energies of the optimized **T6F** and **T2F** isomers calculated at the B3LYP/6-31G(d, p) level are equal to –1702.1059422 and –1702.1037699 a.u, respectively. Thus, the clock-wise isomer **T2F** is more stable although the energy difference is small, only 5.7 kJ/mol.

Thus, comparative analysis of the calculated IR spectra of two isomers **T6F** and **T2F** affords us to conclude finally that the experimental spectrum of **T2F** compound belongs to the **T6F** compound, where the fluorine substituent is in the position 2 clock-wise orientation of the aromatic ring, therefore, the synthesized **T2F** compound will be referred to as **T6F** (or **T2F** clock-wise orientation).

The calculated normal vibration frequencies and their intensity in IR of the **3F** and **4F** molecules are presented in Tables S6 and S7 of **Supplementary Materials**, respectively, and compared with experimental spectra of these compounds.

For ease of comparison, the experimental and theoretically predicted IR spectra of benzoylthianthrene and all fluorobenzoylthianthrene derivatives in the 3100–3000 cm⁻¹ range are shown in Figures S1 and S2, respectively, and in the 1700–500 cm⁻¹ range are shown in Figures 8 and 9, respectively. Assignment of selected bands in the IR absorption spectra for all studied compounds summarized in the Table S8.
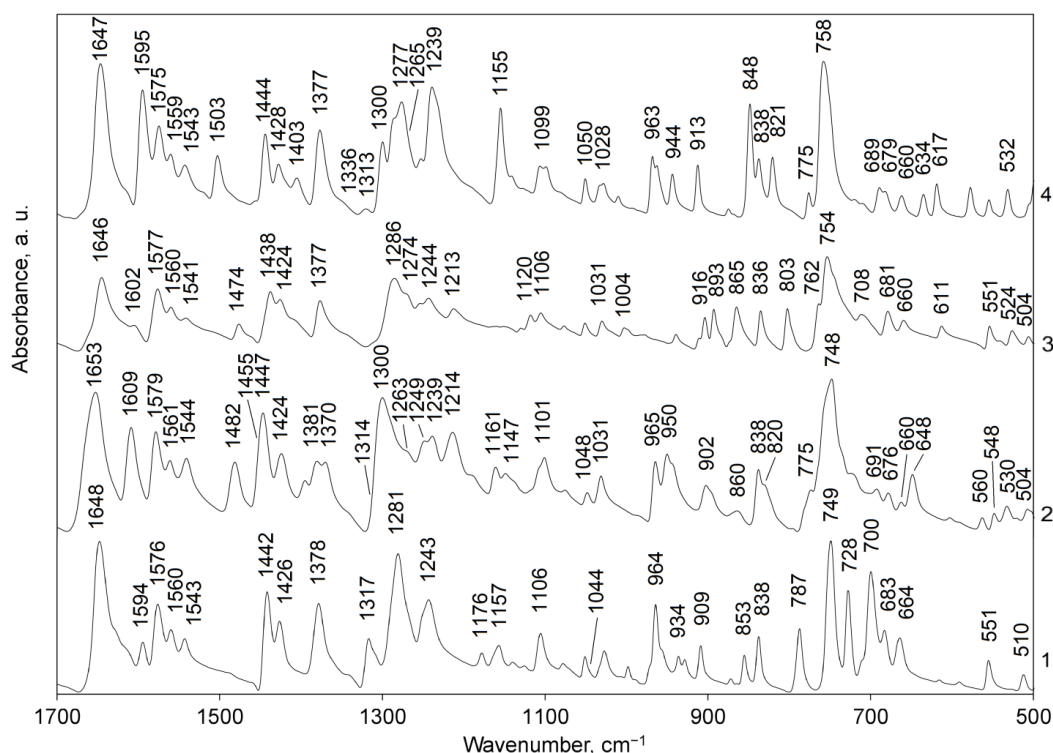
Curve 1 — IR spectrum for **TBO** compound; curve 2 — IR spectrum for **T6F (T2F** clock-wise orientation) compound; curve 3 — IR spectrum for **T3F** compound; curve 4 — IR spectrum for **T4F** compound

Figure 8. Experimental IR spectra of solid-state samples of the studied compounds in the 1700–500 cm⁻¹ range

As can be seen in the calculated IR spectra (Fig. 9), the C=O band of the **T2F** isomer is observed at a higher frequency (1665 cm⁻¹, curve 5) compared to the **TBO** molecule (1651 cm⁻¹, curve 1) and **T3F**, **T4F** and **T6F** isomers (1653, 1649, and 1652 cm⁻¹, respectively; curves 3, 4, and 5), which is consistent with a decrease in the C=O bond length (Table S1). The calculated intensity of the C=O normal mode is the highest for **T2F** (191 km/mol, Table S4) compared to 145, 156 and 167 km/mol for the **T3F**, T4F and **T6F** particles (Table S6, S7 and S5). It should be noted that the Mulliken's atomic charges calculated at the O17 atom of the carbonyl group in **T2F** molecule (–0.447*e*) is also different from those for **TBO, T3F**, **T4F** and **T6F** molecules (–0.464, –0.460, –0.465, and –0.468*e*, respectively, Table); thus, the polarity of the bonds could increase but the derivative of dipole moment along displacement could be lower.

The substitution of hydrogen atom by fluorine atom in phenyl ring does not cause a significant change the frequencies of stretching vibrations of C=C bonds in the thianthrene fragment and their IR intensities (Table S8). However, if vibrations of C=C bonds occur in the phenyl ring of the benzoyl fragment, then the IR frequencies and intensity change. So, the asymmetric C=C stretching vibrations occurring in the phenyl

ring of the **T4F** molecule at 1504 cm⁻¹ (exp. 1503 cm⁻¹) appear in the calculated and measured IR spectra of the other fluoro-isomers at lower frequencies and in **T2F** — with higher intensity (Fig. 8, 9). The corresponding IR band in the calculated and measured IR spectra of **TBO** species is not observed, since it is too weak according to our calculations (Table S8, $I_{\text{calc.}}$ = 1 km/mol). It should be noted that this calculated mode in the IR spectrum of **T4F** have a contribution from C–F stretching vibrations. The strong band at 1438 cm⁻¹ (calc.: 1433 cm⁻¹) in the IR spectrum of **T3F** and the band of weak intensity at 1403 cm⁻¹ (calc.: 1406 cm⁻¹) in the IR spectrum of **T4F** also belong to asymmetric C=C stretching vibrations occurring in the phenyl ring.
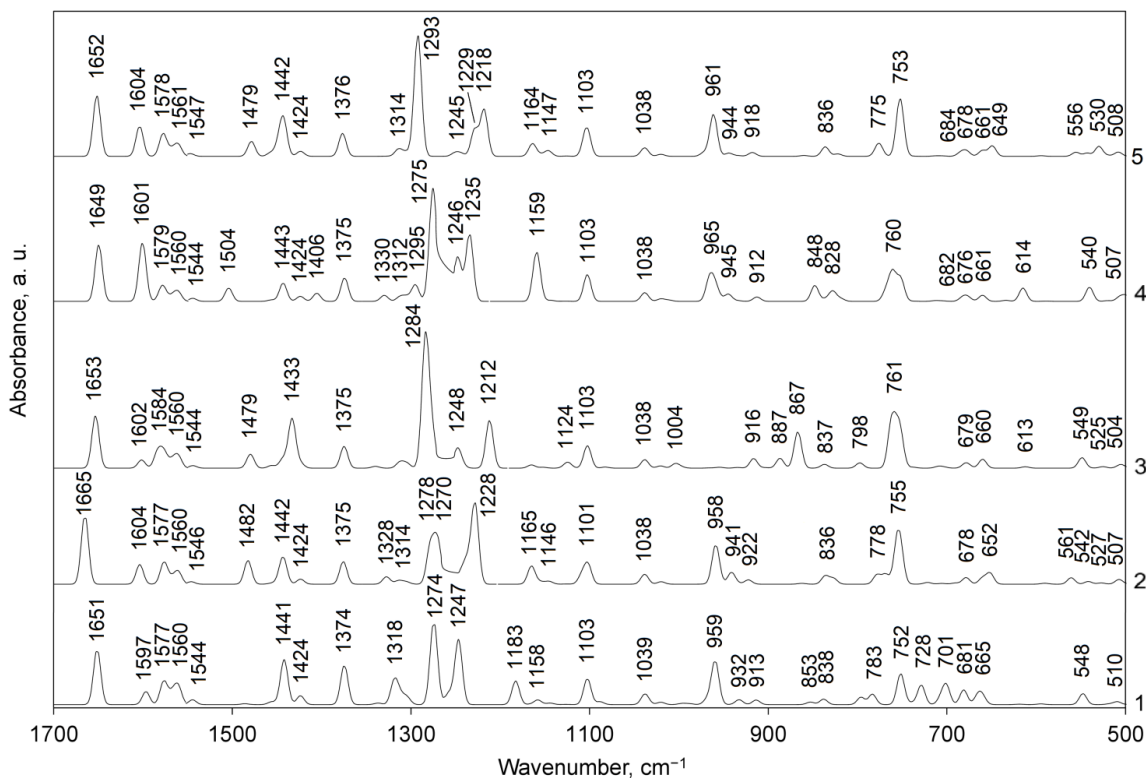
Curve 1 — IR spectrum for **TBO** molecule; curve 2 — IR spectrum for **T2F** molecule; curve 3 — IR spectrum for **T3F** molecule; curve 4 — IR spectrum for **T4F** molecule; curve 5 — IR spectrum for **T6F** molecule

Figure 9. Calculated absorption IR spectra of the benzoylthianthrene and fluorobenzoylthianthrene derivatives in the 1700–500 cm⁻¹ range

The weak bands with close frequencies in the calculated and measured IR spectra in the range 1303–1317 cm⁻¹ (Fig. 8, 9, Table S8) for all studied compounds are formed by Kekule vibrations in the benzene rings of the thianthrene fragment, which include subsequent alternations of the C=C bonds stretching and compression of large amplitude. In the phenyl ring of the benzoyl moiety the same type of mode occurs at higher frequency and forms in the calculated IR spectra of the **T2F** and **T4F** molecules the weak bands at 1328 and 1330 cm⁻¹. The corresponding bands in the IR spectra of the **TBO**, **T2F** and **T4F** molecules are not observed, since they are too weak according to our calculations. The largest changes in the IR spectra of fluorosubstituted benzoylthianthrenes are observed in the frequency range of 1300–1120 cm⁻¹ where asymmetric stretching vibrations of C–C(O)–C bonds of the carbonyl link occur with participation of the C–F bonds stretching and CH groups bending vibrations. We discussed these differences above when comparing the IR spectra of **T2F** and **T6F** compounds. They are also observed for the **T3F** and **T4F** compounds as compared to **T2F**, **T6F** and **TBO** samples (Fig. 8, 9, Table S8).

In the simulated and experimental IR spectra of all studied compounds the weak bands with close frequencies in the range 1099–1106 cm⁻¹ (Fig. 8, 9, Table S8) are formed by CH bending vibrations in plane in thiantrene fragment. Asymmetric ring in-plane vibrations in thiantrene fragment are calculated at 1038 and 1041 cm⁻¹ but they show the weak absorption intensity according to DFT calculation (Table S8). IR bands below 970 cm⁻¹ we assigned to the out-of-plane =CH deformation, and to the out-of-plane ring deformation, in-plane or

out-of-plane vibrations. Many modes have a contribution from the C–F stretching vibrations. In the frequency range of 1000–700 cm^{-1}, substitution of a hydrogen atom by a fluorine atom in the phenyl ring significantly affects not only the IR frequencies and intensities, but also the shape of the vibrational modes. We shall only note the main similarities and differences in this respect (Table S8). Thus; the asymmetric non-planar =CH bending vibrations of the aromatic ring **3** and **4** (in-phase) in the vicinity 960 cm^{-1} in the **TBO**, **T2F**, **T4F** and **T6F** samples form medium IR bands, but the corresponding vibration in **T3F** (calc.: 965 cm^{-1}) provides low calculated intensity (0.5 km/mol) and therefore it is invisible in the **T3F** IR spectrum. The asymmetric in-plane ring deformations in the phenyl moiety and the nearest benzene ring of the thiantrene fragment with a contribution of the C–F stretching vibrations in the vicinity 770 cm^{-1} show the weak absorption intensity (16–18 km/mol); however, in the **T3F** spectrum, this type of vibrations occurs at a much higher frequency (867 cm^{-1}) and shows a higher IR intensity (67 km/mol). The medium bands with close frequencies in the measured IR spectra in the vicinity 838 cm^{-1} belong to =CH out-of-plane deformations with contribution C–F stretching vibrations, however, the calculated intensities are smaller. The strong band in the measured IR spectra **T4F** sample at 848 cm^{-1} (calc. too 848 cm^{-1}) formed by asymmetric out-of-plane =CH bending vibrations in benzene ring (number **3**) of the thiantrene fragment and symmetric vibrations of the same type in the phenyl ring of the benzoyl fragment. The strong bands with close frequencies in the vicinity 750–760 cm^{-1} (Fig. 8, 9) for all the studied compounds are formed by the superposition of three modes symmetric out-of-plane =CH bending vibrations in aromatic rings. IR bands below 710 cm^{-1} we assigned to ring vibrations out-of- plane or symmetric ring deformations in- plane in aromatic rings.

We connect the observed differences with the significant changes in the electronic properties and structural parameters of the phenyl ring depending on the position of the substituent (fluorine atom), as well as with the slight changes in those parameters in the benzene ring **3** of the thiantrene fragment connected with the benzoyl moiety.

The pseudo-Jahn-Teller effect role in the sructural distortion of thiantrene and its derivatives

This scrutinize analysis of the IR spectral differences for the studied thiantrene-benzoyl derivatives afford to clearly distinguish two isomers **T6F** and **T2F** and also to understand photophysical parameters of the whole isomers family obtained from UV-vis absorption and lumineascence studies [3]. Knowing the accurate force field of all studied molecules we can now analyze in details the structure of the thiantrene ancestor molecule in the ground and excited states in order to transfer the similar vibronic perturbation theory to other benzoyl-containing derivatives accounting the pseudo-Jahn–Teller (PJT) effect.

The best approach to solve the problem of the molecular shape prediction should rise the question: *how do electrons influence and control nuclear configurations?* Or how do electronic states deformations affect the nuclear mutual displacements in terms of vibronic perturbation theory? The Jahn–Teller (JT) theorem says that nonlinear polyatomic molecule in the degenerate electronic states is unstable and spontaneously distorts in order to remove the degeneracy [4]. The most important sequence of the JT theorem is the pseudo-JT effect, which considers excited states involvement into vibronic coupling [4, 5]: when two electronic states are not strictly degenerate but are close in energy (pseudo-degenerate), the JT effect is not quenched but only modified, producing similar structural distortions like those caused by the original JT effect. The PJT effect received little attention from the beginning, but a few decades latter Bersuker et al. showed that there is no limitation on the perturbing states energy gap and that the PJT effect is the only source of distortions (instability) of high-symmetry configurations of any polyatomic molecule [4, 5].

If we know the detailed mechanism of the thiantrene distortion from the planar anthrene configuration via the pseudo-JT effect (since one has revealed the vibronically active excited state in this mechanism), we can try to influence the system by means of external perturbations that violate the pseudo-JT-induced B_{3u} condition of thiantrene instability in the ground state. Such perturbation technique could help us to modulate proper excited state properties of various thiantrene derivatives. In principle, there are four possibilities to provide such perturbation treatment: (a) to increase the energy gap between those electronic states which are mixed by the pseudo-Jahn-Teller vibronic coupling (for example, by conjugation with new substituent like benzoyl outside system), (b) to change the symmetry of the vibronically active excited state by adding number of electrons (which could change the parameters of the pseudo-JT effect and the energy gap), (c) to add appropriate substituents that restore the planarity of molecular structure, and (d) by spectroscopic photoexcitation. The method (a) was used in the studies of the mechanism of hemoglobin oxygenation [4, 5] in which the out-of-plane displacement of Fe(II) ion from the hem-porphyrin ring (induced by forces driven by

pseudo JT effect) returns back into the porphyrin plane by oxygenation due to increase of the energy gap from the active state; this illustrates suppressing of the pseudo-JT effect.

The mechanism (b) was demonstrated recently by Bersuker [5] by coordination of two Cl-anions to on-planar (distorted by the PJTE) chair structures of the Si_6Cl_{12} cluster in order to obtain dianion $[Si_6Cl_{14}]_2^-$ with a planar Si_6-ring; here the pseudo-JT effect is suppressed because the empty molecular orbitals of the excited active state in the Si_6-ring became occupied by electrons from two chloride ions [5].

Bersuker et al. [4, 5] have studied numerous manifestations of the pseudo Jahn-Teller (JT) effect in molecular and solid states structure. They considered the influence of heteroatom substitution in series of tricyclic compounds containing 1,2-dithiine and 1,4-dithiine moieties (carbon sulfide C_6S_8, thianthrene, and anthracene, their redox products and derivatives) in order to demonstrate the mechanism of suppression and enhancement of the puckering distortions in redox processes and in chemical substitutions.

In the most recent study [5] they demonstrated for the first time the chemical substitution ability to restore the planarity of cyclic compounds. Spectroscopic photo-excitations in this respect have not yet been studied exploring the pseudo-JT effect [4], and we will try to perform such perturbation analysis based on our knowledge of the force field for new derivatives.

Let us compare anthracene and thianthrene molecules in the planar structure of the D_{2h} symmetry. The puckering distortion in respect to the 9-10 positions transforms as the B_{3u} irreducible representation of the D_{2h} point group; thus, only excited states of the B_{3u} symmetry need to be considered in the vibronic perturbation of the ground A_{1g} state of anthracene upon its transformation into thianthrene by the sulfur substitution in 9-10 positions. Our choice of axes (z-is perpendicular to the anthracene plane, x-the long axis) differs from that in Ref. [5]; thus, their B_{1u} symmetry corresponds to our B_{3u} representation.

Vibronic mixing of the B_{3u} excited singlet state with the ground S_0 state of the A_{1g} symmetry can be calculated accounting geometry distortion along with the B_{3u} vibrational mode. Thus, we can explain this *butterfly-like* distortion in terms of the pseudo JT effect and explain the real non-planar structure of the thianthrene molecule.

It was shown in Ref. [5] that while the thianthrene molecule is bent at the S-S axis, the oxidized thianthrene dication exhibits a planar configuration with the D_{2h} molecular symmetry. The thianthrene highest occupied molecular orbital (HOMO) b_{3u} is getting empty upon oxidation; that is, it becomes the lowest unoccupied molecular orbital (LUMO) in dication. The thianthrene excited state $b_{3u} \rightarrow a_g$ ($^1B_{3u}$) disappears in the dication, as well as the driving force of the puckering distortion [5]. The reason of the PJT effect in the oxidized thianthrene also disappears which leads to the planar dication structure.

Similarly, we have shown that the first excited S_1 state of thianthrene tends to planarization. In the planar structure S_1 state possesses the $^1B_{3g}$ symmetry ($b_{3u} \rightarrow a_u$ excitation). The perturbing state along the puckering b_{3u} mode could be the ^1A_u state associated with the $a_u \rightarrow a_g$ excitation. Such state has a very large energy (6.2 eV) and the distorting PJT effect in the S_1 excited thianthrene is less pronounced than in the ground S_0 state. This vibronic analysis of the b_{3u} puckering distortion is completely supported by TD DFT geometry optimization. The dihedral angle 2-3-4-9 is close to planarity; it changed from 128 to 167° upon excitation. Geometry optimization in the lowest triplet T_1 state with the UB3LYP functional produces larger planarization with additional distortion and strong spin polarization in one phenyl ring. Thus, the thianthrene molecule in the T_1 state has no symmetry elements, which could explain more efficient spin-orbit coupling and enhanced phosphorescence of the thianthrene crystal [1–3].

*Hirshfeld surfaces analysis for the **T3F** crystal*

The nature of the intermolecular contacts stabilizing the crystal structures of the **T3F** and the peculiarities of the influence of these intermolecular interactions on the IR spectrum were explained by the HS analysis. The **T3F** compound crystallizes in the monoclinic (P2₁/n) space group. The cell packing and HS of the **T3F** mapped over d_{norm} is presented in Figure 10.

As can be seen in the Hirshfeld d_{norm} surface plot, the crystal structure of **T3F** is stabilized by weak long-ranged CH…F, CH…S and CH…O intermolecular interactions with experimental distances of 2.610 Å, 2.923 Å and 2.827/2.860 Å, respectively, which are indicated as barely visible pale red spots in HS. The shortest contact 2.293 Å in **T3F** crystal belongs to weak H…H intermolecular contacts.
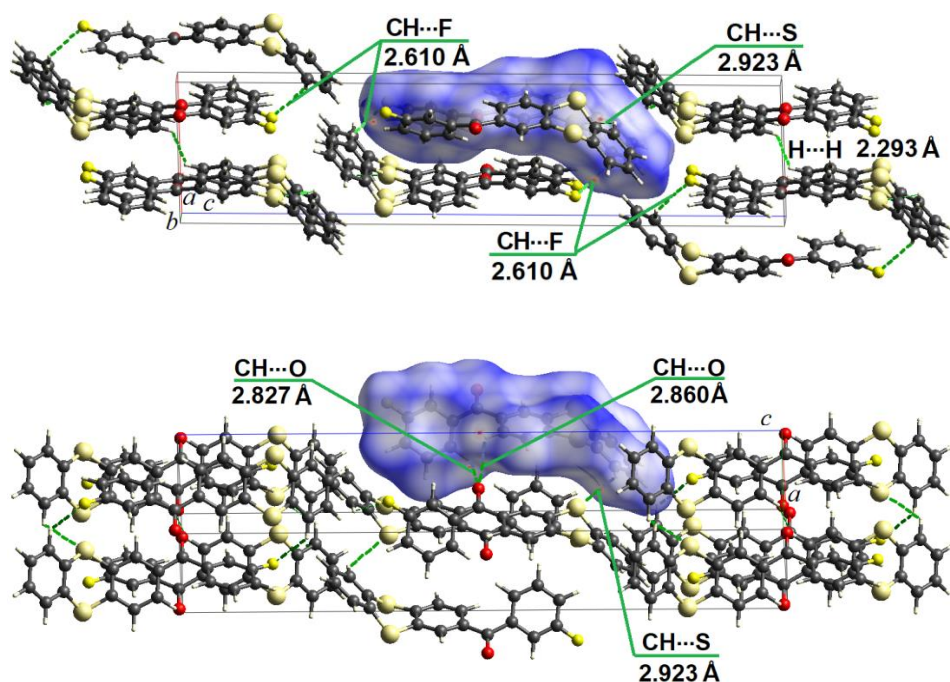
Figure 10. The cell packing and Hirshfeld d_{norm} surface of the intermolecular interactions for **T3F** compound demonstrating CH…F and CH…S interactions (top view) and CH…O interactions (bottom view). Intermolecular interaction is shown by green dashed lines

The study of the manifestation of intermolecular interactions in the IR spectrum of **T3F** was carried out by isolating two dimers (Fig. 11) from the crystal with their further optimization by the B3LYP/6-31G(d, p) method (Fig. S5 in **Supplementary Materials**). This approach has proved to be successful in our recent paper [21–23]. Dimer 1 represents the presence of H…F intermolecular interactions, while dimer 2 displays the shortest H…S and H…O intermolecular interactions. In addition, the CH…S intermolecular interaction between the hydrogen atom of ring I of the thianthrene fragment and the sulfur atom of the neighboring dimer with a distance of 2.923 Å was established (Fig. 10).

Dimer 1   Dimer 2
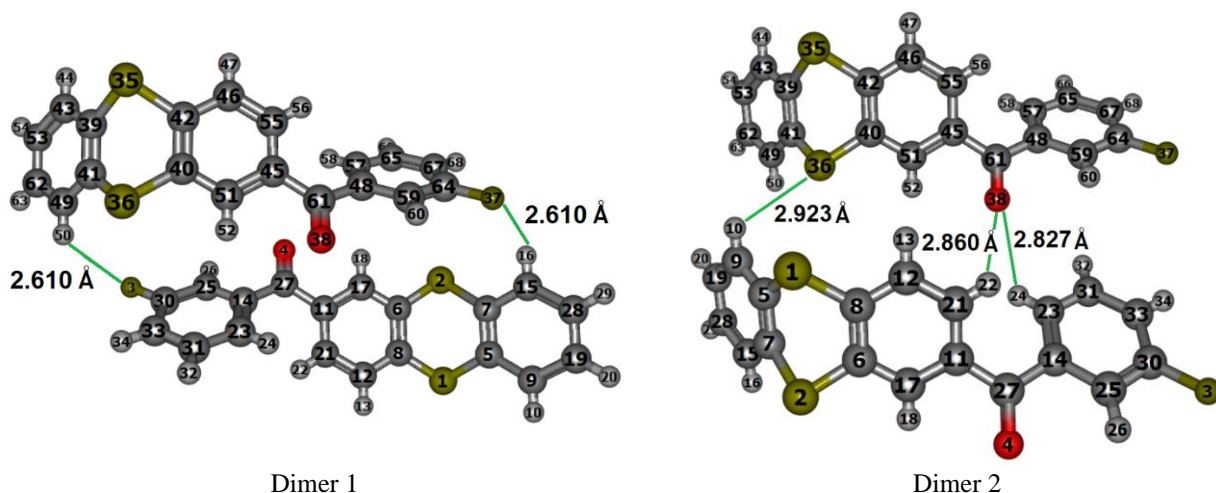
Figure 11. The structures of dimers 1 and 2 of **T3F** selected from the X-ray crystal data.
Selected experimental intermolecular distances (Å) for the dimers are indicated. The S atoms are 1, 2, 35 and 36,
O atoms are 4 and 38, F atoms are 3 and 37. The numbering of atoms in dimers is set by the program
and does not coincide with the numbering of atoms in the **T3F** molecule

Theoretically predicted IR spectra of **T3F** molecule and both dimers are compared with experimental results of **T3F** compound in Figures S3 (in the 3100–3300 cm^{-1} range) and S4 (in the 1700–500 cm^{-1} range). Each of the dimers has 184 normal vibrations. Dimer 1 has the C_h symmetry. For the C_h point group sym-

metry, the normal vibrations of the Dimer 1 can be classified as follows: $92A_g$ (gerade) and $92A_u$ (ungerade). According to the IR vibrational selection rules only A_u vibrations are allowed in the IR spectrum. The calculated Dimer 2 has no symmetry; therefore, all normal vibrations in the IR spectrum of dimer 2 are allowed. As can be seen in Figures S3, S4, the experimental IR spectrum of the **T3F** compound and theoretically predicted IR spectra of both **T3F** dimers and molecule are close. The calculated IR intensities of the corresponding IR bands of Dimers 1 and 2 (Figures S3, S4, curves 2, 3) are much higher than those for the molecule (curve 1), since the calculated intensities are almost doubled for two molecules.

Intermolecular interactions H…F and H…S found in Dimer 1, and H…S found in Dimer 2 do not affect the IR spectrum. The intermolecular interactions H…O found in Dimer 2 form two vibrational modes: ν_{198} (=C21–H (**1**)···O (**2**) and=C23–H (**1**)···O (**2**) stretching in-phase) and ν_{197} (the same stretching out-of-phase) in with frequencies 3084 and 3078 cm^{-1}, respectively; however, their calculated intensities are very weak (0.2 and 2 km/mole, respectively) and therefore they do not give visible bands in the IR spectrum of Dimer 2 (Figures S3, curve 3).

Conclusions

The recently synthesized benzoyl-containing thianthrene derivatives were thoroughly studied by DFT optimization of their ground and excited states structures. The thianthrene donor (D) and benzoyl acceptors (A) moieties connected through the strong carbonyl π-link provide an effective platform for electroluminescent materials, and their detailed electronic structure studies are useful for new molecular electronics device technology. The ground singlet state geometry optimizition by density functional theory with the gradient and Hessian calculations made it possible to study IR spectra of thianthrene molecule and five benzoyl derivatives including series of fluoro-substituted isomers. Detailed comparison of all vibrational modes helped to carry out full assignments of the experimental FTIR spectra of newly synthesized compounds and solve structural problems associated with the X-ray diffraction analysis. It was shown that the change of fluorine atom position in the phenyl ring of benzoyl moiety leads to significant changes of dihedral angles and atomic charger distribution; this in turn leads to notable differences in dipole moments of these four isomers. As a result, in the IR spectra of fluoro-substituted isomers of benzoylthianthrene there are not only frequency shifts but also significant changes in the intensity of the corresponding IR bands. Although the experimental IR spectrum of thianthrene is well known, we have made its first ab initio assignment of all 60 vibrational modes. On this background, we explained the non-planar distortion of the thianthrene molecule in comparison with its planar ancestor — anthracene molecule, accounting vibronic activity of the b_{3u} vibrational mode (with imaginary frequency -i 67 cm^{-1}) of the D_{2h} point group. Knowledge of the accurate force field of all studied molecules made it possible to analyze the structure distortions of thianthrene in the ground and excited states and to transfer the similar vibronic perturbation theory to the benzoyl-containing derivatives accounting the pseudo-Jahn–Teller (PJT) effect.

Comparing the planar thianthrene configuration of the D_{2h} molecular symmetry, it was noted that the highest occupied molecular orbital b_{3u} becomes half-empty upon excitation to the S_1 and T_1 states. In the planar structure the S_1 state possesses the $^1B_{3g}$ symmetry ($b_{3u} \rightarrow a_u$ excitation). The pseudo-Jahn–Teller perturbing state along the puckering b_{3u} mode is the ^1A_u state produced by the $a_u \rightarrow a_g$ excitation. Such a state has a very high energy, and the distorting PJT effect in the S_1 excited thianthrene is strongly suppressed in comparison with the ground S_0 state. This vibronic analysis of the b_{3u} puckering distortion was supported here by TD DFT geometry optimization of the S_1 excited thianthrene, which showed obvious trend to planarization. At the same time the fully optimized S_1 and T_1 states lost their symmetry and exhibited some pseudo-in-plane distortion.

The Hirshfeld surface analysis indicated the weak CH…F, CH…S and CH…O intermolecular interactions as barely visible pale red spots in the d_{norm} surface of the **T3F** crystal. We used the dimeric approach to determine their influence on the IR spectrum of **T3F**. It was found that only CH…O intermolecular interactions appear in the IR spectrum of **T3F** crystal as two very weak stretching in-phase and stretching out-of-phase vibrations at 3084 and 3078 cm^{-1}, respectively.

References

1   Arena, A., Campagna, S., Mezzasalma, M., Saija, R. & Saitta, G. (1993). Analysis of the Phosphorescence of Thianthren Crystals. *Nuovo Cimento*, *15*, 1521–1532. https://doi.org/10.1007/BF02451943

2   Pander, P., Swist, A., Soloducho, J. & Dias, F.B. (2017). Room temperature phosphorescence lifetime and spectrum tuning of substituted thianthrenes. *Dyes and Pigments*, *142*, 315–322. http://dx.doi.org/10.1016/j.dyepig.2017.03.049

3   Volyniuk, L., Gudeika, D., Panchenko, A., Minaev, B.F., Mahmoudi, M., Simokaitiene, J., Bucinskas, A., Volyniuk, D. & Grazulevicius J.V. (2023). Single-molecular white emission of organic thianthrene-based luminophores exhibiting efficient fluorescence and room temperature phosphorescence induced by halogen atoms. *ACS Sustainable Chemistry & Engineering* (in press).

4   Bersuker, I.B. (2013). Pseudo-Jahn–Teller Effect — A Two-State Paradigm in Formation, Deformation, and Transformation of Molecular Systems and Solids. *Chemical Review, 113*, 1351–1390. https://doi.org/10.1021/cr300279n

5   Gorinchoy, N.N. & Bersuker, I.B. (2017). Pseudo Jahn-Teller effect in control and rationalization of chemical transformations in two-dimensional compounds. *Journal of Physics: Conf. Series, 833*, 012010. https://doi.org/10.1088/1742-6596/833/1/012010

6   Becke, A.D. (1993). Density-functional thermochemistry. III. The role of exact exchange. *J. Chem. Phys., 7*, 5648–5652. https://doi.org/10.1063/1.464913

7   Lee, C., Yang, W. & Parr, R. G. (1988). Development of the Colle-Salvetti correlation-energy formula into a functional of the electron density. *Phys. Rev. B Condens. Matter.*, *37*, 785–789. https://doi.org/10.1103/physrevb.37.785

8   Raghavachari, K., Binkley, J.S., Seeger, R. & Pople, J.A. (1980). Selfconsistent molecular orbital methods. 20. Basis set for correlated wave functions. *J. Chem. Phys.*, *72*, 650–654. https://doi.org/10.1063/1.438955

9   Stewart, J.J.P. (1989). Optimization of parameters for semi-empirical methods I. Method. *J. Comput. Chem., 10*, 209–220. https://doi.org/10.1002/jcc.540100208

10   Stewart, J.J.P. (2004). Optimization of parameters for semi-empirical methods IV: extension of MNDO, AM1, and PM3 to more main group elements. *J. Mol. Model.*, *10*, 155–164. https://doi.org/10.1007/s00894-004-0183-z

11   Cambridge Crystallographic Data Centre. (2023, May 15) CCDC deposition number 2160882. https://www.ccdc.cam.ac.uk/structures/Search? Ccdcid=2160882&DatabaseToSearch=Published

12   Scott, A. P. & Radom, L. (1996). Harmonic vibrational frequencies: an evaluation of Hartree−Fock, Møller−Plesset, quadratic configuration interaction, density functional theory, and Semiempirical scale factors. *J. Phys. Chem.*, *100*, 16502–16513. https://doi.org/10.1021/jp960976r

13   Dennington, R., Keith, T.A., Millam & J.M. (2016). GaussView, Version 6. Semichem Inc., Shawnee Mission, KS. https://gaussian.com/gaussview6/

14   Zhurko, G.A., Zhurko, G.A. & Romanov, A. (2011). Chemcraft — graphical software for visualization of quantum chemistry computations. http://www.chemcraftprog.com/

15   Frisch, M.J., Trucks, G.W., Schlegel, H.B., Scuseria, G.E., Robb, M.A., Cheeseman, J.R. et al. (2016). Gaussian 16, Revision A.03, Gaussian, Inc., Wallingford, CT. https://gaussian.com/

16   Turner, M.J., McKinnon, J.J., Wolff, S.K., Grimwood, D.J., Spackman, P.R., Jayatilaka, D. & Spackman, M.A. (2017). Crystal Explorer 17.5. University of Western Australia. https://crystalexplorer.net/

17   McKinnon, J.J., Spackman, M.A. & Mitchell, A.S. (2004). Novel tools for visualizing and exploring intermolecular interactions in molecular crystals. *Acta Crystallogr. Sect. B Struct. Sci., 60*, 627–668. https://doi.org/10.1107/S0108768104020300

18   Lynton, H. & Cox, E.G. (1956). The Crystal and Molecular Structure of Thianthren. *J. Chem. Soc.,* 4886–4895. https://doi.org/10.1039/JR9560004886

19   NIST Chemistry WebBook. (2023, May 15). Thianthrene. https://webbook.nist.gov/cgi/cbook.cgi? ID=C92853&Mask=80

20   Socrates, G. (2001). Infrared Raman Characteristic Group Frequencies — Tables and Charts, 3rd ed. J. Wiley&Sons, Chichester. https://doi.org/10.1021/ja0153520.

21   Minaeva, V.A., Karaush-Karmazin, N.N., Panchenko, A.A., Heleveria, D.N. & Minaev, B.F. (2021). Hirshfeld surfaces analysis and DFT study of the structure and IR spectrum of N-ethyl-2-amino-1-(4-chlorophenyl)propan-1-one (4-CEC) hydrochloride. *Comput. Theor. Chem.*, 1205, 113455. https://doi.org/10.1016/j.comptc.2021.113455

22   Minaeva, V., Panchenko, A., Karaush-Karmazin, N., Nycz, J. & Minaev, B. (2023). Manifestation of Intermolecular Interactions in the IR Spectra of 2- and 4-Methylmethcathinones Hydrochlorides: DFT Study and Hirshfeld Surfaces Analysis. *Biointerface Res. Appl. Chem.*, 13, 202. https://doi.org/10.33263/BRIAC133.202

23   Minaeva, V., Karaush-Karmazin, N., Panchenko, A., Minaev, B. & Ågren, H. (2023). Hirshfeld and AIM Analysis of the Methylone Hydrochloride Crystal Structure and Its Impact on the IR Spectrum Combined with DFT Study. *Crystals*, 13, 383. https://doi.org/10.3390/cryst13030383

Information about authors*

Minaeva, Valentina Alexandrovna — Senior Researcher, Assistant Professor, Department of Chemistry and Nanomaterials Science, Bohdan Khmelnytsky National University, 18031, Cherkasy, Ukraine; e-mail: minaeva@cdu.edu.ua; https://orcid.org/0000-0001-9318-1661

Karaush-Karmazin, Natalia Mikolaevna (*corresponding author*) — Senior Researcher, Department of Chemistry and Nanomaterials Science, Bohdan Khmelnytsky National University, 18031, Cherkasy, Ukraine; e-mail: karaush22@ukr.net; https://orcid.org/0000-0001-9360-2593

Panchenko, Olexandr Olexandrovich — Researcher, Department of Chemistry and Nanomaterials Science, Bohdan Khmelnytsky National University, 18031, Cherkasy, Ukraine; e-mail: panchenko9b@gmail.com; https://orcid.org/0000-0001-7669-1424

Chernyk, Maryana Vitalievna — Undergraduate, Department of Chemistry and Nanomaterials Science, Bohdan Khmelnytsky National University, 18031, Cherkasy, Ukraine; e-mail: maryana2001a@gmail.com;

Simokaitiene, Jurate — Dr., Department of Polymer Chemistry and Technology, Kaunas University of Technology Barsausko 59, LT-51423, Kaunas, Lithuania; e-mail: jurate.simokaitiene@ktu.lt, https://orcid.org/0000-0003-0657-4980

Volyniuk, Dmytro Yu. — Dr., Department of Polymer Chemistry and Technology, Kaunas University of Technology, Barsausko 59, LT-51423, Kaunas, Lithuania; e-mail: dmytro.volyniuk@ktu.lt; https://orcid.org/0000-0003-3526-2679

Grazulevicius, Juozas Vidas — Professor, Department of Polymer Chemistry and Technology, Kaunas University of Technology, Barsausko 59, LT-51423, Kaunas, Lithuania; e-mail: juozas.grazulevicius@ktu.lt; https://orcid.org/0000-0002-4408-9727

Minaev, Boris Filippovich (*corresponding author*) — Doctor Of Chemical Sciences, Professor, Department of Chemistry and Nanomaterials Science, Bohdan Khmelnytsky National University, 18031, Cherkasy, Ukraine; Senior Researcher, Department of Physics and Astronomy, Uppsala University, SE-752 37 Uppsala, Sweden; e-mail: bfmin43@ukr.net; https://orcid.org/0000-0002-9165-9649

Reshetnyak, Oleksandr Volodimirovich — Professor, Chairperson, Department of Physical and Colloid Chemistry, Ivan Franko National University of Lviv, Universitetskaya st., 1, 79000, Lviv, Ukraine; e-mail: oleksandr.reshetnyak@lnu.edu.ua; https://orcid.org/0000-0001-9669-9431

_____

*The author's name is presented in the order: *Last Name, First and Middle Names*

Andrey V. Ryabykh [ID], Olga A. Maslova [ID], Sergey A. Beznosyuk* [ID]

Department of Physical and Inorganic Chemistry, Altai State University, Barnaul, Russia
(*Corresponding author's e-mail: bsa1953@mail.ru)

Mechanisms of Docking of Superoxide Ions in the Catalytic Cycle of Manganese and Iron Superoxide Dismutases

In this paper, we propose an approach to resolving some questions about the catalytic action of manganese and iron superoxide dismutases. At the level of a pure quantum-chemical calculation using an ORCA 5.0.3 program, a PBE functional and a def2-SVP and def2-TZVP basis sets, the possible mechanisms of superoxide ions binding to the active sites of enzymes, the electron transfer distances and their characteristics were established. It is shown that the initial form of the fifth ligand in both active sites is the hydroxide ion OH^-. Before the primary electron transfer, active sites are protonated, the hydroxide ion is converted into a water molecule H_2O. Primary electron transfers from the superoxide ion to Mn^{3+}-SOD and Fe^{3+}-SOD occur by the associative mechanism, with the formation of an octahedral complex, at a transfer distance of 1.95 Å and 2.56 Å, respectively. At the second stage, the superoxide ion accepts the electron by the substitution mechanism from Mn^{2+}-SOD at the transfer distance of 2 Å to form bonds with the water molecule and a tyrosine. The superoxide ion accepts the electron from Fe^{2+}-SOD through the outer-sphere mechanism, where it binds to a histidine and the water molecule at the transfer distance of 4.24 Å.

Keywords: manganese superoxide dismutase, iron superoxide dismutase, electron transfer, computer simulation, density functional theory, catalytic mechanism.

Introduction

In the course of metabolic transformations in a living organism, oxygen O_2 is able to turn into extremely reactive particles — reactive oxygen species (ROS). One of the first in the sequence of formation of free radicals is the superoxide ion O_2^-. Their accumulation can adversely affect the state of cellular components, destroying them and leading to various diseases of the body as a whole [1]. In a healthy body, antioxidants and antioxidant enzymes provide protection against excessive ROS production. Enzymes of the superoxide dismutase (SOD) group ensure the neutralization of superoxide ions O_2^- to molecular oxygen O_2 and hydrogen peroxide molecules H_2O_2. These enzymes contain 3d-metals (for example, Mn-SOD considered in this study contains Mn^{3+} ion and Fe-SOD contains Fe^{3+} ion). In the first half of the catalytic cycle, the SOD active site takes one electron from the superoxide ion, while the Me^{3+} ion is reduced to Me^{2+}. In the second half of the catalytic cycle, the SOD active site donates one electron to the superoxide ion, while the Me^{2+} ion is oxidized to Me^{3+} [2, 3]. Manganese superoxide dismutase is present in all eukaryotic organisms. It is contained in the mitochondrial matrix, where ROS are directly formed. Thus, Mn-SOD is one of the first steps in the antioxidant protection of cell components [4]. Iron superoxide dismutase is found mainly in prokaryotes [5]. It is noteworthy that the active sites of manganese and iron superoxide dismutases have the same structure.

At the moment, some questions regarding the mechanism of ROS neutralization by these superoxide dismutases still remain debatable. There are reasons for this that somewhat limit direct experimental studies. It is noted that these reasons are the extremely high rate of the catalytic reaction, the low half-life of the superoxide ion in an aqueous-protein medium, and the difficulty in detecting protons and protonated amino acid residues. The corresponding problems are covered in the review article [4]. Since more stable azide ions N_3^- are often used instead of them in studies of the mechanisms of reactions involving superoxide ions O_2^-, the question remains whether the superoxide ion and the metal ion are directly bound during electron transfer, or whether the transfer proceeds at a long distance with the participation of ligands. In addition, there are controversial points regarding the conditions for the participation of protons in this reaction, since their presence is important in the second stage, where hydrogen peroxide is formed from the superoxide ion. There are the following questions. At what distance do electron transfers occur? What is the nature of the fifth ligand

attached to the metal ion during electron transfers: a hydroxide ion or a water molecule? When does the first proton transfer occur: before the primary electron transfer or after? What is the main source of the proton in electron transfers?

In this study, the authors propose a solution to these issues based on computer simulation using a pure quantum chemical method. Since manganese and iron superoxide dismutases have the same structure of the active center, it is possible to compare the role of the nature of the metal ion in the efficiency of ROS neutralization. Methods for docking the superoxide ion and the active center of manganese and iron superoxide dismutase were studied with an estimate of the electron transfer distance at two stages of catalytic cycles. The thermodynamic and kinetic characteristics of electron transfers are obtained according to the Marcus transfer theory [6].

Computational Details

Modeling was carried out using the ORCA software package version 5.0.3 [7]. As a calculation method, we used the level of density functional theory using the GGA density functional of Perdew–Burke-Ernzerhof PBE [8]. The def2-TZVPD basis set [9] was used to optimize the geometry and calculate single point energies of small particles (O_2^-, O_2, HO_2, HO_2^-, H_2O, H_3O^+). When optimizing the geometry of the active site, a simplified def2-SVP basis [9] was used with additional restrictions in the form of pinning 8 hydrogen atoms of the methyl groups to simulate the fact that the active site is retained by the protein environment [10]. After geometry optimization, the single point energy of the active site structure was calculated with the def2-SVPD basis. In addition, in all cases, when calculating the active site, the oxygen atoms O, manganese Mn, and iron Fe were always subject to the def2-TZVPD basis set. In any calculation, to take into account fine dispersion interactions, the atomic pair dispersion correction algorithm based on rigidly coupled partial charges D4 was used [11]. The influence of the dielectric medium was taken into account using the CPCM continuum model. The surface type is Gaussian VdW [12]. Since the active sites in the protein are located in the solvent access zone, the corresponding values of the dielectric constant and refractive index of water were taken as parameters of the solvent model ($\varepsilon = 80{,}4$; $n = 1{,}333$).

Figure 1 shows a structure of the active site of the enzymes that were modeled. The proposed sources of the proton during the secondary electron transfer are indicated there. Position 4, which is an external solvent, is not shown in the figure. Two histidine ligands (His) and one aspartate ion (Asp) are in equatorial positions. The third His and the aqueous ligand are in axial positions. The aqueous ligand can be either a hydroxide ion OH^- or the water molecule H_2O. The second coordination sphere contains the amino acid tyrosine (Tyr).
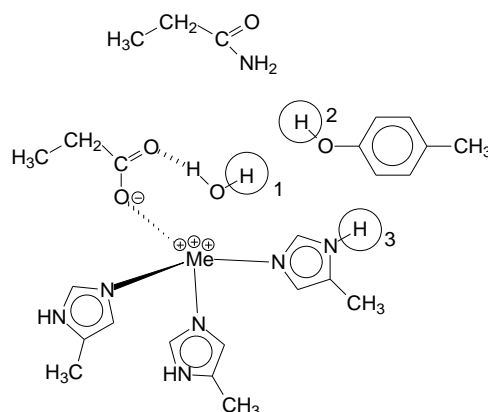
1 — proton of the water molecule; *2* — proton of the hydroxyl group;
3 — proton of the histidine ligand. Me = Mn, Fe

Figure 1. Proton sources in the Me-SOD active site

The electron transfer distances R and the corresponding Marcus transfer rate constants k_{obs} served as the main selection criteria for a possible mechanism of superoxide ion binding to active sites. Estimating the electron transfer distance is often a rather non-trivial task, and often this value is introduced, for example, by fitting. In this work, the following approach was used. The transfer distance R was estimated by constructing the potential energy surface (PES) profile when donor D and acceptor A approached each other. For the systems under consideration (oxygen–superoxide dismutase), the variable distance was the distance between the

active form of oxygen and the metal atom (Mn, Fe). The points of local minima on the PES were taken as the transfer distance. Under the conditions of being in the energy minimum, the system can stay longer. Therefore, the probability of electron transfer increases when the electron terms of the donor and acceptor cross. However, only the energy minimum is not a sufficient condition, since there can be several such extrema on one PES. An analysis of the spin population of atoms according to Mulliken can serve as a sufficient criterion for selecting the required minimum. We plotted the functions of the dependence of the difference between the spin populations of the donor and acceptor on the distance. The combination of minima on the PES and a sharp change in the function of the population difference gave the estimated transfer distance R. This study considers three variants of the superoxide ion docking mechanism. The first is associative, in which the superoxide ion enters the first coordination environment of the metal to form an octahedral structure. The second is substitutional, in which the superoxide ion enters the first coordination environment of the metal and replaces one of the five ligands. The third is outer-sphere, in which the superoxide ion combines with one of the ligands without forming a bond with the metal ion.

The rate constant of the Marcus second-order electron transfer reaction k was estimated using the following equation [6]:

$$k = k_{et} \cdot K_{pre}^{\neq} = \frac{8 \cdot \pi^3}{3 \cdot h} \cdot \frac{H_{DA}^2}{\sqrt{\pi \cdot \lambda_{tot} \cdot k_B \cdot T}} \cdot N_A \cdot R^3 \cdot \exp\left(-\frac{\Delta G^{\neq} + W_R}{k_B \cdot T}\right),$$ (1)

where h — the Planck's constant, J·s; H_{DA} — an electronic interaction matrix element, J; λ_{tot} — a total energy of the system reorganization, J; k_B — the Boltzmann constant, J/K; T — the temperature, K; N_A — the Avogadro constant, mol^{-1}; R — the electron transfer distance, dm; $\Delta G^{\neq}$ — the transfer activation energy, J; W_R — an electrostatic work of convergence of donor and acceptor, J.

The algorithm for estimating the quantities H_{DA}, λ_{tot}, $\Delta G^{\neq}$ and W_R is given in the article [13].

Equation (1) is suitable for the case when the electronic terms intersect insignificantly, the matrix element H_{DA} has values of the order of $1.5 \cdot k \cdot T$, and the electron transfer proceeds non-adiabatically. If the electronic terms overlap significantly, then an adiabatic splitting of the PES occurs. In this case, it is preferable to calculate the electron transfer rate constant using the following equation [14]:

$$k^{AD} = k_{et}^{AD} \cdot K_{pre}^{\neq} = \frac{v \cdot \varepsilon}{3 \cdot n^2} \cdot \sqrt{\frac{\pi \cdot \lambda_{tot}}{k_B \cdot T}} \cdot N_A \cdot R^3 \cdot \exp\left(-\frac{\Delta G^{\neq} + W_R}{k_B \cdot T}\right),$$ (2)

where v — the solvent nuclear reorganization rate = $1.25 \cdot 10^{11}$ s^{-1} (at 298.15 K); ε — the solvent dielectric constant; n — the solvent refractive index.

The donor and acceptor radii used in the calculation of the energy of reorganization and electrostatic work are also ambiguous from the point of view of their estimation. The radius of an oxygen-containing particle is estimated as the sum of half of the O–O bond length and the radius of an oxygen atom. The radius of the active site strongly depends on the distance R and is estimated in each case separately for the atoms atomic orbitals of which are involved in the formation of the molecular orbital involved in electron transfer. For the cases of associative and substitutional mechanisms, where R is less than 3 Å, the covalent radii of atoms were taken (0.66 Å for O and 0.71 Å for N [15]). For the case of the outer sphere mechanism, the van der Waals radii of atoms were taken (1.55 Å for O and 1.60 Å for N [16]).

The electron transfer accompanies the diffusion of reactants to each other. Therefore, the experimentally observed value of the rate constant k_{obs} of the catalytic process is a combination of the second-order rate constants k of electron transfer and diffusion of reactants k_{diff} [17]:

$$k_{obs} = \frac{k \cdot k_{diff}}{k + k_{diff}},$$ (3)

where k — the rate constant of the Marcus second-order electron transfer reaction, M^{-1}·s^{-1}; k_{diff} — the diffusion rate constant of transfer reagents, M^{-1}·s^{-1}.

The constant k_{diff} in the continuum solvent model can be estimated using the Smoluchowski equation [18]:

$$k_{diff} = 4 \cdot \pi \cdot N_A \cdot (D_D + D_A) \cdot (r_D + r_A),$$ (4)

where D — a diffusion coefficient, m^2·s^{-1}; r — the radii of the reactants, m.

At T = 298.15 K in the aqueous medium for an oxygen-containing particle $D = 2.1 \cdot 10^{-9}$ m^2/s [17]. D for the active site as a massive slow-moving particle is taken as 0. Based on k and k_{diff}, the observed electron transfer rate constant k_{obs} is calculated.

To assess the intermolecular and coordination bonds of atoms, the topological analysis of the electron density according to Bader was used in the framework of the QTAIM theory of atoms in molecules. Based on the results of the topological analysis, the bond critical points (3; –1) were identified and the values of the electron density ρ and the Laplacian of the electron density $\Delta\rho$ at these points were calculated using the Multiwfn 3.8 software package [19]. For the topological analysis of the electron density, the following designations of atoms are introduced here. The ligand containing the N^1 atom is axial in the trigonal bipyramid and is located opposite the hydroxide ion. Ligands containing N^2 and N^3 atoms are equatorial and located opposite the aspartate ligand.

Results and Discussion

The results of this study showed that the high-spin structures of active sites are the most stable. Thus, the active site of Mn^{3+}-SOD in the oxidized form due to Mn^{3+} has a quintet state, and the active site of Fe^{3+}-SOD in the oxidized form due to Fe^{3+} has a sextet state. In the reduced form, the Mn^{2+}-SOD and Fe^{2+}-SOD active sites have sextet and quintet states, respectively.

Consider the first half of the catalytic cycle. Here, the superoxide ion is the electron donor and the superoxide dismutase active site is the electron acceptor. In the oxidized original form of these enzymes, the first coordination environment of the metal contains the hydroxyl ion OH^-. During the catalytic process, this ligand can be replaced by the water molecule. What form of the active site is an electron acceptor: with an OH^- or H_2O ligand? Let us consider two options for the implementation of the primary electron transfer. In the first variant, the electron acceptor will be the active site, where the ligand for the metal ion is the hydroxide ion. In this case, the change in the Gibbs function of primary electron transfer for active centers is $\Delta G^0(Mn) = +0.434$ eV and $\Delta G^0(Fe) = +0.014$ eV. Positive values indicate that the interaction of the superoxide ion with the active site in the presence of the hydroxide ion is thermodynamically unfavorable. In the second case, the electron acceptor will be the active site, where the ligand for the metal ion is the water molecule. In this case, the change in the Gibbs function of primary electron transfer for active sites is $\Delta G^0(Mn) = -0.695$ eV and $\Delta G^0(Fe) = -1.109$ eV. Strongly negative values indicate that the interaction of the superoxide ion with the active site in the presence of a water molecule is thermodynamically favorable. Based on these data, it can be concluded that before the primary electron transfer, a proton transfer occurs, while it attaches to the hydroxide ion to form the water molecule. The source of the proton is the hydronium ion from the solvent.

Next, we consider the interaction of the superoxide ion with the transfer of an electron to the active site of manganese and iron superoxide dismutases. The attack of the low-molecular particle occurred from the side of the solvent, where in the natural form of the protein, no atoms prevented the passage of the ion to the metal. In Figure 2, under (*a*), the potential energy curves of the approach of the superoxide ion O_2^- to the manganese ion Mn^{3+} and the corresponding differences in spin population are shown, and under (*b*), the energies of the approach of the superoxide ion O_2^- to the iron Fe^{3+} ion and the corresponding differences in the spin population are shown.

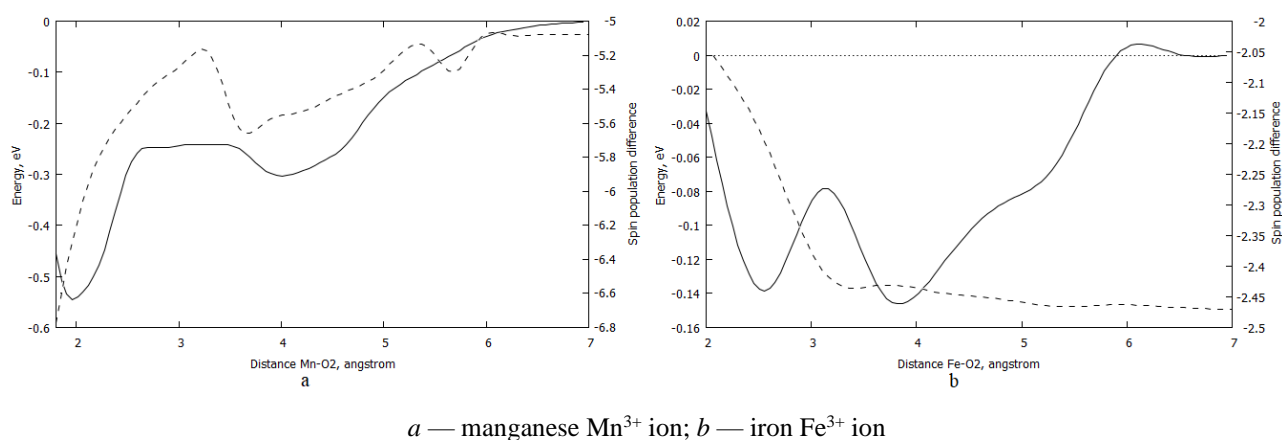

a — manganese Mn^{3+} ion; *b* — iron Fe^{3+} ion

Figure 2. Curves of the potential energy of the interaction between the superoxide ion O_2^-
and the active site of superoxide dismutase (left y-axis and solid line)
and the corresponding spin population differences (right y-axis and dashed line)

For the case with the manganese active site, two minima are observed. The first at $R_1 = 4.1$ Å is due to the interaction of the superoxide ion and the water molecule. The most stable and characteristic minimum is observed at $R_2 = 1.95$ Å. The superoxide ion enters the first coordination sphere of manganese. In this case, the trigonal-bipyramidal coordination will change to octahedral. A sharp change in the spin population difference starts from 3.2 Å. This coincides with the equilibrium distance of 1.95 Å. The most probable electron transfer distance is in the vicinity of this minimum. This allows us to discard the outer-sphere and substitution mechanisms and consider only the associative mechanism of electron transfer. The acceptor radius r_A is estimated as the sum of the distance from the manganese atom to the hydroxide ion (2.157 Å) and the covalent radius of the oxygen atom (0.66 Å).

For the case with the iron active site, stable and characteristic minima are observed at $R_1 = 3.8$ Å and $R_2 = 2.6$ Å. A sharp change in the spin population difference starts from 3.3 Å. This coincides with the equilibrium distance of 2.6 Å. The most probable electron transfer distance is in the vicinity of this minimum. The superoxide ion enters the first coordination sphere of iron. In this case, the trigonal-bipyramidal coordination will change to octahedral. This interaction does not imply substitution and outer sphere mechanisms. The reason may be the very nature of the water ligand. With the manganese ion Mn^{3+}, after the formation of the water molecule, the proton goes to Asp. As a result, the hydroxide ion OH^- is there, which, as the superoxide ion approaches, again acquires a proton from the Asp ligand. Further, this proton oscillates between the oxygen of the water and the oxygen of the superoxide ion, providing additional stabilization of the system. With an iron ion, this phenomenon is not observed. The acceptor radius r_A is estimated as the sum of the average distance from the iron atom to nitrogen atoms (2.012 Å) and the covalent radius of the nitrogen atom (0.77 Å). Table 1 shows changes in the Gibbs functions ΔG^0, reorganization energy λ_{tot}, and activation energy $\Delta G^{\neq}$, as well as estimates of the first and second order electron transfer rate constants in the framework of the Marcus paradigm for the primary electron transfer from the superoxide ion to the active site. The rate constants are given for non-adiabatic and adiabatic calculation options. The preferred option is in bold.

T a b l e   1

Kinetic and thermodynamic characteristics according to Marcus of the primary electron transfer from the superoxide ion to the Me-SOD active site

Parameter	Association mechanism	
	Mn-SOD	Fe-SOD
ΔG^0, eV	−0.695	−1.109
r_D, Å	1.337	1.337
r_A, Å	2.817	2.648
R, Å	1.95	2.56
λ_{tot}, eV	1.840	2.114
$\Delta G^{\neq}$, eV	0.065	0.015
H_{DA}, eV	0.0861	0.2038
k_{diff}, $M^{-1} \cdot s^{-1}$	$2.02 \cdot 10^9$	$2.02 \cdot 10^9$
k_{et} (k_{et}^{AD}), s^{-1}	$7.29 \cdot 10^{12}$ (**$7.18 \cdot 10^{11}$**)	$2.64 \cdot 10^{14}$ (**$5.34 \cdot 10^{12}$**)
k (k^{AD}), $M^{-1} \cdot s^{-1}$	$4.14 \cdot 10^{13}$ (**$4.08 \cdot 10^{12}$**)	$2.59 \cdot 10^{15}$ (**$5.24 \cdot 10^{13}$**)
k_{obs} (k_{obs}^{AD}), $M^{-1} \cdot s^{-1}$	$2.02 \cdot 10^9$ (**$2.02 \cdot 10^9$**)	$2.02 \cdot 10^9$ (**$2.02 \cdot 10^9$**)

Transitions in Mn^{3+}-SOD-O_2^- are transitions between the quartet ground (Q0) and quartet first (Q1) states. Unlike Fe^{3+}-SOD-O_2^-, Mn^{3+}-SOD-O_2^- transfer involves α-electrons. The unpaired electrons of the Mn^{3+}-SOD active center and the O_2^- superoxide ion have oppositely directed spins. The transition in Fe^{3+}-SOD-O_2^- is a transition between the septet ground (H0) and septet first excited (H1) states. All interactions are adiabatic due to the high value of the H_{DA} matrix element.

It is noteworthy that the inner-sphere reorganization energy is 2 times lower for Fe^{3+}-SOD than for Mn^{3+}-SOD, which is associated with smaller structural perturbations after the primary electron transfer. But at the same time, the outer-sphere reorganization energy is higher for Fe^{3+}-SOD. The reactions of electron transfer from superoxide ions to the active site of manganese and iron superoxide dismutases by the associative mechanism proceed in the diffusion mode. The primary electron transfer in the case of iron superoxide dismutase is an order of magnitude faster than in the case of manganese superoxide dismutase.

Thus, the primary electron transfer from the superoxide ion to the active site of Mn^{3+}-SOD and Fe^{3+}-SOD proceeds according to the associative mechanism with the formation of an octahedral coordination of

the metal ion. This indicates a high chemical affinity between the negatively charged superoxide ion and the positively charged metal ion. The metal ion exerts a strong polarizing effect on the superoxide ion and detaches an electron from it. Next, we consider the features of the behavior of the electron density at the bonding critical points of the complex of the superoxide ion and the Me-SOD active site in various versions of the mechanism of binding the superoxide ion and the metal (Table 2).

T a b l e 2

Critical bonding points (3; –1) for primary electron transfer in the Me-SOD donor-acceptor complex.
Parameters ρ and Δρ are expressed in atomic units

Bond	Parameter	Associative mechanism	
		Mn-SOD	Fe-SOD
Me–N^1	ρ	0.0790	0.0709
	Δρ	+0.302	+0.282
Me–N^2	ρ	0.0737	0.0709
	Δρ	+0.275	+0.266
Me–N^3	ρ	0.0540	0.0705
	Δρ	+0.191	+0.284
Me–O^{Asp}	ρ	0.0704	0.0846
	Δρ	+0.293	+0.381
Me–H$_2$O	ρ	0.0598	0.0596
	Δρ	+0.234	+0.241
Me–O$_2^-$	ρ	0.1002	0.0244
	Δρ	+0.382	+0.075

The Mn–N^3 bond, which is located perpendicular to the Mn–O$_2$ bond in the octahedron, is strongly weakened. In other bonds, the share of ionicity increases. Since the superoxide ion in the octahedral Fe-SOD complex is located at a greater distance than in the Mn-SOD complex, it has less effect on other iron ligands. The Fe–Asp bond is weakened the most. The superoxide ion is much more strongly bound to the Mn^{3+} ion than to the Fe^{3+} ion.

Consider the second half of the catalytic cycle. Here, the active site Me^{2+}-SOD acts as a donor, and the superoxide ion O$_2^-$ acts as an acceptor. The secondary electron transfer, like the primary one, is complicated by the coupled proton transfer. In view of the instability of the peroxide ion O$_2^{2-}$ in an aqueous medium, it makes sense to assume that prior to electron transfer, a proton is transferred to the superoxide ion O$_2^-$, and the hydroperoxide radical HO$_2$· is formed [13].

In the Mn-SOD and Fe-SOD active sites, there are several variants of the proton source that attaches to the superoxide ion after it is attached to the active site. They are shown in Figure 1. We have four main sources of the proton. 1. A proton is split off from the water molecule, which is in the first ligand environment of the Me^{2+} ion. 2. The proton is split off from the hydroxyl group from the phenol residue, which is in the second ligand environment of the Me^{2+} ion. 3. The proton is split off from the nitrogen atom of the histidine residue, which is in the first ligand environment of the Me^{2+} ion. 4. The proton joins the O$_2^-$ ion in a place outside the active site. Consider the energy of protonation ΔG$_{pr}$ followed by electron transfer ΔG^0. These data are presented in Table 3.

T a b l e 3

Protonation (ΔG$_{pr}$) and secondary electron transfer (ΔG^0) energies in Me-SOD

Source	1	2	3	4
Mn^{2+}-SOD				
ΔG$_{pr}$, eV	+0.692	+0.369	+0.356	–
ΔG^0, eV	–0.927	+0.236	+0.072	+0.202
Fe^{2+}-SOD				
ΔG$_{pr}$, eV	+0.647	+0.384	+0.360	–
ΔG^0, eV	–0.508	+0.151	+0.353	+0.616

It can be seen that protonation of superoxide from the water molecule (source 1) is most advantageous, followed by electron transfer to the hydroperoxide radical HO$_2$·. In this case, the water molecule is converted into the hydroxide ion OH$^-$.

Next, we consider the interaction of the superoxide ion with electron transfer from the active site of manganese and iron superoxide dismutases to the hydroperoxide radical. In Figure 3, under (*a*), the potential energy curves of the approach of the superoxide ion O$_2^-$ to the manganese ion Mn^{2+} and the corresponding differences in spin population are shown, and under (*b*), the energies of the approach of the superoxide ion O$_2^-$ to the iron Fe^{2+} ion and the corresponding differences in the spin population are shown.
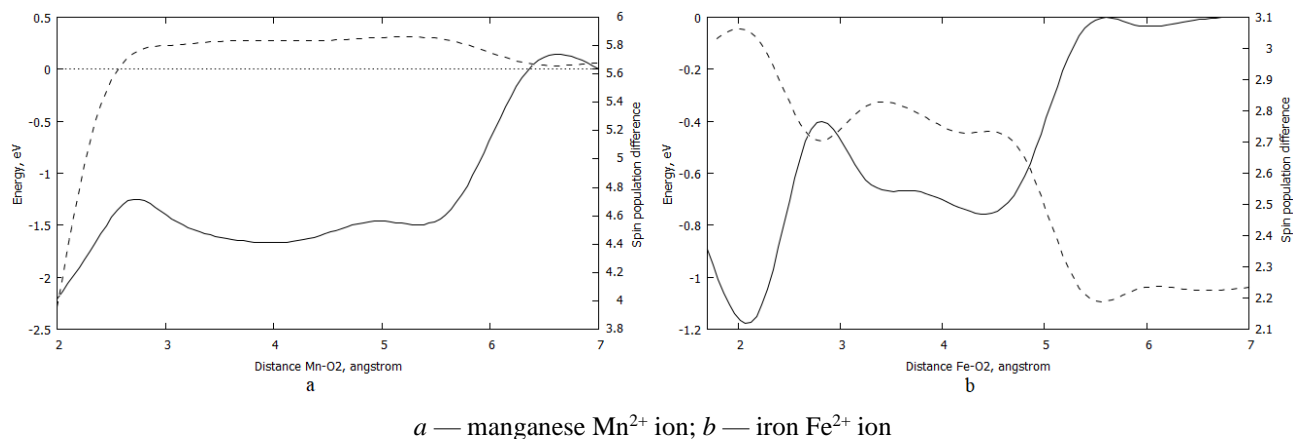

a — manganese Mn^{2+} ion; *b* — iron Fe^{2+} ion

Figure 3. Curves of the potential energy of the interaction between the superoxide ion O$_2^-$
and the active site of superoxide dismutase (left y-axis and solid line)
and the corresponding spin population differences (right y-axis and dashed line)

It is noteworthy that directed along the same trajectory as during the primary electron transfer in the active site of manganese superoxide dismutase (Fig. 2*a*), this time the superoxide ion bound to the proton of the hydroxyl group of the amino acid Tyr. This amino acid accompanied the superoxide ion throughout its path to manganese. This is shown by smeared minima 3 Å ≤ R ≤ 5.5 Å. At the characteristic minimum $R = 2.0$ Å, the superoxide ion entered the manganese coordination sphere and completely replaced the water molecule. In this case, the superoxide ion formed two hydrogen bonds: with the water molecule and Tyr. As the calculation showed (Table 2), the hydroperoxide radical is in any case formed by splitting off a proton from water, and the second proton from Tyr forms a hydrogen peroxide molecule H$_2$O$_2$. Tyrosine is then protonated from the solvent and the cycle is completed. A sharp change in the difference between spin populations is within 2 Å ≤ R. This criterion allows one to discard the variants of the associative and outer-sphere mechanisms and consider only the substitution mechanism. The donor radius is estimated as the sum of the average distance from the manganese atom to the histide ligands (2.031 Å) and the covalent radius of the nitrogen atom (0.71 Å).

A completely different phenomenon is observed for the case of iron superoxide dismutase. Two characteristic minima are observed. The first minimum $R_1 = 4.3$ Å is due to the stabilization of the system by the formation of two hydrogen bonds from the superoxide ion (to the water molecule and to the histidine ligand). This reflects the outer-sphere mechanism of secondary electron transfer. The second minimum $R_2 = 2.1$ Å is due to the stabilization of the system by the incorporation of the hydroperoxide radical into the first iron coordination sphere to form an octahedral structure. A sharp change in the difference of spin populations is within 3.4 Å ≤ R ≤ 6 Å. This criterion allows us to discard the variant of the associative mechanism and consider only the outer-sphere mechanism. The donor radius is estimated as the sum of the distance from the iron atom to the hydroxide ion (2.114 Å) and the Van der Waals radius of the oxygen atom (1.55 Å).

Table 4 shows changes in the Gibbs functions ΔG^0, reorganization energy λ_{tot}, and activation energy $\Delta G^{\neq}$, as well as estimates of the first and second order electron transfer rate constants in the framework of the Marcus paradigm for the secondary electron transfer from the active site to the hyrdroperoxide radical. The rate constants are given for non-adiabatic and adiabatic calculation options. The preferred option is in bold.

Kinetic and thermodynamic characteristics according to Marcus of the secondary electron transfer from the Me-SOD active site to the hydroperoxide radical

Parameter	Substitution mechanism	Outer-sphere mechanism
	Mn-SOD	Fe-SOD
ΔG^0, eV	−0.927	−0.508
r_D, Å	2.723	3.664
r_A, Å	1.337	2.217
R, Å	2.00	4.24
λ_{tot}, eV	1.774	1.540
$\Delta G^{\neq}$, eV	0.089	0.159
H_{DA}, eV	0.2226	0.1754
k_{diff}, M^{-1}·s^{-1}	2.02·10^9	2.02·10^9
k_{et} (k_{et}^{AD}), s^{-1}	1.92·10^{13} (**2.73·10^{11}**)	9.11·10^{10} (**1.68·10^{10}**)
k (k^{AD}), M^{-1}·s^{-1}	3.87·10^{11} (**5.50·10^9**)	1.75·10^{10} (**3.22·10^9**)
k_{obs} (k_{obs}^{AD}), M^{-1}·s^{-1}	2.01·10^9 (**1.48·10^9**)	1,81·10^9 (**1.24·10^9**)

Transitions in Mn^{2+}-SOD-O$_2^-$ are transitions between the quintet ground (Qt0) and the quintet first excited (Qt1) state. Unlike Fe^{2+}-SOD-O$_2^-$, Mn^{2+}-SOD-O$_2^-$ transfer involves α-electrons. The unpaired electrons of the Mn^{2+}-SOD active center and the O$_2^-$ superoxide ion have oppositely directed spins. The transition in Fe^{2+}-SOD-O$_2^-$ is a transition between the sextet ground (St0) and sextet first excited (St1) states. All two interactions are adiabatic due to the high value of the H$_{DA}$ matrix element.

As shown earlier, tyrosine is an important element for secondary electron transfer in manganese superoxide dismutase, which directs the superoxide ion to manganese. Tyr is displaced from its equilibrium position, and after the transfer of a proton and an electron, it returns to its original position. This increases the inner-sphere reorganization energy compared to iron superoxide dismutase. The first proton is split off from the water molecule, and the hydroxide ion OH$^-$ is formed, which is located at a distance from manganese, and the hydroperoxide radical in the first coordination sphere of manganese. After electron transfer, the hydroperoxide ion retains a strong inner-sphere bond with the Mn^{3+} manganese ion. The second proton is immediately split off from the phenol group Tyr. The resulting hydrogen peroxide H$_2$O$_2$ molecule is easily split off from Mn^{3+}, and the hydroxide ion returns to its original position. At the end of the Mn-SOD catalytic cycle, a proton from the solvent protonates the Tyr phenolate ion. If we consider the mechanism of primary electron transfer in Mn-SOD as an associative one, then it can be noted that the values of the reorganization and activation energies are close to those for the secondary electron transfer by the substitution mechanism. The rate constants for the secondary electron transfer are two orders of magnitude smaller, but are above the diffusion limit.

Unlike manganese Mn^{2+}, iron Fe^{2+} exhibits a lower tendency to form a complex with the hydroperoxide radical. Here, only the outer-sphere mechanism is mainly realized. Compared to the manganese ion, the superoxide ion binds to iron during the primary electron transfer at a greater distance (by 0.56 Å), and during the secondary electron transfer, it does not show the formation of a stable bond at all. This indicates that iron binds less well with small anions than manganese. The rate constants for the secondary electron transfer are an order of magnitude smaller, but are above the diffusion limit.

Next, we consider the features of the behavior of the electron density at the bonding critical points of the complex of the superoxide ion and the Me-SOD active site in various versions of the mechanism of binding the superoxide ion and the metal (Table 5).

After the primary electron transfer at the manganese ion, the hydroxide ion OH$^-$ splits off a proton from Asp and becomes a water molecule H$_2$O. Water is weaker bound to Mn^{2+} than to Mn^{3+}. Therefore, here it became possible to completely replace the water molecule with the superoxide ion. The Mn–HO$_2$ bond is quite strong and comparable to the Mn–His and Mn–Asp bonds. The topological characteristics of bonds involving Fe are similar to those for Fe^{3+}-SOD. This indicates the possibility of the outer-sphere mechanism.

Critical bonding points (3; –1) for secondary electron transfer in the Me-SOD donor-acceptor complex.
Parameters ρ and Δρ are expressed in atomic units

Bond	Parameter	Substitution mechanism	Outer-sphere mechanism
		Mn-SOD	Fe-SOD
$Me–N^1$	ρ	0.0795	0.0600
	$\Delta\rho$	+0.311	+0.255
$Me–N^2$	ρ	0.0811	0.0748
	$\Delta\rho$	+0.318	+0.347
$Me–N^3$	ρ	0.0880	0.0703
	$\Delta\rho$	+0.352	+0.293
$Me–O^{Asp}$	ρ	0.0759	0.0764
	$\Delta\rho$	+0.347	+0.339
$Me–H_2O$	ρ	–	0.0633
	$\Delta\rho$		+0.279
$Me–O_2^-(HO_2)$	ρ	0.0893	–
	$\Delta\rho$	+0.323	

Conclusions

Before the primary electron transfer from the solvent, a proton in the form of hydronium ion H_3O^+ enters the active site of Me^{3+}-SOD, which protonates the hydroxide ion OH^- to the water molecule H_2O. Due to the high chemical affinity of the Mn^{3+} ion with the strong hydroxide ligand and the low polarizing effect of the manganese ion, the water molecule splits off the proton to form the hydroxide ion. The proton passes to the carbonyl oxygen atom of the aspartate ion at manganese.

The primary electron transfers from the superoxide ion to the Mn^{3+}-SOD and Fe^{3+}-SOD active sites occur according to the associative mechanism. This indicates a high chemical affinity between the negatively charged superoxide ion and the positively charged metal ion. Substitution of the water molecule or the aspartate ion is not observed. The primary electron transfer precursor complex has an octahedral structure. The superoxide O_2^- ion binds more strongly to the Mn^{3+} ion with an electron transfer distance of 1.95 Å than to the Fe^{3+} ion with a transfer distance of 2.56 Å. The primary electron transfer for manganese superoxide dismutase by the associative mechanism has the reorganization energy of 1.840 eV and the activation energy of 0.065 eV with an energy release of 0.695 eV. The primary electron transfer for iron superoxide dismutase by the associative mechanism has the reorganization energy of 2.114 eV and the activation energy of 0.015 eV, which means a practically activationless transfer. The release of energy in this case is 1.109 eV. According to the values of the transfer rate constants in the case of Fe^{3+}-SOD, the elementary stage of electron transfer is an order of magnitude faster than in the case of Mn^{3+}-SOD.

Due to the instability of the O_2^{2-} peroxide ion, the secondary electron transfer is coupled with the proton transfer. It is unambiguous that the source of the proton is the water molecule. The proton is split off from the fifth ligand at the metal ion to form the hydroxide ion OH^-. The superoxide ion accepts the proton and becomes the peroxide radical $HO_2\cdot$. This is achieved by the active interaction of the superoxide ion and the water molecule. The mechanisms of secondary electron transfer are significantly different for Mn^{2+}-SOD and Fe^{2+}-SOD. In manganese superoxide dismutase, the superoxide ion forms a hydrogen bond with the hydroxyl group of tyrosine. Secondary electron transfer in manganese superoxide dismutase occurs by substitution mechanism at a distance of 2.0 Å. The transfer has the reorganization energy of 1.774 eV and the activation energy of 0.089 eV with an energy release of 0.927 eV. In iron superoxide dismutase, the superoxide ion combines with the water molecule and the histidine ligand at a distance of 4.24 Å from iron. The transfer has the reorganization energy of 1.540 eV and the activation energy of 0.159 eV with an energy release of 0.508 eV. According to the values of the transfer rate constants in the case of Mn^{2+}-SOD, the elementary stage of electron transfer is somewhat faster than in the case of Fe^{2+}-SOD.

References

1 Barja, G. (1999). Mitochondrial Oxygen Radical Generation and Leak: Sites of Production in States 4 and 3, Organ Specificity, and Relation to Aging and Longevity. *J. Bioenergetics and Biomembranes*, *31*, 347–366. https://doi.org/10.1023/A:1005427919188

2 Cabelli, D.E., Riley, D., Rodriguez, J.A., Valentine, J.S. & Zhu, H. (1999). Models of superoxide dismutases. Biomimetic Oxidations Catalyzed by Transition Metal Complexes. *Imperial College Press*, 461–508. https://doi.org/10.1142/9781848160699_0010

3 Fridovich, I. (1997). Superoxide anion radical (O₂⁻), superoxide dismutase and related matters. *J. Biol. Chem.*, *272*, 18515–18517. https://doi.org/10.1074/jbc.272.30.18515

4 Azadmanesh, J. & Borgstahl G.E.O. (2018). A Review of the Catalytic Mechanism of Human Manganese Superoxide Dismutase. *Antioxidants, 7, 25.* https://doi.org/10.3390/antiox7020025

5 Lah, M. S., Dixon, M. M., Pattridge, K. A., Stallings, W. C., Fee, J. A. & Ludwig, M. L. (1995). Structure-function in Escherichia coli iron superoxide dismutase: comparisons with the manganese enzyme from Thermus thermophilus. *Biochemistry*, *34*(5), 1646–1660. https://doi.org/10.1021/bi00005a021

6 Marcus, R.A. & Sutin, N. (1985). Electron transfers in chemistry and biology. *Biochimica et Biophysica Acta*, *811*, 265–322. https://doi.org/10.1016/0304-4173(85)90014-x

7 Neese, F. (2012). The ORCA program system. *Wiley interdisciplinary Reviews — Computational Molecular Science*, *2*(1), 73–78. https://doi.org/10.1002/wcms.81

8 Perdew, J.P., Burke, K. & Ernzerhof, M. (1996). Generalized Gradient Approximation Made Simple. *Phys. Rev. Letters*, *77*, 3865. https://doi.org/10.1103/physrevlett.77.3865

9 Weigend, F. & Ahlrichs, R. (2005). Balanced basis sets of split valence, triple zeta valence and quadruple zeta valence quality for H to Rn: Design and assessment of accuracy. *Phys. Chem. Chem. Phys.*, *7*, 3297. https://doi.org/10.1039/b508541a

10 Xerri, B., Petitjean, H., Dupeyrat, F., Flament, J.-P., Lorphelin, A., Vidaud, C. et al. (2014). Mid- and Far-Infrared Marker Bands of the Metal Coordination Sites of the Histidine Side Chains in the Protein Cu, Zn-Superoxide Dismutase. *European Journal of Inorganic Chemistry, 2014*(27), 4650–4659. https://doi.org/10.1002/ejic.201402263

11 Caldeweyher, E., Bannwarth, C. & Grimme, S. (2017). Extension of the D3 dispersion coefficient model. *J. Chem. Phys.*, *147*, 034112. https://doi.org/10.1063/1.4993215

12 Cossi, M., Rega, N. & Scalmani, G. et al. (2003). Energies, structures and electronic properties of molecules in solution with the C-PCM solvation model. *Chem. Phys.*, *24*, 669–681. https://doi.org/10.1002/jcc.10189

13 Ryabykh, A.V., Maslova, O.A., Beznosyuk, S.A. & Masalimov, A.S. (2022). The Role of Zinc Ion in the Active Site of Copper-Zinc Superoxide Dismutase. *Bulletin of the University of Karaganda — Chemistry, 106(2), 77-86.* https://doi.org/10.31489/2022Ch2/2-22-20

14 Alexandrov, I.V. (1980). Physical aspects of charge transfer theory. *Chemical Physics*, *51*(3), 449–457.

15 Cordero, B., Gómez, V., Platero-Prats, A. E., Revés, M., Echeverría, J., Cremades, E., Barragán, F. & Alvarez, S. (2008). Covalent radii revisited. *Dalton Transactions*, (21), 2832–2838. https://doi.org/10.1039/B801115J

16 Batsanov, S.S. (2001). Van der Waals radii of elements. *Inorganic materials*, *37*(9), 871–885. https://doi.org/10.1023/A:1011625728803

17 Eberson, L. (1985). The Marcus theory of electron transfer, a sorting device for toxic compounds. *Advances in Free Radical Biology & Medicine*, *1*(1), 19–90. https://doi.org/10.1016/8755-9668(85)90004-3

18 Rosso, K.M. & Rustad, J.R. (2000). Ab initio calculation of homogeneous outer sphere electron transfer rates: application to $M(OH_2)_6^{3+/2+}$ redox couples. *The Journal of Physical Chemistry A*, *104*(29), 6718–6725. https://doi.org/10.1021/jp994164h

19 Lu, T. & Chen, F. (2012). Multiwfn: A multifunctional wavefunction analyzer. *Journal of computational chemistry*, *33*(5), 580–592. https://doi.org/10.1002/jcc.22885

Information about authors*

Ryabykh, Andrey Valerievich — Assistant and Engineer, Department of Physical and Inorganic Chemistry, Altai State University, Lenin avenue, 61, 656049, Barnaul, Russia; e-mail: ryabykh@chem.asu.ru; https://orcid.org/0000-0003-3699-3932

Maslova, Olga Andreevna — Candidate of Physical and Mathematical Sciences, Associate Professor, Physical and Inorganic Chemistry Department, Altai State University, Lenin avenue, 61, 656049, Barnaul, Russia; e-mail: maslova_o.a@mail.ru; https://orcid.org/0000-0003-3862-3687

Beznosyuk, Sergey Alexandrovich (*corresponding author*) — Doctor of Physical and Mathematical Sciences, Professor, Head of the Physical and Inorganic Chemistry Department, Altai State University, Lenin avenue, 61, 656049, Barnaul, Russia; e-mail: bsa1953@mail.ru; https://orcid.org/0000-0002-4945-7197

*The author's name is presented in the order: *Last Name, First and Middle Names*

Dinara A. Birimzhanova[1] , Irina S. Irgibaeva[1*] , Nikolay N. Barashkov[2]

[1]L.N. Gumilyov Eurasian National University, Astana, Kazakshtan;
[2]Micro Tracers, Inc., San Francisco, California, USA
(*Corresponding author's e-mail: irgsm@mail.ru)

Quantum-Chemical Study of Aggregation of 5-(4'-Dimethylaminobenzylidene)Barbituric Acid

Decreasing fluorescence efficiency in the solid-state is general and is mainly attributed to the intermolecular vibronic interactions, which induce the nonradiative deactivation process. Whereas the isolated dye molecules are virtually non-luminescent in dilute solutions, they become highly emissive upon solution thickening or aggregation in poor solvents or in the solid-state show an increase of luminescence intensity, the phenomenon of the aggregation-induced emission (AIE phenomenon). The development of efficient luminescent materials is a topic of great current interest. Theoretical calculation shows that the dye molecules' aggregation-induced emission characteristics result from intermolecular interactions. Utilizing such features, the molecules can be employed as fluorescent probes for the detection of the ethanol content in aqueous solutions. Quantum-chemical calculations using the method of density functional theory the computations of structure and electronic spectra of aggregated forms of 5-(4'-dimethylaminobenzylidene)barbituric acid and the Gaussian 98 program packages have been performed. The unusual spectral behavior of 5-(4'-dimethylamino-benzylidene)barbituric acid was investigated theoretically by the DFT method and its time-dependent variant TDDFT. Carried out calculations using Zindo, as well as *ab initio* calculations, confirm the appearance of a new band during aggregation and its shift to the red region when the number of molecules increases.

Keywords: barbituric acid, electronic spectra, dye molecules, aggregation-induced emission, theoretical study, hydrogen bond, electronic states, valence vibrations.

Introduction

Currently, fluorescent organic nanoparticles (FONs) are less studied than fluorescent inorganic semiconductors or metallic nanoparticles, which have attracted significant research interest due to their unique properties related to quantum effects at the micro level. Due to these properties, organic nanoparticles are intensively studied for use in various fields, including fluorescent biological markers, photovoltaic cells, LEDs and optical sensors. It is expected that fluorescent organic nanoparticles have a higher potential in comparison with their inorganic counterparts, since they are more diverse and there are many methods of their synthesis and preparation of nanoparticles.

One of the many potential applications of FON is related to their ability to show a change in fluorescence depending on the size, while this fluorescence property is very different from the similar characteristic for the molecular form of the organic compound of the same nature. It is well known the fluorescence quantum yield of organic chromophores usually decreases in the solid state, although they have a high fluorescence quantum yield in solution. This decrease in the fluorescence quantum yield in the solid state is usually associated with intermolecular vibrational interactions, which cause nonradiative relaxation processes, such as exciton binding, excimer formation, migration of excitation energy to trapped impurities, etc. However, some exceptions have been reported [1–6], for example, for derivatives of barbituric acid [7–9], which show enhanced emission in the solid state, rather than quenching of the glow.

This work is devoted to the theoretical study of optical electronic and vibrational spectra of 5-(4'-dimethylaminobenzylidene)barbituric acid (DM).

Computational Details

Quantum-chemical calculations of the geometric structure of the DM molecule (Fig. 1) were carried out with the density functional method (DFT) using the Gaussian 98 software package. Geometry optimization was carried out using a three-parametric hybrid Becke method with gradient-correction correlation of the Lee, Yang and Parr functional (B3LYP) and a standard 6-31G(d) basis set. The electronic spectra were ob-

tained taking into account the time dependence of the density functional theory (TDDFT) method, where discrete spectra of energy excitation and corresponding oscillator strengths were estimated for several tens of low-energy singlet transitions [10, 11].
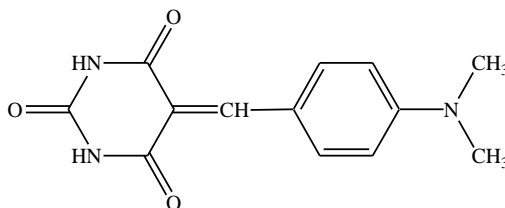
Figure 1 Structural formula of DM

Results and Discussion

Electronic absorption spectra of the DM molecule and its complexes were calculated using wave functions of the ground state. The absorption wavelength for a molecule is 371.58 nm, for aggregations of two, three and four molecules this band shifts to the long-wavelength region and is 379 nm. As mentioned above, the observed absorption band in the long-wavelength region of 460 nm was not found in model calculations of complexes of DM molecules of two, three, and four.

Complex formation occurs due to intermolecular hydrogen bonding. Table 1 shows the frequencies of valence vibrations of DM for an optimized geometric configuration.

T a b l e 1

Frequencies and forms of valence vibrations of bonds of DM

Valence vibrations, cm^{-1}	Forms of vibrations
$\upsilon\ (C_1\text{-}O_7)$ 1841.99	$0.65\ d^x(C_1) + 0.22\ d^y(C_1) - 0.37\ d^x(O_7) - 0.12\ d^y(O_7)$
$\upsilon\ (N_2\text{-}H_8)$ 3615.50	$-0.05\ d^x(N_2) + 0.05\ d^y(N_2) + 0.73\ d^x(H_8) - 0.64\ d^y(H_8)$
$\upsilon\ (C_3\text{-}O_9)$ 1790.45	$0.06\ d^x(C_3) + 0.53\ d^y(C_3) - 0.03\ d^x(O_9) - 0.32\ d^y(O_9)$
$\upsilon\ (C_4\text{-}C_{12})$ 1602.07	$-0.17\ d^x(C_4) - 0.05\ d^y(C_4) + 0.29\ d^x(C_{12}) + 0.05\ d^y(C_{12})$
$\upsilon\ (C_5\text{-}O_{10})$ 1752.57	$-0.33\ d^x(C_5) + 0.46\ d^y(C_5) + 0.21\ d^x(C_{10}) - 0.26\ d^y(C_{10})$
$\upsilon\ (N_6\text{-}H_{11})$ 3612.97	$-0.02\ d^x(N_6) - 0.07\ d^y(N_6) + 0.21\ d^x(H_{11}) + 0.95\ d^y(H_{11})$

Due to structural features, derivatives of barbituric acid can form intermolecular hydrogen bonds. Let's look at dimera as an example (Fig. 2).
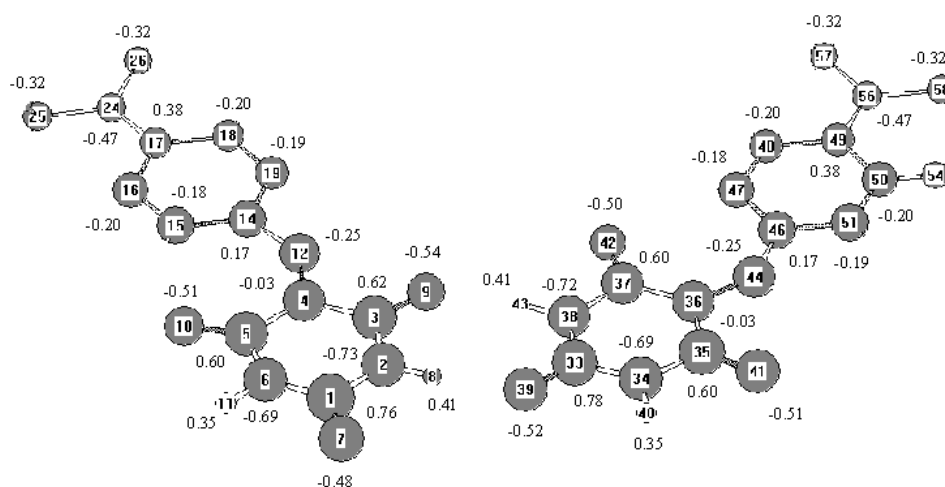
Figure 2. Complex of two molecules — configuration 1

As can be seen in Figure 2, two hydrogen bridges (N_2H_8…….O_{39}) and ($N_{38}H_{43}$…….O_9) with lengths of 2.88 Å and 2.89 Å are formed in the dimer, respectively. The calculation of vibrational frequencies (Table 2)

indicates the formation of a hydrogen bond: the valence vibration of N_2-H_8 shifts to the low-frequency region, from 3615.50 cm^{-1} in the monomer (Table 1) to 3323.90 cm^{-1} in the dimer. The characteristic vibration of the C_{33}-O_{39} carbonyl bond varies from 1841.99 cm^{-1} to 1802.80 cm^{-1}. The same is observed for the second hydrogen bridge.

T a b l e 2

Frequency and form of valence vibration bonds in a complex of two DM molecules

| Valence vibrations, cm^{-1}	Forms of vibrations
υ (C_1-O_7) 1844.87	$-0.08\ d^x(C_1) + 0.64\ d^y(C_1) + 0.05\ d^x(O_7) - 0.36\ d^y(O_7)$
υ (N_2-H_8) 3323.90	$-0.05\ d^x(N_2) + 0.02\ d^y(N_2) + 0.67\ d^x(H_8) - 0.28\ d^y(H_8)$
υ (C_3-O_9) 1731.72	$0.41\ d^x(C_3) + 0.28\ d^y(C_3) - 0.23\ d^x(O_9) - 0.15\ d^y(O_9)$
υ (C_4-C_{12}) 1599.45	$0.03\ d^x(C_4) - 0.15\ d^y(C_4) - 0.07\ d^x(C_{12}) + 0.24\ d^y(C_{12})$
υ (C_5-O_{10}) 1774.74	$0.51\ d^x(C_5) - 0.12\ d^y(C_5) - 0.30\ d^x(C_{10}) + 0.07\ d^y(C_{10})$
υ (N_6-H_{11}) 3612.30	$-0.06\ d^x(N_6) - 0.05\ d^y(N_6) + 0.77\ d^x(H_{11}) + 0.64\ d^y(H_{11})$
υ (C_{33}-O_{39}) 1802.80	$0.48\ d^x(C_{33}) + 0.37\ d^y(C_{33}) - 0.26\ d^x(O_{39}) - 0.19\ d^y(O_{39})$
υ (N_{34}-H_{40}) 3613.95	$0.01\ d^x(N_{34}) - 0.07\ d^y(N_{34}) - 0.08\ d^x(H_{40}) + 0.99\ d^y(H_{40})$
υ (C_{35}-O_{41}) 1790.78	$0.36\ d^x(C_{35}) - 0.21\ d^y(C_{35}) - 0.21\ d^x(O_{41}) + 0.12\ d^y(O_{41})$
υ (C_{36}-C_{44}) 1602.67	$-0.14\ d^x(C_{36}) - 0.10\ d^y(C_{36}) + 0.20\ d^x(C_{44}) + 0.18\ d^y(C_{44})$
υ (C_{37}-O_{42}) 1756.02	$-0.15\ d^x(C_{37}) + 0.49\ d^y(C_{37}) + 0.07\ d^x(O_{42}) - 0.30\ d^y(O_{42})$
υ (N_{38}-H_{43}) 3352.15	$-0.05\ d^x(N_{38}) + 0.02\ d^y(N_{38}) + 0.66\ d^x(H_{43}) - 0.29\ d^y(H_{43})$

Analysis of the vibrational frequencies and forms of normal vibrations of the DM and its dimer shows the mode with the largest contribution from the valence bond NH, which participates in the formation of a hydrogen bond with the C=O group of the neighboring molecule, has the highest amplitude of oscillations during complex formation. At the same time, it was interesting to find out how the formation of hydrogen bonds affects the electronic spectrum of the compound in solution.

As can be seen from Table 3, the absorption band at 371.58 nm, characteristic of a monomolecule, is slightly shifted to the long-wave region (378.49 nm) and at the same time a new absorption band (396.17 nm) appears for the S1 state with zero oscillator strength.

T a b l e 3

Calculated energies and wavelengths of electronic transitions of two DM molecules

Transition	Energy of transition, eV	Wave function	Wavelength nm	Oscillator strength
S_1 ($^1\pi\rightarrow\pi^*$)	3.13	$^1\Phi_1 = 0.71\ (\varphi_{136}\rightarrow\varphi_{137})$	396.17	0.0
S_3 ($^1\pi\rightarrow\pi^*$)	3.27	$^1\Phi_1 = 0.40\ (\varphi_{135}\rightarrow\varphi_{137}) - 0.39\ (\varphi_{136}\rightarrow\varphi_{138})$	378.49	0.0623
S_4 ($^1\pi\rightarrow\pi^*$)	3.39	$^1\Phi_1 = 0.38\ (\varphi_{135}\rightarrow\varphi_{137}) + 0.39\ (\varphi_{136}\rightarrow\varphi_{138})$	365.22	0.1248

In the case of a complex of three molecules, two models with different structures are formed — flat (Fig. 3) and non-planar (Fig. 4). The flat configuration of three molecules is more stable by 4.15 kcal/mol.
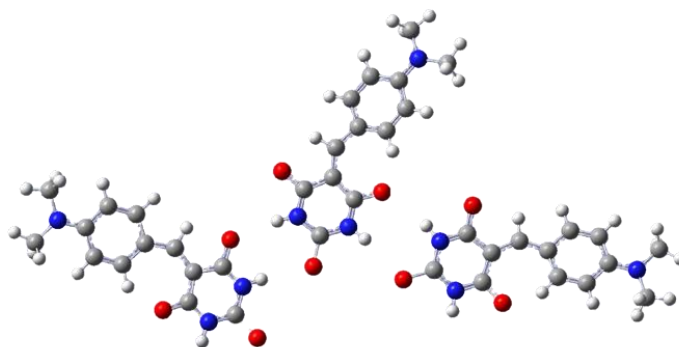
Figure 3. Complex of three molecules with flat structure — configuration 1
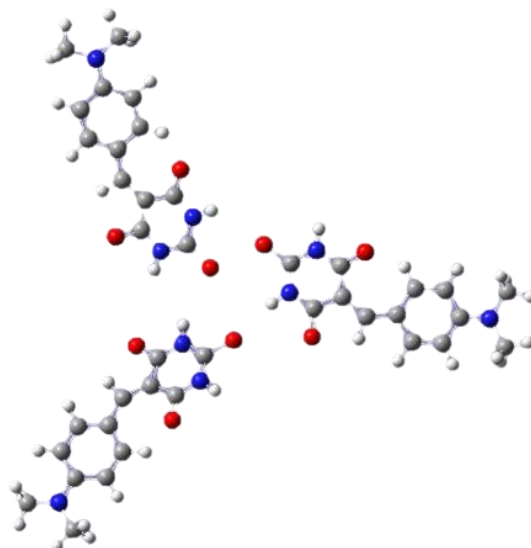
Figure 4. Complex of three molecules with a non–planar structure — configuration 1

Models of two, three and four molecules (Fig. 5) with a configuration different from the above were also calculated.
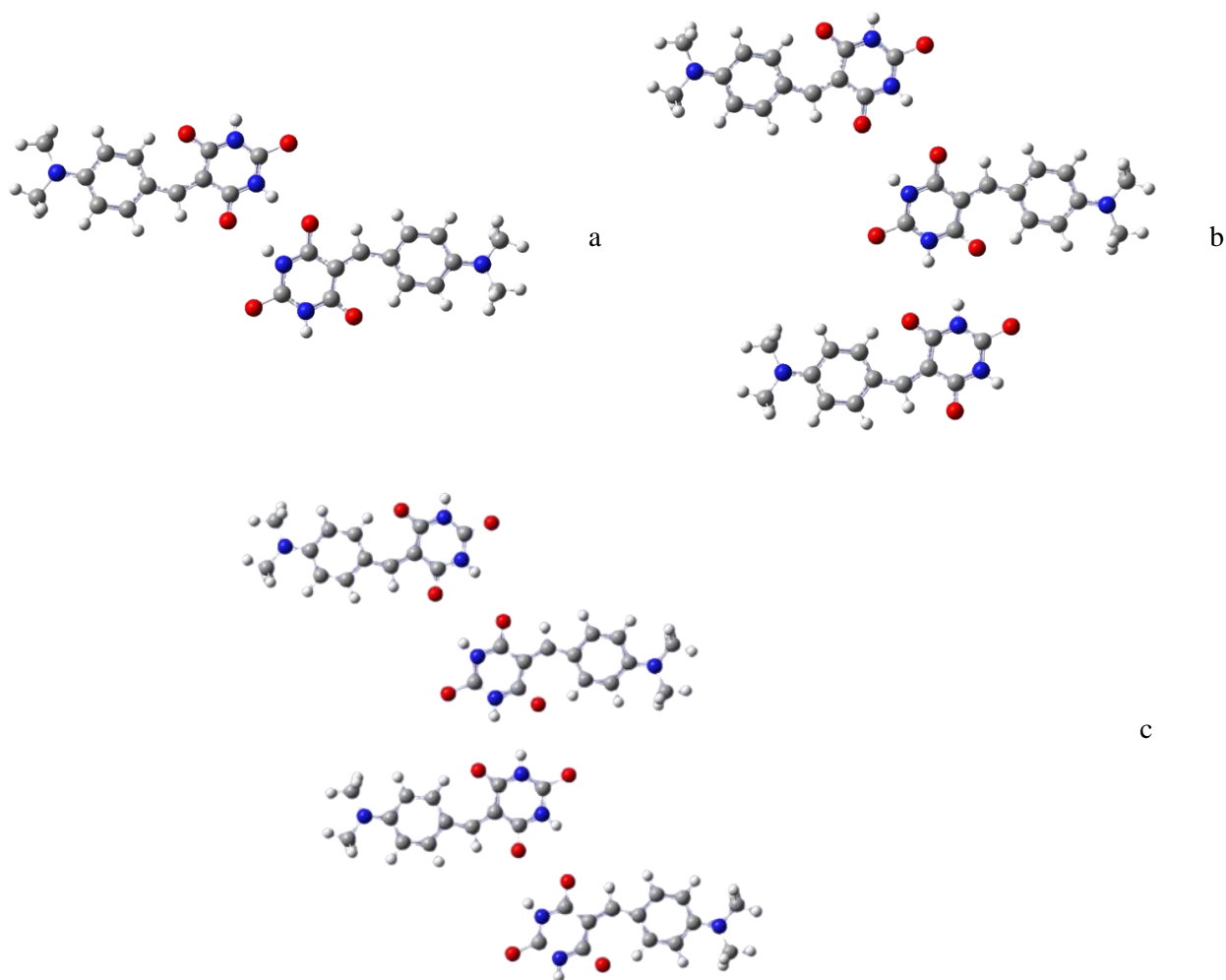
Figure 5. Complex of two (*a*), three (*b*) and four molecules (*c*) — configuration 2

Figure 6 shows the distribution of electronic levels for a monomolecule and complexes of several molecules. The electronic levels corresponding to the absorption band of the monomolecule are selected. When the number of molecules increases, new low-lying electronic levels appear. In both cases, both for configuration 1 and for configuration 2, a new absorption band (absorption band for aggregation), electronic level S_1, appears. For configuration 1, the oscillator strength for this band is zero, for configuration 2, this band has a weak oscillator strength: for two molecules, the absorption band is 392.55 nm, for three molecules — 407.80 nm, for four molecules — 409.32 nm. Also, when the number of molecules increases, degenerate states appear, for example, for a complex of four molecules $S_1 = S_2 = 3.03$ nm, $S_3 = S_4 = 3.05$ nm.

It follows from the given data that upon aggregation of a large number of molecules DM, the absorption band of the monomolecule shifts to a longer wavelength region and a new band characteristic of aggregation appears.
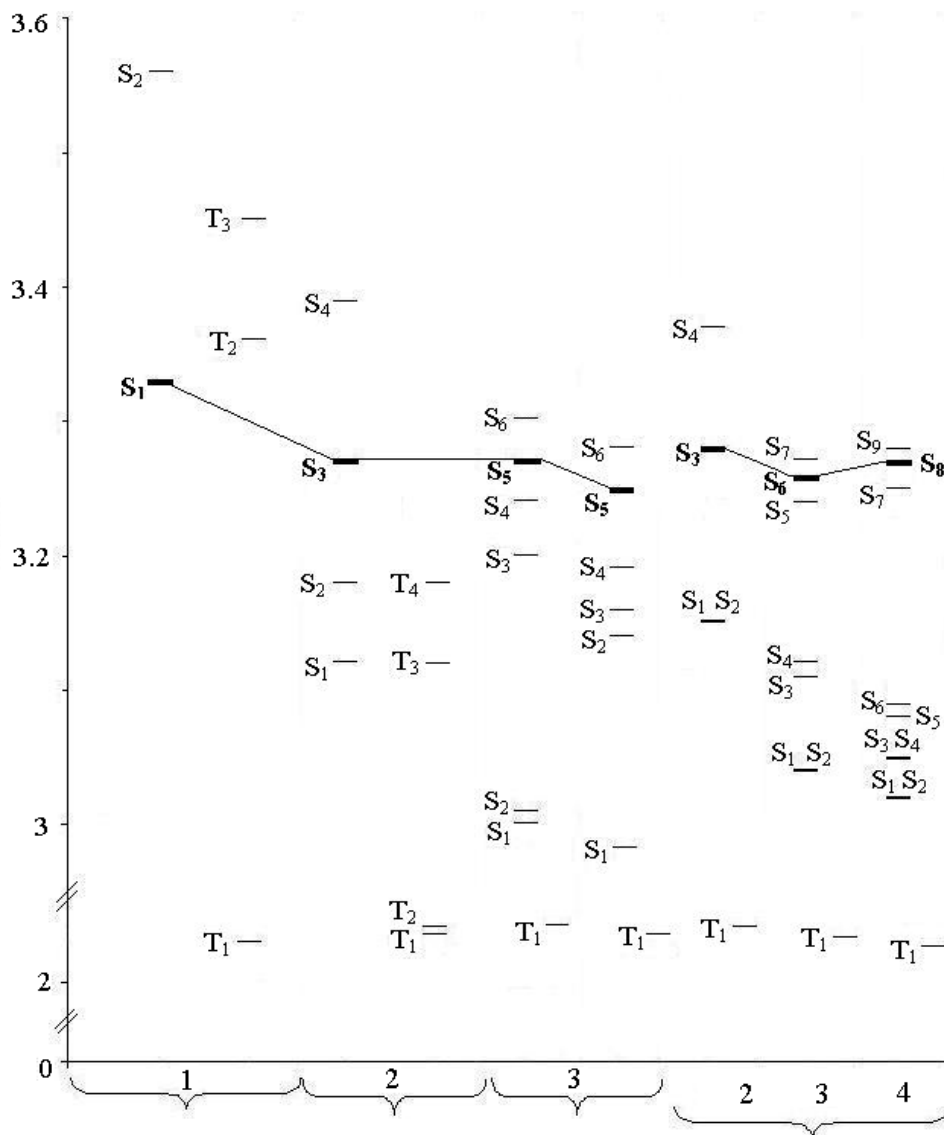
Axis y — Energy, eV, axis x — electronic levels.
Configuration 1: *1* — monomolecule; *2* — a complex of two molecules; *3* — a complex of three molecules (non-planar and planar structure). Configuration 2: *2, 3, 4* — complexes of two, three and four molecules

Figure 6. Distribution of electronic levels for monomolecules and complexes of two, three and four DM molecules with different configurations

According to calculations, the energy difference between the highest occupied and the lowest unoccupied molecular orbitals, the gap between HOMO and LUMO decreases with an increase in the number of molecules, this is observed both for configuration 1 and configuration 2.

It has also been suggested that an intermolecular proton transfer reaction from a nitrogen atom to an oxygen atom may occur during aggregation. Two-proton proton transfer for a monomolecule, complexes of two, three and four molecules with different configurations was calculated. However, according to the distribution of electronic levels for a complex of three molecules, two-proton transfer does not occur. There is only stabilization in the excited state, that is, a decrease in the energy barrier for two-proton transfer. Energy difference in the ground state is 1.05 eV for configuration 1 and configuration 2, energy difference in the excited state for levels S_6, S_5, S_4 is 0.99 eV for both configurations. States S_6, S_5, S_4 correspond to the absorption wavelength of the monomolecule (371 nm). The S_1 states correspond to a new absorption band shifted to the long-wavelength region (for aggregation). For configuration 1, the oscillator strength for the S_1 state is zero. For configuration 2, the oscillator strength for the first excited state is 0.0004 (NH) and 0.0011 (2OH).

Figure 7 shows a hydrogen bond diagram for a dimer, a complex of three, four, five, and six molecules. As can be seen, with an increase in the number of molecules, the energy of hydrogen bond increases. It is assumed that with a further increase in the number of aggregating DM molecules, this tendency is preserved.
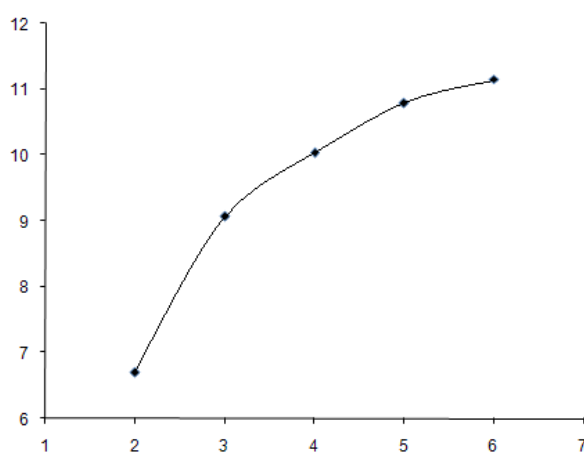
Axis y — hydrogen bond energy, eV, axis x — number of molecules

Figure 7. Diagram of changes in the energy of the hydrogen bond between DM molecules

When the number of aggregating molecules increases, this band shifts to a longer wavelength region. For a complex of two molecules, this band is 392 nm, for three — 408 nm, for four molecules — 409 nm, and for a complex of five molecules, the band with charge transfer is 411 nm.

Sandwich complexes of two, four, six, eight and ten molecules were also calculated using the Zindo method (Fig. 8, Table 4).

Figure 8. Sandwich complexes of two and four molecules DM

**Energy and wavelengths of electronic transitions calculated by the Zindo method
for molecular DM sandwich complexes**

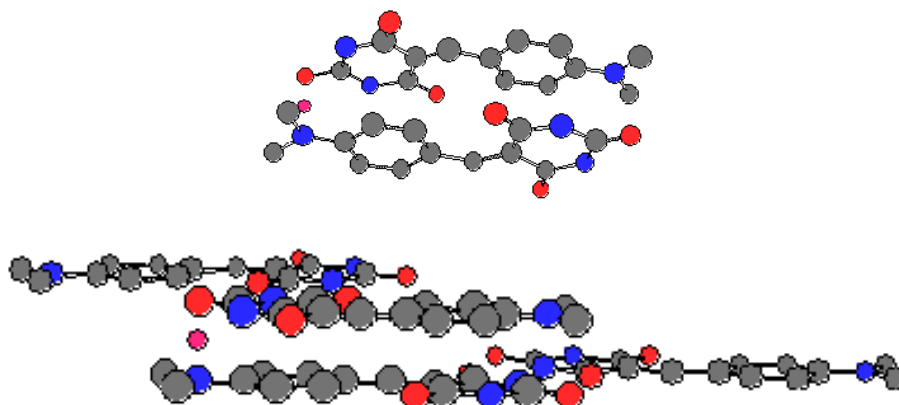| 2 molecules				4 molecules			
R (N-O), Å	E, eV	λ, nm	f	R (N-O), Å	E, eV	λ, nm	f
2.4	2.10	591	0.3485	2.4	2.17	572	0.4320
	3.51	353	0.1107		3.53	351	1.1046
	3.84	323	0.2026		3.82	324	0.6658
2.5	2.42	513	0.4722	2.5	2.48	500	0.5498
	3.50	354	0.2054		3.50	354	1.3224
	3.86	321	0.1089		3.83	323	0.3824
6 molecules				8 molecules			
R (N-O), Å	E, eV	λ, nm	f	R (N-O), Å	E, eV	λ, nm	f
2.4	2.19	567	0.4293	2.4	2.23	556	0.5073
	3.55	349	0.9919		3.56	348	0.5275
	3.86	321	0.8270		3.83	323	1.0770
2.5	2.50	496	0.5686	2.5	2.52	491	0.6202
	3.54	350	1.4535		3.55	349	1.4867
	3.86	321	0.3540		3.88	319	1.1954
10 molecules							
R (N-O), Å	E, eV	λ, nm	f				
2.4	2.28	543	0.5653				
	3.45	360	0.5595				
	3.85	321	0.5798				
2.5	2.58	480	0.6573				
	3.48	356	0.8648				
	3.87	320	1.9797				
Note. R (N-O) — distance between molecules in the upper and lower planes.							

Table 4 shows three absorption bands. Two bands in the region of about 350 and 320 nm, don't change with increasing molecules. The longer wavelength band has a red shift with a larger number of molecules. The band at 320 nm is the band of π-electrons of the benzene ring. By its nature, the maximum at 350 nm is characterized by the transfer of π-electrons from the benzene ring to the barbituric acid ring (intramolecular transfer). A band having a red shift is observed during aggregation and is a band with charge transfer from one molecule to another (intermolecular transfer).

Conclusion

The unusual fluorescence of DM was investigated theoretically by the DFT method and its time-dependent variant TDDFT.

Calculations carried out using Zindo, as well as *ab initio* calculations, confirm the appearance of a new band during aggregation and its shift to the red region when the number of molecules increases.

According to the calculated data, when aggregation of a large number of DM molecules, the absorption band of a monomolecule splits into several, and at the same time, a charge transfer band appears, which shifts to a longer wavelength region as the number of molecules increases.

The obtained theoretical calculations are consistent with experimental data [12]. According to experimental data, the maximum absorption and fluorescence of DM in the solid state compared to solutions is shifted to a longer wavelength region. Moreover, the intensity of fluorescence of DM in the solid state is significantly higher than that of fluorescence in solution. This is due to the fact that many intermolecular hydrogen bonds are formed in the solid state, that is, aggregations are obtained.

Calculations confirm that the greater the number of molecules involved in aggregation, that is, the more hydrogen bonds between DM molecules, the more the absorption maximum shifts. Thus, our calculations confirm the fact that due to the formation of hydrogen bonds between molecules, the intensity of the absorption and fluorescence bands increases and a shift to the red region is observed.

References

1   He W., Zhang Z., Luo Y., Kwok R.T.K., Zhao Zh. & Tang B.Zh. (2022). Recent advances of aggregation-induced emission materials for fluorescence image-guided surgery. *Biomaterials*, *288*, 121709. https://doi.org/10.1016/j.biomaterials.2022.121709

2   Chen L., Wang X., Yuan Y., Hu R., Chen Q., Zhu L., Gu M. & Shen Ch. (2022). Photosensitizers with aggregation-induced emission and their biomedical applications. *Engineered regeneration*, *3*(1), 59-72. https://doi.org/10.1016/j.engreg.2022.01.005

3   Sa Sh., Sahoo A., Mukherjee S., Perumal A. & Venkatasubbaiah K. (2022). N-C chelated tetraaryl-pyrazole based organoboranes: A new class of aggregation induced enhanced emission materials. *Dyes and Pigments*, *206*, 110585. https://doi.org/10.1016/j.dyepig.2022.110585

4   Yin Y., Hu H., Chen Zh., Liu H., Fan C. & Pu Sh. (2021). Tetraphenylethene or triphenylethylene-based luminophors: Tunable aggregation-induced emission (AIE), solid-state fluorescence and mechanofluorochromic characteristics. *Dyes and Pigments*, *184*, 108828. https://doi.org/10.1016/j.dyepig.2020.108828

5   Yu Q., Chen Sh., Han Ch., Guo H. & Yang F. (2020). High solid fluorescence of novel tetraphenylethene-porphyrin. *Journal of Luminescence*, *220*, 117017. https://doi.org/10.1016/j.jlumin.2019.117017

6   Liu Y., Tang Yh., Barashkov N.N., Irgibaeva I.S., Lam J.W.Y., Hu R., Birimzhanova D., Yu Y. & Tang B.Zh. (2010). Fluorescent chemosensor for detection and quantitation of carbon dioxide gas. *J. Am. Chem. Soc.*, *132*(40), 13951-13953. https://doi.org/10.1021/ja103947j

7   Shafiq N., Arshad U., Zarren G., Parveen Sh., Javed I. & Ashraf A. (2020). A comprehensive review: bio-potential of barbituric acid and its analogues. *Current organic chemistry*, *24*(2), 129-161. https://doi.org/10.2174/1385272824666200110094457

8   Zhang H., Tian Y., Tao F., Yu W., You K., Zhou L-R., Su X., Li T. & Cui Y. (2019). Detection of nitroaromatics based on aggregation induced emission of barbituric acid derivatives. *Biomolecular Spectroscopy*, *222*, 117168. https://doi.org/10.1016/j.saa.2019.117168

9   Shi W., Zhao S., Su Y., Hui Y. & Xie Z. (2016). Barbituric acid-triphenylamine adduct as an AIEE-type molecule and optical probe for mercury (II). *New J. Chem.*, *40*(9), 7814-7820. https://doi.org/10.1039/C6NJ00894A

10   Gaussian 98, Revision A3. Gaussian, Inc., Pittsburgh, PA, 1998.

11   Casida M.E. (1995). Recent Advances in Density Functional Methods, Part I, World Scientific, Singapore.

12   Mendigalieva S.S., Birimzhanova D.A., Irgibaeva I.S., Barashkov N.N. & Sakhno Y.E. (2022). Aggregation-induced emission of 5-(benzylidene)pyrimidine-2,4,6-triones. Bulletin of the Karaganda University. *Chemistry Series*, *105*(1), 39-49. https://doi.org/10.31489/2022Ch1/39-49.

Information about authors*

Birimzhanova, Dinara Asylbekovna — PhD on Chemical Sciences, Senior lector, L.N. Gumilyov Eurasian National University, Satpayev street, 2, 010000, Astana, Kazakhstan; e-mail: dinarabirimzhanova@gmail.com; https://orcid.org/0000-0002-5572-9339

Irgibaeva, Irina Smailovna (*corresponding author*) — Doctor of Chemical Sciences, Professor of Chemistry Department, L.N. Gumilyov Eurasian National University, Satpayev street, 2, 010000, Astana, Kazakhstan; e-mail: irgsm@mail.ru; https://orcid.org/0000-0003-2408-8935

Barashkov, Nikolay Nikolayevich — Doctor of Chemical Sciences, Director of R&D and Technical Services Micro-Tracers, Inc. 1370 Van Dyke Avenue San Francisco, CA 94124, USA; e-mail: nikolay@microtracers.com; https://orcid.org/0000-0003-2494-9248

_____
*The author's name is presented in the order: *Last Name, First and Middle Names*

Lenara I. Valiulina [iD], Kirill Khoroshkin, Victor N. Cherepanov [iD], Rashid R. Valiev* [iD]

National Research Tomsk State University, Tomsk, Russia
(Corresponding author's e-mail: valievrashid@mail.ru)

Magnetic Properties of Cyclo[*n*]Carbons (*n* = 10–34)

Quantum-chemical calculations of the magnetic properties (magnetically induced ring-current strength, magnetizability) of even- and odd-number cyclo[*n*]carbons (*n* = 10–34) were carried out. The total energy of the studied molecules as a function of the external magnetic field was found for the first time. The obtained dependences predict correctly the magnetic nature of cyclo[*n*]carbons. For even-number aromatic cyclo[*n*]carbons the energy of the system increases with increasing magnetic field, while for antiaromatic systems, the energy decreases. Such behavior indicates that aromatic even-number cyclo[*n*]carbons (*n* = 4*k*+2) are diamagnetic, whereas antiaromatic even-number cyclo[*n*]carbons (*n* = 4*k*) are paramagnetic. These results are confirmed by the previously calculated average magnetizability values. In the case of odd-number cyclo[*n*]carbons, all structures except C13 are diamagnetic. Antiaromatic C13 is paramagnetic according to average magnetizability calculations. It was shown that nonaromatic cyclo[*n*]carbons (*n* = 28–34) at high magnetic fields (*B* > 300 T) possess a nonlinear effect of the increase in the energy of the system with increasing magnetic field. This effect can be observed experimentally in NMR spectra at a magnetic field greater than 300 T. The performed calculations demonstrate that the HF method correctly predicts the magnetic and aromatic properties of cyclo[*n*]carbons (*n* = 10–34).

Keywords: cyclo[*n*]carbons, magnetizability, magnetically induced current, magnetic properties, aromaticity, chemical calculations, magnetic field.

Introduction

Carbon is a unique chemical element that has the largest number of allotropic modifications, each of them has different chemical structure. As a result, these structures have special physicochemical properties. Cyclo[*n*]carbons are allotropes of carbon formed by sp-hybridized carbon atoms linked in a ring [1]. Cyclo[*n*]carbons can arise as a result of condensation processes in the atmospheres of carbon-rich stars [2]. In addition, they appear as intermediates in the plasma used to produce thin diamond films [3].

The cyclo[18]carbon was firstly observed in 1989, however due to its high reactivity it was difficult to separate and characterize the structure of this compound [4]. Subsequent theoretical studies showed the existence of two different forms of molecules: density functional theory and Møller–Plesset perturbation theory (MP2) calculations indicated alternating cumulene structure with non-bond-length [5, 6], while calculations using the Hartree-Fock method [4], the high-level Monte Carlo, *ab initio* (CASSCF) and coupled clusters methods predicted a structure with alternating conjugated single and triple bonds [7, 8]. In 2019, for the first time, the alternating single and triple bonds structure of cyclo[18]carbon was determined experimentally [9].

Subsequently, density functional calculations revealed that the amount of Hartree-Fock exchange in functional is important to determine the correct structure of cyclo[n]carbons [10]. Thus, functionals with a small amount of Hartree-Fock exchange due to overestimation of the correlation energy predict a cumulene structure, while functionals with a large amount of Hartree-Fock exchange [>40 %], such as M062X, BHHLYP, CAM-B3LYP give the correct structure with alternating conjugated single and triple bonds (polyyne-type structure) [10–12]. In addition, it was shown that the cumulene structure of cyclo[18]carbon is a transition state for the single-triple bond inversion process [10].

Synthesis of cyclo[18]carbon gave rise to intense interest in studying the properties and structure of molecules with a different number of carbon atoms in the ring, including odd-number cyclo[*n*]carbons [13–16]. It was shown that odd-number cyclo[*n*]carbons have a carbene structure with a singlet ground state [16]. It should be noted that cyclo[10]carbon and cyclo[16]carbon have already been synthesized. Successes in the synthesis of these systems point to subsequent syntheses of other forms of cyclo[*n*]carbons in the future.

The presence of triple bonds in the structure of cyclo[*n*]carbons leads to their high chemical activity. However, despite the high reactivity, studies of spectroscopic, aromatic, structural, mechanical and electronic

properties reveal that cyclo[*n*]carbons are promising materials that can find application in various fields [10, 16–23]. Thus, due to pronounced electron delocalization, cyclo[*n*]carbons exhibit high electron mobility, which makes it possible to consider them as semiconductor materials [19, 20]. Cyclo[*n*]carbon rings can mechanically interlock to form catenanes, which in turn can bind with bioactive molecules and used to deliver drugs [21]. In addition, cyclo[*n*]carbon rings are highly elastic, and their energy gap can vary depending on the deformation of the ring, which can be used in nanomechanical systems and molecular electronic devices [22, 23].

Cyclo[*n*]carbons also have special magnetic properties, which occur due to the double aromaticity of the molecules [10, 24, 25]. Because of the specific structure, molecules have two independent orthogonal conjugated systems located above and in the plane of a molecule. In an external magnetic field cyclo[*n*]carbons sustain magnetically induced ring currents, which determine their magnetic nature. Antiaromatic cyclo[*n*]carbons with *n* = 8, 12, 16, 20, 24 are paramagnetic [26, 27]. As shown in [27], paramagnetism in closed-shell molecules arises due to strong paratropic ring currents ($|I| > 20$ *n*A/T).

The study of ionization potentials, electron affinities, energy gaps between electronic states for cyclo[*n*]carbons (*n* = 8–100) showed that for *n* > 32 the difference in the properties disappears [28]. This can be explained by the fact that for *n* > 32 the electrons are localized on triple bonds. In this case, the distortion of electron delocalization leads to the loss of aromatic properties. Starting from *n* = 34, systems become non-aromatic [26].

Studies of the magnetic properties of cyclo[*n*]carbons mentioned above were carried out within the framework of the quadratic response theory. However, the detailed study of the magnetic field effect on the properties of cyclo[*n*]carbons has not yet been carried out. Today, the progress in quantum-chemical calculations has led to the inclusion of the magnetic field in the software. Recently, the codes have been implemented in BAGEL and TURBOMOLE [29]. It should be noted that BAGEL implements Dirac equation calculations which allows taking into account relativistic effects [29].

The aim of this work was to study the magnetic properties of a series of the odd- and even-number cyclo[*n*]carbons (*n* = 10–34) in an external magnetic field using quantum chemistry methods.

Computational Details

Previously, it was mentioned that the Hartree-Fock (HF) method correctly predict the polyyne structure of cyclo[*n*]carbons. In addition, the amount of Hartree-Fock exchange in the density functionals plays a decisive role in predicting the structural and magnetic properties of cyclo[*n*]carbons [10]. Therefore, we used the Hartree-Fock (HF) method to study the properties of cyclo[*n*]carbons in an external magnetic field. The optimized structures of the studied cyclo[*n*]carbons (*n* = 10–34) were taken from [16, 26]. Structures with an even-number of carbon atoms were optimized at the DFT level using the M06-2X functional and the def2-TZVP basis set [26]. Cyclo[*n*]carbons with an odd-number of carbon atoms were optimized at the *ab initio* complete active space self-consistent field (CASSCF) level with the 6-31G(d, p) basis set [16]. All of the studied cyclo[*n*]carbons have a polyyne structure. The energy of systems in an external magnetic field was calculated at the HF level of theory using split-valence polarization basis sets (SVP) [30] with the BAGEL program [31].

Magnetically induced ring currents were calculated using the GIMIC method, which uses as input data the atomic orbital density matrix, the perturbed atomic orbital density matrices and the basis-set information [32, 33]. The density matrices were obtained by performing nuclear magnetic resonance (NMR) shielding calculations. The density matrices were computed at the HF/def2-TZVP [34] level using Gaussian 09 [35]. The strengths of the ring currents (*n*A/T) were computed by integrating the current-density flux that passes through a plane placed perpendicular to the molecular plane. We evaluated the accuracy of HF ring current calculations by comparing the results with previously calculated magnetically induced currents obtained at the M06-2X level [27]. The choice of the M06-2X [36] functional is due to its ability to correctly calculate the strength of ring currents, including strongly antiaromatic species [10].

The obtained curves of the dependence of the molecular energy on the magnitude of the external magnetic field were used to calculate the magnetic susceptibility:

$$\chi = -\frac{\partial^2 E}{\partial B^2},$$

where *E* — the total energy; *B* — the magnetic field.

The magnetic susceptibility results were compared with the Gaussian magnetic susceptibility results obtained for even-number cyclo[*n*]carbons at the M06-2X/def2-TZVP level [36]. The magnetic susceptibility

for odd-number cyclo[n]carbons was obtained for the first time at the M06-2X/def2-TZVP level. Calculations were carried out using Gaussian 09 [35].

Results and Discussion

We investigated molecular properties for even- and odd-number cyclo[n]carbons from C_{10} to C_{32} and C_{34}. Molecular structures of the studied cyclo[n]carbons are presented in Figure 1.

Even-Number Cyclo[n]carbons　　　　　**Odd-Number Cyclo[n]carbons**
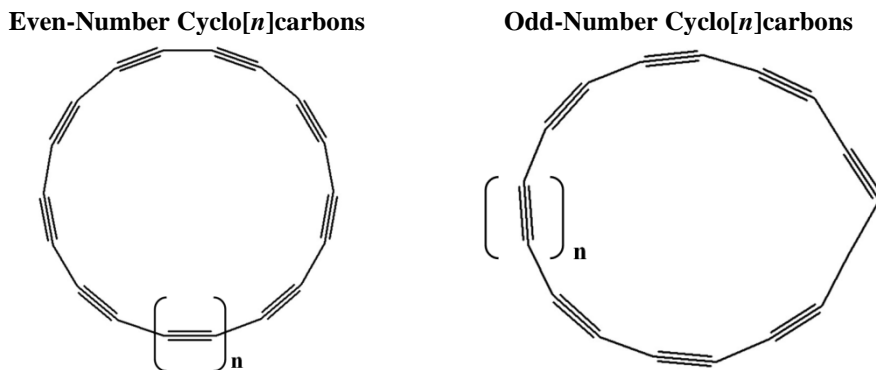
Figure 1. Molecular structures of the studied cyclo[n]carbons

As can be seen in Figure 1, the odd-number cyclo[n]carbons have an extra carbon atom, which leads to a specific geometry with a sharp angle at the carbene atom of these systems. Despite this fact, all odd-number cyclo[n]carbons are planar.

The results of magnetically induced current and magnetizability calculations for the studied cyclo[n]carbons are presented in Tables 1−2. The dependence of the molecular energy on the magnetic field is shown in Figure 2.

T a b l e 1

Magnetically induced ring-current strength of the studied cyclo[n]carbons

Even-number C_n	I, nA/T		Odd-number C_n	I, nA/T	
	HF	M062X		HF	M062X
10	24.5	29.2	11	10.8	12.3
12	−18.6	−40	13	−8.3	−27
14	30.5	43.2	15	5.8	9
16	−13.1	−36.1	17	−3.5	−12.8
18	13.8	31.6	19	2.5	5.5
20	−7.1	−27.1	21	−1.3	−5.7
22	6.4	18.1	23	1.03	1.7
24	−3.6	−18.4	25	−0.5	−1.8
26	3	10.5	27	0.4	0.8
28	−1.7	−15.3	29	−0.1	−0.7
30	1.5	6.4	31	0.3	0.5
32	−0.8	−4.3			
34	0.7	5.0			

As can be seen in Table 1, that even-number cyclo[n]carbons satisfy Hückel's rule. Cyclo[n]carbons ($n = 4k+2$) sustain the net diatropic currents, indicating their aromatic character, while cyclo[n]carbons ($n = 4k$) are clearly antiaromatic, sustaining a net paratropic ring currents. Odd-number cyclo[n]carbons satisfy the following aromaticity rule: the systems with $n = 4k+1$ are antiaromatic, whereas ones with $n = 4k+3$ are aromatic. In the series of even-number cyclo[n]carbons, the most aromatic is C_{14} with diatropic ring currents of 43.2/30.5 nA/T at the M062X/HF levels. The most antiaromatic is C_{12} with a total paratropic ring current of −40.0/−18.6 nA/T at the M062X/HF levels. In the case of odd-number cyclo[n]carbons, the most aromatic is C_{11} with a ring current of 12.3/10.8 nA/T at the M062X/HF levels, while

the most antiaromatic is C_{13} with a ring current of –27.0/–8.3 nA/T at the M062X/HF levels. As n increases, the ring-current strength in cyclo[*n*]carbons decreases. In contrast to even-number cyclo[*n*]carbons, odd-number cyclo[*n*]carbons are generally less aromatic/antiaromatic that is confirmed by weaker ring currents. Starting from $n > 21$ odd-number cyclo[*n*]carbons become nonaromatic ($|I|<3$ nA/T).

The results obtained at the HF level correctly assess the aromatic character of cyclo[*n*]carbons. The ring-current strength for cyclo[*n*]carbons with $n = 10, 11$ obtained at the HF level agree with the results of M062X calculations. However, there is a strong discrepancy in ring-current strengths for the HF and M062X calculations as n increases. The HF predicted ring-current strengths are generally much smaller than ones obtained at the M062X level. The largest cyclo[*n*]carbon possessing aromatic properties according to HF calculations is the antiaromatic C_{24}, which has the net paratropic ring current of –3.6 nA/T, whereas the M062X provides for C_{24} the ring current of –18.4 nA/T. In the case of odd-number cyclo[*n*]carbons, C_{17} has the ring current of –3.5 nA/T (–12.8 nA/T at the M062X level). The subsequent odd-number cyclo[*n*]carbons ($n > 17$) and even-number cyclo[*n*]carbons ($n > 24$) are already nonaromatic.

a) aromatic even-number cyclo[*n*]carbons;   *b*) antiaromatic even-number cyclo[*n*]carbons;

c) odd-number cyclo[*n*]carbons
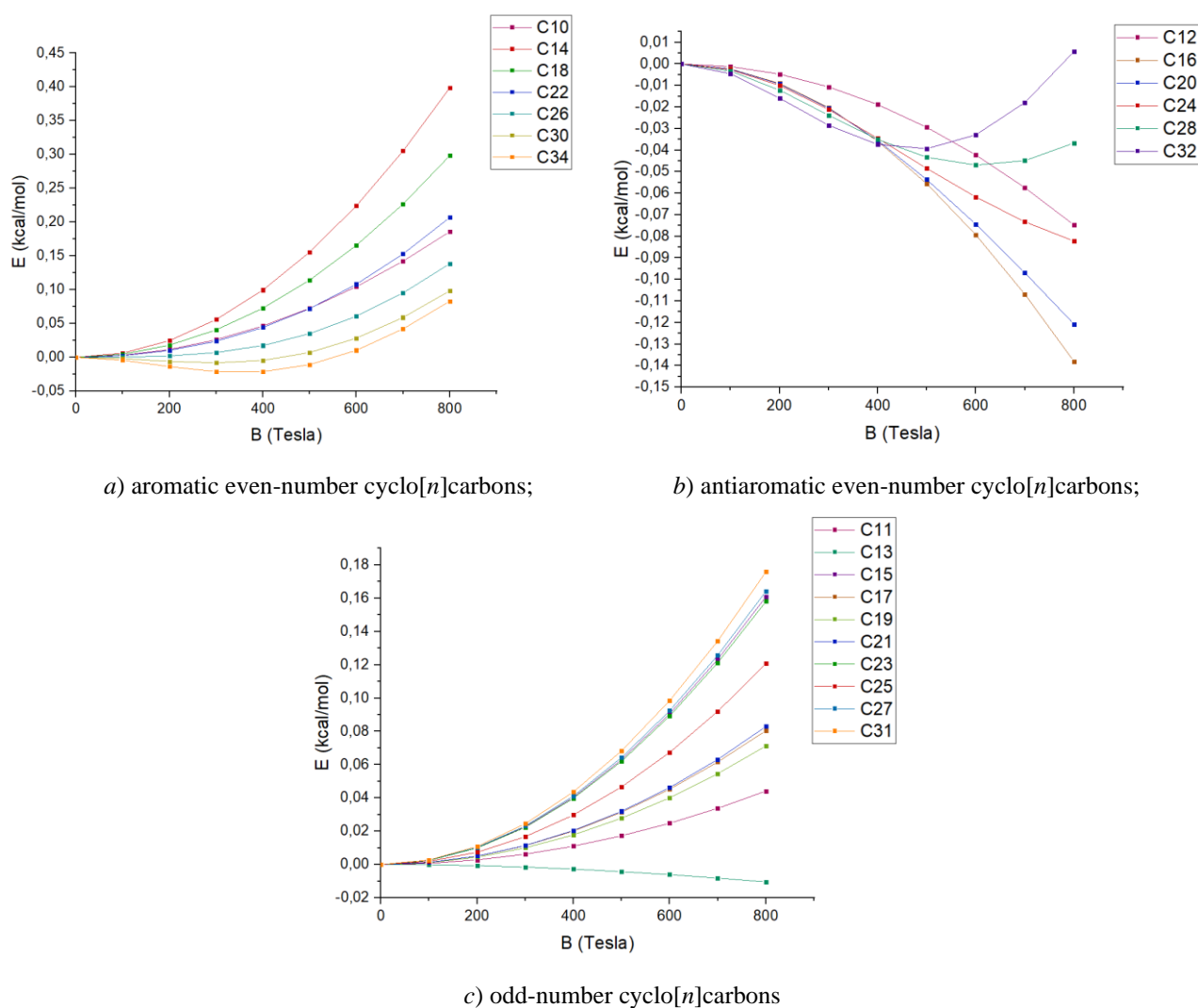
Figure 2. The energy dependence of cyclo[*n*]carbons (C_n) on the magnetic field

Figure 2 demonstrates the change in the energy of the system depending on the magnetic field. It is clearly seen that the change in energy for aromatic and antiaromatic even-number cyclo[*n*]carbons is different. For aromatic cyclo[*n*]carbons ($n = 4k + 2$), the energy of the system increases with increasing magnetic field. This dependence indicates a diamagnetic character of aromatic cyclo[n]carbons, which is confirmed by the average magnetizability calculations (Table 2). Another picture is observed for antiaromatic even-number cyclo[*n*]carbons. The energy of antiaromatic species ($n = 4k$) decreases with increasing the magnetic field.

Such a decrease in energy indicates the paramagnetic nature of antiaromatic cyclo[n]carbons, which is also confirmed by calculations of average magnetizabilities (Table 2).

Average magnetizability of the studied cyclo[n]carbons

Even-number C_n	χ, a.u.		Odd-number C_n	χ, a.u.	
	HF	M062X		HF	M062X
10	−51	−25	11	−12	−19
12	22	14	13	3	3137
14	−54	−57	15	−44	−13
16	40	18	17	−23	−113
18	−78	−68	19	−20	−63
20	41	16	21	−23	−60
22	−44	−63	23	−43	−56
24	46	7	25	−32	−56
26	−6	−70	27	−45	−54
28	58	−6	29	−41	−41
30	36	−66	31	−47	−46
32	82	−20			
34	79	−61			

An interesting trend is the energy changes occurs when C_{28}-C_{34} cyclo[n]carbons lose their aromatic/antiaromatic properties and become nonaromatic at high magnetic field. At magnetic fields B > 300 T for C_{30}, C_{34} and B > 400 T for C_{32} and B > 600 T for C_{28}, the energy of the systems begins to increase. This indicates that nonaromatic systems at high magnetic fields change their magnetic nature from paramagnetic to diamagnetic. Such changes in energy indicate the effects that can arise in NMR spectra at high magnetic field.

Regarding the odd-number cyclo[n]carbons, the energy of these systems increases with increasing magnetic field. The exception is the antiaromatic C_{13}, for which the energy decreases with increasing magnetic field. Thus, we can conclude that all odd-number cyclo[n]carbons are diamagnetic with the exception of C_{13}, which exhibits a paramagnetic nature. These observations are confirmed by calculations of the average magnetizabilities (Table 2). The surprisingly large value of the average magnetizability 3137 a.u. (at the M062X level) is observed for C_{13}. The paramagnetic nature of C_{13} arises from the large value of the paratropic ring current (−27 nA/T at the M062X level).

According to the results presented in Table 2, the magnetizability values obtained from the dependence of energy on the magnetic field are in good agreement with the results obtained at the M062X level. Differences in the results are observed for nonaromatic cyclo[n]carbons C_{28}-C_{34}, in which there is a deviation in the energy change at high magnetic field. The results of magnetizability calculations based on the dependence of energy on the magnetic field determine these structures as paramagnetic, while the results at the M062X level indicate their diamagnetic nature. The reason may be the fact that the calculation of magnetizability was carried out in the range of 0 to 50 T, where the energy of the systems decreases with increasing magnetic field. In general, the obtained dependences of the energy of the system on the magnetic field correctly predict the magnetic properties of cyclo[n]carbons.

Conclusions

In this work, the magnetically induced ring-current strengths and magnetizabilities for a series of cyclo[n]carbons ($n = 10$–34) were computed. The calculations reveal that the dependence of the total energy of studied even-number cyclo[n]carbons on the magnetic field is determined by their aromatic character. For aromatic molecules the energy increases with growth of magnetic field, while for antiaromatic molecules the energy decreases. An unusual effect is observed for nonaromatic C_{28}-C_{34} cyclo[n]carbons. The feature is that the energy for these system decreases in the range of 0 to 300-600 T and increase for higher magnetic fields. Another case occurs for odd-number cyclo[n]carbons. For these molecules the total energy increases with growth of magnetic field regardless of their aromatic character. The exception is the strongest antiaromatic C_{13}.

It is important to note, that the results of calculations obtained by the HF method are generally consistent with more accurate M062X level of theory. Therefore, the HF method correctly predicts the magnetic and aromatic properties of cyclo[n]carbons.

It should be noted that BAGEL implements multiconfiguration calculations at the CASSCF (Complete Active Space SCF) level of theory. In the future, CASSCF method can be applied to provide high-level theory calculations of the structural and magnetic properties of cyclo[n]carbons in an external magnetic field.

References

1   Anderson, H.L., Patrick, C.W., Scriven, L.M. & Woltering, S.L. (2021). A Short History of Cyclo[n]carbons. *Bull. Chem. Soc. Jpn., 94*, 798−811. https://doi.org/10.1246/bcsj.20200345

2   Zack, L.N. & Maier, J.P. (2014). Laboratory spectroscopy of astrophysically relevant carbon species. *Chem. Soc. Rev., 43*, 4602–4614. https://doi.org/10.1039/C4CS00049H

3   Weltner, Jr W. & Van Zee, R.J. (1989). Carbon Molecules, Ions, and Clusters. *Chemical Reviews., 89*, 1713–1747. https://doi.org/10.1021/cr00098a005

4   Diederich, F., Rubin, Y., Knobler, C.B., Whetten, R.L., Schriver, K.E., Houk, K.N. & Li, Y. (1989). All-carbon Molecules: Evidence for the Generation of Cyclo[18]carbon from a Stable Organic Precursor. *Science, 245*, 1088–1090. https://doi.org/10.1126/science.245.4922.1088

5   Parasuk, V., Almlof, J. & Feyereisen, M.W. (1991). The [18] All-carbon Molecule: Cumulene or Polyacetylene? *J. Am. Chem. Soc., 113*, 1049–1050. https://doi.org/10.1021/ja00003a052

6   Neiss, C., Trushin, E. & Görling, A. (2014). The Nature of One-dimensional Carbon: Polyynic Versus Cumulenic. *ChemPhysChem, 15*, 2497–2502. https://doi.org/10.1002/cphc.201402266

7   Torelli, T. & Mitas, L. (2000). Electron Correlation in C4*N*+2 Carbon Rings: Aromatic Versus Dimerized Structures. *Phys. Rev. Lett., 85*, 1702–1705. https://doi.org/10.1103/PhysRevLett.85.1702

8   Arulmozhiraja, S. & Ohno, T. (2008). CCSD Calculations on C14, C18, and C22 Carbon Clusters. *J. Chem. Phys., 128*, 114301. https://doi.org/10.1063/1.2838200

9   Kaiser, K., Scriven, L.M., Schulz, F., Gawel, P., Gross, L. & Anderson, H.L. (2019). An sp-hybridized molecular carbon allotrope, cyclo[18]carbon. *Science, 365*, 1299–1301. https://doi.org/10.1126/science.aay1914

10   Baryshnikov, G.V., Valiev, R.R., Kuklin, A.V., Sundholm, D. & Ågren, H. (2019). Cyclo[18]carbon: Insight into Electronic Structure, Aromaticity, and Surface Coupling. *J. Phys. Chem. Lett., 10*, 6701–6705. https://doi.org/10.1021/acs.jpclett.9b02815

11   Charistos, N.D. & Muñoz-Castro, A. (2020). Induced Magnetic Field in sp-Hybridized Carbon Rings: Analysis of Double Aromaticity and Antiaromaticity in Cyclo[2N]carbon Allotropes. *Phys. Chem. Chem. Phys., 22*, 9240–9249. https://doi.org/10.1039/D0CP01252A

12   Brémond, E., Pérez-Jiménez, A.J., Adamo, C. & Sancho-Garcia, J.C. (2019). *J. Chem. Phys., 151*, 211104. https://doi.org/10.1063/1.5133639

13   Martin, J.M.L., E1-Yazal, J. & Francois, J.-P. (1996). Structure and Relative Energetics of C2*n*+l (*n* = 2–7) Carbon Clusters Using Coupled Cluster and Hybrid Density Functional Methods. *Chem. Phys. Lett., 252*, 9–18. https://doi.org/10.1016/S0009-2614(96)00180-7

14   Brito, B.G.A., Hai, G.-Q. & Cândido, L. (2018). Quantum Monte Carlo Study on the Structures and Energetics of Cyclic and Linear Carbon Clusters Cn (*n* = 1, ..., 10). *Phys. Rev. A, 98*, 062508. https://doi.org/10.1103/PhysRevA.98.062508

15   Yen, T.W. & Lai, S.K. (2015). Use of Density Functional Theory Method to Calculate Structures of Neutral Carbon Clusters Cn (3 ≤ n ≤ 24) and Study Their Variability of Structural Forms. *J. Chem. Phys., 142*, 084313. https://doi.org/10.1063/1.4908561

16   Baryshnikov, G.V., Valiev, R.R., Valiulina, L.I., Kurtsevich, A.E., Kurtén, T., Sundholm, D., Pittelkow, M., Zhang, J. & Ågren, H. (2022). Odd-Number Cyclo[*n*]Carbons Sustaining Alternating Aromaticity. *J. Phys. Chem. A, 126*, 2445–2452. https://doi.org/10.1021/acs.jpca.1c08507

17   Liu, Z., Lu, T. & Chen, Q. (2020). An sp-hybridized All-carboatomic Ring, Cyclo[18]carbon: Electronic Structure, Electronic Spectrum, and Optical Nonlinearity. *Carbon, 165*, 461–467. https://doi.org/10.1016/j.carbon.2020.05.023

18   Ng, R.A., Portnoi, M.E. & Hartmann, R.R. (2022). Tuning Terahertz Transitions in Cyclo[n]carbon Rings. *Phys. Rev. B 106*, L041403. https://doi.org/10.1103/PhysRevB.106.L041403

19   Zhang, L., Li, H., Feng, Y.P. & Shen, L. (2020). Diverse Transport Behaviors in Cyclo[18]carbon-based Molecular Devices, *J. Phys. Chem. Lett., 11*, 2611e2617. https://doi.org/10.1021/acs.jpclett.0c00357

20   Li, M., Gao, Z., Han, Y., Zhao, Y., Yuan, K., Nagase, Sh., Ehara, M. & Zhao, X. (2020). Potential Molecular Semiconductor Devices: Cyclo-Cn (*n* = 10 and with Higher Stabilities and Aromaticities than Acknowledged Cyclo-C18, *Phys. Chem. Chem. Phys., 22*, 4823–4831. https://doi.org/10.1039/D0CP00167H

21 Fedik, N., Kulichenko, M., Steglenko, D. & Boldyrev, A. I. (2020). Can Aromaticity be a Kinetic Trap? Example of Mechanically Interlocked Aromatic [2-5]catenanes Built of Cyclo[18]carbon. *Chem. Commun., 56*, 2711–2714. https://doi.org/10.1039/C9CC09483K

22 Fang, S. & Hu, Y.H. (2021). Cyclo[18]carbon as an Ultra-elastic Molecular O-ring with Unique Mechanical Properties. *Carbon, 171*, 96–103. https://doi.org/10.1016/j.carbon.2020.08.082

23 Hou, L., Hu, H., Yang, G. & Ouyang, G. (2021). Giant Switching Effect and Spintronic Transport Properties in Cyclo[18]carbon-Based Molecular Devices. *Phys. Status Solidi,15,* 2000582. https://doi.org/10.1002/pssr.202000582

24 Hoffmann, R. (1966). Extended Hückel Theory—V: Cumulenes, Polyenes, Polyacetylenes and C*n. Tetrahedron, 22*, 521–538. https://doi.org/10.1016/0040-4020(66)80020-0

25 Fowler, P. W., Mizoguchi, N., Bean, D. E. & Havenith, R. W.A. Double Aromaticity and Ring Currents in All-Carbon Rings. *Chem. Eur. J. 15*, 6964–6972. https://doi.org/10.1002/chem.200900322

26 Baryshnikov, G.V., Valiev, R.R., Nasibullin, R.T., Sundholm, D., Kurten, T. & Ågren, H. (2020). Aromaticity of Even-Number Cyclo[n]carbons ($n = 6{-}100$). *J. Phys. Chem. A*, 124, 10849–10855. https://doi.org/10.1021/acs.jpca.0c09692

27 Valiev, R.R., Baryshnikov, G.V., Nasibullin, R.T., Sundholm, D. & Ågren, H. (2020). When are Antiaromatic Molecules Paramagnetic? *J. Phys. Chem. C, 124*, 21027–21035. https://doi.org/10.1021/acs.jpcc.0c01559

28 Seenithurai S. & Chai J.D. (2020). TAO-DFT Investigation of Electronic Properties of Linear and Cyclic Carbon Chains. *Scientific reports, 10*, 1-13. https://doi.org/10.1038/s41598-020-70023-z

29 Reynolds, R.D. & Shiozaki, T. (2015). Fully Relativistic Self-consistent Field under a Magnetic Field. *Phys. Chem. Chem. Phys., 17*, 14280–14283. https://doi.org/10.1039/C4CP04027A

30 Schäfer, A., Horn, H. & Ahlrichs, R. (1992). Fully Optimized Contracted Gaussian-basis Sets for Atoms Li to Kr. *J. Chem. Phys., 97*, 2571–2577. https://doi.org/10.1063/1.463096

31 BAGEL, Brilliantly Advanced General Electronic-structure Library. http://www.nubakery.org.

32 Fliegl, H., Taubert, S., Lehtonen, O. & Sundholm, D. (2011). The Gauge Including Magnetically Induced Current Method. *Phys. Chem. Chem. Phys., 13*, 20500–20518. https://doi.org/10.1039/C1CP21812C

33 Sundholm, D., Fliegl, H. & Berger, R. (2016). Calculations of Magnetically Induced Current Densities: Theory and Applications. *Wiley Interdiscip. Rev.: Comput. Mol. Sci., 6*, 639–678. https://doi.org/10.1002/wcms.1270

34 Weigend, F. & Ahlrichs, R. (2005). Balanced Basis Sets of Split Valence, Triple Zeta Valence and Quadruple Zeta Valence Quality for H to Rn: Design and Assessment of Accuracy. *Phys. Chem. Chem. Phys., 7*, 3297–3305. https://doi.org/10.1039/B508541A

35 Gaussian 09, Revision A.02, Frisch, M.J., Trucks, G.W., Schlegel, H.B., Scuseria, G.E., Robb, M.A., Cheeseman, J.R. et al., *Gaussian, Inc.*, Wallingford CT, 2016.

36 Zhao, Y. & Truhlar, D.G. The M06 Suite of Density Functionals for Main Group Thermochemistry, Thermochemical Kinetics, Noncovalent Interactions, Excited States, and Transition Elements: Two New Functionals and Systematic Testing of Four M06-class Functionals and 12 other Functionals. *Theor. Chem. Acc., 120*, 215−241. https://doi.org/10.1007/s00214-007-0310-x

Information about authors*

Valiulina, Lenara Ilmirovna — 1st year PhD student, Department of Optics and Spectroscopy, National Research Tomsk State University, Tomsk, 36 Lenin Avenue, 634050, Russia; e-mail: valiulina-lenara@mail.ru; https://orcid.org/0000-0002-3364-0448

Khoroshkin, Kirill — 4th year student, Department of Optics and Spectroscopy, National Research Tomsk State University, Tomsk, 36 Lenin Avenue, 634050, Russia; horoshkink@gmail.com

Cherepanov, Victor Nikolaevich — Doctor of Physics and Mathematics, Head of Department of Optics and Spectroscopy National Research Tomsk State University, Tomsk, 36 Lenin Avenue, 634050, Russia; e-mail: vnch1626@mail.ru; https://orcid.org/0000-0002-5952-5202

Valiev, Rashid Rinatovich (*corresponding author*) — Doctor of Chemical Sciences, Assistant professor, National Research Tomsk State University, Tomsk, 36 Lenin Avenue, 634050, Russia; e-mail: valiev-rashid@mail.ru; http://orcid.org/0000-0002-2088-2608

_____

*The author's name is presented in the order: *Last Name, First and Middle Names*

Irina V. Uvarova, Anuar A. Aldongarov[*] ⓘD, Zhadyra Y. Baitassova

Laboratory of physical and quantum chemistry, L.N. Gumilyov Eurasian National University, Astana, Kazakhstan
(*Corresponding author's e-mail: enu-2010@yandex.kz)

Theoretical Study of Charge Mobility Properties of Complexes Si(DPP)(CH₃)₂ and Si(Bzimpy)(CH₃)₂

The direction of organic electronics research is attracting more and more interest from the scientific community. One of the indicators of such interest is the appearance of commercially available products with screens based on organic compounds. Therefore, conducting experimental and theoretical research in this area is an urgent task. Pentacoordination neutral complexes of silicon are poorly studied from the point of view of application in organic electronics, as well as six-coordination analogues. We present data on the calculation of reorganization energies, intermolecular transfer integrals, transfer rates and charge mobility for the optimized structures of pentacoordinated silicon complexes $Si(DPP)(CH_3)_2$ and $Si(bzimpy)(CH_3)_2$. We have applied Marcus-Hush model for calculation of charge mobilities. The $Si(DPP)(CH_3)_2$ structure contains one diphenylpyridine (DPP = 2,6-diphenylperidine) ligand. The $Si(bzimpy)(CH_3)_2$ structure contains one benzimidazole (bzimpy = 2,6-bis(benzimidazole-2'-il)pyridine) ligand. Computational data were obtained using the B3LYP hybrid functional and the basis set 6-31G*. All calculations were performed using Gaussian09 program package. The charge mobility data obtained for $Si(DPP)(CH_3)_2$ and $Si(bzimpy)(CH_3)_2$ pentacoordinated silicon complexes were compared with their six-coordinate counterparts $Si(DPP)_2$ and $Si(bzimpy)_2$ for which experimental data on charge mobilities become available last years. Comparison with six-coordination analogues of complexes showed that penta-coordination complexes $Si(DPP)(CH_3)_2$ and $Si(bzimpy)(CH_3)_2$ have much higher mobility of electrons, while $Si(bzimpy)(CH_3)_2$ also has higher hole mobility. We suppose this could be related to different symmetry of the pentacoordinated and hexacoordinted complexes. It is shown that the mobility of holes is much higher in the complex $Si(bzimpy)(CH_3)_2$ than in $Si(DPP)(CH_3)_2$.

Keywords: density functional method DFT, silicon pentacoordinated complexes, pyridine-containing ligands, charge mobility, reorganization energy, internal reorganization energy, intermolecular transfer integral, charge transfer rate, charge carrier diffusion coefficient.

Introduction

In recent years, there has been considerable interest in the study of light emitting diodes based on organic materials, which are usually called organic light emitting diodes (OLEDs) [1, 2]. But at the same time, a huge wave of commercial success creates a great need to improve the efficiency, stability and sustainability of new materials [3]. The need is exacerbated by recent advances in organic electronics [4–6]. Organic semi-conductors also find application in various organic photovoltaic (OPV) [7–10] and OLED [11–14] devices, in particular as a hole conduction layer (HTL) [15, 16] or as an electronic conduction layer (ETL) [17]. It is worth to mention that hexacoordinated silicon complexes have shown remarkable stability [18, 19].

At the moment pentacoordinated silicon complexes are new type of molecules that attract scientists due to their properties. They can also be used in organic electronics, allowing improvements to existing devices that are of interest for further research. The desire to improve the physical properties of materials led to the study of charge transport characteristics. Determination of structural-functional relationships between the mobility of electrons and holes is of high importance for the development of efficient devices. In this work, the objects of study are pentacoordination silicon complexes: $Si(DPP)(CH_3)_2$ containing one diphenylpyridine ligand and $Si(bzimpy)(CH_3)_2$ with a benzimidazole ligand. The purpose of this work is a theoretical study of the properties of charge transport in these compounds using the density functional theory.

I.V. Uvarova, A.A. Aldongarov, Zh.Y. Baitassova

Figure 1. Left — 2D structure of Si(bzimpy)(CH₃)₂ complex, right — 2D structure of Si(DPP)(CH₃)₂ complex

Computational Details

For quantum-chemical studies, models of the Si(DPP)(CH$_3$)$_2$ and Si(bzimpy)(CH$_3$)$_2$ structures were built, for which the DFT (density functional theory method) method implemented in the GaussianW09 Rev.E01 software package was used [20]. This software package includes a wide range of different functionals. In our calculations we have used B3LYP hybrid functional [21–23]. Subsequently, the structures were optimized using the basis set: 6-31G* [24–27]. An analysis of the nature of the molecular orbitals, the highest occupied molecular orbital (HOMO) and the lowest unoccupied molecular orbital (LUMO), has been studied. Calculations of vibrational frequencies showed the absence of negative values, which indicates that all the obtained structures correspond to the absolute minimum of energy.

Results and Discussion

We have obtained optimized structures of Si(DPP)(CH$_3$)$_2$ and Si(bzimpy)(CH$_3$)$_2$. Tables 1 and 2 demonstrate basic geometrical parameters of optimized molecules Si(DPP)(CH$_3$)$_2$ and Si(bzimpy)(CH$_3$)$_2$.

T a b l e 1

Data on geometrical parameters of optimized Si(bzimpy)(CH₃)₂

Si(bzimpy)(CH₃)₂	Bond length (Å)		Angles (º)	
	^{10}Si-^{6}N	1.94032	^{10}Si-^{6}N-^{1}C	119.239
	^{10}Si-^{35}C	1.88533	^{1}C-^{11}C-^{15}N	113.439
	^{10}Si-^{15}N	1.92868	^{11}C-^{15}N-^{10}Si	117.116
	^{6}N-^{1}C	1.35863	^{6}N-^{1}C-^{2}C	120.439
	^{15}N-^{14}C	1.37820	^{1}C-^{2}C-^{3}C	118.372
	^{1}C-^{2}C	1.39367	^{11}C-^{15}N-^{14}C	103.805
	^{2}C-^{7}H	1.08330	^{15}N-^{11}C-^{12}N	116.957
	^{13}C-^{14}C	1.43169	^{14}C-^{13}C-^{21}C	120.271
	^{31}C-^{32}C	1.41447	^{6}N-^{10}Si-^{35}C	119.432

T a b l e 2

Data on geometrical parameters of optimized Si(DPP)(CH₃)₂

Si(DPP)(CH₃)₂	Bond length (Å)		Angles (º)	
	^{10}Si-^{6}N	2.12188	^{10}Si-^{6}N-^{1}C	118.139
	^{10}Si-^{36}C	1.98610	^{1}C-^{11}C-^{33}C	114.041
	^{10}Si-^{26}C	1.91774	^{6}N-^{10}Si-^{33}C	76.733
	^{6}N-^{1}C	1.34211	^{11}C-^{33}C-^{10}Si	119.004
	^{15}C-^{14}C	1.37820	^{1}C-^{2}C-^{3}C	118.336
	^{1}C-^{2}C	1.39976	^{6}N-^{1}C-^{2}C	119.371
	^{2}C-^{7}H	1.08395	^{1}C-^{6}N-^{5}C	123.721
	^{13}C-^{14}C	1.39847	^{13}C-^{14}C-^{15}C	120.251
	^{11}C-^{33}C	1.40953	^{33}C-^{10}Si-^{26}C	97.194

Next, we have calculated energies of reorganization of holes λ_{hole} and electrons $\lambda_{electron}$ for the molecules using formula (1) [28–30]. Reorganization energies are summation of relaxation energies during the transition from neutral molecule to cation/anion and back on potential energy surfaces.

$$\lambda_{hole} = [E+(A) - E+(A+)] + [E(A+) - E(A)],$$
$$\lambda_{electron} = [E-(A) - E-(A-)] + [(A-) - (A)], \tag{1}$$

where $E(A)$ — energy of neutral molecule after optimization; $E(A+)$ — energy of cation of a molecule after optimization; $E+(A+)$ — energy of positively charged molecule with the geometry of a neutral molecule; $E+(A)$ — energy of a neutral molecule with geometry of cation; $E(A-)$ — energy of an anion after optimization; $E-(A-)$ — energy of negatively charged molecule with the geometry of a neutral molecule; $E-(A)$ — energy of a neutral molecule with the geometry of an anion.

Tables 3 and 4 demonstrate data for calculation of reorganization energies of charges for the molecules Si(bzimpy)(CH$_3$)$_2$ and Si(DPP)(CH$_3$)$_2$.

T a b l e 3

Data for calculation of reorganization energies of holes in Si(bzimpy)(CH$_3$)$_2$ and Si(DPP)(CH$_3$)$_2$

Molecule	$E(A)$ (eV)	$E(A+)$ (eV)	$E+(A+)$ (eV)	$E+(A)$ (eV)	λ_{hole} (eV)
Si(bzimpy)(CH$_3$)$_2$	–37368.9106	–37361.9183	–37361.8213	–37368.8130	0.0006
Si(DPP)(CH$_3$)$_2$	–29336.2819	–29329.6028	–29338.9966	–29333.9283	11.7474

T a b l e 4

Data for calculation of reorganization energies of electrons in Si(bzimpy)(CH$_3$)$_2$ and Si(DPP)(CH$_3$)$_2$

Molecule	$E(A)$ (eV)	$E(A-)$ (eV)	$E-(A-)$ (eV)	$E-(A)$ (eV)	$\lambda_{electron}$ (eV)
Si(bzimpy)(CH$_3$)$_2$	–37368.9106	–37370.2840	–37370.0787	–37368.7221	–0.0168
Si(DPP)(CH$_3$)$_2$	–29336.2819	–29336.7976	–29336.5080	–29336.0409	–0.0486

On the next step we have estimated energies of HOMO and LUMO. Figures 2 and 3 represent visualized HOMO and LUMO for molecules Si(bzimpy)(CH$_3$)$_2$ and Si(DPP)(CH$_3$)$_2$. As one can see from Figures 2 and 3 HOMOs and LUMOs are formed by π orbitals of the ligands.

Figure 4 demonstrate boundary MOs energy levels diagram of molecules Si(bzimpy)(CH$_3$)$_2$ and Si(DPP)(CH$_3$)$_2$. According to Figure 4 both molecules have about the same energy of HOMO but different energies of LUMO. Therefore, band gap in Si(bzimpy)(CH$_3$)$_2$ is about 2.7 eV while for Si(DPP)(CH$_3$)$_2$ it is about 4 eV.
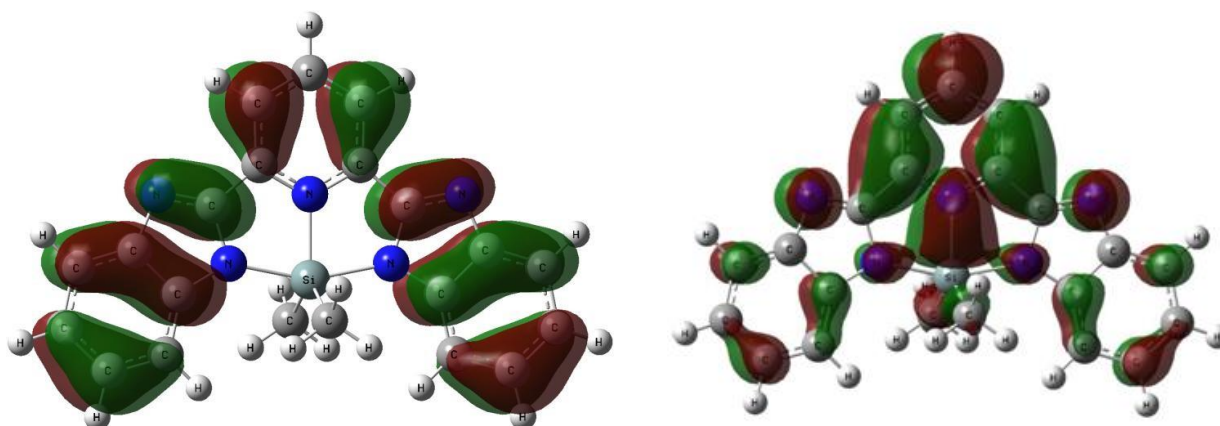
Figure 2. Visualized HOMO (left) and LUMO (right) of the complex Si(bzimpy)(CH$_3$)$_2$
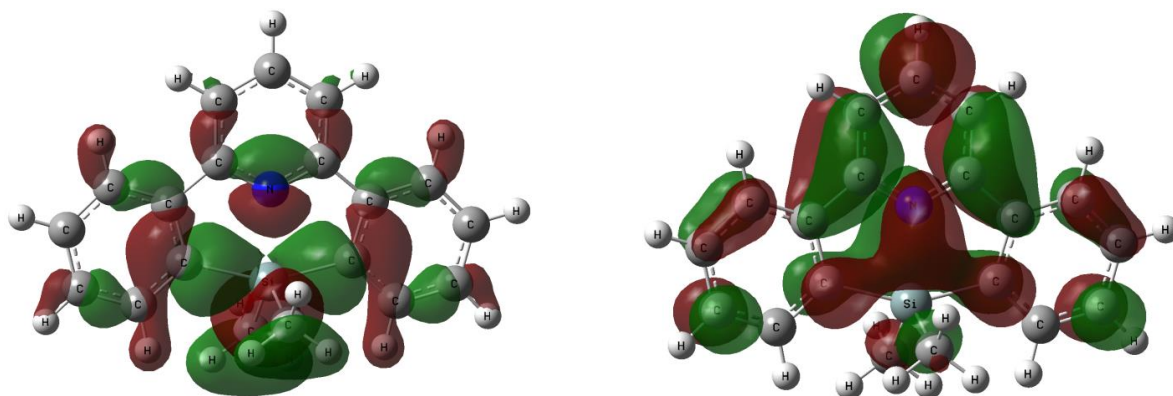
Figure 3. Visualized HOMO (left) and LUMO (right) of the complex Si(DPP)(CH$_3$)$_2$
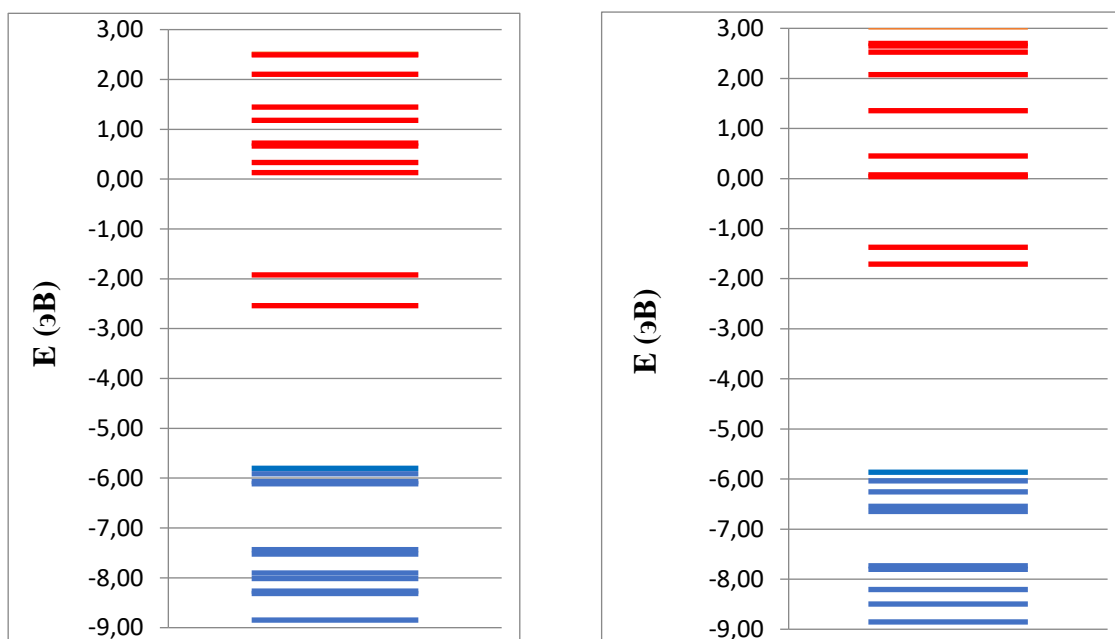
Figure 4. Energy levels diagram of boundary MOs for the molecules Si(bzimpy)(CH$_3$)$_2$ (left)
and Si(DPP)(CH$_3$)$_2$ (right). Blue color indicates occupied MOs and red indicates unoccupied MOs

Using Koopmans theorem approximation and energy splitting in dimer method we have used formula (2) for calculation of the integral of intermolecular charge transfer V$_{h/e}$ for holes and electrons [31–33]:

$$V_{h/e} = \frac{\varepsilon_{H[L+1]} - \varepsilon_{H-1[L]}}{2},\qquad(2)$$

where $\varepsilon_{H[L+1]}$ — energy of HOMO (LUMO+1); $\varepsilon_{H-1[L]}$ — energy of HOMO-1 (LUMO) in dimer. In order to perform these calculations we have optimized structures of dimers for Si(bzimpy)(CH$_3$)$_2$ and Si(DPP)(CH$_3$)$_2$ molecules. Figures 5 and 6 demonstrate optimized structures of the dimers. For these dimers structures we have calculated energies of frontier MO energies. Figure 7 demonstrates diagram of MOs for the dimers.

Table 5 demonstrates data for energies of HOMO-1, HOMO, LUMO и LUMO+1 for calculation of $V_{h/e}$.

T a b l e   5

Data for calculation of V$_{h/e}$ for the compounds Si(bzimpy)(CH$_3$)$_2$ and Si(DPP)(CH$_3$)$_2$

Molecule	E_{HOMO} (eV)	E_{HOMO-1} (eV)	V_{hole} (eV)	E_{LUMO} (eV)	E_{LUMO+1} (eV)	$V_{electron}$ (eV)
Si(bzimpy)(CH$_3$)$_2$	−5.78272	−5.84283	0.030055	−2.49696	−2.47139	0.012785
Si(DPP)(CH$_3$)$_2$	−5.92525	−6.05472	0.064735	−1.75821	−1.56509	0.09656
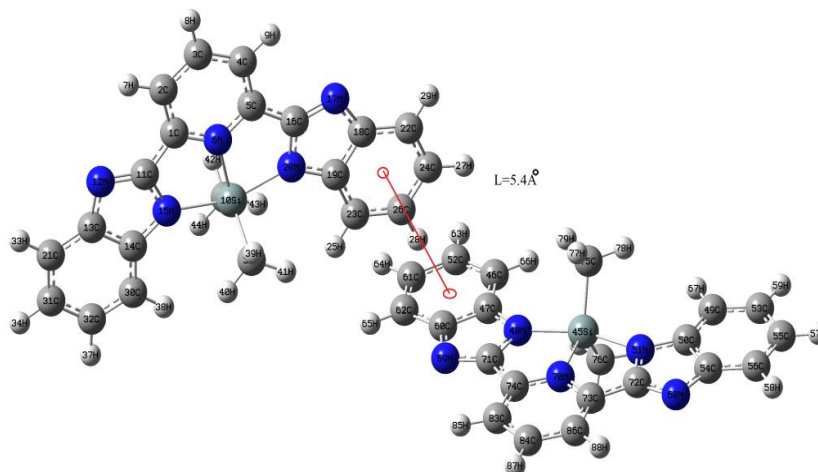
Figure 5. Structure of dimer for molecule Si(bzimpy)(CH$_3$)$_2$
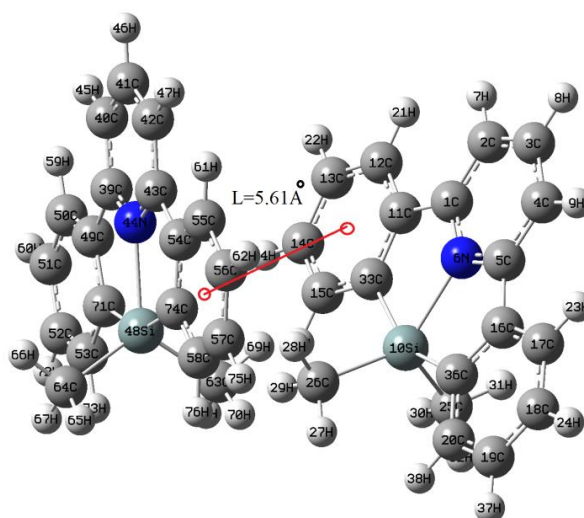
Figure 6. Structure of dimer for molecule Si(DPP)(CH$_3$)$_2$
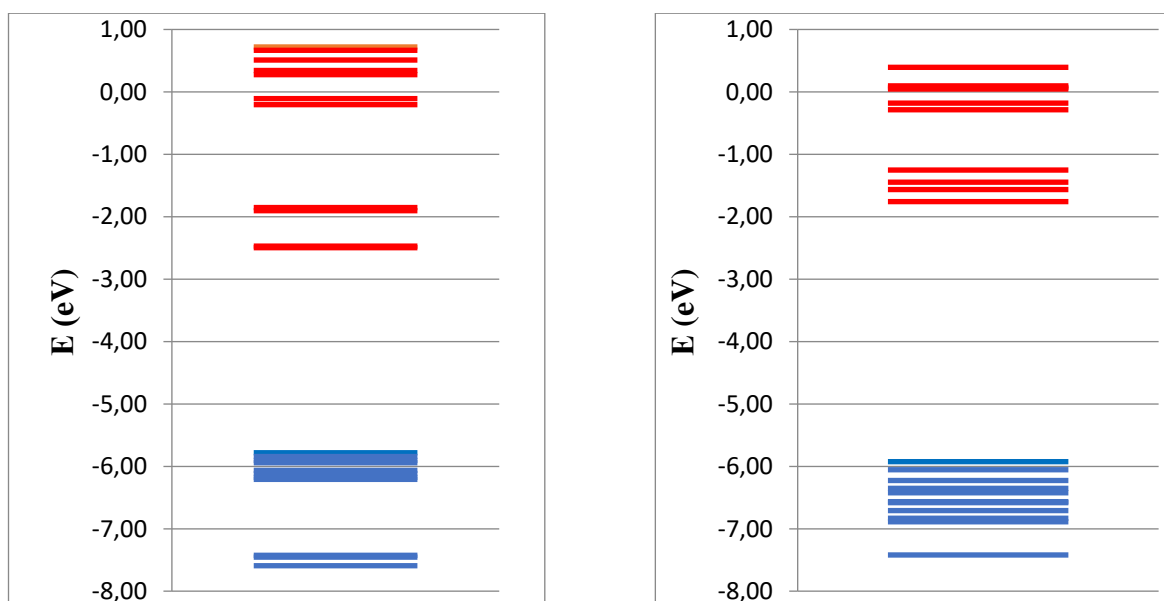
Figure 7. Energy levels diagram of boundary MOs for the dimers of Si(bzimpy)(CH$_3$)$_2$ (left) and Si(DPP)(CH$_3$)$_2$ (right). Blue color indicates occupied MOs and red indicates unoccupied MOs

Next, we have calculated transfer rate of holes and electrons $Ket_{h/e}$ which is described by the formula (3) in accordance with Marcus-Hush theory [34, 35]:

$$Ket_{h/e} = \sqrt{\frac{\pi}{\lambda_{h/e} k_B T}} \cdot \frac{V_{h/e}^2}{\hbar} \cdot \exp\left(-\frac{\lambda_{h/e}}{4K_B T}\right), \tag{3}$$

where k_B — Boltzmann constant; T — temperature, $\hbar$ — Plank constant, $\lambda_{h/e}$ — reorganization energy of hole and electron.

Using data obtained above and known constants we have calculated transfer rates for the molecules. Table 6 demonstrates data for $Ket_{h/e}$. As one can see from Table 6 transfer rate for holes in $Si(DPP)(CH_3)_2$ is very small. This is mostly due to large value of λ_{hole} in $Si(DPP)(CH_3)_2$.

T a b l e 6

Calculated transfer rates for Si(bzimpy)(CH₃)₂ and Si(DPP)(CH₃)₂

Molecule	Ket_{hole} (s⁻¹)	$Ket_{electron}$ (s⁻¹)
$Si(bzimpy)(CH_3)_2$	$6.21 \times 10^{+14}$	1.81×10^{13}
$Si(DPP)(CH_3)_2$	6.79×10^{-38}	4.43×10^{14}

In order to estimate diffusion coefficient of charge carriers it is necessary to know the distance between molecules in a dimer. Therefore, we have estimated distance between molecules in the dimers for molecules $Si(bzimpy)(CH_3)_2$ and $Si(DPP)(CH_3)_2$. Figures 5 and 6 demonstrate distances between the molecules.

The diffusion coefficient could be estimated based on the Einstein-Smoluchowski formula [36]:

$$D = \frac{L^2 Ket}{2}, \tag{4}$$

where Ket — charge transfer rate, L — distance between molecules in a dimer. Using calculated values of Ket and L we have obtained D values for holes and electrons, which are shown in Table 7.

T a b l e 7

Charge carriers diffusion coefficients for molecules Si(bzimpy)(CH₃)₂ and Si(DPP)(CH₃)₂

Molecule	L (Å)	D_{hole} (cm² s⁻¹)	$D_{electron}$ (cm² s⁻¹)
$Si(bzimpy)(CH_3)_2$	5.40	9.05×10^{-1}	2.64×10^{-2}
$Si(DPP)(CH_3)_2$	5.61	1.07×10^{-52}	6.97×10^{-1}

In a weak field approximation charge mobility could be estimated by the Einstein formula [37]:

$$\mu = \frac{eD}{kT}, \tag{5}$$

where e — electron charge, D — diffusion coefficient of charge carriers. Using obtained data from above we have calculated charge mobilities for the molecules. Table 8 demonstrates calculated charge mobilities.

T a b l e 8

Charge carriers mobilities for molecules Si(bzimpy)(CH₃)₂ and Si(DPP)(CH₃)₂

Molecule	μ_{hole} (cm² V⁻¹ s⁻¹)	$\mu_{electron}$ (cm² V⁻¹ s⁻¹)
$Si(bzimpy)(CH_3)_2$	3.58×10^1	1.04×10^0
$Si(DPP)(CH_3)_2$	4.23×10^{-51}	2.76×10^1

According to the obtained results, presence of bzimpy ligand provides much higher value of hole mobility in comparison with DPP ligand, and DPP ligand provides higher electron mobility than bzimpy in the considered molecules. To estimate relatively values of $\mu_{hole/electron}$ we may mention experimental data for sixcoordinated analogues $Si(DPP)_2$ [38] $\mu_{hole} = 1.1 \times 10^{-5}$ (cm² V⁻¹ s⁻¹), $\mu_{electron} = 18 \times 10^{-5}$ (cm² V⁻¹ s⁻¹) and $Si(bzimpy)_2$ $\mu_{hole} = 5.31 \times 10^{-6}$ (cm² V⁻¹ s⁻¹), $\mu_{electron} = 9.68 \times 10^{-5}$ (cm² V⁻¹ s⁻¹) [39]. Comparison of charge mobilities for pentacoordinated and sixcoordinated silicon analogues demonstrates that pentacoordinated $Si(bzimpy)(CH_3)_2$ has much higher values, while $Si(DPP)(CH_3)_2$ has high electron mobility and very low hole

mobility. This could be due to lower symmetry of pentacoordinated silicon compounds in comparison with highly symmetrical sixcoordinated ones.

Conclusions

In this paper we have considered properties of charge transport in neutral pentacoordinated silicon complexes $Si(DPP)(CH_3)_2$ and $Si(bzimpy)(CH_3)_2$ using DFT method. For the molecule $Si(bzimpy)(CH_3)_2$ we have shown that hole mobility is higher than for electrons. Our calculations for $Si(DPP)(CH_3)_2$ have demonstrated very low mobility of holes. The comparison of the results obtained for compounds $Si(DPP)(CH_3)_2$ and $Si(bzimpy)(CH_3)_2$ has demonstrated that $Si(bzimpy)(CH_3)_2$ has higher charge mobility for holes than $Si(DPP)(CH_3)_2$ while $Si(DPP)(CH_3)_2$ has higher electron mobility. Also, we have compared the values of $\mu_{hole/electron}$ for pentacoordinated and sixcoordinated complexes with ligands bzimpy and DPP and it was revealed that pentacoordinated analogues have much lower values of charge mobilities. We believe that this fact is related to high symmetry of sixcoordinated silicon complexes.

Acknowledgements

References

1 Kwon, B. et al. (2021). Organic/Inorganic Hybrid Thin-Film Encapsulation Using Inkjet Printing and PEALD for Industrial Large-Area Process Suitability and Flexible OLED Application. *ACS Appl. Mater. Interfaces*, *13*, 55391–55402. https://doi.org/10.1021/ic011003v

2 Joo, W. et al. (2020). Metasurface-Driven OLED Displays Beyond 10,000 Pixels per Inch. *Science*, *370*, 459−463. https://doi.org/10.1126/science.abc8530

3 Song, J. et al. (2020). Organic Light-Emitting Diodes: Pushing Toward the Limits and Beyond. *Adv. Mater*, *32*, 1907539. https://doi.org/10.1002/adma.201907539

4 Zhang, D. et al. (2020). Emerging Self-Emissive Technologies for Flexible Displays. *Adv. Mater*, *32*, 1902391. https://doi.org/10.1002/adma.201902391

5 Bae, S.K. et al. (2020). Transparent Ultra-Thin Silver Electrodes Formed via a Maskless Evaporation Process for Applications in Flexible Organic Light-Emitting Devices. *Nano Energy*, *71*, 104649. https://doi.org/10.1016/j.nanoen.2020.104649

6 Li, N. et al. (2020). Molecular Engineering by σ-Bond Spacer Enables Solution-Processable Host Materials for TADF Emitter towards High-Performance OLEDs. *Chem. Eng. J*, 396, 125276. https://doi.org/10.1016/j.cej.2020.125276

7 Green, M.A. et al. (2017). Solar cell efficiency tables (version 50). *Progress in Photovoltaics: Research and Applications*, *25*, 668-676. https://doi.org/10.1002/pip.3371

8 Zhao, W. et al. (2017). Molecular Optimization Enables over 13 % Efficiency in Organic Solar Cells. *J. Am. Chem. Soc.*, *139*, 7148–7151. https://doi.org/10.1021/jacs.7b02677

9 Kang, H. et al. (2016). Bulk-Heterojunction Organic Solar Cells: Five Core Technologies for Their Commercialization. *Adv. Mater.*, *28*, 7821–7861. https://doi.org/10.1002/adma.201601197

10 Hedley, G.J. et al. (2017). Light Harvesting for Organic Photovoltaics. *Chem. Rev.*, *117*(2), 796-837. https://doi.org/10.1021/acs.chemrev.6b00215

11 Tremblay, J.-F. (2016). The rise of OLED displays. *C&EN*, 94(28), 30-34.

12 Kim, Y. et al. (2015). An ultra thin implantable system for cerebral blood volume monitoring using flexible OLED and OPD //2015 IEEE International Electron Devices Meeting (IEDM). *IEEE International Electron Devices Meeting (IEDM)*, 29.6.1 — 26.6.4. https://doi.org/10.1109/IEDM.2015.7409796

13 Man, J.-X. et al. (2017). Black Phase-Changing Cathodes for High-Contrast Organic Light-Emitting Diodes. *ACS Photonics*, *4*, 1316-1321. https://doi.org/10.1021/acsphotonics.7b00203

14 Levermore, P. et al. (2016). Ink-Jet-Printed OLEDs for Display Applications. *SID Int. Symp. Dig. Tec.*, *47*, 484-486. https://doi.org/10.1002/sdtp.10714

15 Xu, H. et al. (2020). Printable Hole Transport Layer for 1.0 cm^2 Organic Solar Cells. *ACS Appl. Mater. Interfaces*, *12*(46), 52028–52037. https://doi.org/10.1021/acsami.0c16124

16 Kang, S. et al. (2020). Improved Electroluminescence Performance of Perovskite Light-Emitting Diodes by a New Hole Transporting Polymer Based on the Benzocarbazole Moiety. *ACS Appl. Mater. Interfaces*, *12*(46), 51756–51765. https://doi.org/10.1021/acsami.0c16593

17 Kim, J.-H. et al. (2017). Designing an electron-transport layer for highly efficient, reliable, and solution-processed organic light-emitting diodes. *J. Mater. Chem. C.*, *5*(12), 3097–3106. https://doi.org/10.1039/C7TC00488E

18 Peloquin, D.M. et al. (2016). Recent advances in hexacoordinate silicon with pyridine-containing ligands: Chemistry and emerging applications. *Coord. Chem. Rev.*, *323*, 107–119. https://doi.org/10.1016/j.ccr.2016.02.005

19 Li, Y. et al. (2019). Optical dielectric function of Si(2,6-bis(benzimidazol-2'-yl)pyridine)2 determined by spectroscopic ellipsometry. *Opt. Mat. Express*, *9*(8), 3469-3475. https://doi.org/10.1364/OME.9.003469

20 Frisch, M.J. et al. Gaussian Inc, Wallingford, CT 2009. Gaussian 09, Revision E.01, M.

21 Becke, A.D. (1993). Density-functional thermochemistry. III. The role of exact exchange. *J. Chem. Phys.*, *98*, 5648. https://doi.org/10.1007/s002149900065

22 Lee, C. et al. (1988). Development of the Colle-Salvetti correlation-energy formula into a functional of the electron density. *Phys. Rev.*, *37*, 785. https://doi.org/10.1103/PhysRevB.37.785

23 Stephens, P.J. et al. (1994). Ab Initio Calculation of Vibrational Absorption and Circular Dichroism Spectra Using Density Functional Force Fields. *J. Phys. Chem.*, *98*, 11623. https://doi.org/10.1021/j100096a001

24 Hehre, W.J. et al. (1972). Self-Consistent Molecular Orbital Methods. Further extensions of Gaussian-type basis sets for use in molecular-orbital studies of organic-molecules. *J. Chem. Phys.*, *56*, 2257. https://doi.org/10.1063/1.1677527

25 Hariharan, P.C. et al. (1973). Influence of polarization functions on molecular-orbital hydrogenation energies. *Theor. Chem. Acc.*, *28*, 213-22. https://doi.org/10.1007/BF00533485

26 Hariharan, P.C. et al. (1974). Accuracy of AH equilibrium geometries by single determinant molecular-orbital theory. *Mol. Phys.*, *27*, 209-214. https://doi.org/10.1080/00268977400100171

27 Gordon, M.S. (1980). The isomers of silacyclopropane. *Chem. Phys. Lett.*, *76*, 163-68. https://doi.org/10.1016/0009-2614(80)80628-2

28 Hutchison, G.R., Ratner, M.A. & Marks, T.J. (2004). Hopping Transport in Conductive Heterocyclic Oligomers: Reorganization Energies and Substituent Effects. *J. Am. Chem. Soc.*, *127*, 2339-2350. https://doi.org/10.1021/ja0461421

29 Oliveira, E.F. & Lavarda, F.C. (2016). Reorganization energy for hole and electron transfer of poly(3-hexylthiophene) derivatives. *Polymer*, *99*, 105-111. http://dx.doi.org/10.1016/j.polymer.2016.07.003

30 Lin, B. Ch., Cheng, Ch. P. & Lao, Zh. P. M. (2003). Reorganization Energies in the Transports of Holes and Electrons in Organic Amines in Organic Electroluminescence Studied by Density Functional Theory. *J. Phys. Chem. A*, *107*, 5241-5251. https://doi.org/10.1021/jp0304529

31 Coropceanu, V. et al. (2007). Charge Transport in Organic Semiconductors. *Chem. Rev.*, *107*, 926. https://doi.org/10.1021/cr050140x

32 Valeev, E.F. et al. (2006). Effect of Electronic Polarization on Charge-Transport Parameters in Molecular Organic Semiconductors. *J. Am. Chem. Soc.*, *128*, 30, 9882–9886. https://doi.org/10.1021/ja061827h

33 Li, X.-Y. et al. (1999). Electron transfer in poly(p-phenylene) oligomers: Effect of external electric field and application of Koopmans theorem. *Chem. Phys.*, *248*, 137–146. https://doi.org/10.1016/S0301-0104(99)00239-6

34 Marcus, R.A. et al. (1985). Electron transfers in chemistry and biology. *Biochimica et Biophysica Acta (BBA)-Reviews on Bioenergetics*, *811*(3), 265-322. https://doi.org/10.1016/0304-4173(85)90014-X

35 Marcus, R.A. (1993). Electron transfer reactions in chemistry. Theory and experiment. *Reviews of modern physics*, *65*(3), 599. https://doi.org/10.1103/RevModPhys.65.599

36 Kuo, M.Y et al. (2007). Providing a Three-in-One Advantage for the Design of n-Type Organic Field-Effect Transistors. *Chemistry–A European Journal*, *13*(17), 4750-4758. https://doi.org/10.1002/chem.200601803

37 Wang, L. et al. (2010). Computational methods for design of organic materials with high charge mobility. *Chemical Society Reviews*, *39*(2), 423-434. https://doi.org/10.1039/B816406C

38 Earnhardt, A. W. et al. (2022) Bipolar charge transport in a robust hexacoordinate organosilane. *Journal of Organometallic Chemistry*, *961*, 122208. https://doi.org/10.1016/j.jorganchem.2021.122208

39 Kocherga, M. et al. (2022). Exploring the molecular electronic device applications of synthetically versatile silicon pincer complexes as charge transport and electroluminescent layers. *Mater. Adv.*, *3*, 2373–2379. https://doi.org/10.1039/D1MA00737H

Information about authors*

Uvarova, Irina Vladimirovna — Master student of 2nd year, L.N. Gumilyov Eurasian National University, Kazhymukan str., 13, 010008, Astana, Kazakhstan; e-mail: ira.uvarova.17@bk.ru

Aldongarov, Anuar Akylkhanovich (*corresponding author*) — PhD, associate professor, head of laboratory of physical and quantum chemistry, L.N. Gumilyov Eurasian National University, Kazhymukan str., 13, 010008, Astana, Kazakhstan; e-mail: enu-2010@yandex.kz; https://orcid.org/0000-0001-7784-0524

Baitassova, Zhadyra Yryskeldievna — PhD student of 1st year, L.N. Gumilyov Eurasian National University, Kazhymukan str., 13, 010008, Astana, Kazakhstan; e-mail: baitasova_8855@mail.ru

_____

*The author's name is presented in the order: *Last Name, First and Middle Names*

Article

Kamshat Sh. Makhadiyeva, Lyazzat K. Abulyaissova*, Maral S. Kasymova

Karaganda University of the name of academician E.A. Buketov, Karaganda, Kazakhstan
(*Corresponding author's e-mail: abu.lyazzat@gmail.com)

DFT-Based Study of the Intramolecular Interactions of Some Aminoglycosides

The quantum chemical modeling and full geometry optimization of sisomicin and gentamicin were carried out by the correlation functional B3LYP using augmented with polarization functions for heavy atoms 6-311G(d) and Dunning's correlation consistent cc-pVDZ basis sets. The effect of the basis set on the calculation results of molecular structure and quantum chemical descriptors of the titled compounds was studied. Special attention was paid to the intramolecular NH…N, OH…N, OH…O, NH…O hydrogen bonds in sisomicin and gentamicin. According to theoretical calculations, the distances between hydrogen and acceptor atoms are a bit longer than a typical length due to a significant deviation of the intramolecular H-bonds from a linearity. To evaluate the extent of electron density delocalization from the lone pairs of atoms into the antibonding neighboring orbitals and inside H-bonds within the systems, NBO (Natural Bond Orbital) analysis was used at two levels of theory. The most intensive interactions between electron donor and electron acceptor in the structures under consideration are determined and their delocalization energies are evaluated. Based on the obtained data, classical electrostatic nature of the weak H-bonds and conjugation effects stabilizing the molecules are suggested.

Keywords: aminoglycoside antibiotics, sisomycin, gentamicin, DFT calculation, B3LYP, NBO analysis, hydrogen bond, delocalization energy.

Introduction

Antibiotics are the antimicrobial substances for the treatment of bacterial infections [1, 2]. They can destroy or kill only bacteria with a cellular structure. Unlike bacteria, viruses do not have the cellular structure, so antibiotics do not affect them. Therefore, the use of antibiotics in the treatment of viral infections, in particular, coronavirus infection, is ineffective [3].

One of these wonderful antibiotics that can fight tuberculosis, tularemia, plague, pneumonia, brucellosis, endocarditis, staphylococcal and nosocomial infections are aminoglycoside antibiotics, a group of drugs with homogeneous pharmacokinetic properties. The first antibiotic of this group, streptomycin, was discovered in 1944 [4] and was the result of efforts to identify antibacterial agents from the fermentation products of soil microbes [5]. After a discovery of streptomycin, many additional aminoglycosides were developed. Semi-synthetic derivatives such as amikacin were created, resulting in more than 20 representatives of this class, many of which are effective antimicrobials [6].

Aminoglycosides are structurally different and consist of two or more amino-modified sugars associated with the aminocyclite core [7]. All members of this group bind to rRNA and 30s ribomes within the protein; however, interaction and binding differ depending on the chemical structure of the drug. Members of the aminoglycoside group with a 2-deoxystreptamine (2-DOS) core, such as gentamicin, sisomicin, kanamycin, and tobramycin, are particularly effective against many gram-negative bacterial pathogens [6–8]. This class of aminoglycosides is substituted at the positions 4 (ring I) and 6 (ring III) of the 2-DOS core (ring II) by the aminomodified sugars, and these substituents are called primary and double primary rings, respectively:
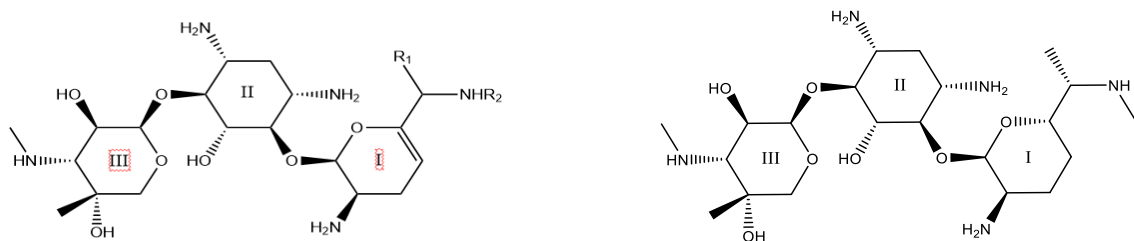
where R$_1$, R$_2$ = H for sisomicin (left) and CH$_3$ for gentamicin (right; cycle I is without a double bond).

Gentamicin is a bactericidal aminoglycoside that was discovered and isolated from *Micromonospora purpurea* in 1963. It is one of the most frequently prescribed aminoglycosides due to its spectrum of activity, low cost, and availability [9]. Sisomicin is a broad-spectrum aminoglycoside antibiotic and is structurally similar to gentamicin but has a unique unsaturated diamino sugar ring. Among aminoglycoside antibiotics, sisomicin has the highest activity against gram-positive bacteria [7, 8].

Sisomicin and gentamicin are also of interest due to a multiple hydrogen-bond (HB) network. There are the N-H…N, O-H…N, O-H…O, N-H…O intramolecular bonds. It is known that the hydrogen bonding plays an important role in many chemical and bioactive systems, and the study of structure and nature of HB is relevant. This work presents the results of a quantum chemical calculation and NBO analysis of structurally similar sisomicin and gentamicin.

Computational Details

Equilibrium molecular geometries for the ground states of the compounds studied in this work were determined in vacuum using density functional theory (DFT)-based [10] method with a split-valence 6-311G(*d*) and Dunning's cc-pVDZ basis sets [11, 12]. For the DFT calculations, the Becke three-parameter Lee–Yang–Parr (B3LYP) exchange-correlation functional [13] was employed. Sisomicin and gentamicin molecules were modeled with the GaussView 6.0.16 program, and all these calculations were performed using the Gaussian 16 computational package [14]. The local symmetry of methylene, methyl and amino groups was not taken into account because the molecules as a whole were asymmetric. All calculations converged to the optimized geometries corresponding to true minima, as revealed by the lack of imaginary values in the wavenumber calculations. NBO analysis [15] was used to explore intramolecular interactions in the optimized structures.

Results and Discussion

Molecular structure. The main thermodynamic and electrical properties of the titled compounds are listed in Table 1 that shows a comparison of the two sets of quantum chemical results. The most stable structures of sisomicin and gentamicin, atomic numbering, and the HB network are shown in Figure 1.
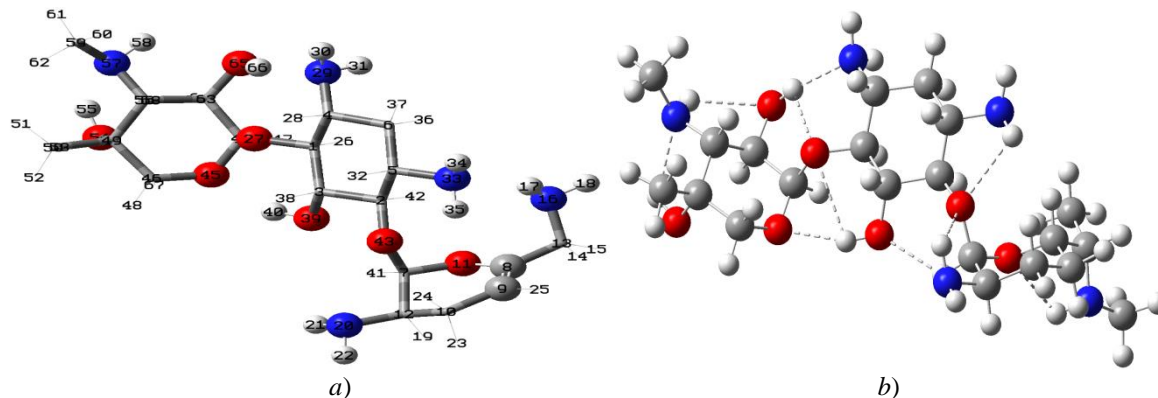

a)   *b)*

Figure 1. The optimized structures (B3LYP/6-311G(*d*)) of the ground state of: a) sisomicin, with the numbering of the atoms; b) gentamicin, witn possible intramolecular H-bonds represented by dashed lines

The presence of hydroxyl, amino and methyl groups makes ample opportunities for conformational transformations and changes in the polarity of molecules, which can affect the implementation of biological activity. In this study, we refer to the ground state structures of entitled compounds.

In general, sisomicin calculated by two basis sets has almost the same structure. Similarly in gentamicin, the cc-pVDZ geometry slightly deviates from that optimized at the B3LYP/6-311G(*d*) level of theory. However, in the case of the last basis set, the total energies of both of these molecules are markedly lower as compared to the cc-pVDZ set (the energy differences are 170.19 and 181.11 kcal/mol for sisomicin and gentamicin, respectively) (Table 1). So, we use the B3LYP/6-311G(*d*) data during the discussion of the results.

According to the gas-phase calculations of the structures under consideration, the six-membered rings I-III in gentamicin have the form of a classic undistorted "chair". For the optimized sisomicin and gentamicin molecules, the differences between their ring I geometries are considerable. In sisomicin, the ring I due to the presence of a double C=C-bond is distorted and other rings are identical to those of gentamicin (Fig. 2).
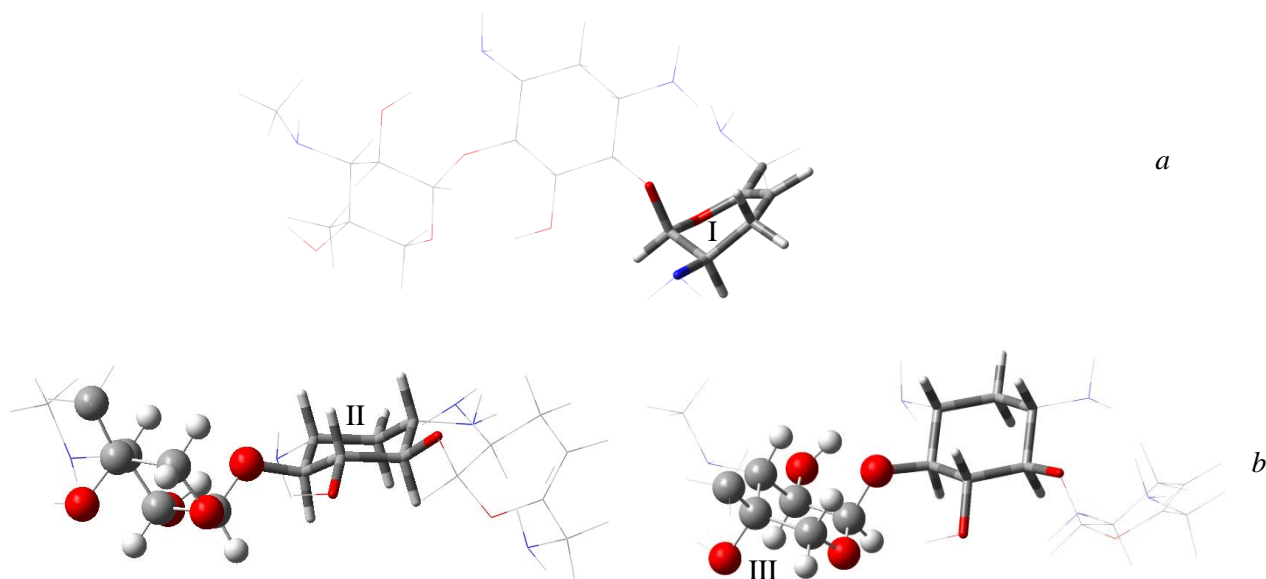
Figure 2. Optimized sisomicin molecule: a) the ring I with a partially planar conformation;
b) the rings II, III with a chair conformation

The functional OH- and NH_2-groups are oriented to each other to form intramolecular H-bonds: OH-group of the ring II is directed to the O atom of the ring III and other hydroxyl groups are oriented to the N atoms etc.

Table 1

Some quantum chemical descriptors of sisomicin and gentamicin (DFT/B3LYP method)

No.	Descriptor	Basis set 6-311G(d) / cc-pVDZ	
		Sisomicin	Gentamicin
1	SCF energy (a.u.)	-1546.92597 / -1546.65473	-1626.789512 / -1626.500865
2	Thermal energy (kJ/mol)	393.572 / 391.006	446.075 / 442.567
3	Zero-point energy (kJ/mol)	1563.92 / 1553.35	1776.03 / 1760.21
4	Heat capacity (cal/mol·K)	124.889 / 125.220	136.329 / 137.514
5	Entropy (cal/mol·K)	198.940 / 197.444	211.606 / 215.370
6	Dipole moment (D)	5.528 / 5.091	6.684 / 6.142

Also, as one can see from Table 1, there is the changing tendency of the other calculation results with a change in the computation level. The enormous molecular dipole moments of the compounds occur due to electron density delocalization, contributions of lone pairs (LP) and indicate a high reactivity of them. The addition of electron donor methyl groups increases the dipole moment of gentamicin. Based on the NBO analysis data, the electron lone pairs of atoms located in sp^n-hybrid orbitals and contributing to the total dipole moment were determined. They are presented in Table 2.

Table 2

Contribution of lone pairs of atoms to the total dipole moment

NBO (LP)	Sisomicin	Gentamicin
N16	$sp^{4.08}$	$sp^{5.45}$
N20	$sp^{3.68}$	$sp^{4.04}$
N29	$sp^{3.96}$	$sp^{3.97}$
N33	$sp^{3.73}$	$sp^{3.73}$
N57	$sp^{4.78}$	$sp^{4.79}$

Hydrogen bonding. Both sisomicin and gentamicin have hydroxyl and amino functional groups which can form the intramolecular and intermolecular hydrogen bonds. Intramolecular H-bonding geometry parameters are collected in Table 3.

Proposed hydrogen bonding geometry for sisomicin and gentamicin (DFT/B3LYP/6-311G(*d*) method)

H-bond	Bond length, Å			Bond angle, º
	Sisomicin (Gentamicin)			Sisomicin (Gentamicin)
	R(O(N)-H)	r(H…O(N))	r(O(N)…O(N))	φ(O- H…O(N))
N16-H17…N33	1.019	2.282	3.216	151.78
O65-H66...O27	0.981 (0.981)	*2.334 (2.347)*	2.780 (2.784)	*106.76 (106.19)*
O65-H66…N29	0.981 (0.981)	2.040 (2.038)	2.978 (2.975)	159.18 (159.09)
O54-H55...N57	0.972 (0.972)	*2.189 (2.204)*	2.781 (2.788)	*117.93 (117.39)*
O39-H40...O27	0.971 (0.971)	*2.487 (2.521)*	2.879 (2.872)	103.88 (101.21)
O39-H40…O45	0.971 (0.971)	2.141 (2.167)	3.055 (3.056)	156.55 (151.71)
N33-H35...O43	1.017 (1.015)	*2.352 (2.375)*	2.794 (2.777)	*105.03 (102.45)*
N57-H58...O65	1.015 (1.015)	*2.350 (2.353)*	2.886 (2.887)	*111.84 (111.68)*

As seen from the values of the H-bond parameters, the valence bonds are similar for the titled compounds. Also, in the case of two compounds, the bifurcated bonds with the same acceptor (donor) oxygen (nitrogen) atom can be formed in them (Fig. 1, Table 3). The N16-H17…N33 hydrogen bond is observed only in sisomicin. The H…N distance of the O65-H66…N29 hydrogen bond is the shortest among all similar bond lengths. This H-bond can be expected to be stronger than the others. The distances between donor and acceptor atoms are ideal for all hydrogen bonds, but the distances of 2.3-2.5Å between a hydrogen and the acceptor are a bit longer than a typical length due to a considerable deviation of the intramolecular H-bonds from a linearity. Accordingly, it can be conclude that such HBs may be weak.

To evaluate the extent of delocalization causing stabilization of the systems and to understand a nature of hydrogen bonding, NBO analysis was performed at the two theory levels. Table 4 lists the most significant delocalization energies, which show that the electron density delocalization occurs from the lone pairs into the antibonding neighboring orbitals and inside H-bonds.

Delocalization energy for the titled compounds at B3LYP/6-311G(*d*) level of theory

Delocalization	Energy, kJ/mol		Delocalization	Energy, kJ/mol	
	Sisomicin	Gentamicin		Sisomicin	Gentamicin
LP(1)O11 → σ*(C8-C9)	24.83	8.58	LP(1)N33 → σ*(N16-H17)	15.95	-
LP(2)O11 → π*(C8-C9)	119.25	-	LP(2)O39 → σ*(C1-C3)	24.24	26.75
LP(2)O11 → σ*(C8-C9)	-	16.08	LP(2)O39 → σ*(C3-H38)	28.68	24.66
LP(2)O11 → σ*(C7-O43)	49.78	57.74	LP(2)O43 → σ*(C2-C3)	27.17	28.05
LP(1)N16 → σ*(C13-H15)	34.38	7.29	LP(2)O43 → σ*(C7-O11)	51.37	47.48
LP(1)N16 → σ*(C13-C15)	-	36.97	LP(2)O45 → σ*(O27-C44)	53.76	54.93
LP(1)N20 → σ*(C12-H19)	34.46	7.96	LP(2)O45 → σ*(O39-H40)	10.97	9.30
LP(1)N20 → σ*(C10-C12)	-	35.84	LP(2)O45 → σ*(C46-H67)	28.14	28.30
LP(2)O27 → σ*(C44-O45)	50.45	49.11	LP(2)O54 → σ*(C49-C50)	34.25	34.04
LP(1)N29 → σ*(C4-C6)	29.10	28.72	LP(1)N57 → σ*(C59-H60)	29.85	29.85
LP(1)N29 → σ*(O65-H66)	45.22	45.39	LP(2)O65 → σ*(C56-C63)	30.06	29.48
LP(1)N33 → σ*(C5-H32)	30.86	33.50	-	-	-

The delocalization energy was estimated from the second-order perturbation theory [16]. As can be seen in Table 4, the LP(2)O11 → π*(C8-C9) interaction in sisomicin has an enormous delocalization energy of 119.25 kJ/mol. This is the most intensive interaction between electron donor and electron acceptor in sisomicin. In the case of gentamicin, there is no such double bond, so, the electron density transfer occurs from the lone pairs LP(1)O11 and LP(2)O11 to the neighboring σ*(C8-C9) antibond. Their delocalization energy in total is equal to the energy of the LP(1)O11 → σ*(C8-C9) interaction in sisomicin. For two considered molecules, the substantial electronic delocalization is observed for LP(2)O11 → σ*(C7-O43), LP(2)O27 → σ*(C44-O45), LP(2)O43 → σ*(C7-O11), and LP(2)O45 → σ*(O27-C44) interactions.

The stabilization energy of the same order for two molecules corresponds to the through-space electron delocalization between the lone pair of nitrogen LP(1)N29 and the hydroxyl σ*(O65-H66) anti-

bonding orbital (intramolecular H-bond). Small energies were identified for the other two interactions inside hydrogen bonds: LP(1)N33 → σ*(N16-H17) and LP(2)O45 → σ*(O39-H40). All these energy values correlate with corresponding H-bond geometries: r(H…O(N)) and φ(O-H…O(N)) (Table 3). The delocalization energies of remaining H-bonds (they are represented by italics in the Table 3) are considerably smaller (< 5 kJ/mol) than that discussed above. This may indicate the classical electrostatic nature of the weak H-bonds. It should be noted that interactions with the delocalization energy of 25-35 kJ/mol, occurring from filled lone pairs of the atoms to σ* orbitals of vicinal C-C or C-H bonds, are hyperconjugative interactions.

Conclusions

In this work, a comparative analysis of the quantum chemical calculation results for the ground states of two aminoglycoside antibiotics was performed using DFT-based B3LYP method with a split-valence 6-311G(d) and Dunning's correlation consistent cc-pVDZ basis sets. Upon computation with 6-311G(d) set, the total energies of both aminoglycosides are markedly lower as compared to the cc-pVDZ set. So, we used the B3LYP/6-311G(d) data during the discussion of other results.

To explore intramolecular interactions within the sisomicin and gentamicin molecules, NBO analysis was used. The most intensive interaction between electron donor and electron acceptor in sisomicin is the LP(2)O11 → π*(C8-C9) interaction with an enormous delocalization energy of 119.25 kJ/mol. In the case of gentamicin, the most intensive interaction is observed for LP(2)O11 → σ*(C7-O43) with an energy almost two times less than the previous one. For two molecules, the stabilization energy of the same order corresponds to the through-space electron delocalization for intramolecular LP(1)N29 → σ*(O65-H66) H-bond. The delocalization energies of the remaining H-bonds are considerably smaller than above, which may indicate the classical electrostatic nature of these bonds. Interactions with the delocalization energy of 25-35 kJ/mol occuring from filled lone pairs of the atoms to σ* orbitals of vicinal C-C or C-H bonds are hyperconjugative interactions.

References

1 Gould, K. (2016). Antibiotics: from prehistory to the present day. *Journal of Antimicrobial Chemotherapy*, *71*(3), 572–575. https://doi.org/10.1093/jac/dkv484

2 Abulyaissova, L.K., Kasymova, M.S. & Minayeva, Ye.V. (2018). Theoretical calculations of natural penicillins: structural and electronic properties. *Bulletin of the University of Karaganda Chemistry, 4*(92), 28–34. https://doi.org/10.31489/2018ch4/28-34

3 Pauter, K., Szultka-Młyńska, M. & Buszewski, B. (2020). Determination and Identification of Antibiotic Drugs and Bacterial Strains in Biological Samples. *Molecules, 25*(11), 2556. https://doi.org/10.3390/molecules25112556

4 Comroe, JH. Jr. (1978). Pay dirt: the story of streptomycin. Part I: from Waksman to Waksman. *American Review of Respiratory Disease*, *117*(4), 773–781. https://doi.org/10.1164/arrd.1978.117.4.773

5 Waksman, S.A. (1944). Antibiotic substances, production by microorganisms—nature and mode of action. *Am J Public Health Nations Health*, *34*(4)*, 358–364. https://doi.org/10.2105/ajph.34.4.358

6 Becker, B. & Cooper, M.A. (2013). Aminoglycoside antibiotics in the 21st century, *ACS Chem. Biol.*, *8*, 105–115. https://dx.doi.org/10.1021/cb3005116

7 Magnet, S. & Blanchard, J.S. (2005). Molecular insights into aminoglycoside action and resistance. *Chem Rev, 105,* 477–498. https://doi.org/10.1021/cr0301088

8 Chittapragada, M., Roberts, S. & Ham, Y.W. (2009). Aminoglycosides: molecular insights on the recognition of RNA and aminoglycoside mimics. *Perspect. Med. Chem.*, *3*, 21–37. https://doi.org/10.4137/pmc.s2381

9 Rivera, J.A., Larsson, J., Volkov, I.L., Seefeldt, A.C., Sanyal, S. & Johansson, M. (2021). Real-time measurements of aminoglycoside effects on protein synthesis in live cells. *Proc Natl Acad Sci USA. 118*(9)*, e2013315118. https://doi.org/10.1073/pnas.2013315118

10 Parr, R.G. & Yang, W. (1989). Density-functional theory of atoms and molecules. Oxford: Press.

11 McLean, A.D. & Chandler, G.S. (1980). Contracted Gaussian-basis sets for molecular calculations. 1. 2nd row atoms, Z=11-18. *J. Chem. Phys., 72*, 5639-48. https://doi.org/10.1063/1.438980

12 Dunning, Jr. T.H. (1989). Gaussian basis sets for use in correlated molecular calculations. I. The atoms boron through neon and hydrogen. *J. Chem. Phys., 90,* 1007-1023. https://doi.org/10.1063/1.456153

13 Becke, A.D. (1993). Density-functional thermochemistry. III. The role of exact exchange. *J. Chem. Phys., 98,* 5648-5652. https://doi.org/10.1063/1.464913

14 Frisch, M.J., Trucks, G.W., Schlegel, H.B. et al. (2016). *Gaussian 16, Revision A.03, Wallingford: CT.*

15 Reed, A.E., Curtiss, L.A. & Weinhold, F. (1988). Intermolecular interactions from a natural bond orbital, donor-acceptor viewpoint. *Chem. Rev., 88,* 899–926. https://doi.org/10.1021/cr00088a005

16 Foster, J.P. & Weinhold, F. (1980). Natural hybrid orbitals. *J. Am. Chem. Soc., 102*(24), 7211–7218. https://doi.org/10.1021/ja00544a007

Information about authors*

Makhadiyeva, Kamshat Shyngyskyzy — Master of Chemistry, Karaganda University of the name of academician E.A. Buketov, Universitetskaya street, 28, 100024, Karaganda, Kazakhstan; e-mail: kamshat_mahadieva@mail.ru

Abulyaissova Lyazzat Kabylashevna (*corresponding author*) — Candidate of Chemical Sciences, Professor, Karaganda University of the name of academician E.A. Buketov, Universitetskaya street, 28, 100024, Karaganda, Kazakhstan; e-mail: abu.lyazzat@gmail.com; https://orcid.org/0000-0002-7530-3378

Kasymova, Maral Sairanovna — Candidate of Chemical Sciences, Associate Professor, Karaganda University of the name of academician E.A. Buketov, Universitetskaya street, 28, 100024, Karaganda, Kazakhstan; e-mail: maral.kasymova.77@mail.ru; https://orcid.org/0000-0003-4084-7989

_____
*The author's name is presented in the order: *Last Name, First and Middle Names*

Alfiya F. Kurmanova[1*] (ID), Farida Zh. Abilkanova[2] (ID),
Irina A. Pustolaikina[1] (ID), Sergey N. Nikolskiy[1, 3] (ID)

[1]Karaganda University of the name of academician E.A. Buketov, Karaganda, Kazakhstan;
[2]Karaganda Industrial University, Temirtau, Kazakhstan;
[3]Altay State University, Barnaul, Russia
(*Corresponding author's e-mail: alfiya_kurmanova@mail.ru)

DFT Study of Intermolecular Proton Exchange with Some Derivatives of Benzoic Acids

A theoretical study of proton transfer dynamics in complexes of some substituted benzoic acids with 3,6-di-tert-butyl-2-hydroxyphenoxyl (DTBPO) radical is presented. To elucidate the transfer mechanism, reaction pathways for various complexes of benzoic acid derivatives with DTBPO were modeled. The calculations were performed by the DFT method at the UB3LYP/6-31G+(d, p) level of theory using QST3, IRC procedures, in vacuum and toluene medium (PCM solvation model). Geometric and kinetic parameters of complexes with o-, p-, and m-isomers of nitrobenzoic and chlorobenzoic acids were calculated. Theoretically estimated activation barrier of 29-30 kJ/mol turned out to be approximately 30 % higher than the previously obtained experimental data. It was noted that in the case of o-isomers of aromatic acids the coplanarity of the transition state structure is violated, in contrast to the initial state. This leads to a change in the proton transfer mechanism. The dynamics of charge distribution, dipole moment and electrostatic potential in the studied complexes were analyzed. Based on the calculated data, it was shown that the studied intermolecular proton exchange process occurs throughout Hydrogen Atom Transfer (HAT), and not throughout Proton-Coupled Electron Transfer (PCET) mechanism.

Keywords: DFT, spin probe, nitrobenzoic acid, chlorobenzoic acid, 3,6-di-tert.butyl-2-hydroxyphenoxyl, radical, OH-acids, proton exchange, proton transfer, Hydrogen Atom Transfer (HAT).

Introduction

Reactions with proton transfer are widespread in living and non-living nature [1–5]. They arouse the unrelenting interest of researchers in relation to both proton transfer and proton exchange reactions [6–9]. The rate of such processes can have a wide range and can be studied by different methods, such as NMR spectroscopy for the diamagnetic and EPR spectroscopy for the paramagnetic systems [10–12]. The main advantage of these methods is the direct control over the reaction; however, they are also limited by the time interval available for research. This range includes $10–10^5$ c^{-1} for NMR, while for EPR it is within $10^6–10^9$ c^{-1}. However, even such a high time resolution does not allow one to fix the transition states formed during both intra- and intermolecular processes, since the lifetime of such states far exceeds the capabilities of these methods. The presence of a huge amount of experimental material on proton exchange in radical systems necessitates the application of computational chemistry methods to interpret these results [13–15]. Previously, we have obtained EPR experimental data on the kinetics of proton exchange between 3,6-di-tert-butyl-2-oxyphenoxyl (DTBPO) radical as a spin probe and a number of aromatic acids [16–18], which require theoretical interpretation. Kinetic parameters of intermolecular proton exchange for the systems m-nitrobenzoic acid — 3,6-di-tert-butyl-2-hydroxyphenoxyl and o-chlorobenzoic acid — DTBPO by dynamic EPR spectroscopy was obtained in toluene medium for which the proton exchange rate constant — 10^8 and 10^9 l/mol.s and activation parameters 22.7 and 23.9 kJ/mol, respectively [19]. Therefore, the aim of this work was to theoretically substantiate the previously obtained EPR data using a computational DFT study of proton exchange in systems containing the DTBPO radical and derivatives of nitrobenzoic and chlorobenzoic acids. The present work will provide more detailed information about the processes occurring in similar systems at different medium.

Computational Details

In this study density functional theory (DFT) computations with the UB3LYP [20, 21] functional and the 6-31G+(d, p) basis set, taking into account the dispersion with the original damping function D3 with the generation of electrostatic potentials, were used to optimize the structures of the initial, final as well as transition states of the complexes. The B3LYP functional is one of the most reliable methods to study the thermodynamics and kinetics of radical reactions [22, 23], this method is often used to assess the proton transfer radical reactions [24, 25]. The QST3 procedures were used to find the transition state, and the authenticity of the transition state was assessed by the presence of an imaginary frequency of normal vibrations along the reaction coordinate and its magnitude. The PES profile, the dynamics of charge distribution and dipole moment during the process under study were calculated using the Intrinsic Reaction Coordinate (IRC) procedure with optimization of all geometric parameters [26]. The effect of the solvent (toluene) was taken into account using the Polarizable Continuum Model (PCM) [27]. All calculations were carried out using the Gaussian 16 software [28], visualization of the obtained data was performed using the GaussView 6.0.16 graphical interface [29].

Results and Discussion

In general, the proton exchange reaction between the DTBPO radical and the studied benzoic acids can be represented by the following scheme:
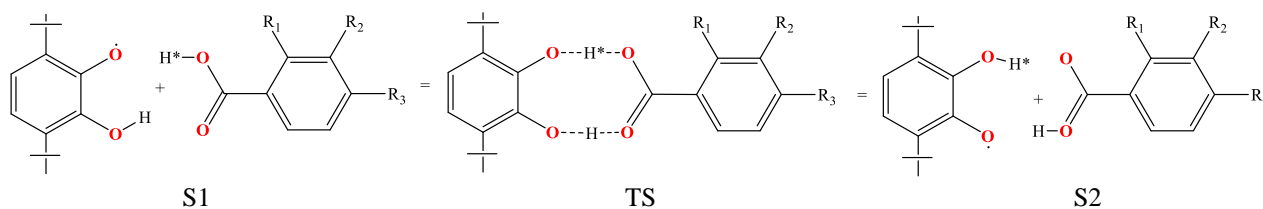
Scheme 1

where

R1 = R2 = R3 =H for unsubstituted benzoic acid;
R1 = NO$_2$ (or Cl), R2 = R3 =H for ortho-substituted benzoic acid;
R2 = NO$_2$ (or Cl), R1 = R3 = H for meta-substituted benzoic acid;
R3 = NO$_2$ (or Cl), R1 = R2 = H for para-substituted benzoic acid.

As can be seen from Scheme 1, proton exchange is facilitated by the formation of a cyclic complex between the DTBPO radical and the acid as the initial state S1 of the system (Fig. 1, *a*). The transition state TS of the system is characterized by approximately equal distance of both hydrogen atoms from the interacting molecules (Fig. 1, *b*). In the final state S2, the exchange of hydrogen atoms between the DTBPO radical and the acid is fixed (Fig. 1, *c*).

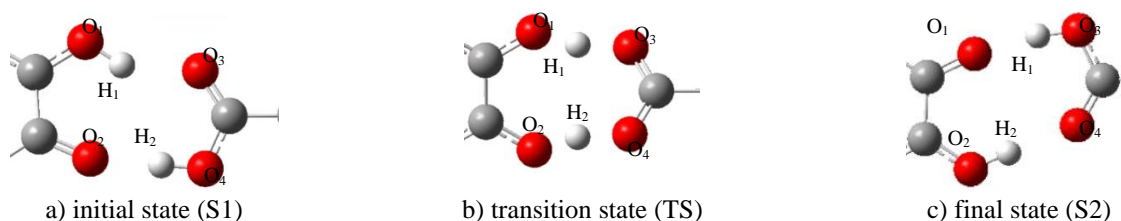a) initial state (S1)   b) transition state (TS)   c) final state (S2)

Figure 1. Cyclic fragments of the complex between DTBPO radical and benzoic acid

Firstly, by employing UB3LYP/6-31G+(d, p) method, we have obtained optimized geometry structures for studied radical and acids: 3,6-di-tert-butyl-2-hydroxyphenoxyl (DTBPO) radical, o-nitrobenzoic (o-NBA), m-nitrobenzoic (m-NBA), p-nitrobenzoic (p-NBA), o-chlorobenzoic (o-ClBA), m-chlorobenzoic (m-ClBA) and p-chlorobenzoic (p-ClBA) (Fig. 2).

DTBPO radical

o-NBA   m-NBA   p-NBA

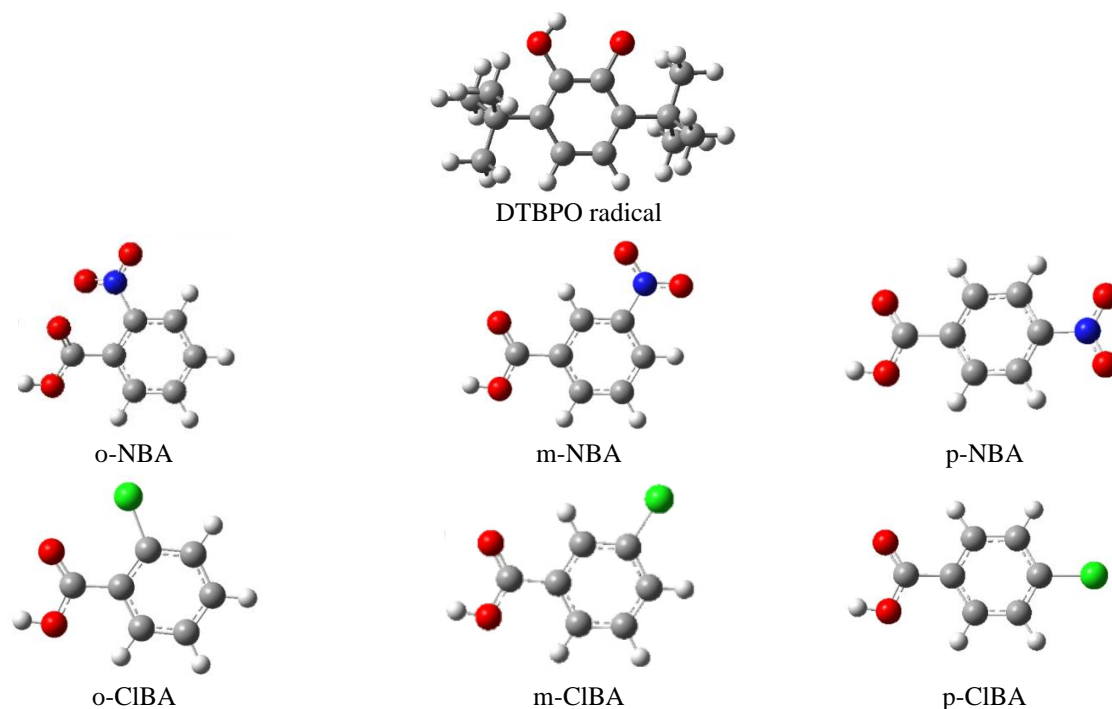o-ClBA   m-ClBA   p-ClBA

Figure 2. Optimized structures of studied molecules

The spin probe 3,6-di-tert-butyl-2-hydroxyphenoxyl (DTBPO) radical was used as a partner in the proton exchange reaction. For this DTBPO radical, the kinetic data of intermolecular processes of proton transfer and exchange with various bases and acids in non-aqueous media were previously obtained by us using dynamic EPR spectroscopy [16–19].

The next step was to optimize the geometry of the initial S1, final S2, and transition TS states of the studied complexes between the DTBPO radical and benzoic acids (Fig. 3).
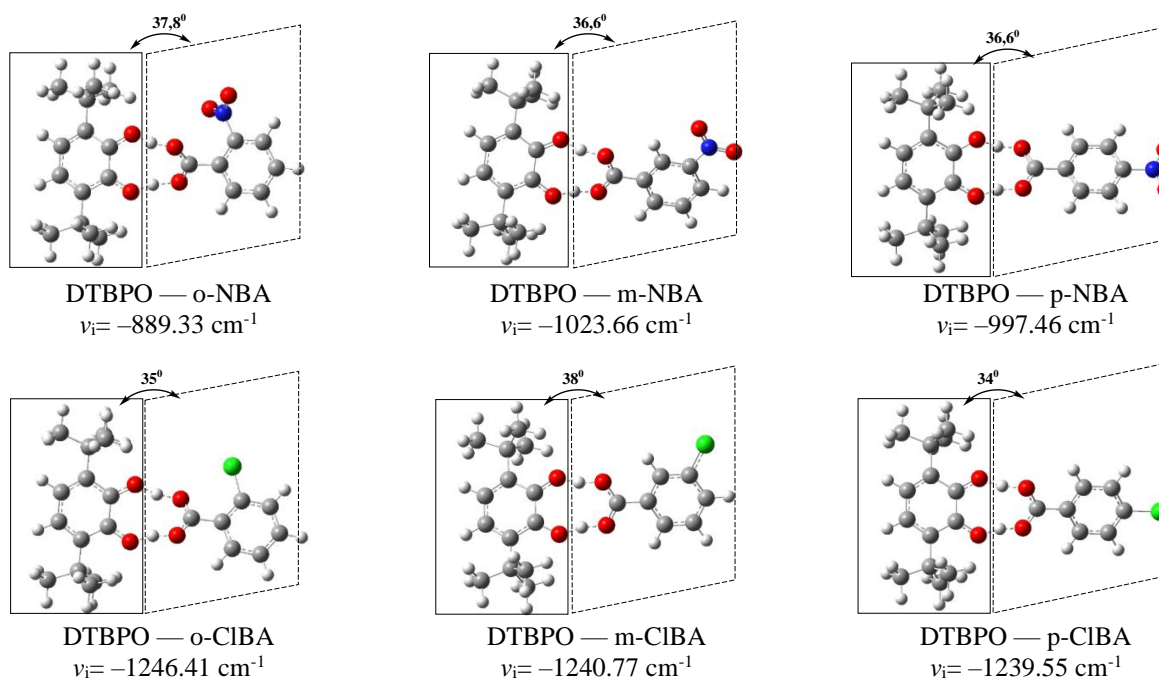

DTBPO — o-NBA
v_i = –889.33 cm^{-1}

DTBPO — m-NBA
v_i = –1023.66 cm^{-1}

DTBPO — p-NBA
v_i = –997.46 cm^{-1}

DTBPO — o-ClBA
v_i = –1246.41 cm^{-1}

DTBPO — m-ClBA
v_i = –1240.77 cm^{-1}

DTBPO — p-ClBA
v_i = –1239.55 cm^{-1}

Figure 3. TS structures of the DTBPO radical — benzoic acids proton exchange pathway.
v_i — imaginary vibrational frequency

It should be noted that the planarity of the cyclic fragment is violated during the formation of the transition state. For example, if in the initial and final states the dihedral angle between the radical and acid parts of the complex is 0°, then in the transition state it is already equal to 37.8° in the case of the ortho-substituted acid isomer and 36.6° in the case of meta- and para -substituted isomers. It should be clarified that if in the case of an ortho-substituted acid the change is accompanied only by a distortion of the plane of the cyclic fragment, while for meta and para-substituted acids, the phenolic ring of nitrobenzoic acid also rotates. At the same time, the aromatic rings of the o-isomer of the acid and of the radical turned around by 9° relative to each other.

Similar change in the dihedral angle between the planes of the benzene rings of the radical and of the acid is observed in complexes with isomers of chlorobenzoic acids: the rotation angle is 35° in the case of o-ClBA, 38° in the case of m-ClBA, and 34° in the case of p-ClBA.

The obtained imaginary vibrational frequency of the transition state corresponding to the proton transfer are: -889.33 cm^{-1} for the o-NBA, -1023.66 cm^{-1} for the m-NBA, -997.46 cm^{-1} for the p-NBA and -1246.41 cm^{-1} for the o-ClBA, -1240.77 cm^{-1} for the m-ClBA, and -1239.55 cm^{-1} for the p-ClBA.

Some interesting for us geometrical parameters of the optimized structures of the studied complexes of the DTBPO radical with benzoic acids are presented in Tables 1-2 (the numbering of the atoms corresponds to Fig. 1).

T a b l e 1

Bond lengths in the cyclic fragment of DTBPO — NBA complexes

	$R(O_1H_1)$, Å	$R(H_1O_3)$, Å	$R(O_2H_2)$, Å	$R(H_2O_4)$, Å	$R(O_1O_3)$, Å	$R(O_2O_4)$, Å
o-NBA						
S1	0.9916	1.78919	1.60677	0.99902	2.70052	2.60535
TS	1.13052	1.28989	1.13287	1.28364	2.40569	2.39966
S2	1.60164	1.00074	0.9924	1.76537	2.60223	2.68356
m-NBA						
S1	0.99262	1.77182	1.60938	0.99843	2.68551	2.60773
TS	1.14308	1.27078	1.14178	1.2718	2.39692	2.39703
S2	1.60301	0.99958	0.99277	1.76721	2.60259	2.68243
p-NBA						
S1	0.99241	1.77262	1.60743	0.99887	2.686	2.60626
TS	1.13999	1.27477	1.14001	1.27472	2.3978	2.39778
S2	1.60724	0.99885	0.99225	1.77409	2.60605	2.68807

T a b l e 2

Bond lengths in the cyclic fragment of DTBPO — ClBA complexes

	$R(O_1H_1)$, Å	$R(H_1O_3)$, Å	$R(O_2H_2)$, Å	$R(H_2O_4)$, Å	$R(O_1O_3)$, Å	$R(O_2O_4)$, Å
o-ClBA						
S1	0.99491	1.73996	1.62713	0.9959	2.65933	2.62301
TS	1.19869	1.20249	1.19624	1.20579	2.38601	2.38647
S2	1.62474	0.99685	0.9952	1.74141	2.62158	2.66096
m-ClBA						
S1	0.99469	1.74959	1.61759	0.99683	2.66757	2.61442
TS	1.18599	1.216	1.18619	1.2162	2.38613	2.38619
S2	1.62098	0.99671	0.9947	1.749	2.61766	2.66685
p-ClBA						
S1	0.99506	1.74442	1.62433	0.99626	2.66334	2.62057
TS	1.20062	1.20038	1.20082	1.20041	2.38508	2.3854
S2	1.62367	0.99634	0.99509	1.74385	2.62	2.66291

Based on the data presented in Tables 1-2, an analysis of interatomic distances in complexes was made. It was shown that in the complexes of DTBPO radical with substituted NBA, the length of the hydrogen bridge in the initial molecules varies in a small range from 2.6 Å to 2.7 Å, while at the same time in the transition state $R(O_1O_2)$ is 2.4 Å. It was noted in the case of complexes between DTBPO radical and substituted

ClBA, that the length of the hydrogen bridge in the initial molecules varies in a small range from 2.62 Å to 2.66 Å, while in the transition state $R(O_1O_2)$ is 2.38 Å.

The next step was to estimate the activation energy of the studied proton exchange process. Figures 4-5 show the calculated energies of minima and transition states for the studied complexes. The activation energy ΔE of the two-proton transfer between the structures of stable complexes S1 and S2 and the transition state TS are given in Table 3.
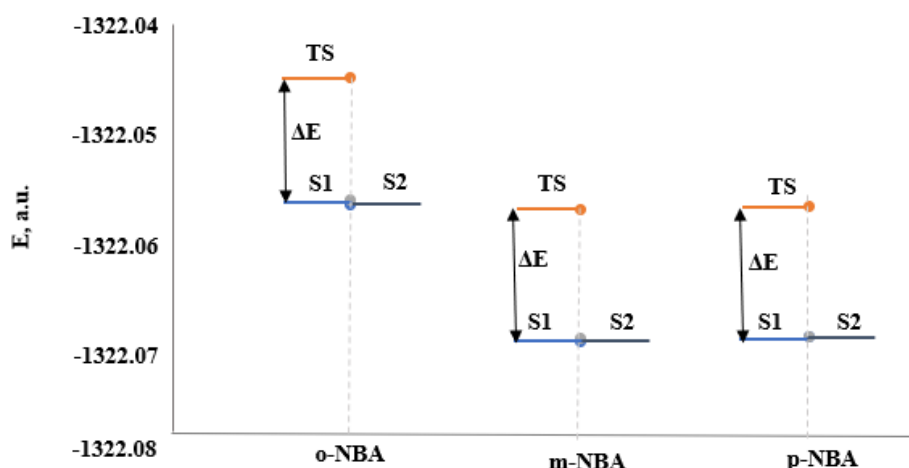

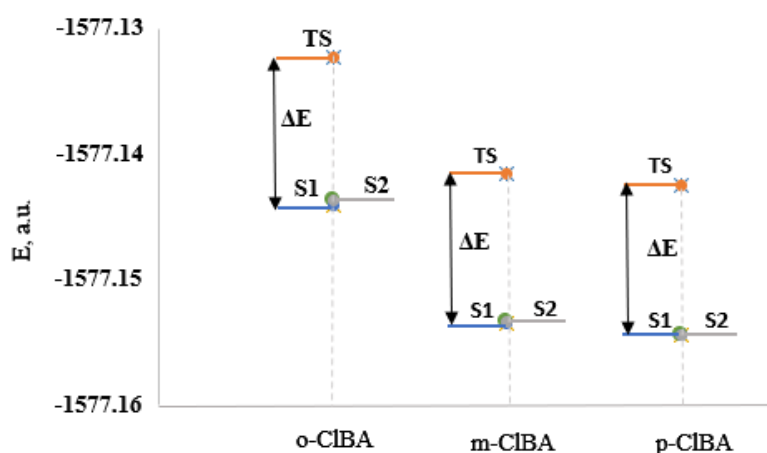Figure 4. Energy minima and transition states for DTBPO — NBA complexes

Figure 5. Energy minima and transition states for DTBPO — ClBA complexes

T a b l e 3

Activation energy ΔE of the proton exchange process in intermolecular complexes of DTBPO radical and substituted benzoic acids

Acid	ΔE, kJ/mol		
	NBA (vacuum)	NBA (toluene)	ClBA (vacuum)
o-acid	29.55	30.20	30.33
m-acid	30.71	29.66	31.16
p-acid	30.79	29.65	30.99

As can be seen from Table 3, the activation kinetic characteristics increase in the series of complexes: o-NBA < m-NBA < p-NBA, while in complexes with ClBA the maximum value corresponds to the complex with m-ClBA. It can be seen from the calculated data that complexes with o-isomers of the studied acids are more stable. In the case of the o-isomers of the studied acids, we have a minimum activation barrier approx-

imately equal to 29 kJ/mol, while in the case of the m-isomer ClBA, it is more than 30 kJ/mol. Previously obtained EPR spectroscopic data on proton exchange in toluene between DTBPO radical and m-NBA or o-ClBA acids have the following values of activation energy: ~ 22.7 kJ/mol and ~ 23.9 kJ/mol, respectively [29]. A comparison of the calculated and experimental values of the activation energy shows an almost 30 % excess of the first. We assumed that this may be due to the lack of the solvent effect and performed PCM calculations in the toluene medium for the DTBPO radical — o-NBA acid system (Table 3). However, calculations with a solvent did not lead to a significant decrease in the barrier. A decrease in the activation barrier by 1 kJ/mol was obtained in the case of the m- and p-isomers, while an increase by 0.5 kJ/mol was noted in the case of the o-isomer. Therefore, the reason is not only the solvent effect, but also a possible other mechanism of proton exchange, different from our model.

In order to better understand our proton exchange model, the next step was to study the change in charge distribution, dipole moment, electrostatic potential, and spin density in the DTBPO radical — o-NBA system during a reaction. Figure 6 shows the change in the charge distribution on the O and H interacting atoms of the DTBPO radical — o-NBA complex during the reaction.
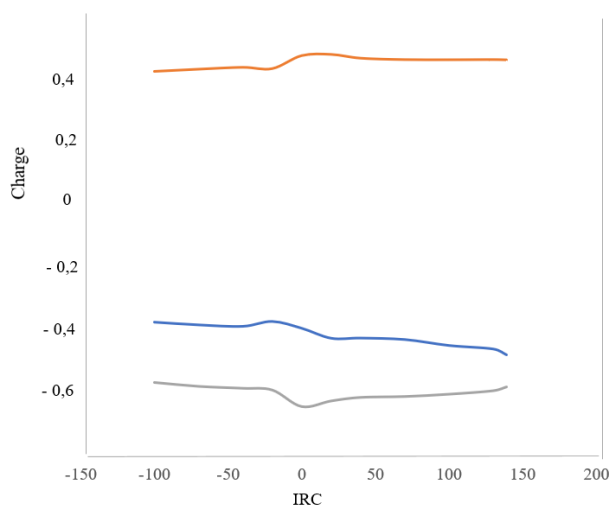

Figure 6. Charge distribution dynamics in the DTBPO radical — o-NBA complex. The blue line is the radical oxygen atom, the gray line is the acid oxygen atom, the red line is the acid hydrogen atom
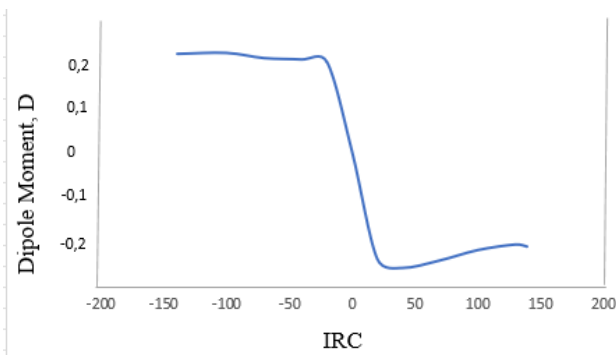
Figure 7. Dipole moment dynamics in the DTBPO radical — o-NBA complex

As can be seen in Figure 6, there is no charge transfer during the reaction. Thus, the charge on the H_2 acid hydrogen atom varies in the range from $+0.42$ to $+0.46e$, whereas the charge on the O_1 radical oxygen atom varies in the range from -0.38 to $-0.48e$, and the charge on the O_3 acid oxygen atom varies in the range from -0.57 to $-0.65e$. Comparison of the charge distribution dynamics in the system DTBPO radical — nitrobenzoic acids isomers with the phenoxy radical — phenol and 2,4,6-tri-tert-butylphenoxy radical — 2,4,6-tri-tert-butylphenol systems shows that the values of the studied system take intermediate position between the values of the unsubstituted phenoxy radical — phenol system and the benzyl radical — toluene system [30–31].

A similar analysis of the charge distribution dynamics for the complex of the semiquinone radical with chlorobenzoic acid showed, that the charge on the H_2 acid hydrogen atom varies in the range from $+0.25$ to $+0.53e$, while the charge on the O_1 radical oxygen atom varies from -0.28 to $-0.59e$, and the charge on the O_3 acid oxygen atom varies in the range from -0.32 to $-0.59e$. Such small changes in the charge distribution indicate that a hydrogen atom is transferred, but not a proton. It should be noted that earlier studies of the radical itself intramolecular tautomerism also showed the transfer of a hydrogen atom [32].

Based on the foregoing, we can assume that our computational model simulates the HAT mechanism for the process under study. Although it is possible that the proton exchange is simultaneously several competing mechanisms, including both the PCET mechanism and proton tunneling. This assumption will be tested in our future studies.

Next step was to analyze the dipole moment dynamics during proton exchange reaction in the DTBPO radical — o-NBA system (Fig. 7). As can be seen from the graph in Figure 7, the change in dipole moment

was only 0.2 Debye. It can serve as another proof for the hydrogen atom transfer, since change in several units of the dipole moment is observed during the proton transfer [30]. A similar dependence is typical for other complexes.

The dynamics of the electrostatic potential was also studied during the proton exchange reaction in the DTBPO radical — o-NBA system (Fig. 8).

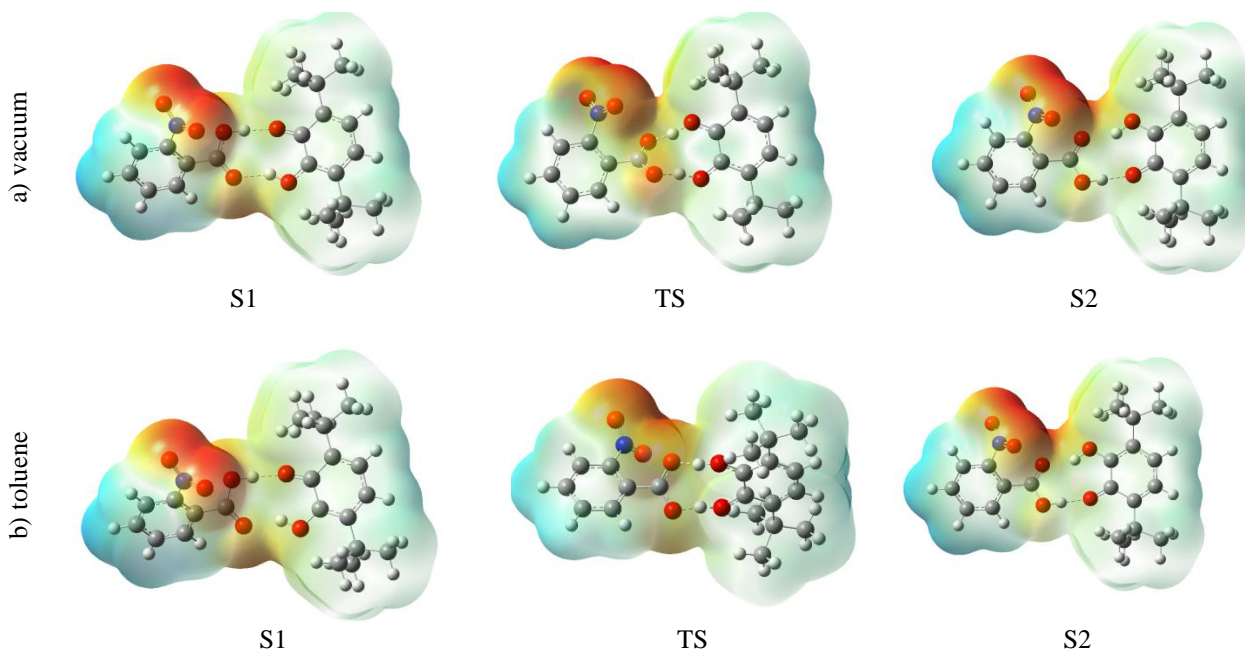a) vacuum

S1 TS S2

b) toluene

S1 TS S2

Figure 8. Electrostatic potential maps for the DTBPO radical — o-NBA complex.
Negatively and positively charged regions are marked in red and blue, respectively

As can be seen from the data presented in Figure 8, the excess electronic charge of the DTBPO radical — o-NBA system is localized mainly on the acid molecule. In the transition state (TS), an insignificant redistribution of the electrostatic potential is observed. This observation is consistent with the dynamics of dipole moment and charge distribution presented in Figures 6 and 7. Moreover, such changes are typical not only for the gas phase (vacuum), but also for the toluene medium, the geometry of the transition complex is also distorted in this case. The observed changes in electrostatic potentials emphasize the HAT mechanism in the DTBPO radical — o-NBA system and contrast it with the PCET mechanism in the phenoxyl — phenol complex [30–32].

At the final stage of the study, we analyzed the spin density dynamics during the proton exchange reaction in the DTBPO radical — o-NBA system (Fig. 9).
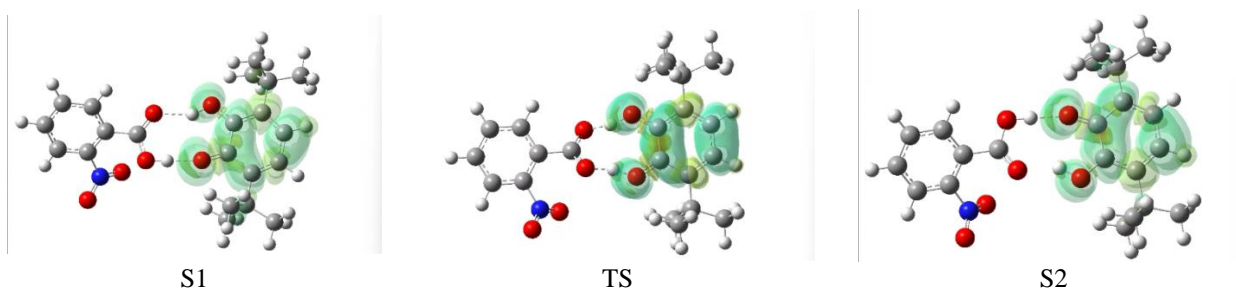

S1 TS S2

Figure 9. Spin density dynamics in the DTBPO radical — o-NBA system

As can be seen in Figure 9, the spin density is localized on the π-system of the radical benzene ring and does not pass over the acid molecule even in the transition state. It should be noted that in the transition state the spin density also extends on the both hydrogen atoms participating in the exchange process. These changes correspond to the dynamics observed in the experimental EPR spectra of the intermolecular proton exchange with DTBPO radical.

Conclusions

In this work, DFT modeling of proton exchange in DTBPO radical — substituted benzoic acids systems was performed for the purpose of its theoretical consideration. To study the mechanism of the proton exchange, the TS, QST3, IRC procedures, as well as the PCM model of the solvent effect (toluene) were used. Activation energy in the range of 29–30 kJ/mol for the proton exchange in DTBPO radical — substituted benzoic acids systems was estimated. The calculated activation energy is almost 30 % higher than the experimental value determined by EPR spectroscopy. This may be due to the limitations of the applied calculation model. An analysis of the dynamics of charge distribution, dipole moment, electrostatic potential, and spin density for the DTBPO radical — o-NBA system was performed. On the basis of the data obtained, a conclusion was made to confirm the Hydrogen Atom Transfer (HAT) model for the studied exchange reaction mechanism. Finally, these computational results and mechanism insights prove that DFT modeling is an effective method to study proton transfer process dynamics of similar systems.

References

1   Tyburski, R., Liu, T., Glover, S. D. & Hammarström, L. (2021). Proton-Coupled Electron Transfer Guidelines, Fair and Square. *Journal of the American Chemical Society*, *143*(2), 560–576. https://doi.org/10.1021/jacs.0c09106

2   Warburton, R. E., Soudackov, A. V. & Hammes-Schiffer, S. (2022). Theoretical Modeling of Electrochemical Proton-Coupled Electron Transfer. *Chemical Reviews*, *122*(12), 10599–10650. https://doi.org/10.1021/acs.chemrev.1c00929

3   Agarwal, R. G., Coste, S. C., Groff, B. D., Heuer, A. M., Noh, H., Parada, G. A., Wise, C. F., Nichols, E. M., Warren, J. J. & Mayer, J. M. (2021). Free Energies of Proton-Coupled Electron Transfer Reagents and Their Applications. *Chemical Reviews*, *122*(1), 1–49. https://doi.org/10.1021/acs.chemrev.1c00521

4   Pustolaikina, I. A., Kurmanova A. F. & Embergenova, A. K. (2011). Evaluation of protolytic ability for the series of OH-acids by the semiempirical methods of quantum chemistry. *Bulletin of the University of Karaganda Chemistry*, *61*(1), 4-9.

5   Murray, P. R. D., Cox, J. H., Chiappini, N. D., Roos, C. B., McLoughlin, E. A., Hejna, B. G., Nguyen, S. T., Ripberger, H. H., Ganley, J. M., Tsui, E., Shin, N. Y., Koronkiewicz, B., Qiu, G. & Knowles, R. R. (2021). Photochemical and Electrochemical Applications of Proton-Coupled Electron Transfer in Organic Synthesis. *Chemical Reviews*, *122*(2), 2017–2291. https://doi.org/10.1021/acs.chemrev.1c00374

6   Darcy, J. W., Koronkiewicz, B., Parada, G. A. & Mayer, J. M. (2018). A Continuum of Proton-Coupled Electron Transfer Reactivity. *Accounts of Chemical Research*, *51*(10), 2391–2399. https://doi.org/10.1021/acs.accounts.8b00319

7   Kutzhanova, K. Zh., Kurmanova, A. F., Pustolaikina, I. A. & Ismagulov, B. M. (2018). Nonempirical modeling of protolytic processes in dimeric molecules of amino acids. *Bulletin of the University of Karaganda Chemistry*, *90*(2), 58–63. https://doi.org/10.31489/2018ch2/58-63

8   Mayer, J. M. (2011). Simple Marcus-Theory-Type Model for Hydrogen-Atom Transfer/Proton-Coupled Electron Transfer. *The Journal of Physical Chemistry Letters*, *2*(12), 1481–1489. https://doi.org/10.1021/jz200021y

9   Martinez, K., Koehne, S. M., Benson, K., Paul, J. J. & Schmehl, R. H. (2023). Bimolecular Excited-State Proton-Coupled Electron Transfer within Encounter Complexes. *Journal of the American Chemical Society*, *145*(8), 4462–4472. https://doi.org/10.1021/jacs.2c10165

10 Capaldo, L. & Ravelli, D. (2017). Hydrogen Atom Transfer (HAT): A Versatile Strategy for Substrate Activation in Photocatalyzed Organic Synthesis. *European Journal of Organic Chemistry*, *2017*(15), 2056–2071. Portico. https://doi.org/10.1002/ejoc.201601485

11 Limbach, H.-H., Baumgärtner, S., Franke, R., Männle, F., Scherer, G. & Denisov, G. S. (2021). Double Proton Tautomerism via Intra- or Intermolecular Pathways? The Case of Tetramethyl Reductic Acid Studied by Dynamic NMR: Hydrogen Bond Association, Solvent and Kinetic H/D Isotope Effects. *Molecules*, *26*(14), 4373. https://doi.org/10.3390/molecules26144373

12 Yu, Q. & Hammes-Schiffer, S. (2022). Multidimensional Quantum Dynamical Simulation of Infrared Spectra under Polaritonic Vibrational Strong Coupling. *The Journal of Physical Chemistry Letters*, *13*(48), 11253–11261. https://doi.org/10.1021/acs.jpclett.2c03245

13 Martinez, K., Koehne, S. M., Benson, K., Paul, J. J. & Schmehl, R. H. (2023). Bimolecular Excited-State Proton-Coupled Electron Transfer within Encounter Complexes. *Journal of the American Chemical Society*, *145*(8), 4462–4472. https://doi.org/10.1021/jacs.2c10165

14 Limbach, H.-H., Klein, O., Lopez Del Amo, J. M. & Elguero, J. (2004). Kinetic Hydrogen/Deuterium Isotope Effects in Multiple Proton Transfer Reactions. *Zeitschrift Für Physikalische Chemie*, *218*(1), 17–50. https://doi.org/10.1524/zpch.218.1.17.25386

15 Sirjoosingh, A. & Hammes-Schiffer, S. (2011). Proton-Coupled Electron Transfer versus Hydrogen Atom Transfer: Generation of Charge-Localized Diabatic States. *The Journal of Physical Chemistry A*, *115*(11), 2367–2377. https://doi.org/10.1021/jp111210c

16 Nikolskiy, S.N., Abilkanova, F.Z., Golovenko, A.S., Pustolaikina, I.A. & Masalimov, A.S. (2020). Investigation of intermolecular proton exchange of 3,6-di-tert-butyl-2-oxyphenoxyl with N-phenylanthranilic acid by ESR spectroscopy method. *Bulletin of the University of Karaganda Chemistry, 98*(2), 35-41. https://doi.org/10.31489/2020Ch2/35-41

17 Masalimov, A.S., Tur, A.A. & Nikolskiy, S.N. (2016). Protolytic Reactions of 3,6-Di-tert-Butyl-2-Hydroxyphenoxyl with Nitrogen Bases. *Theoretical and Experimental Chemistry, 52(1),* 57-65. https://doi.org/10.1007/s11237-016-9451-0

18 Stadnik, I. L., Abilkanova, F. Zh., Kudryavtseva, Ye. V., Nikolskiy, S. N. & Masalimov, A. S. (2022). ESR-Study of the Proton Exchange with Aliphatic Amino Acids in Toluene. *Bulletin of the University of Karaganda Chemistry,* (106), 69-76. https://doi.org/10.31489/2022ch2/2-22-15

19 Masalimov, A.S., Bocharova A.V., Kurmanova A.F., Khasanova E.R. & Nikolskiy, S. N. (2009). ESR spectroscopy of the protolytic ability of carboxylic acids. *Bulletin of the University of Karaganda Chemistry, 55*(3), 4-10.

20 Devlin, F. J., Stephens, P. J., Cheeseman, J. R. & Frisch, M. J. (1997). Ab Initio Prediction of Vibrational Absorption and Circular Dichroism Spectra of Chiral Natural Products Using Density Functional Theory: Camphor and Fenchone. *The Journal of Physical Chemistry A*, *101*(35), 6322–6333. https://doi.org/10.1021/jp9712359

21 Becke, A. D. (1993). Density-functional thermochemistry. III. The role of exact exchange. *The Journal of Chemical Physics*, *98*(7), 5648–5652. https://doi.org/10.1063/1.464913

22 Nguyen, T.-N., Tuan, V. A., Bac, P. T. V., Anh, L. P. & Nguyen, H. M. T. (2022). Theoretical study on the reactions of C_2H_5 with $C_nH_{2n+1}OH$ (n = 1–4): Predicted rate constants and branching ratios. PREPRINT (Version 1) available at Research Square https://doi.org/10.21203/rs.3.rs-1224120/v1

23 Kuzhanthaivelan, S., Sunitha, S. & Rajakumar, B. (2023). Computational investigation of thermochemistry and kinetics of the reaction between n-butyl peroxy and hydroperoxyl radicals. *Chemical Physics Letters, 810*, 140191. https://doi.org/10.1016/j.cplett.2022.140191

24 Wu, J., Chen, X., Peng, L. Y., Cui, G. & Xia, S. H. (2022). Excited-State Deactivation Mechanism of 3,5-bis(2-hydroxyphenyl)-1H-1,2,4-triazole: Electronic Structure Calculations and Nonadiabatic Dynamics Simulations. *The Journal of Physical Chemistry A*, *126*(25), 4002-4012. https://doi.org/10.1021/acs.jpca.2c02080

25 Yang, W.-Y., Yan, C.-C., Wang, X.-D. & Liao, L.-S. (2022). Recent progress on the excited-state multiple proton transfer process in organic molecules. *Science China Chemistry, 65*(10), 1843–1853. https://doi.org/10.1007/s11426-022-1375-y

26 Fukui, K. (1981). The path of chemical reactions — the IRC approach. *Accounts of Chemical Research*, *14*(12), 363–368. https://doi.org/10.1021/ar00072a001

27 Tomasi, J., Mennucci, B. & Cammi, R. (2005). Quantum Mechanical Continuum Solvation Models. *Chemical Reviews*, *105*(8), 2999–3094. https://doi.org/10.1021/cr9904009

28 Gaussian 16, Revision A.03, M.J. Frisch, G.W. Trucks et al. Gaussian, Inc., Wallingford CT, 2016.

29 GaussView, V. (2016). 6.1, Roy Dennington, Todd A. *Keith, and John M. Millam, Semichem Inc., Shawnee Mission, KS*, *201*.

30 Bächle, J., Marković, M., Kelterer, A.-M. & Grampp, G. (2017). Insights into the Hydrogen-Atom Transfer of the Blue Aroxyl. *ChemPhysChem*, *18*(20), 2932–2938. Portico. https://doi.org/10.1002/cphc.201700603

31 Yamamoto, T. & Kato, S. (2007). Ab initio calculation of proton-coupled electron transfer rates using the external-potential representation: A ubiquinol complex in solution. *The Journal of Chemical Physics*, *126*(22). https://doi.org/10.1063/1.2737048

32 Limbach, H. -H., Miguel Lopez, J. & Kohen, A. (2006). Arrhenius curves of hydrogen transfers: tunnel effects, isotope effects and effects of pre-equilibria. *Philosophical Transactions of the Royal Society B: Biological Sciences, 361*(1472), 1399–1415. https://doi.org/10.1098/rstb.2006.1872

Information about authors*

Kurmanova, Alfiya Faridovna (*corresponding author*) — Candidate of Chemical Sciences, Professor, Karaganda University of the name of academician E.A. Buketov, Universitetskaya street, 28, 100024, Karaganda, Kazakhstan; e-mail: alfiya_kurmanova@mail.ru, https://orcid.org/0000-0003-4548-8145

Abilkanova, Farida Zhumageldyevna — PhD student, Karaganda University of the name of academician E.A. Buketov, Universitetskaya street, 28, 100024, Karaganda, Kazakhstan; e-mail: Farida_b88@mail.ru, https://orcid.org/0000-0002-6894-5276

Pustolaikina, Irina Anatolevna — Candidate of Chemical Sciences, Associate Professor, Karaganda University of the name of academician E.A. Buketov, Universitetskaya street, 28, 100024, Karaganda, Kazakhstan; e-mail: ipustolaikina@gmail.com; https://orcid.org/0000-0001-6319-666X

Nikolskiy, Sergey Nikolaevich — Doctor of Chemical Sciences, Full Professor, Karaganda University of the name of academician E.A. Buketov, Universitetskaya street, 28, 100024, Karaganda, Kazakhstan; e-mail: sergeynikolsky@mail.ru; https://orcid.org/0000-0003-3175-6938

_____

*The author's name is presented in the order: *Last Name, First and Middle Names*